

The immune response to SARS-CoV-2 infection in tissue: A multi-omic spatial investigation

Dr Matthew Richard Pugh
University of Birmingham

PhD Thesis

Institute of Immunology and Immunotherapy
University of Birmingham
January 2023

UNIVERSITY OF
BIRMINGHAM

University of Birmingham Research Archive

e-theses repository

This unpublished thesis/dissertation is copyright of the author and/or third parties. The intellectual property rights of the author or third parties in respect of this work are as defined by The Copyright Designs and Patents Act 1988 or as modified by any successor legislation.

Any use made of information contained in this thesis/dissertation must be in accordance with that legislation and must be properly acknowledged. Further distribution or reproduction in any format is prohibited without the permission of the copyright holder.

Abstract

The SARS-CoV-2 virus primarily infects the lung and can induce a localised and systemic immune response, which in some patients, can be fatal. The virus can also infect other non-respiratory tissues such as the placenta. SARS-CoV-2 infection in the placenta is associated with fetal compromise and intra-uterine death. Whilst much work has been done to describe the systemic immune response to SARS-CoV-2 infection, little has been done to describe the immune response in primary tissue. Adopting a multi-modal, spatial profiling approach on fixed tissue specimens from post-mortem and pathology archives, I describe the characteristics of the immune response in COVID-19 lung tissue and COVID-19 placentitis. Multi-modal approaches contributing towards this deep phenotypic characterisation included bulk and spatial transcriptomics, multiplex immunohistochemistry, singleplex immunohistochemistry and RNAscope, enabling robust cross-validation.

Lung tissues from 8 post mortem COVID-19 patients were analysed and compared to diseased and normal controls. On histological assessment, the lungs of COVID-19 patients invariably showed diffuse alveolar damage, with varying degrees of fibrosis, vasculitis, thrombosis and secondary infection. SARS-CoV-2 virus was predominantly detected in early-stage disease within the epithelium and a small proportion of macrophages. Macrophages were the predominant immune cells, with less numerous infiltrations of granulocytes and lymphocytes. The immediate virus microenvironment was enriched for immune evasive PDL1 expressing macrophages and depleted of lymphocytes. Whilst virus was apparently cleared in later stage disease, the immune infiltrate appeared to increase. Collagens were upregulated in the interstitium of COVID-19 lungs, in particular collagen VI. Serum pro-collagen VI was measured in the serum of a cohort of living patients with variable severity COVID-19. Increased serum pro-collagen VI was associated with severe disease and poor outcome.

Placentas from 13 SARS-CoV-2 positive mothers histologically showed chronic histiocytic intervillitis (CHI) and massive peri-villous fibrin deposition (MPVFD) in most cases, with a small subset showing chronic villitis. Trophoblastic SARS-CoV-2 infection and intra-uterine death was exclusively associated with CHI/MPVFD. Trophoblastic SARS-CoV-2 infection, compared to diseased and normal controls, was associated with prominent M1 macrophage infiltration and enrichment for CD4⁺ T-cells and B-cells. Macrophages showed CXCL10 expression which is associated with immune cell recruitment and fibrin deposition. The immediate immune microenvironment showed enrichment for CD4⁺ T-cells and PDL1 expressing macrophages. Interferon responses were transcriptomically blunted in viral rich regions of the placenta. A subset of placentas from SARS-CoV-2 infected with CHI morphology showed no evidence of virus, which may represent viral clearance akin to lung infection.

In summary, both diseases are characterised by florid localised immune responses with prominent innate and adaptive immune cell infiltrates and marked alterations in tissue architecture. There are competing antiviral and immune evasive responses present in both infected tissue, which ultimately lead to the observed pathological changes. The changes observed in lung and placenta can be used to infer novel prognosticators and treatments. Specifically, the elevated collagen VI signature observed in post-mortem lung translates into a novel serum-based prognosticator for mortality in hospitalised COVID-19 patients. Furthermore, the observed upregulation of CXCL10 in macrophages in COVID-19 placentitis could represent a novel therapeutic target.

Overall, the study demonstrates how spatial profiling techniques can be harnessed to understand complex phenomena in fixed archival tissue, inferring data of clinical relevance.

Acknowledgements

I am grateful to the MRC, Jean Shanks/ Pathsoc and Birmingham Health Partners for funding my studies here in Birmingham, and all of the patients, families and deceased who have contributed to the study.

I'd like to say thank you to my supervisors Dr Graham Taylor and Prof Paul Murray for your unwavering support. Also, a thanks to Dr Neil Steven and Dr Lalit Pallan for your support on the clinical side.

I'd like to say a special thank you to my ever supportive and long-suffering partner Alys and our beautiful daughter Heulwen, for keeping me going when times were tough. Finally, I'd like to dedicate this thesis to my parents, Marlene and Derrick Pugh. Without their love and support I never would have made it this far.

Contents

Chapter 1 Introduction	12
1.1 The COVID-19 pandemic and the SARS-CoV-2 virus	13
1.1.1. <i>Global impact of the pandemic</i>	13
1.1.2. The SARS-CoV-2 virus and COVID-19	13
1.2. Clinical characteristics of COVID-19 infection	14
1.3. The systemic immune response to SARS-CoV-2 infection	16
1.4 Local immune response to COVID-19 infection in lung	17
1.5. SARS-CoV-2 and the placenta	18
1.6. The problem	20
1.7. Aim of the study	21
Chapter 2 Materials and methods	22
2.1. Materials, reagents & Resources	23
2.2. Ethical and regulatory approvals	30
2.3. Tissue samples and clinical data acquisition	30
2.3.1. Post-mortem tissue samples from fatal COVID-19	30
2.3.2. Serum samples from COVID-19 patients and controls.	31
2.3.3 Tissue samples from COVID-19 placentitis cases	31
2.4. Histopathological assessment	31
2.5. Immunohistochemistry	32
2.5.1. Chromogenic immunohistochemistry	32
2.5.2. Multiplex immunohistochemistry – Akoya CODEX Phenocycler	32
2.4.3. Multiplex immunohistochemistry – Lunaphore COMET	34
2.5. Spatial transcriptomics	36
2.5.1. Nanostring GeoMX digital spatial profiling	36
2.5.2. RNAscope.	37
2.6. Bulk Quantseq RNA sequencing	38
2.7. T-cell receptor sequencing	39
2.8. Virus variant identification	40
2.9. Fluorescent in-situ hybridisation for X/Y chromosomes.	40
2.10. SARS-CoV-2 infection of VERO cells	40
2.11. Serum ELISA assays	41
2.12. Computational and statistical analysis	42
2.12.1. Multiplex immunohistochemistry image pre-processing	42
2.12.2. Phenotyping & virus identification	42
2.12.3. Virus microenvironment quantification	43

2.12.4. Collagen content quantification	43
2.12.5. Spatial Transcriptomic Pre-processing & Analysis.....	43
2.12.6. RNAscope FISH Analysis	44
2.12.7. QuantSeq RNA Alignment & Analysis.....	45
2.12.8. Differential Gene Expression & Pathway Analysis.....	46
2.12.9. TCR sequence alignment	46
2.12.10. Serum Proteomic Analysis.....	46
2.12.11. COMET mIHC image processing and analysis	47
Chapter 3 The immunopathology of fatal COVID-19 respiratory infection	50
3. The immunopathology of fatal COVID-19 respiratory infection.....	51
3.1. Clinicopathological characteristics	52
3.1.1. Clinical characteristics	52
3.1.2. Macroscopic and histopathological characteristics.....	53
3.1.3. Assimilation of clinicopathological features.....	55
3.2. Virus detection	55
3.2.1. SARS-CoV-2 virus protein detection by CODEX multiplex immunohistochemistry.....	56
3.2.2. SARS-CoV-2 virus detection by Quantseq bulk transcriptomic sequencing	57
3.2.3. SARS-CoV-2 virus detection by Nanostring GeoMx digital spatial profiling	59
3.2.4. SARS-CoV-2 virus detection by RNAscope <i>in-situ</i> hybridisation	61
3.2.5. Cross validation of SARS-CoV-2 virus detection	62
3.3. Immune cell composition in COVID-19 lungs.	63
3.3.2. Estimation of cell abundance based on deconvoluted GeoMX DSP.....	63
3.3.3. Determination of cell composition by CODEX multiplex immunohistochemistry	64
3.3.4. TCR sequencing	69
3.4. SARS-CoV-2 virus microenvironment and inflammatory drivers.....	73
3.4.1. Characterisation of the virus niche by CODEX mIHC.	73
3.4.2. Tissue wide virus-associated changes by bulk sequencing.....	75
3.4.2. Characterisation of virus niche by Nanostring GeoMx.....	76
3.4.3. IL6 expression in the viral niche by RNAscope	77
3.4.4. Assimilation of SARS-CoV-2 microenvironment data.	78
3.5. Discussion and conclusions	79
Chapter 4 Characterisation of the collagen microenvironment and its prognostic role of in COVID-19 respiratory infection	83
4. Characterisation of the collagen microenvironment and its prognostic role in COVID-19 respiratory infection.....	84
4.1. Spatial gene expression of collagen genes in COVID-19 post-mortem lung.....	85

4.1.1. Pseudo-bulk gene expression of collagen genes by Nanostring GeoMx	85
4.1.2. Spatial analysis of collagen gene expression by Nanostring GeoMx	86
4.1.3. Temporal analysis of collagen gene expression by Quantseq bulk sequencing	89
4.1.4. Assimilation of collagen gene expression data.....	89
4.2. Characterisation of collagen protein in COVID-19 post-mortem lung.....	90
4.2.1. Chromogenic single plex.....	90
4.2.2. COMET multiplex immunohistochemistry of collagen deposition	91
4.3. Serum collagen VI is increased hospitalised COVID-19 patients and is a biomarker for mortality	92
4.3.1. Serum ELISA measurements of collagen breakdown and synthesis.	94
4.3.2. Temporal changes in serum collagen.	96
4.3.3. Serum collagen markers and outcome.....	99
4.4. Discussion and conclusions	104
Chapter 5 The immunopathology of COVID-19 placentitis.	107
5. The immunopathology of COVID-19 placentitis.	108
5.1. Clinicopathological characteristics	109
5.1.1. Clinical characteristics	109
5.1.2. Histopathological characteristics.....	111
5.1.3. Clinicopathological correlation.....	114
5.2. Virus detection	115
5.2.1. Virus RNA detection by Quantseq bulk RNA sequencing	115
5.2.2. Virus RNA detection by RNA scope.....	116
5.2.3. Virus detection by chromogenic single-plex immunohistochemistry.....	117
5.2.4. Virus protein detection by multiplex immunohistochemistry	118
5.2.4. Determination of virus strain	121
5.2.5. Virus entry receptors expression.....	121
5.3. Immune infiltrate	123
5.3.1. Qualitative assessment of the immune infiltrate	123
5.3.2. Quantitative assessment of the immune composition.....	125
5.2.3. Detailed quantitative analysis of T-cells.....	128
5.2.4. Detailed quantitative analysis of macrophages.....	129
5.4. Inflammatory pathways	133
5.4.1. Gene set enrichment analysis and interferon stimulated genes.....	134
5.4.2. Spatially resolved gene expression of interferon genes.....	136
5.5. SARS-CoV-2 virus niche in COVID-19 placentitis.....	137
5.5.1. SARS-CoV-2 virus niche analysis by COMET mIHC.....	137

5.5.2. SARS-CoV-2 virus niche analysis by GeoMx DSP	139
Discussion and conclusions	140
Chapter 6 Discussion and future work.	146
6.1. Comparison of the tissue immune response to SARS-CoV-2 in lung and placenta	147
6.2. Role of the autopsy, archival specimens and spatial profiling	148
6.3. Limitations of the study.....	149
6.4. Future work	149
Chapter 7 References	151
Chapter 8 Appendices	163
Appendix 1: Nanostring GeoMx lung experiment design and validation	164
Appendix 2: RNAscope QC	165
Appendix 3: Validation of SARS-CoV-2 antibodies and probes	166
Appendix 4: Assimilation of virus detection data.....	167
Appendix 5: Detailed TCR data.....	168
COVID-19 Lung early stage case 1	168
COVID-19 lung early stage case 2.....	174
COVID-19 lung late stage case 1.....	181
COVID-19 lung late stage case 2.....	188
COVID-19 lung late stage case 3.....	195
COVID-19 lung late stage case 4.....	202
MERS lung.....	209
Rhinovirus lung.....	216
Non-virus lung case 1	222
Non-virus lung case 2	229
Non-virus lung case 3	236
Non-virus lung case 4	242
Non-virus lung case 5	248
Tree plots of TCR sequences.....	254
Appendix 6. Collagen gene expression in the blood vessel compartment.....	256
Appendix 7: Serum ELISA blood clot and neutrophil markers.....	257

Table of figures

Figure 1-1 (A). Schematic representation of the SARS-CoV-2 genome and(B) the assembled virus.....	14
Figure 3-1. Experimental overview of the immunopathological characterisation of COVID-19 lungs, including cohorts, samples, assays and analysis.....	52

Figure 3-2. Summary of clinical course, demographics and pathological features of the COVID-19 respiratory infection cohort.....	52
Figure 3-3. Histopathological features of COVID-19 respiratory infection across the disease timeline. Diffuse alveolar damage DAD of varying maturity is seen in all cases, whilst other pathological features such as thrombosis, secondary infection and vasculitis is enriched in late phase disease....	54
Figure 3-4. Dual spike and nucleocapsid staining by CODEX mIHC. Double spike and nucleocapsid staining in an epithelial cell is shown. Note other cells showing spike-only staining which was regarded as a false negative.	56
Figure 3-5. A. case-by-case plot of the number of SARS-CoV-2 virus positive cells showing double spike and nucleocapsid staining by IHC. Only three cases of early phase COVID-19 lung showed SARS-CoV-2 protein expression. B. Summary bar and whisker plot of positive virus staining in early stage and late stage COVID-19 lung, and non-COVID-19 controls.	57
Figure 3-6. Viral load assessed by Quantseq bulk gene expression profiling	58
Figure 3-7. SARS-CoV-2 virus gene expression in COVID-19 lung. Expression is predominantly seen in early stage disease	58
Figure 3-8. Pseudo-bulk analysis of SARS-CoV-2 gene expression by Nanostring GeoMx DSP showed virus gene expression in early stage COVID-19 lung only	60
Figure 3-9. Interrogation of Nanostring GeoMx SARS-CoV-2 gene expression by compartment showed evidence of virus expression in the alveolar compartment of early stage disease only.	61
Figure 3-10. Virus spike mRNA transcripts were detected by RNAscope in AE1/AE3+ epithelial cells (yellow arrows) and in AE1/AE3- non-epithelial cells (red arrows), likely macrophages.	62
Figure 3-11. Correlation analysis of SARS-CoV-2 virus loads/virus infected cells detected across different modalities.	62
Figure 3-12. Cell deconvolution of the Nanostring GeoMx data shows the relative abundances of various cell types in COVID-19 lung and non-COVID-19 controls.	64
Figure 3-13. Qualitative assessment of CODEX mIHC images in COVID-19 lung showed intra-alveolar infiltrates of macrophages and sparser interstitial infiltrates of lymphocytes.	65
Figure 3-14. Qualitative assessment of the abundance of immune cell subsets in early vs late stage COVID-19 lungs.....	66
Figure 3-15. CELESTA cell phenotype annotation of four phenotypes from CODEX mIHC staining	67
Figure 3-16. A. A tSNE plot displaying the relative frequencies immune cell subsets present in the four analysed COVID-19 lungs. B. Relative cell abundances in various regions of COVID-19 lungs.	68
Figure 3-17. Immune subset abundance of major subsets according to length of illness.....	69
Figure 3-18. Measures of TCR diversity comparing (A) clone count and (B) Shannon diversity in COVID-19 lung vs non-COVID-19 controls.	70
Figure 3-19. Comparison of (A) Shannon diversity and (B) richness of TCR sequences in early and late COVID-19 lungs.....	70
Figure 3-20. Measures of diversity, (A) clone count and (B) Shannon diversity, plotted against T-cell abundance determined by CODEX mIHC.....	71
Figure 3-21. Bar plot showing the proportion of TCR sequences according to their relative proportion in.....	72
Figure 3-22. Frequencies of TCR sequences with known specificities for viruses according to three databases.	73
Figure 3-23. Immune cells identified by CD45 positivity were significantly reduced in the immediate microenvironment of SARS-CoV-2 infected epithelial cells compared to the microenvironment of non-infected epithelium from the same patients.	74
Figure 3-24. Immune cell abundances in the immediate virus positive and negative microenvironment.....	74

Figure 3-25. CODEX mIHC image showing aggregates of PDL1 and IDO expressing macrophages adjacent to virus (nucleocapsid NCP) infected epithelial cells	75
Figure 3-26. Volcano plot of Quantseq bulk sequencing comparing tissue wide gene expression in SARS-CoV-2 infected vs non-infected lung	76
Figure 3-27. Virus RNA expression by Nanostring GeoMx. Alveolar regions with virus expression over 250 were regarded as virus high, and regions with expression below 250 virus low.	77
Figure 3-28. (A) Differential gene expression comparing virus-high and virus-low alveolar lung regions. (B) Pathway analysis of gene sets upregulated in virus-high regions of lung	78
Figure 3-29. IL6 expression on RNAscope comparing SARS-CoV-2 infected regions with non-infected regions from the same lungs.	78
Figure 3-30. Summary of the immune microenvironmental changes observed within the SARS-CoV-2 positive niche compared to virus negative lung regions	79
Figure 4-1. Schematic overview of the collagen characterisation and clinical validation in COVID-19 lung	85
Figure 4-2. Volcano plot showing differential gene expression of a pseudobulk GeoMx analysis comparing COVID-19 lung with normal lung	86
Figure 4-3	87
Figure 4-4. Pan-collagen gene expression in the alveolar compartment by GeoMx DSP shows upregulation of collagens in SARS-CoV-2 and MERS.	87
Figure 4-5. Pan-collagen gene expression in the alveolar compartment by GeoMx DSP shows more prominent upregulation of collagens in late stage COVID-19 lungs compared to early stage disease.	87
Figure 4-6. Bar and whisker plot showing expression of specific collagen in the alveolus based on GeoMx DSP gene expression	88
Figure 4-7. Correlation analysis of macrophage activation markers and collagen genes in the alveolar space based on GeoMx DSP	88
Figure 4-8. Association with length of illness and collagen gene expression based on Quantseq bulk gene expression data.	89
Figure 4-9. Single-plex chromogenic staining for collagen VI showed increased collagen deposition in the alveolar wall of COVID-19 lungs compared to normal controls.	90
Figure 4-10. COMET multiplex immunohistochemistry showed increased collagen VI deposition in the alveolar wall	91
Figure 4-11. Fluorescent mIHC images showing increased collagen IV and VI in the alveolar walls of COVID-19 lung compared to normal control lungs (inset).	92
Figure 4-12. Quantitative analysis of collagen VI and VI deposition showed increased collagen content in early stage COVID-19 lungs compared to late stage COVID-19 lungs and normal controls.	92
Figure 4-13. Schematic overview of the serum measurement of collagen metabolism in COVID-19 patients	93
Figure 4-14. Principle component analysis shows acute hospitalised and acute ITU patients form separate clusters based on ELISA analysis of serum markers of collagen, neutrophil and thrombosis data.	94
Figure 4-15. Comparative levels of serum biomarkers of collagen synthesis and breakdown across the cohorts.	96
Figure 4-16. Temporal association between duration of illness and collagen biomarkers of synthesis and degradation	99
Figure 4-17. Collagen biomarkers comparing acute hospitalised and ITU patients who died with those that survived	102

Figure 4-18. Survival curve for all ITU and non-ITU hospital patients combined, divided into serum collagen VI synthesis high vs low groups.....	103
Figure 4-19. Survival curve for ITU COVID-19 patients comparing collagen VI high vs low serum levels.	103
Figure 4-20. Survival curve for non-ITU hospital patients combined comparing collagen VI high vs low	104
Figure 5-1. Experimental overview of the multi-modal characterisation of COVID-19 placentitis.....	109
Figure 5-2. Summary of the clinic-pathological features of 13 SARS-CoV-2 infected mothers with obstetric complications.....	110
Figure 5-3. Macroscopic assessment of placentas from SARS-CoV-2 positive mothers showed widespread lesional involvement in 9/13 cases with extensive fibrin deposition in a 'lace-like' pattern.....	112
Figure 5-4. Two patterns of pathology were observed amongst SARS-CoV-2 infected mothers- CHI/MPVFD and CV predominant.	113
Figure 5-5. Trophoblast necrosis in COV19 ^{CHI} showing circumferential involvement of the placental trophoblast.	113
Figure 5-6. Single-plex chromogenic immunohistochemistry showing macrophages (CD68+) palisading and closely abutting the placental villi compared to (inset) control ^{CHI} which has macrophages in the middle of the maternal space.....	114
Figure 5-7. Comparison of complications associated with CHI and CV predominant pathologies shows that IUD is strongly associated with CHI pathology	115
Figure 5-8. Quantseq bulk RNA sequencing showing SARS-CoV-2 gene expression in placentas from SARS-CoV-2 positive mothers and controls.	116
Figure 5-9 . Dual RNAscope against 'orf1ab' sense and 'spike' anti-sense RNA showed co-localisation of expression in the syncytiotrophoblast in 6/13 Cov19 placentas (A). Pseudo-chromogenic image processing shows isolated spike (B) and more abundant orf1ab (C) expression, consistent with active viral replication	117
Figure 5-10. Chromogenic immunohistochemistry for SARS-CoV-2 spike showed virus protein expression in the trophoblast of 6 placentas (left panel), the remainder were negative (right panel)	118
Figure 5-11. COMET mIHC image showing co-expression of spike and nucleocapsid proteins in the cytotrophoblast (AE1/AE3) positive trophoblast layer.	119
Figure 5-12. Quantitative analysis of the COMET mIHC images shows that virus protein is present mostly in the trophoblast layer, and in a small proportion of macrophages.	119
Figure 5-13. COMET mIHC images showing expression of virus protein in macrophages abutting the virus infected trophoblast.....	120
Figure 5-14. Predominant SARS-CoV-2 viral strains in the community at the time of placental sampling	121
Figure 5-15. SARS-CoV-2 viral entry receptor expression by Nanostring GeoMx DSP.	122
Figure 5-16. COMET mIHC images showing an altered tram-track maternal and ante-luminal distribution of ACE2 expression in a representative Cov19 placenta compared to the ante-luminal ACE2 expression present in a control placenta.	123
Figure 5-17. COMET mIHC image showing massive perivillous fibrin and macrophages abutting virus infection trophoblast (white arrow). Control placenta inset.....	124
Figure 5-18. COVID-19 placentitis showing a mixed population of macrophages and lymphocytes (white arrows)	125
Figure 5-19. Validation of metaclusters using the mIHC images.	126
Figure 5-20. Metaclusters identified on quantitative assessment of mIHC images.	126

Figure 5-21. tSNE plot representing the 10 metaclusters identified on quantitative analysis of mIHC images.	127
Figure 5-22. PCA showing SARS-CoV-2 placentas forming a unique cluster (right). Inspection of the loads (left) shows the features responsible for the unique clustering.....	127
Figure 5-23. Abundances of the key cell and immune subtypes based on COMET mIHC images.....	128
Figure 5-24. Co-expression of immune markers in CD4+ and CD8+ placental T-cells based on COMET mIHC images.....	129
Figure 5-25. M1:M2 macrophage ratio based on COMET mIHC imaging.....	130
Figure 5-26. COMET mIHC image showing M1 polarised macrophages in the intervillous space and M2 macrophages in the villous stroma.	131
Figure 5-27. Upper panel: Stromal macrophages showing an XY complement of chromosomes. Lower panel: Intervillous macrophages showing an XY complement of chromosomes.	131
Figure 5-28. Marker co-expression on M1 and M1 macrophages based on mIHC images.	132
Figure 5-29. RNAscope showing highly upregulated expression of CXCL10, IL6 and IL8 in P+COV19 ^{CHI} compared to controls.....	133
Figure 5-30. RNAscope for CXCL10 combined with CD68 IHC shows that CXCL10 and IL8 are abundantly expressed in macrophages.	133
Figure 5-31. Gene set enrichment analysis showing pathways upregulated in P+COV19CHI placentas compared to all other groups.....	135
Figure 5-32. ISGs show enriched expression in P+Cov19 placentas compared to controls.....	135
Figure 5-33. Gene expression of SARS-CoV-2 restriction factors by Quantseq bulk sequencing	136
Figure 5-34. Comparison of bulk sequencing expression of interferon genes compared to spatially resolved expression.....	137
Figure 5-35. Assessment of the viral immune niche by COMET mIHC.	138
Figure 5-36. COMET mIHC image showing enrichment of PDL1+ macrophages in the vicinity of SARS-CoV-2 infected trophoblast.....	139
Figure 5-37. Differential gene expression in virus high vs virus low region of the same placenta by GeoMx DSP.....	140
Figure 5-38. Summary of the main findings in COVID-19 placentitis.....	141
Figure 5-39. Analysis of the temporal relationship between length of illness and viral load.....	142

Chapter 1 Introduction

1.1 The COVID-19 pandemic and the SARS-CoV-2 virus

1.1.1. *Global impact of the pandemic*

The WHO was informed of outbreak of pneumonia in Wuhan, China, in December 2019. By January 30th 2020, the WHO had declared that the SARS-CoV-2 epidemic was a public health emergency of international concern, and by February COVID-19 was declared a pandemic (Sun et al., 2020). Since the beginning of the pandemic in 2020, COVID-19 has had a devastating human and economic impact worldwide (Belitski, 2022). Over 6.6M deaths have been confirmed from COVID-19 as of November 2022, with an estimated overall death toll that is in excess of 4 times this figure (Karlinsky, 2021). The impact of the disease has also been compounded in developing countries, where lack of resources has hampered efforts to combat the virus. (Levin et al., 2022). Consequently, the burden of the disease in these countries has been far greater.

1.1.2. The SARS-CoV-2 virus and COVID-19

COVID-19 is the respiratory illness caused by the SARS-CoV-2 coronavirus. The virus belongs to the betacoronavirus lineage and shares 79.5% sequence homology with SARS-CoV (Wang et al., 2020b). Betacoronaviruses contain a positive single stranded RNA genome within a capsid (Mariano et al., 2020) (Figure 1-1 A). This capsid comprises the nucleocapsid protein which is surrounded by a membrane containing three further proteins; membrane protein, spike protein and envelope protein. The virus infects bronchial epithelial cells and type-II pneumocytes through interactions between the viral spike protein with cellular angiotensin converting enzyme (ACE-2) in the same way previously described SARS-CoV (Khan et al., 2020); SARS-CoV and SARS-CoV-2 spike proteins show only minor structural differences. Spike is a transmembrane homotrimer that protrudes from the viral surface, and comprises two functional subunits; S1 and S2. S1 comprises the N-terminal domain (NTD) along with

the receptor binding domain (RBD), and functions to bind the ACE2 receptor. Following bindings, S2 functions to fuse the membrane of the virus with host cell. The S protein has two forms; open and closed. When open, the spike protein protrudes from the viral surface and the RBD is present in the up position to enable binding with the ACE2 receptor. TMPRSS2 and TMPRSS4 are serine proteases specific to the mucosa, and facilitate fusion of the spike protein with ACE2. These proteins are critical for the pathogenesis of the virus.

These four structural proteins are complimented by a further 16 non-structural proteins (nsp1-16), which are involved in diverse functions such as RNA processing and replication (Nsp1), survival signaling (Nsp2), polyprotein replication (Nsp5), ssRNA binding (Nsp9) and proofreading (Nsp14).

The SARS-CoV-2 virus genome is made up of 13-15 open reading frame (ORFs), which include 12 functional ORFs (Figure 1-1 B). In 5' to 3' order, the genome is arranged as replicase and protease (ORF1a and ORF1b), followed by spike, envelope, membrane and nucleocapsid proteins (Mariano et al., 2020). ORF1a and 1b encode two polyproteins (pp), namely pp1a and pp1ab, the latter of which is encoded by a ribosomal frame shift mechanism of the ORF1b gene. These polyproteins are processed by viral proteases to yield 16 non-structural proteins. The genes that encode the structural proteins and other interspersed ORFs are contained in the 3' one third of the viral genome, and are transcribed from the 3' end. These form a set of nested sub-genomic mRNAs (sg mRNA) which give rise to the respective proteins.

The virus life cycle is complex (Figure 1-1 C). First, virions bind the ACE2 receptor of the host cell via the spike protein(Khan et al., 2020). Helped by host factors such as TMPRSS2, the virus fuses with the cell membrane, and is take into cell via an endosome. Next, the virus genomic RNA is uncoated and released, leading to translation of ORF1a and ORF1b at the

endoplasmic reticulum. This gives rise to polyproteins pp1a and pp1ab, which are co-translationally and post-translationally processed into the 16 Nsp (Wang et al., 2020b). Alongside nsp translation, viral replication organelles are created within the endoplasmic reticulum, called 'double membrane vesicles' (DMV), 'convoluted vesicles' (CM), and 'double membrane spherules' (DMS). These provide a protective environment for viral genomic RNA replication and transcription of sg mRNA. These sg mRNA give rise to the structural proteins which translocate into the endoplasmic reticulum membrane and transit through the ER-to-Golgi intermediate compartment (ERGIC). Here, the translated structural proteins interact with N-encapsidated genomic RNA, resulting in budding of secretory vesicular compartments. Virions are finally secreted from the cell by exocytosis.

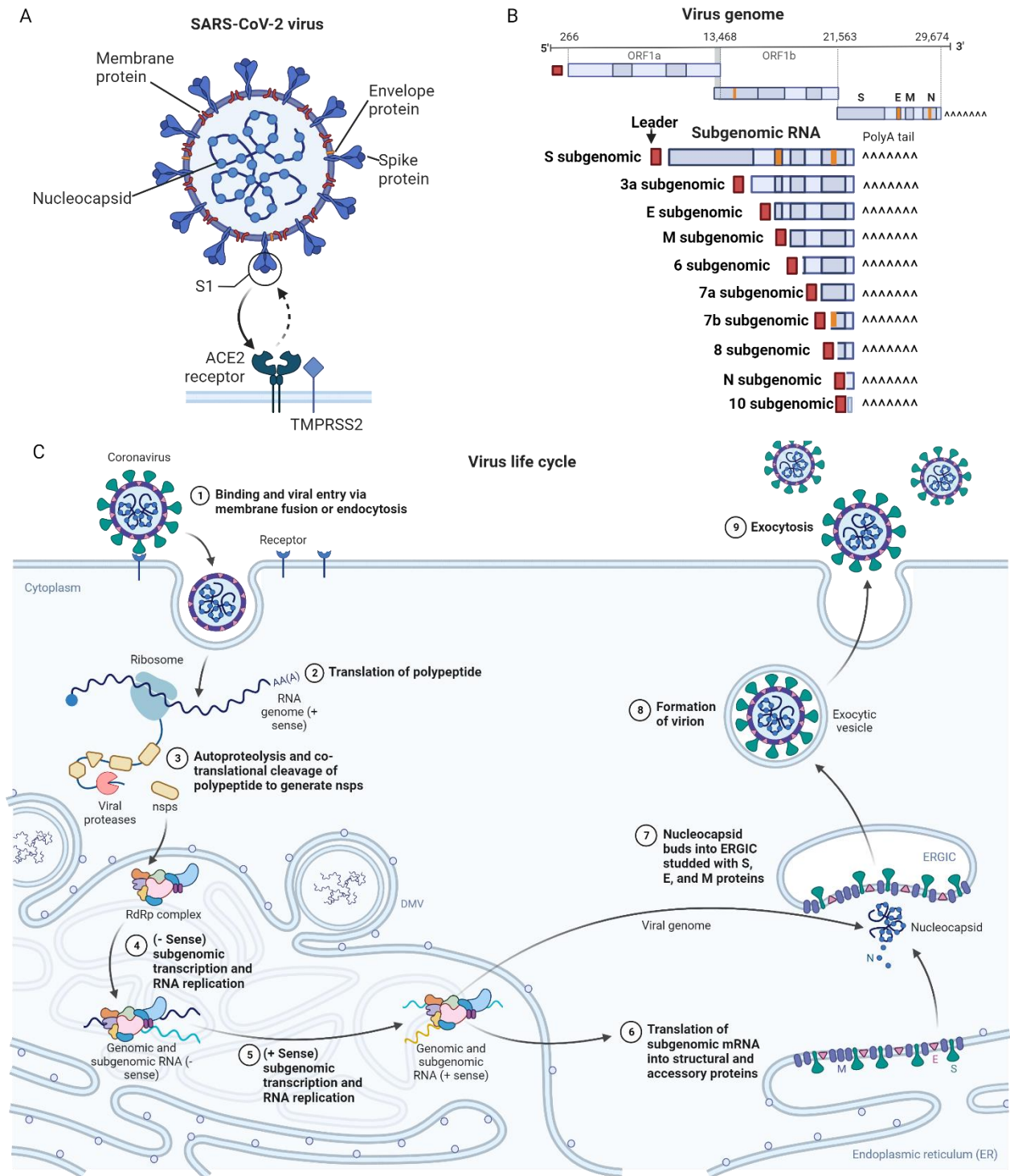


Figure 1-1 (A). Schematic representation of the SARS-CoV-2 viral proteins and structure. Viral entry into human epithelial cells is mediated via the S1 subunit of the spike protein, which binds to cellular ACE2, aided by TMPRSS2/4 (B) The SARS-CoV-2 genome comprises 12 functional open reading frames (ORFs). ORF1a and ORF1b give rise to 16 non-structural proteins (nsp). The 3' third of the genome codes for structural proteins, which are translated via subgenomic mRNAs (sg mRNAs). (C) The virus life cycle is complex (see text) and starts with the virus binding the cellular membrane via spike, followed by viral replication and finally, exocytosis of new virions. Key: S = spike; E = envelope; M = membrane; N = nucleocapsid; RdRp = RNA-dependent RNA polymerase; ERGIC = ER to Golgi intermediate compartment (created with Biorender).

1.2. Clinical characteristics of COVID-19 infection.

The clinical response to SARS-CoV-2 is highly variable and mainly observed in adults (Khan et al., 2020). The clinical manifestation of SARS-CoV-2 is termed COVID-19 and comprises moderate fever (typically up to 38.5°C, but minorities with <37.3°C or >39°C), cough (dry or white sputum), dyspnoea or chest tightness, sore throat, rhinorrhoea, headache, nausea, myalgia, uncommonly diarrhoea (Han et al., 2020). More severe patterns manifest as pneumonia, with radiological patterns affecting from one to five lobes. Associated features may be a moderate leucopenia and lymphopenia and raised C-reactive protein (CRP), a marker of inflammation. Covid-19 pneumonia may progress to acute respiratory distress syndrome (ARDS) characterised by extensive pneumonia, hypoxia (reduction of O₂ in the blood) and later hypercapnia (a build-up of CO₂ in the blood). Asymptomatic incubation period is 1-14 days. Clinical series indicate a range of outcomes, with >80% cases experiencing no or mild symptoms, 15% pneumonia, 5% ARDS and around a 2-3% mortality. There is a clear association between increasing age and increasing severity of covid-19, with mean ages by case severity reported as 29 years (mild), 44.5 years (common), 54.7 years (severe) and 65.7 years (critical). Modelling shows a powerful effect of age on case fatality rate (CFR), with a low CFR of 0.004% for those aged less than 34, rising to 0.068% in 35-44 year olds, 0.23% in 45-54 year olds, 0.75% in 55-64 year olds, 2.5% in 65-74 year olds, 8.5% in 75-84 year olds, and 28.3% if >85 year olds (Levin et al, 2020).

The radiological findings in the lungs of COVID-19 patients are well described (Han et al., 2020). In severe cases, the radiological signs of acute respiratory distress syndrome (ARDS) are ubiquitous. One report of 108 patients with mild (i.e. not ARDS) features showed involvement of two or more lobes (65%), patchy ground glass opacities (GGO) with (86%), or without (42%), consolidation, vascular thickening (80%), crazy paving pattern (scattered or

Page 17 of 261

diffuse ground-glass attenuation with superimposed interlobular septal thickening and intralobular lines - 40%), air bronchogram (48%) and halo sign (GGO surrounding a mass or nodule - 69%). No patient had mediastinal or hilar enlargement, pleural effusion, or pleural thickening. Radiological changes were generally more pronounced in lower lobes. One case showed a pleural effusion. Less severe cases appeared to mainly show ground glass opacities or halo signs. In severe or critical cases, multiple patches or an integrated larger patch of GGO, consolidation or mixed consolidation and ground glass opacity might have presented in bilateral lungs, and consolidation and thickened interlobular septa were linked to greater severity (13).

1.3. The systemic immune response to SARS-CoV-2 infection

The clinical response, and therefore the underlying immunobiological reaction, to SARS-CoV-2 infection is variable, ranging from mild, to a severe life-threatening immune reaction characterised by ARDS, cytokine storm and associated multiorgan failure (Cao, 2020). Clinical laboratory investigations show a higher CRP in severe cases, lymphopenia in 30-75% of cases and eosinopenia in approximately 50% of cases. It is unclear if lymphopenia is the result of immune cell sequestration into affected tissues, or other cytokine mediated mechanisms. A subset of patients with severe COVID-19 disease show a haemophagocytic lymphohistiocytosis (HLH)-like syndrome. HLH is a group of hyperferritinaemic, hyperinflammatory syndromes which are classified into primary (familial with a genetic aetiology) and secondary, with a range of underlying aetiologies (Retamozo, *et al*, 2021). Virus infections are commonly associated with secondary HLH, including Epstein Barr virus and various respiratory viruses. In such cases, breakdown of tolerance to self-antigens is considered a potential mechanism of HLH development. Regardless of the underlying aetiology, HLH is characterised by a common

Page 18 of 261

terminal pathway in which excess cytokine production result in persistent fever, progressive cytopenias and multiorgan dysfunction. Circulating proinflammatory cytokines typically associated with haemophagocytic lymphohistiocytosis (HLH), such as IL2, IL6, IL7, G-CSF and TNF-alpha are seen in a subset of severe COVID-19 cases. Higher levels of cytokines have been associated with lower lymphocyte counts (Zhang et al., 2020). Other features typical of HLH such as raised ferritin are also observed in association with a poor prognosis. Low blood counts are also part of HLH syndromes and may explain the lymphopenia seen in COVID-19. Deeper analysis of the lymphopenia seen in severe COVID-19 shows a reduction of CD4, CD8, NK cells and B- cells in the peripheral blood. Markers of exhaustion such as NKG2A have been shown to be upregulated on CD8 and NK cells. Following treatment, higher CD8 counts and lower CD4:CD8 ratio is an indicator of a better prognosis (Cao, 2020; Wang et al., 2020b). This may be due to the function of CD8+ T-cells, which are involved in the direct elimination of virus infected cells (Urra, et al, 2020). Furthermore, failure to mount an effective adaptive response with high numbers of virus-eliminating CD8+ T-cells, may favour higher levels of inflammation and poor outcome. Following the acute phase of infection, a short-lived antibody response and a longer-lived T- cell response has been described, which has important implications for vaccination design (Peng et al., 2006). SARS coronavirus (SARS-CoV) B-cell and T-cell epitopes have been defined experimentally and cognate immune responses can be detected using *ex vivo* assays in blood from previously infected individuals (Ahmed, et al, 2020). A substantial number of these SARS-CoV spike and nucleocapsid epitopes map onto the same epitopes in SARS-CoV-2, are conserved between the two viruses, and are restricted by common HLA alleles. These epitopes show no variation amongst >120 SARS-CoV-2 sequences currently available. Additional SARS-CoV-2 specific epitopes likely exist, however, the conservation of epitopes between various coronavirus strains means that patients may harbor cross-reactive responses due to previous exposure to other pre-pandemic viruses.

1.4. Local immune response to COVID-19 infection in lung

The diagnosis of SARS-CoV-2 infection and COVID-19 is based on clinical assessment, radiology and laboratory investigations. Lung biopsy is not required for any diagnostic or prognostic element in the management of the disease. Consequently, far less is known about the local immune response in tissue compared to the systemic immune response.

Despite this, clinical and radiological data combined with reports from a few post-mortem studies have offered some insight into the activity of SARS-CoV-2 and the associated immune response in tissue. The common radiological manifestation of COVID-19 in the lung comprising patchy, ground glass opacities, is consistent with the clinical picture of ARDS. This has been confirmed on histological assessment in the limited number of post-mortems published to date, which show diffuse alveolar damage (DAD)(Barton et al., 2020). DAD is said to be the morphological manifestation of ARDS and is seen in conjunction with variable lymphocytic infiltrate. The lymphocytic infiltrate in lung is predominantly CD4+. Infiltration of megakaryocytes, platelet precursors typically found in the bone marrow, have also been described in COVID-19; the significance of which is uncertain. One report described hyaline microthrombi in the microvasculature of the lung (Allotey et al., 2020; Xu et al., 2020). This may be indicative of a hypercoagulable state. Type II pneumocytes are the proposed cell to which the SARS-CoV-2 virus binds in the lung. Hyperplasia and desquamation (sloughing off of pneumocytes into the respiratory lumen) of these type II pneumocytes are constant features of COVID-19 pneumonitis in the published literature.

Many reports have described cardiac injury and presumed myocarditis in COVID-19, with associated elevation in cardiac enzymes. Many mechanisms have been postulated for these changes including increase metabolic demand and direct effects of the virus. The viral

receptor ACE2 is expressed on the myocardium and may facilitate a viral myocarditis. Histological descriptions of the heart in COVID-19 have included patchy myocyte necrosis and an associated lymphocytic infiltrate.

In addition to respiratory symptoms, a proportion of COVID-19 patients experience gastrointestinal symptoms (Barton et al., 2020). Again, this is postulated to be due to the presence of ACE2 receptor on gastrointestinal epithelial cells. Furthermore, high levels of viral load have been measured in the gastrointestinal tract for long periods following infection. It is unclear at present whether there is active viral transcription in the gut and whether the shed virus is infectious. In severe cases of COVID-19, liver failure has been described. This may be due to the generalised effects of a systemic inflammatory response and it is unclear at this stage whether the virus has a direct effect on the liver.

There are no reports describing detailed immune phenotyping in tissue, or, correlating immune response with viral and cellular gene expression. Furthermore, the clinical correlates of the immune infiltrate are yet to be revealed.

1.5. SARS-CoV-2 and the placenta

SARS-CoV-2 has been shown to infect a number of extrapulmonary sites, including the placenta. The placenta is an anatomical barrier between maternal and fetal circulations. Placental integrity is vital to protect the fetus from infection and to prevent immune rejection of the semi-allogeneic fetus. Structurally, the placenta predominantly comprises fetal-derived villi lined by a bilayer of cytotrophoblasts and a fused syncytiotrophoblast layer collectively referred to as the trophoblast layer. These villi, which contain circulating fetal blood, invade the maternal uterine decidua and are surrounded by the intervillous space

through which maternal blood flows allowing nutrient and gas exchange to occur. Diverse mechanisms operate at the maternal-fetal interface to prevent or limit virus infections (Hoo et al., 2020), including constitutive interferon responses, proinflammatory cytokine expression, the presence of maternal derived innate cells in the decidua and fetal derived macrophages, called Hofbauer cells, in the villous stroma (Wells and Coyne, 2018).

Several viruses cause harm to the fetus, either through the systemic effects of virus infection or, despite the placenta's anti-viral defenses, through direct infection of the placenta (Senegas et al., 2009; Yockey et al., 2018). COVID-19 infection during pregnancy is associated with an increased risk of serious obstetric complications which can include intrauterine growth restriction, premature labour and stillbirth (Allotey et al., 2020; Delahoy et al., 2020). In some cases, these adverse outcomes are due to the systemic effects of severe respiratory disease. However, recent case reports and series have described obstetric complications in association with a characteristic inflammatory pathology of the placenta, termed COVID-19 placentitis (Babal et al., 2021; Schwartz et al., 2022a). Notably, severe obstetric complications arising from COVID-19 placentitis, occur even in cases of mild or even asymptomatic maternal SARS-CoV-2 respiratory infection. COVID-19 placentitis has three characteristic pathological features: macrophage infiltration in the intervillous space, termed chronic histiocytic intervillitis (CHI); fibrin deposition in the intervillous space amounting to massive perivillous fibrin deposition (MPVFD); and extensive trophoblast necrosis (TN) (Watkins et al., 2021). These pathologies typically affect most of the placenta, leading to placental destruction and fetal demise in most cases (Schwartz, 2020). Some placentas from mothers with COVID-19 respiratory infection show other pathologies not widely regarded to fulfil the criteria for COVID-19 placentitis. These include inflammation of the fetal villous stroma, termed chronic villitis (CV) (Menter et al., 2021). The exact role SARS-CoV-2 plays in mediating COVID-19

placentitis is uncertain because the virus is only detectable in around one-half of affected placentas. Furthermore, MPVFD, CHI and CV are known to occur in the absence of maternal SARS-CoV-2 infection. Thus, it is not known how COVID-19 placentitis differs from other placentitides with similar pathologies of unknown aetiology.

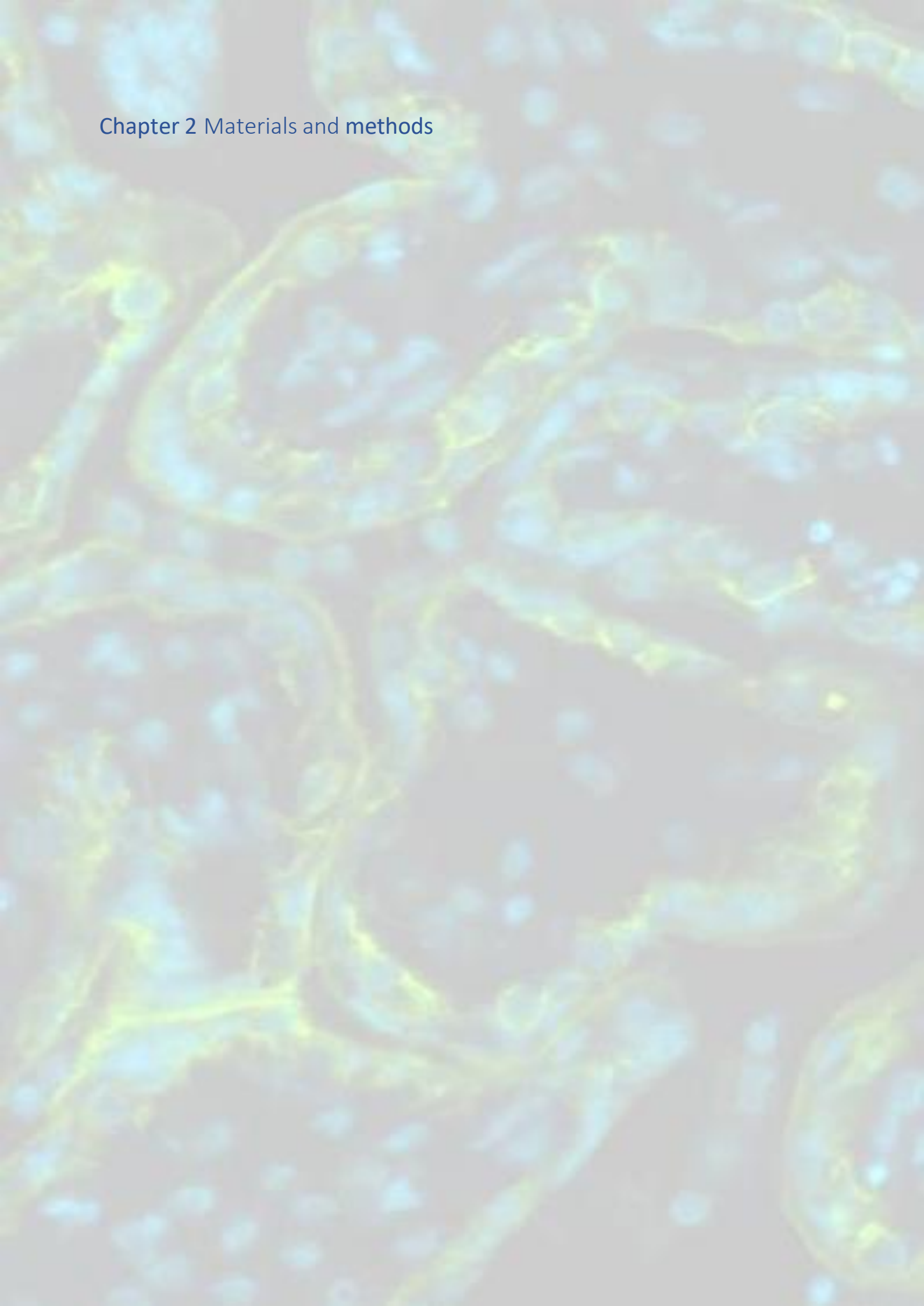
1.6. The problem

A great deal of work was undertaken to characterise the systemic immune responses to COVID-19. Less was carried out to examine the tissue response to COVID-19 in primary infected tissues, including lung and placenta. This has largely been due to inaccessibility of the tissue. Detailed insights into the virus-host interaction in COVID-19 infected tissues are required to develop better targeted therapies for the elderly, the immunocompromised and those with co-morbidities who are ineligible for, or respond poorly to, vaccination (Herold et al., 2020; Liu et al., 2020; Scherger et al., 2020). Moreover, knowledge of the mechanisms that drive disease progression could further our understanding of the long-term effects of SARS-CoV-2, termed 'long-COVID', and assist in reducing the health and socioeconomic impacts associated with this condition.

1.7. Aim of the study

The aim of this study is to characterise the immune responses to SARS-CoV-2 infection in tissue, focusing on lung, the primary site of infection, and placenta, a non-pulmonary site of infection with a well-defined clinicopathological consequences.

Chapter 2 Materials and methods



2.1. Materials, reagents & Resources

Antibodies			
Antibody/clone/species	Supplier	Catalogue number	Experiment in which antibody/reagent used
CD3e/MRQ39/Rabbit	CellMarque	103R-96	COMET mIHC panel in lung and placenta.
CD4/EPR6855/Rabbit	Abcam	ab133616	COMET mIHC panel in lung and placenta.
CD8/4B11/Mouse	Biorad	MCA1817	COMET mIHC panel in lung and placenta.
CD15/Carb-3/Mouse	Agilent	M363101-2	COMET mIHC panel in lung and placenta.
CD20/L26/Mouse	CellMarque	120M-86	COMET mIHC panel in lung and placenta.
CD39/EPR20627/Rabbit	Abcam	ab223842	COMET mIHC panel in lung and placenta.
CD45/2B11+PD726/Mouse	Agilent	M070101-2	COMET mIHC panel in lung and placenta. COMET mIHC panel in lung and placenta.
CD45RO/UCH-L1/Mouse	Santa Cruz	sc1183	COMET mIHC panel in lung and placenta.
CD56/MRQ-42/Rabbit	CellMarque	156R-96	COMET mIHC panel in lung and placenta.
CD68/KP1/Mouse	Thermofisher scientific	MA5-13324	COMET mIHC panel in lung and placenta.
CD80/EPR1157/Rabbit	Abcam	ab134120	COMET mIHC panel in lung and placenta.
CD103/EP206/Rabbit	CellMarque	437R-16	COMET mIHC panel in lung and placenta.
CD163/EPR19518/Rabbit	Abcam	Ab182422	COMET mIHC panel in lung and placenta.
PD1/EPR4877/Rabbit	Abcam	ab137132	COMET mIHC panel in lung and placenta.

PDL1/IHC411/Rabbit	GenomeMe	IHC411-100	COMET mIHC panel in lung and placenta.
SARS-CoV-2 Nucleocapsid/ Polyclonal/Rabbit	Sino Biological	40143-T62	COMET mIHC panel in lung and placenta.
SARS-CoV-2 Spike/ 3A2/Mouse	Abcam	ab272420	COMET mIHC panel in lung and placenta.
ACE2/EPR4435/Rabbit	Abcam	ab108252	COMET mIHC panel in lung and placenta.
IP10/Polyclonal/Rabbit	Abcam	ab9807	COMET mIHC panel in lung and placenta.
MUM1/MUM1p/Mouse	Agilent	M725901-2	COMET mIHC panel in placenta
GranzymeB/EPR20129/ Rabbit	Abcam	ab208586	COMET mIHC panel in lung and placenta.
Vimentin/RV202/Mouse	Santa Cruz	sc-32322	COMET mIHC panel in lung and placenta.
CTLA4/CAL49/Rabbit	Abcam	ab237712	COMET mIHC panel in lung and placenta.
FoxP3/SP97/Rabbit	Thermofisher Scientific	MA5-16365	COMET mIHC panel in lung and placenta.
Ki67/MIB1/Mouse	Agilent	M724001-2	COMET mIHC panel in lung and placenta.
Pan-cytokeratin/AE1/AE3/ Mouse	Agilent	M351501-2	COMET mIHC panel in lung and placenta.
Fibrin/Polyclonal/ Rabbit	Agilent	A008002-2	COMET mIHC panel in placenta.
GPNCMB/Polyclonal/ Rabbit	Abcam	ab125898	COMET mIHC panel in placenta.
aSMA/1A4/ Mouse	Thermofisher scientific	14-9760-82	COMET mIHC panel in lung and placenta.
Collagen IV/EPR20966/ Rabbit	Abcam	Ab214417	COMET mIHC panel in lung
Collagen VI/EPR17072/ Rabbit	Abcam	Ab182744	COMET mIHC panel in lung
anti-Rabbit secondary	Thermofisher scientific	A32733	COMET mIHC panel in lung and placenta.

anti-Mouse secondary	Thermofisher scientific	A32727	COMET mIHC panel in lung and placenta.
<i>DAPI (nuclear counterstain)</i>	Thermofisher scientific	62248	COMET mIHC panel in lung and placenta.
HLA-A/ EP1395Y/Rabbit	Akoya	EP1395Y	CODEX/phenocycler lung panels
CD4/ EPR6855/Rabbit	Akoya	EPR6855	CODEX/phenocycler lung panels
CD20/L26/Mouse	Akoya	L26	CODEX/phenocycler lung panels
CD14/ EPR3653/Rabbit	Akoya	EPR3653	CODEX/phenocycler lung panels
CD68/KP1/Mouse	Akoya	KP1	CODEX/phenocycler lung panels
Vimentin/O91D3/Mouse	Akoya	O91D3	CODEX/phenocycler lung panels
CD8/ C8/144B/Mouse	Akoya	C8/144B	CODEX/phenocycler lung panels
CD11c/118/A5/Mouse	Akoya	118/A5	CODEX/phenocycler lung panels
E-Cadherin/4A2C7/Mouse	Akoya	4A2C7	CODEX/phenocycler lung panels
CD45/ D9M81/Mouse	Akoya	D9M81	CODEX/phenocycler lung panels
CD31/ EP3095/Rabbit	Akoya	EP3095	CODEX/phenocycler lung panels
CD45RO/UCHL1/Mouse	Akoya	UCHL1	CODEX/phenocycler lung panels
CD44/156-3C11/Mouse	Akoya	156-3C11	CODEX/phenocycler lung panels
SARS-CoV Spike/Polyclonal/Rabbit	Akoya	40150-T62-COV2	CODEX/phenocycler lung panels
αSMA/1A4/Mouse	Akoya	1A4	CODEX/phenocycler lung panels
SARS-CoV Nucleocapsid/40143-MM08/ Mouse	Akoya	40143-MM08	CODEX/phenocycler lung panels

HLA-DR/ EPR3692/Rabbit	Akoya	EPR3692	CODEX/phenocycler lung panels
Pan-Cytokeratin AE1/AE3/Mouse	Akoya	AE1/AE3	CODEX/phenocycler lung panels
CD34/ QBEND/10/Mouse	Akoya	QBEND/10	CODEX/phenocycler lung panels
CD3e/ EP449E/Rabbit	Akoya	EP449E	CODEX/phenocycler lung panels
Ki67/ B56/Mouse	Akoya	B56	CODEX/phenocycler lung panels
CD66a/c/e/ ASL-32/Mouse	Akoya	ASL-32	CODEX/phenocycler lung panels
CD11b/ EP1345Y/Rabbit	Akoya	EP1345Y	CODEX/phenocycler lung panels
IDO1/ V1NC3IDO/Mouse	Akoya	V1NC3IDO	CODEX/phenocycler lung panels
Granzyme/ D6E9W/Rabbit	Akoya	D6E9W	CODEX/phenocycler lung panels
LAG3/ EPR055/Rabbit	Akoya	EPR055	CODEX/phenocycler lung panels
ICOS/ D1K2T/Rabbit	Akoya	D1K2T	CODEX/phenocycler lung panels
CD21/ EP3093/Rabbit	Akoya	EP3093	CODEX/phenocycler lung panels
CD57/ HNK-1/Mouse	Akoya	HNK-1	CODEX/phenocycler lung panels
ACE2/ EPR4436/Rabbit	Akoya	EPR4436	CODEX/phenocycler lung panels
PD1/ D4W2J/Rabbit	Akoya	D4W2J	CODEX/phenocycler lung panels
Foxp3/259D/C7/Mouse	Akoya	259D/C7	CODEX/phenocycler lung panels
PDL1/ RM320/Rabbit	Akoya	RM320	CODEX/phenocycler lung panels
TFAM/18G102B2E11/Mouse	Akoya	18G102B2E11	CODEX/phenocycler lung panels
TIM3/ D5D5R/Rabbit	Akoya	D5D5R	CODEX/phenocycler lung panels
CD19/ RM332/Rabbit	Akoya	RM332	CODEX/phenocycler lung panels

CD15/ Hi98/Mouse	Akoya	Hi98	CODEX/phenocycler lung panels
CD66b/ G10F5/Mouse	Akoya	G10F5	CODEX/phenocycler lung panels

Table 2-1 Antibodies and counterstains used for multiplex immunohistochemistry assays.

Critical Commercial Assays			
Multi-staining buffer	Lunaphore Technologies	NA	COMET mIHC panel in lung and placenta.
RNAscope 2.5 LS probe - IL6	Bio-techne	310378-C4	Cytokine detection in lung and placenta
RNAscope 2.5 LS probe - IL8	Bio-techne	310388-C3	Cytokine detection in lung and placenta
RNAscope HS IL17A	Bio-techne	310938-C2	Cytokine detection in lung and placenta
RNAscope 2.5 LS probe - V-nCoV2019-orf1ab-sense	Bio-techne	859158	SARS-CoV-2 virus detection in lung and placenta
RNAscope 2.5 LS probe - V-nCoV2019-S-C2	Bio-techne	848568-C2	SARS-CoV-2 virus detection in lung and placenta
RNAscope LS Multiplex Fluorescent Reagent Kit	Bio-techne	322800	SARS-CoV-2 virus/ cytokine detection in lung and placenta
RNAscope LS 4-Plex Ancillary Kit for Multiplex Fluorescence	Bio-techne	322830	Placenta RNAscope experiment
RNAscope 2.5 LS Probe - CXCL10	Bio-techne	311858	Placenta RNAscope experiment
Opal 520	Akoya Biosciences	FP1487001KT	CODEX Lung mIHC panel
Opal 620	Akoya Biosciences	FP1495001KT	CODEX Lung mIHC panel
Opal 690	Akoya Biosciences	FP1497001KT	CODEX Lung mIHC panel
Opal 780	Akoya Biosciences	FP1501001KT	CODEX Lung mIHC panel
GeoMX NGS RNA WTA Hs	Nanostring Technologies	121401102	Placenta digital spatial profiling experiment
GeoMx RNA Slide Prep FFPE PCLN	Nanostring Technologies	121300313	Nanostring GeoMx DSP

GeoMx DSP Collection Plate 4pk	Nanostring Technologies	100473	Nanostring GeoMx DSP
GeoMx Instrument Buff Kit PCLN	Nanostring Technologies	100474	Nanostring GeoMx DSP
GeoMx Seq Code Pack_AB	Nanostring Technologies	121400201	Nanostring GeoMx DSP
S&H 1 - 8 Kits / Slides	Nanostring Technologies	SH0003	Nanostring GeoMx DSP
QuantSeq 3' mRNA-Seq Library Prep Kit FWD for Illumina	Lexogen	139.96	Bulk Sequencing in lung and placenta
Spike SNP-Ext	Sigma Genosys	5' TGAAGTCAGACAA ATCGCTCC 3'	Virus strain detection
Spike SNP-R1	Sigma Genosys	5' TGGTGTCATGTAGA AGTTCAAAAG 3'	Virus strain detection
Qiagen OneStep RT-PCR kit	Qiagen	210212	Quantseq GEP lung and placenta/ virus strain identification
Qiagen RNeasy FFPE purification kit	Qiagen	73504	Virus strain detection
Qiagen Gel extraction kit	Qiagen	28704	

Table 2-2. List of commercial assay kits and associated assays.

Software and Algorithms			
Lunaphore Explorer (MP)	Lunaphore Technologies	NA	COMET mIHC panel in lung and placenta.
Lunaphore Viewer (MP)	Lunaphore Technologies	NA	COMET mIHC panel in lung and placenta.
DeepCell (EF)	(Greenwald et al., 2022)	https://github.com/vanvalenlab/deepcell-tf	CODEX / COMET mIHC panel in lung and placenta.
MISSILE (EF)	NA. Written by Dr Eanna Fennel, University of Limerick	Available upon publication	CODEX / COMET mIHC panel in lung and placenta.
FastPG (EF)	(Bodenheimer et al., 2020)	https://github.com/sararselitsky/FastPG	CODEX / COMET mIHC panel in lung and placenta.
STAR (EF)	(Dobin et al., 2013)	https://github.com/alexdobin/STAR	Quantseq GEP

BBMap (EF)	(Bushnell, 2014)	https://github.com/BioInfoTools/BBMap	Quantseq GEP
FastQC (EF/MP)	(Andrews, 2010)	https://github.com/s-andrews/FastQC	Quantseq GEP
HTSeq (EF)	(Putri et al., 2022)	https://github.com/simon-anders/htseq	Quantseq GEP
Nanostring interactive data analysis and visualisation software (MP)	Nanostring Technologies	NA	Nanostring GeoMx DSP
DESeq (EF)	(Love et al., 2014)	https://github.com/mikelove/DESeq2	Quantseq GEP
GlmmSeq (EF)	(Myles Lewi, 2022)	https://github.com/cran/glmmSeq	Quantseq GEP
GSEA (EF)	Broad Institute	https://www.gsea-	Quantseq GEP
QuPath (MP)	(Bankhead et al., 2017)	https://github.com/qupath/qupath	CODEX / COMET mIHC panel in lung and placenta.
Nanostring GeoMx NGS Pipeline (MP)	Nanostring Technologies	NA	Nanostring GeoMx DSP

Table 2-3. List of software and algorithms used with associated experiments. Software used by Matthew Pugh is suffixed by (MP), and software used by Eanna Fennel is suffixed by (EF).

2.2. Ethical and regulatory approvals

The post-mortem investigation including acquisition of specimens, acquisition of placental tissue and collection of serum from healthy volunteer controls was part of the LoST-SoCC study, which received ethical approval from the Newcastle North Tyneside 1 research ethics committee (19/NE/0336) (IRAS:193197). Serum samples from taken from patients with mild/asymptomatic and severe COVID-19 were collected as part of the Coronavirus Immunological Analysis study (20/NW/0240), which was approved by the North West-Preston Research Committee. The remainder of the serum samples were provided by the Arden biobank following an application to the Arden Tissue Bank (University Hospital, Coventry, UK).

2.3. Tissue samples and clinical data acquisition

2.3.1. Post-mortem tissue samples from fatal COVID-19

In order to acquire post-mortem (PM) tissue samples, a post-mortem study was established in collaboration with the mortuaries at the Royal Glamorgan Hospital (RGH), Llantrisant, and Morriston Hospital (MH), Swansea. The study comprised of either post-mortem tissue collection from prospectively consenting families of deceased patients, or retrospective collection of PM tissue from deceased patients in which the families had previously consented for tissue to be used in ethically approved research. PMs were performed by pathologists Dr Esther Youd (EY, based at RGH) and Dr Gareth Leopold (GL, based at MH).

Criteria for inclusion in the study was a positive COVID-19 PCR swab, either in life during the patient's final illness, or, at post mortem, and COVID-19 written on the patient's death certificate. Due to safety protocols established at the start of the pandemic, tissue samples were fixed for a minimum of 72 hours in paraformaldehyde before dehydration and embedding into paraffin to create Formalin Fixed Paraffin Embedded (FFPE) tissue blocks. Control tissues including viral pneumonitides, bacterial pneumonia and normal (non-respiratory death) controls were obtained from the post mortem archive and underwent post-mortem in the pre-pandemic period. All patients' families has previously consented for the tissue to be used in ethically approved research.

2.3.2. Serum samples from COVID-19 patients and controls.

Serum samples from consenting participants with varying degrees of COVID-19 severity (n=215) and non-infected healthy volunteer controls (n=54) were obtained from existing collections or from a biobank. Blood samples were taken in a green top serum tube. Tubes were left to clot for 60 minutes, after which they were centrifuged at 2000xg for 19 minutes. The serum component was pipetted into screw-capped Eppendorf tubes and frozen at -80°C.

2.3.3 Tissue samples from COVID-19 placentitis cases

FFPE tissue samples of COVID-19 placental tissue and control cases were obtained from pathologists Beata Hargitai (BH) and Tamas Marton (TM) based at Birmingham Women's and Children's Hospital NHS Foundation trust. All patients were confirmed SARS-CoV-2 positive either by nasopharyngeal swab or during examination of the placenta.

2.4. Histopathological assessment

Histological assessment was performed using haematoxylin and eosin (H&E) stained tissue sections. Staining was performed by the pathology department of the donor hospital that collected the tissue samples. H&E stained lung tissue samples were assessed in conjunction with pathologists EY and GT. H&E stained placental tissue samples were assessed in conjunction with BH and TM. Consensus was

achieved with regards to interpretation of the pathology and the features were documented systematically.

2.5. Immunohistochemistry

Antibodies against all immune lineage and structural targets are well validated antibodies described extensively in the literature and used in routine clinical practice. Virus specific antibodies were novel and were tested in greater depth for sensitivity and specificity using virus infected cell lines,

2.5.1. Chromogenic immunohistochemistry

FFPE sections, 5µm thick, were baked for 3 hours prior to staining to ensure tissue adherence. The Leica BondMax IHC protocol F (DAB) was used with the following conditions: bake and de-wax, epitope retrieval 2 for 20 minutes and primary antibody incubation for 30 minutes. Slides were subsequently mounted with DPX mountant media and scanned (Aperio CS2).

2.5.2. Multiplex immunohistochemistry – Akoya CODEX Phenocycler

A broad 38-plex antibody panel was designed for the Akoya CODEX Phenocycler platform to detect lineage and functional markers expected in COVID-19 tissues and controls. Primary antibodies were conjugated to unique DNA oligonucleotide barcodes in preparation for PhenoCycler staining and imaging. Glass slides were prepared, stained, and fixed as per the PhenoCycler protocol. Briefly, slides were deparaffinised in Xylene and re-hydrated in decreasing concentrations of ethanol (100%, 90%, 70% & 50%). Heat Induced Epitope Retrieval (HIER) was performed in a pressure cooker at 120°C for 20 minutes in Tris-EDTA buffer (pH = 9.0). The tissue was then washed and incubated in PhenoCycler Staining Buffer (Akoya Biosciences) for 30 minutes to block non-specific binding of antibodies. Subsequently, the tissue was incubated in a cocktail of the conjugated antibodies for 3 hours at room temperature, then fixed in 4% paraformaldehyde for 10 minutes, 100% methanol for 5 minutes, Fixative Reagent (Akoya Biosciences) for 20 minutes and then stored until imaging. Akoya Reporters were added to the corresponding well of a 96-well plate in preparation for imaging, based on the cycle design of the experiment. Slides were imaged with the PhenoCycler FUSION system (from Akoya Biosciences). Autofluorescent subtraction, stitching and compression were completed in the Akoya FUSION software resulting in qptiff files. Subsequently, a more targeted 10-plex panel was applied to

Page 32 of 261

a wider collection of lung tissues. The staining and imaging protocols used were identical to that of the broader biomarker panel.

PhenoCycler FUSION Broad Panel	
Target	Clone
HLA-A	EP1395Y
CD4	EPR6855
CD20	L26
CD14	EPR3653
CD68	KP1
Vimentin	O91D3
CD8	C8/144B
CD11c	118/A5
E-Cadherin	4A2C7
CD45	D9M81
CD31	EP3095
CD45RO	UCHL1
CD44	156-3C11
SARS-CoV Spike	40150-T62-COV2
aSMA	1A4
SARS-CoV Nucleocapsid	40143-MM08
HLA-DR	EPR3692
Pan-Cytokeratin	AE1/AE3
CD34	QBEND/10
CD3e	EP449E
Ki67	B56
CD66a/c/e	ASL-32
CD11b	EP1345Y
IDO1	V1NC3IDO
GranzymeB	D6E9W
LAG3	EPR055
ICOS	D1K2T
CD21	EP3093
CD57	HNK-1
ACE2	EPR4436
PD1	D4W2J
Foxp3	259D/C7
PDL1	RM320
TFAM	18G102B2E11
TIM3	D5D5R
CD19	RM332
CD15	Hi98
CD66b	G10F5

Table 2-4. Antibodies and clones included in the broad CODEX mIHC panel

PhenoCycler FUSION Targeted	
Target	Clone
CD68	KP1
CD15	MMA
aSMA	1A4
CD4	EPR6855
CD8	C8/144B
CD3e	EP449E
Pan-cytokeratin	AE1/AE3
HLA-DR	EPR3692
SARS-CoV Spike	40150-T62-COV2
SARS-CoV Nucleocapsid	40143-MM08

Table 2-5. Antibodies and clones included in the targeted CODEX mIHC panel

2.4.3. Multiplex immunohistochemistry – Lunaphore COMET

Lung analysis: An 18-plex antibody panel was validated to identify collagen deposition, general lung structure, SARS-CoV-2 localisation, and immune cell abundance (CD45, CD45RO, COLIV, COLVI, CD68, AE1/AE3, vimentin, SMA, CD3, CD20, CD163, spike, nucleocapsid, CD15, PDL1, CD4, CD8, GPNMB). Slides were de-waxed, baked and antigen retrieved (102°C for 1 hour in a pH 9 buffer) using the PT module (Thermofisher) before a brief wash in multi-staining buffer. The slides were then loaded into the COMET stainer (Lunaphore Technologies). Before antibody staining cycles commenced, blank images of the TRITC and Cy5 channels were captured for autofluorescence subtraction during image processing post acquisition. Primary antibodies were diluted to the desired concentrations (see Supplementary Table 5) in multi-staining buffer and incubated for 4 minutes in each cycle. Secondary antibody incubation and elution was carried out for 2 minutes each. Exposure times for DAPI, TRITC and Cy5 were set at 50ms, 400ms and 200ms respectively. Secondary antibodies in the TRITC channel (mouse antibody specific) were diluted to a concentration of 1:100 while Cy5 channel secondaries (rabbit antibody specific) were diluted to 1:400. DAPI images were taken in every staining cycle to ensure alignment of cycles during image processing. All antibodies were optimised using negative staining (secondary antibody only) and elution/re-staining step protocols.

Placenta: A 29-plex biomarker panel was designed and validated to identify cell types present in the placenta as well as quantify functional states and signaling molecules associated with COVID-19 placentitis. Slides were de-waxed, baked and antigen retrieved (102°C for 1 hour in a pH 9 buffer) using the PT module (Thermofisher) before a brief wash in multi-staining buffer. The slides were then loaded into the COMET stainer (Lunaphore Technologies). Before antibody staining cycles commenced, blank images of the TRITC and Cy5 channels were captured for autofluorescence subtraction during image processing post acquisition. Primary antibodies were diluted to the desired concentrations (see SI Table 2) in multi-staining buffer and incubated for 4 minutes in each cycle. Secondary antibody incubation was carried out for 2 minutes with a 2-minute elution. Exposure times used were 50ms for DAPI, 400ms for the TRITC channel and 200ms for Cy5. Secondary antibodies in the TRITC channel (mouse antibody specific) were diluted to a concentration of 1:100 while Cy5 channel secondaries (rabbit antibody specific) were diluted to 1:400. DAPI images were taken in every staining cycle to ensure alignment of cycles during image processing. All images were acquired with a 20x objective. All antibodies were optimised using negative staining (secondary antibody only) and elution/re-staining step protocols.

Cycle position	Total volume (μl)	Mouse antibodies	Concentration (1 in x)	Volume of Antibody (μl)	Rabbit antibodies	Concentration (1 in x)	Volume of Antibody (μl)
1	450	CD45	30	15	Nucleocapsid	2000	0.225
2	450	CD15	200	2.25	Collagen VI	50	9
3	450	Vimentin	50	9	Collagen IV	200	2.25
4	450	CD68	50	9	PD1	500	0.9
5	450	CD8	50	9	PDL1	50	9
6	450	Ki67	25	18	CD4	200	2.25
7	450	CK	50	9	CD3	500	0.9
8	450	Spike	200	2.25	GPNMB	250	1.8
9	450	SMA	1000	0.45			

Table 2-6. Concentration, cycle position and volume of antibodies used in the Lunaphore COMET lung panel

Cycle position	Total volume (μl)	Mouse antibodies	Concentration (1 in x)	Volume of antibody (μl)	Rabbit antibodies	Concentration (1 in x)	Volume of antibody (μl)
----------------	-------------------	------------------	------------------------	-------------------------	-------------------	------------------------	-------------------------

1	450	CD45RO	50	9	Nucleocapsid	2000	0.225
2	450	CD45	30	15	IP10	50	9
3	450	Mum1	20	22.5	CD80	200	2.25
4	450	CD15	200	2.25	Granzyme	300	1.5
5	450	Vimentin	50	9	ACE2	50	9
6	450	CD68	50	9	FoxP3	50	9
7	450	CD8	50	9	PD1	500	0.9
8	450	Ki67	25	18	PDL1	50	9
9	450	CK	50	9	CD4	200	2.25
10	450	CD20	100	4.5	CD3	500	0.9
11	450	Spike	200	2.25	CD163	200	2.25
12	450	NA	NA	NA	Fibrinogen	3000	0.15
13	450	SMA	1000	0.45	GPNMB	250	1.8
14	450				CD39	300	1.5
15	450				CD103	100	4.5
16	450				CTLA4	200	2.25
17	450				CD56	200	0.5

Table 2-7. Concentration, cycle position and volume of antibodies used in the Lunaphore COMET lung panel

2.5. Spatial transcriptomics

2.5.1. Nanostring GeoMX digital spatial profiling

Lung: Spatial transcriptomics, using the Nanostring GeoMx Digital Spatial Profiler, was conducted on tissue sections from three SARS-CoV-2 lungs, one MERS lung, one Rhinovirus lung, one bacterial pneumonia lung and two normal lungs. The three SARS-CoV-2 lungs consisted of two late-stage disease and one early-stage disease. Whole sections were stained with fluorophore-conjugated antibodies and visualised with pan-cytokeratin, CD45, EDG1 and DAPI to identify epithelial, immune, and endothelial compartments of the lung. Alveoli and blood vessels were selected as regions of interest (ROIs) based on this staining. The Nanostring Cancer Transcriptome Atlas (CTA) targeted gene panel was used with the addition of COVID-19 specific gene probes (plus a set of negative probes). Oligonucleotides were cleaved off the antibodies by UV light illumination and gathered within each ROI as per the GeoMx DSP protocol. The eluted oligonucleotides were sequenced on an Illumina NextSeq 550.

Placenta: FFPE TMAs were created for GeoMx DSP analysis, comprising 16 tissue samples over 4 slides.

The TMAs were constructed from 10 placental tissues from COVID19+ mothers (5 SARS-CoV-2 positive

placentas, 5 SARS-CoV-2 negative placentas), 2 CHI, 2 CV and 2 normal placentas. Slides were stained with fluorophore-conjugated antibodies specific for pan cytokeratin (clone AE1/AE3), CD68, and SARS-CoV-2 nucleocapsid proteins along with DAPI to visualise nuclei. These markers were selected to identify trophoblast layer, macrophages and SARS-CoV-2 infected areas of tissue. Regions of interest (ROIs) were selected based on four compartments: villous stroma, decidua, trophoblast layer or macrophage. The virus status of each ROI was also recorded based on nucleocapsid staining. The Nanostring Whole Transcriptome Atlas (WTA) gene assay was employed to characterise gene expression (Zimmerman et al., 2022). Oligonucleotides were collected from each ROI as per the GeoMx DSP protocol and sequenced on an Illumina NextSeq 550.

2.5.2. RNAscope.

Lung: In situ detection of SARS-CoV-2 nucleic acids was performed by multiplex fluorescence using the RNAscope® Leica Multiplex Fluorescent Assay according to the manufacturer's instructions (Advanced Cell Diagnostics (ACD), Newark, CA, USA). Probes against the sense strand of spike gene (V-nCoV2019-S, 845701, ACD) and antisense strand of the orf1ab gene (V-nCoV2019-orf1ab-sense) were used in combination with a probe designed against human *IL6*. RNAscope ISH staining was performed on the Leica Bond RX automated IHC platform. Fluorescent detection of probes was performed with TSA-based Opal fluorophores (Opal 620- spike sense probe; Opal 520 -orf1ab antisense probe). Nuclear counterstaining was performed with DAPI. Slides were imaged using the Vectra Polaris 2.0 imaging platform (Akoya Biosciences). Spectral unmixing and autofluorescence removal was performed with InForm Tissue Analysis Software (Akoya Biosciences) with the resulting tiles stitched together using QuPath software.

Placenta: Two panels utilising RNAscope ISH protocols were implemented to detect sub-genomic RNA and cytokine producing cells, respectively. In the first panel, SARS-CoV-2 and nCoV-2019-S Sense probes were used in a 2-plex panel to detect the virus and replicating virus respectively. In the second

panel, a 3-plex protocol (CXCL10, IL8, IL6) was used to detect cytokine expression across the cohort. Both panels were combined with immunohistochemical detection of CD68. The RNAscope ISH protocols were conducted as specified by the manufacturer (ACD). Briefly, FFPE slides were baked at 60 °C for 1 hour before being deparaffinised in xylene and dehydrated 100% ethanol. Slides were then dried before H₂O₂ was added for 10 min at room temperature (RT). Target retrieval was achieved by incubating the slides in boiling antigen retrieval buffer (<98 °C) for 15 minutes. Slides were then treated with Protease Plus for 15 minutes at 40 °C. For panel 2, C2 and C3 probes were diluted in C1 probes (C2 probe was diluted in C1 for panel 1) at a ratio of 1:50 and were added to the slides for 2 hours at 40 °C. C1 probes were detected with Opal-520 (FP1487001KT, Akoya Biosciences), C2 probes with Opal 620 (FP1495001KT, Akoya Biosciences) and C3 probes with Opal 690 (FP1497001KT, Akoya Biosciences). For IHC detection of CD68, following RNAscope the slides were boiled in citrate buffer for 15 minutes, blocked with casein for 10 minutes and incubated with anti-CD68 primary antibody (clone KP-1, Dako) for 1 hour at RT. Primary antibody was detected using universal HRP secondary antibody (MP750050, Vector Labs) and Opal 780 (FP1501001KT, Akoya Biosciences). The slides were counterstained with DAPI then mounted using Prolong Gold antifade mountant (ThermoFisher). Slides were imaged using a Vectra Polaris automated imaging system (Akoya Biosciences).

2.6. Bulk Quantseq RNA sequencing.

Lung: RNA extraction was conducted using a RNeasy FFPE Kit (Qiagen) according to the manufacturer's instructions. Briefly, curls were deparaffinized in xylene and rehydrated with decreasing concentration ethanol washes. The tissue was digested in Buffer PKD with 10 µL of proteinase K and 2 µL of β-mercaptoethanol at 56°C for 15 min followed by incubation at 80 °C for 15 min. Samples were cooled on ice for 3 min and the digested tissue was pelleted by centrifugation. DNA was digested in DNase Booster Buffer with 10 µL of DNase I for 15 min at room temperature. The binding conditions of the sample were adjusted by adding buffer RBC and ethanol. The RNA was applied to a RNeasy spin column and washed with buffer RPE before eluting in 30 µL of RNase-free water. 5 µL of RNA was

removed to determine the quality and quantity of the extracted RNA using the Agilent 4200 TapeStation and Qubit, respectively. The remaining 25 µL was utilised for QuantSeq library prep. Library prep was conducted using the Lexogen QuantSeq 3' mRNA-Seq Kit FWD for Illumina. QC was monitored by spiking in 0.5uL of SIRV to allow technical evaluation of library prep and sequencing performance. The prepared RNA was sequenced on an Illumina NextSeq 550 by Genomics Birmingham (University of Birmingham, UK).

Placenta: RNA extraction was carried out using the RNeasy FFPE Kit (Qiagen 73504) according to the manufacturer's instructions for samples containing more than 2 curls. Briefly, curls were deparaffinized in xylene and rehydrated with ethanol washes. The tissue was digested in Buffer PKD with 10 µL of proteinase K and 2 µL of β-mercaptoethanol at 56°C for 15 min followed by incubation at 80 °C for 15 min. Samples were cooled on ice for 3 min and the digested tissue was pelleted by centrifugation. DNA was digested in DNase Booster Buffer with 10 µL of DNase I for 15 min at room temperature. The binding conditions of the sample were adjusted by adding buffer RBC and ethanol. The RNA was applied to a RNeasy spin column and washed with buffer RPE before eluting in 30 µL of RNase-free water. 5 µL of RNA was removed to determine the quality and quantity of the extracted RNA using the Agilent 4200 TapeStation and Qubit, respectively. The remaining 25 µL was utilised for QuantSeq library prep. Library prep was completed using the Lexogen QuantSeq 3' mRNA-Seq Kit FWD for Illumina. QC was monitored by spiking in 0.5uL of SIRV to allow technical evaluation of library prep and sequencing performance. The prepared RNA was sequenced on an Illumina NextSeq 550 by Genomics Birmingham (University of Birmingham, UK).

2.7. T-cell receptor sequencing

RNA extraction was conducted according to the above protocol used for QuantSeq preparation. TCR sequencing was conducted with the Oncomine TCR Beta-SR Assay (Thermo Fisher), with preparation on the Ion Chef System and sequencing on the Ion GeneStudio S5.

2.8. Virus variant identification

Analysis of SARS-CoV-2 spike mutations was performed by RT-PCR. RNA, purified from FFPE scrolls using a Qiagen RNeasy FFPE kit, was amplified using Qiagen OneStep RT-PCR reagents and SpikeSNP Ext and R1 primers (Babiker et al., 2021). Cycling conditions were 95C 15'; 40 cycles of 94C 20s, 58C 20s, 72C 40s; and then 72C 7'. Amplicons 350bp in size were purified from agarose gels using a Qiagen gel extraction kit and Sanger sequenced by Source Bioscience (Nottingham UK) using the SpikeSNP Ext and R1 primers.

2.9. Fluorescent in-situ hybridisation for X/Y chromosomes.

This experiment was carried out in collaboration with Graham Halford, based at Birmingham Genomics, at the Birmingham Women's Hospital. Unstained placental sections on positively charged slides were baked at 60°C overnight prior to deparaffination with fresh UltraClear, then cleared using 100% methanol and distilled water. The sections were immersed in 0.2M HCl for 23 minutes, washed using distilled water and placed in the heat pre-treatment solution from Cytocell's LPS100 Tissue PreTreatment Kit for 50 minutes at 95°C. The slides were washed with distilled water and a few drops of the enzyme digestion solution was added to the sections and incubated at 37°C for 40 minutes. The Cytocell LPE0XG and LPE0YqR FISH probes and sections were denatured and hybridised together according to the manufacturer's guidelines. The tissue was counterstained with DAPI obtained from Cytocell and analysed using the Olympus BX51 fluorescent microscope with images captured using Metasystems' Isis software.

2.10. SARS-CoV-2 infection of VERO cells

This experiment was carried out in collaboration with Dr Zania Stamataki and Dr Gary Reynolds, University of Birmingham. SARS-CoV-2 hCoV-19/England/2/2020 was provided by Christine Bruce, UK Health Security Agency, Porton Down, UK and passaged once in Vero-TMPRSS2 cells, provided by Jane McKeating, University of Oxford. Vero cells were infected for 48 hours at MOI 0.04 and fixed with

neutral buffered formalin. Cells were then pelleted by centrifugation at 600rpm for 10 minutes and processed through alcohol and xylene to paraffin wax and embedded. Infection was detected with rabbit anti-spike antibody clone CR3022 (The Native Antigen Company, Oxford UK) or mouse anti-nucleocapsid antibody clone CR3018 (Absolute Antibody Ltd, Cleveland UK) and cell nuclei were visualised with Hoechst 33342 (Thermo Fisher Scientific). Infection was imaged using the Cellinsight CX5 HCS Platform (Thermo Fisher Scientific).

2.11. Serum ELISA assays

This experiment was conducted in collaboration with Nordic Bioscience, Denmark. Ten markers of extracellular matrix formation and degradation and a marker of neutrophil activation were measured by competitive ELISA (Nordic Bioscience; Herlev Denmark) in serum samples of 269 patients, including varying degrees of COVID-19 severity (community, convalescent, acute hospital, acute ITU and convalescent ITU) and healthy controls. 96 well ELISA plates, precoated with streptavidin, were coated with the respective specific peptide at 20°C for 30 minutes at 300 rpm before being washed 5 times in washing buffer. 20uL of diluted sample or standard peptide was added with 100uL of peroxidase conjugated monoclonal antibodies in assay buffer. The plates were incubated for 1 hour at 20°C while being agitated at 300 rpm. Subsequently, the plates were washed 5 times with wash buffer and 100uL of TMB was added and incubated for 15 minutes in the dark at 300 rpm. 100uL of 1% H₂SO₄ was added to stop the reaction. The plates were analysed on an ELISA reader at 450nm (650nm reference).

Assay	Target	Description
C3M	Type 3 collagen degradation	A fragment of type III collagen released by MMP
C6M	Type 6 collagen degradation	A fragment of type VIa1 collagen released by MMP-2
CPA9-HNE	Neutrophil activity	A fragment of S100A9 (calprotectin) released by neutrophil elastase
ELP-3	Stromal reactivity	Neo-epitope of proteinase-3 mediated degradation of elastin
PRO-C20	Type 20 collagen formation	C-terminal of type XX collagen

PRO-C3	Type 3 collagen formation	A fragment of N-terminal type III collagen
PRO-C3X	Type 3x collagen formation	Cross-linked N-terminal pro-peptide of type III collagen
PRO-C4	Type 4 collagen formation	A fragment of the internal 7S domain of type IV collagen
PRO-C6	Type 6 collagen formation	A fragment of C-terminal type VIa3 collagen (endotrophin)
PRO-FIB	Fibrin formation	Neo-epitope of thrombin mediated degradation of fibrinogen
RE-C1M	Type 1 collagen degradation	Neo-epitope of MMP-2,9,13 mediated degradation of type I collagen
X-FIB	Fibrin degradation	Neo-epitope of plasmin mediated degradation of cross-linked fibrin

Table 2-8. ELISA assays performed on the serum of COVID-19 patients and controls.

2.12. Computational and statistical analysis

All computational analysis was guided by Matthew Pugh but some of the technical bioinformatic analysis and coding was conducted Dr Eanna Fennell, University of Limerick. EF will used to denote analyses conducted by Dr Fennell, or EF/MP, if both Matthew Pugh and Dr Fennel undertook the analysis. All coding was performed by Dr Fennel.

2.12.1. Multiplex immunohistochemistry image pre-processing (EF/MP)

Raw TIFF images (qptiff/ome.tiff) were ran through a bespoke pre-processing pipeline comprising de-arraying, pseudo-membrane marker generation, cellular segmentation, and feature extraction. CD45, aSMA, PanCK and CD15 were merged to create a pseudo-membrane marker for segmentation. Segmentation was completed on a per-core basis on the stitched DAPI and pseudo-membrane marker channels using CellSeg (Lee et al., 2022). Segmentation masks and their borders for each core were saved. FCS files were generated using the segmentation masks with the ‘regionprops’ function within Python, exporting the average intensity of each channel and morphological features of each cell.

2.12.2. Phenotyping & virus identification (EF/MP)

All numerical cellular data were imported into MISSiLe for phenotypic and spatial analyses. Cells were first filtered based on size. For the PhenoCyler FUSION images, cells were first screened into four

categories by CELESTA, endothelial, epithelial, immune and aSMA+ based on CD34, pan-cytokeratin, CD45 and aSMA respectively (see supplementary table 7 for CELESTA parameters) (Zhang et al., 2022).

The immune cells were then clustered using PhenoGraph (FastPG) to identify the main subsets (Bodenheimer et al., 2020). All cells were then screened for positivity for functional markers (Ki67, PDL1, HLA-DR, etc.) using silhouette clustering of the histograms on a by core basis, including positivity for SARS-CoV-2 spike and nucleocapsid proteins. Only cells identified as positive for both viral markers were labelled as infected.

2.12.3. Virus microenvironment quantification (EF/MP)

To quantify the immediate immune microenvironment of SARS-CoV-2 infected lung epithelium, cellular abundances were recorded as a function of distance from the infected cells. The nn2 function (RANN library) was used to calculate the N (where N = 10, 20, 40, 80, 100, 200, 400, & 800) number of cells closest to infected cells. The phenotype of each cell was then calculated as a percentage of the total cells and total immune cells in each bin (N) and plotted. For fair comparisons, the microenvironments of virus infected epithelium were compared to microenvironments of non-infected epithelium, with the same number of cells, within the same samples.

2.12.4. Collagen content quantification (EF/MP)

To assess the collagen content of COVID-19 lungs, collagen IV and VI protein channels from the COMET were assessed. To calculate the total tissue area, the intensity of all channels was averaged. Otsu thresholding determined positive tissue pixels and the total number of these was measured. Collagen 4 and 6 channels were also run through Otsu thresholding to define positive pixels for both and the total of each were subsequently divided by total tissue area. This was conducted on a by core basis and plotted as a function of disease state.

2.12.5. Spatial Transcriptomic Pre-processing & Analysis

Lung: Fastq files from the GeoMx DSP sequencing run were concatenated and processed through the Nanostring GeoMx NGS Pipeline to generate Digital Count Conversion (DCC) files. DCC files were imported into the Nanostring interactive data analysis and visualisation software. Regions failing QC were excluded from the analysis and Q3 normalisation was subsequently performed. Gene count and

metadata files were exported in csv format and imported with annotated metadata files into R. Gene set expression was calculated by taking the addition of genes within selected gene sets per region.

Placenta: Fastq files from the GeoMx DSP sequencing run were concatenated and processed through the Nanostring GeoMx NGS Pipeline to generate Digital Count Conversion (DCC) files. DCC files were imported into the Nanostring interactive data analysis and visualisation software. 3 regions were excluded from the analysis through the segment and probe QC steps and Q3 normalisation was subsequently performed. Gene count and metadata files were exported in csv format and imported with annotated metadata files into R. Gene set expression was calculated by taking the addition of genes within selected gene sets per region. Differential expression between disease states within each compartment was conducted with glmmSeq (Myles Lewi, 2022), using age and gestation as fixed effects and sample ID as random effect.

2.12.6. RNAscope FISH Analysis (EF/MP)

Lung: Stitched tiff images were imported into QuPath. TMAs were de-arrayed and linked to tissue type and disease group. Cells were segmented and detection measurements were exported as a CSV file. These files were imported into R and silhouette histogram clustering was used to assign positivity of each channel to every cell. Cells identified as SARS-CoV-2 infected were interrogated for the underlying cell type by pan-cytokeratin protein expression. On a per patient basis, the number of infected cells were correlated with mIHC and bulk mRNA virus data.

Placenta: After RNAscope ISH slide acquisition, images were tiled in Phenochart and spectrally unmixed in 45isual. After unmixing, tiles were stitched and subsequently segmented in QuPath (Bankhead et al., 2017). The intensity of each channel in each cell was extracted using the 'Measurements' functionality. These intensity measurements were concatenated and imported into R. Channels were thresholded and macrophages (denoted by positive CD68 threshold) were assessed for percentage of positive expression of each cytokine (CXCL10, IL6, IL8). The percentage of cytokine

positive macrophages were calculated as a function of total cells and total macrophages and were plotted.

2.12.7. QuantSeq RNA Alignment & Analysis (EF)

Lung: Fastq files from each flow cell were concatenated for each sample replicate. RNA quality control of the fastq files was assessed with FASTQC (Andrews, 2010). According to Lexogen recommendations for the 3' assay, the adapter contamination, polyA read through and low-quality tails were trimmed using bbdut. The SARS-CoV-2 genome files from NCBI were merged with the GRCh38 Homo sapiens genome, and a new reference was created with the STAR aligner (Dobin et al., 2013). Alignment was then conducted using STAR, with duplicate reads subsequently removed with PICARD. The resulting BAM files were indexed using SAMtools and counted using HTSEQ-count (Anders et al., 2015; Putri et al., 2022). The count files were then imported into R and DESeq2 (Love et al., 2014), where they were visualized using the median of ratios. Gene set enrichment analysis was conducted with the GSEA program from the Broad Institute and heatmaps were visualized using the ComplexHeatmap library (Gu et al., 2016; Subramanian et al., 2005). Gene set expression was calculated by taking the addition of genes within selected gene sets per region.

Placenta: Fastq files generated from each flow cell were concatenated for each sample replicate. RNA quality control of the fastq files was then conducted with FASTQC (Andrews, 2010). Subsequently, according to Lexogen recommendations of the 3' assay, the adapter contamination, polyA read through and low-quality tails were trimmed using bbdut. The SARS-CoV-2 genome files from NCBI were merged with the GRCh38 Homo sapiens genome, and a new reference was created with STAR aligner (Dobin et al., 2013). Alignment was then conducted using STAR, with duplicate reads subsequently removed with PICARD. The resulting BAM files were indexed using SAMtools and counted using HTSEQ-count (Li et al., 2009; Putri et al., 2022). The count files were then imported into R and subsequently DESeq2, where they were visualized using the median of ratios (Love et al., 2014). Differential expression was conducted within DESeq2 with maternal age and gestation as covariates. Gene set enrichment analysis was conducted with the GSEA program from the Broad

Institute (Mootha et al., 2003; Subramanian et al., 2005), heatmaps were visualized using the ComplexHeatmap library and differentially expressed genes were visualized using volcano plots from EnhancedVolcano (Gu et al., 2016). Gene set expression was calculated by taking the addition of genes within selected gene sets per region.

2.12.8. Differential Gene Expression & Pathway Analysis (EF/MP)

Differential gene expression testing of Nanostring GeoMx DSP and QuantSeq RNA data was conducted with DeSeq2 and plotted with Enhanced Volcano. EnrichR was used to calculate gene ontologies with significant up-/down-regulated genes with a p-value of less than 0.05 and plotted (Chen et al., 2013).

2.12.9. TCR sequence alignment (MP)

TCR beta sequences from lung tissue samples were quality controlled, removing reads shorter than 6 amino acids in length. TCR beta sequences reported to be specific for pathogens were obtained from the VDJDDB (Goncharov et al., 2022a) and McPAS (Tickotsky et al., 2017) databases. Additional SARS-CoV-2 specific TCR sequences were obtained from (Nolan et al., 2020). Sequencing matching was performed using the GREP function within R v4.0.3.

2.12.10. Serum Proteomic Analysis (MP/EF)

Serum proteomics data were imported into R and organised into assay results per sample. Each assay was plotted against disease group and significance was assessed by the Wilcoxon statistical test. Samples with sufficient appropriate clinical data were plotted against time post symptom onset/evidence of disease and survival curves were plotted, initially for acute hospital and acute ITU cases separately, with the survminer package in R. Subsequently, the acute hospital and ITU cases were combined for a Cox-proportional hazards test with age, sex and ethnicity used as confounding variables.

2.12.11. COMET mIHC image processing and analysis (EF/MP)

After acquisition, images were shading corrected, cycle aligned, stitched and merged into OME-TIFF pyramidal format within the Lunaphore COMET Explorer software. Autofluorescence subtraction for TRITC and Cy5 was conducted in the Lunaphore COMET Viewer v2. Single channels from each OME-TIFF stack were then extracted and TMAs were de-arrayed and saved as individual channel tiff files. The full-face slide sections imaged were split into quadrants in order to run through a deep learning segmentation model. Lineage marker channels (CD45, pan-cytokeratin, vimentin, aSMA and CD15) were merged into a 'pseudo-membrane' image and tiled to 256 x 256 pixel images. These tiles were used as input to the Mesmer model of the DeepCell segmentation library (Greenwald et al., 2022). Default settings for the Mesmer model were used and inference was made on both the membrane and nucleus channels. After inference, labelled cells were contracted by one pixel to ensure no cells were touching and subsequently interpolation-based stitching was used to build back up to the original image size. The image was binarised to negate the effect of interpolation on labelled regions and then re-labelled using the 'label' function of scikit-image. Labelled cells were then expanded back up by one pixel to return to their original size. To extract nuclear information from nuclear channels (DAPI, FoxP3, MUM1 and Ki67), each membrane label was connected with the most appropriate nucleus label using the 'find_nuclear_label_id' function from ARK (Greenwald et al., 2022). The 'region_props' function from scikit-image was then used to extract mean channel intensities as well as other morphological features and saved in an FCS format. Labelled mask images were saved as tiff files.

Clustering and Cell Phenotype Identification (EF/MP)

FCS files generated from COMET imaging were imported into MISSILE. Expression values were compressed to the 99.9th percentile per region. The morphology metrics cell size, solidity and eccentricity were z-scored and used as initial quality control steps ($-2 < \text{cell size} < 2$, $\text{solidity} > -2$, $\text{eccentricity} < 1.95$). Clustering was performed with Phenograph through the FastPG package in R

(Bodenheimer et al., 2020). Two separate clustering runs were conducted: low resolution and a subsequent re-clustering. Only lineage markers were utilised for low resolution clustering to identify main cell phenotypes. Dot plots for the enrichment and expression of each marker per cluster were constructed and clusters were merged to form meta clusters. Clusters were validated by plotting the centroid of each phenotype over the original images and qualitatively assessing matches. To assess batch effects between slides/regions, PCA was run on the phenotype percentages per region. The results were coloured by slide and disease state and qualitatively assessed as to the influence of each on the cell type abundance. Each meta cluster was re-clustered with all functional and immune checkpoint markers and subsequently annotated. Abundances of each cluster were calculated as a percentage of total detected cells as well as per unit of tissue area. For qualitative assessment of the spatial orientation of cell phenotypes, the centroids of each cell were plotted by region of interest and coloured according to cluster annotation.

SARS-CoV-2 Infected Cell Identification (EF/MP)

To ensure correct identification of SARS-CoV-2 infected cells, only cells positive for both SARS-CoV-2 spike and nucleocapsid antibodies by clustering were denoted as infected. Cases with positive cells by COMET mIHC were checked for expression of RNAscope SARS-CoV-2 probes and viral reads to the SARS-CoV-2 transcriptome by bulk RNAseq to ensure correct identification of virus infected cases.

Cellular Interactions and Neighbourhoods (EF/MP)

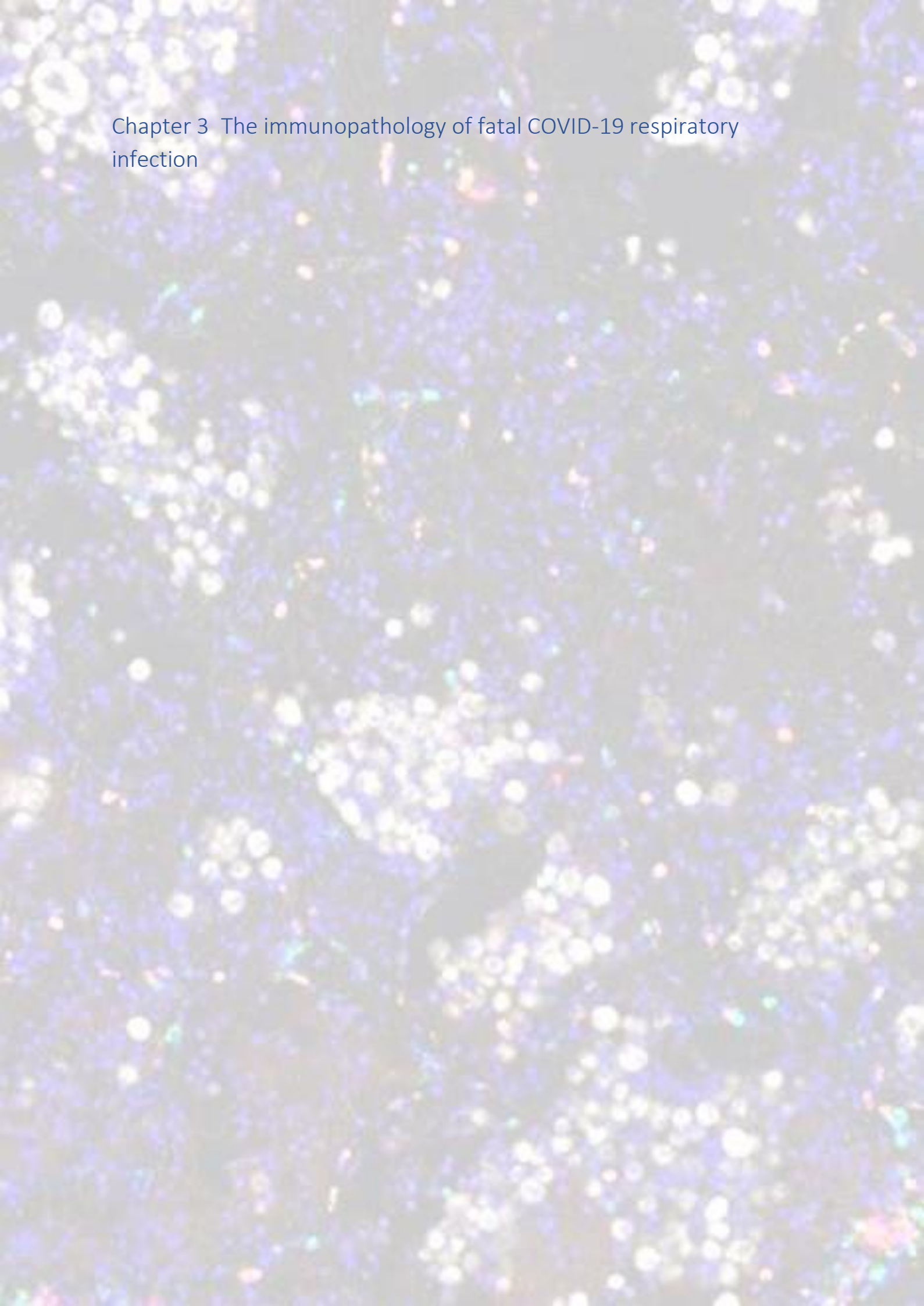
To quantify the interaction of cell phenotypes, a Delaunay triangulation graph was calculated using the centroids of each cell. Vertices that were connected as well as phenotype of that vertex were recorded. The likelihood ratios and relative frequencies of all interactions were subsequently calculated and visualised with boxplots split per disease state (Schurch et al., 2020). Cellular neighbourhoods were calculated by recording the 10 nearest neighbours of each cell and clustering these using k-Nearest Neighbours (kNN) with $k = 10$ as previously described (Schurch et al., 2020).

Distances between two cell types of interest were calculated with the nn2 function of the RANN library.

Virus microenvironment (EF/MP)

To quantify the immediate immune microenvironment of SARS-CoV-2 infected trophoblasts, cell phenotype abundances of each phenotype were recorded as a function of distance from the infected cells (Jiang et al., 2022). The nn2 function of the RANN library was used to calculate the N (where N = 10, 20, 40, 80, 100, 200, 400, & 800) number of cells closest to a SARS-CoV-2 infected trophoblast. The phenotype of each cell was then calculated as a percentage of the total cells in each bin (N) and plotted. For fair comparisons, the microenvironments of virus infected trophoblasts were compared to the number of cells matched microenvironments of non-infected trophoblasts cells from the same case.

Chapter 3 The immunopathology of fatal COVID-19 respiratory infection



3. The immunopathology of fatal COVID-19 respiratory infection

In order to elucidate the immunopathological features of COVID-19 respiratory infection, a post-mortem investigation of fatal COVID-19 respiratory infection was established in conjunction with pathologists at Royal Glamorgan Hospital and Morriston Hospital, South Wales. Consent post-mortem examinations were conducted on patients who has suffered with COVID-19 during their final illness; had a positive PCR SARS-CoV-2 swab test, either in life or at post-mortem examination; and where COVID-19 was given as the cause of death on certification. Tissues were sampled from multiple organs including lung and heart from every patient, followed by formalin fixation and paraffin embedding (FFPE). Control tissue was also sought from the post-mortem FFPE archive in cases with pre-existing consent for research, and included pre-pandemic diseased controls, other respiratory infections, and deaths from non-respiratory causes, regarded as normal controls.

Associated clinical data were collated by means of a standardised proforma for each patient and FFPE tissues then underwent basic histopathological assessment, followed by multi-modal spatial profiling including: i) Bulk Quantseq transcriptomic sequencing, ii) Spatially resolved transcriptomic profiling on the Nanostring GeoMx platform (Appendix 1), iii) *In-situ* RNA transcript detection by RNA scope (Appendix 2), iv) Single-plex chromogenic immunohistochemistry and multiplex immunohistochemistry on the Akoya CODEX, v) T-cell receptor (TCR) sequencing (Figure 3-1).

Data from across these assessments were assimilated to address four areas of the immunopathological response in COVID-19 respiratory infection:

- i) Clinicopathological features of COVID-19 respiratory infection
- ii) SARS-CoV-2 virus presence and distribution.
- iii) The immune composition in COVID-19 lungs.
- iv) SARS-CoV-2 microenvironment and inflammatory drivers.

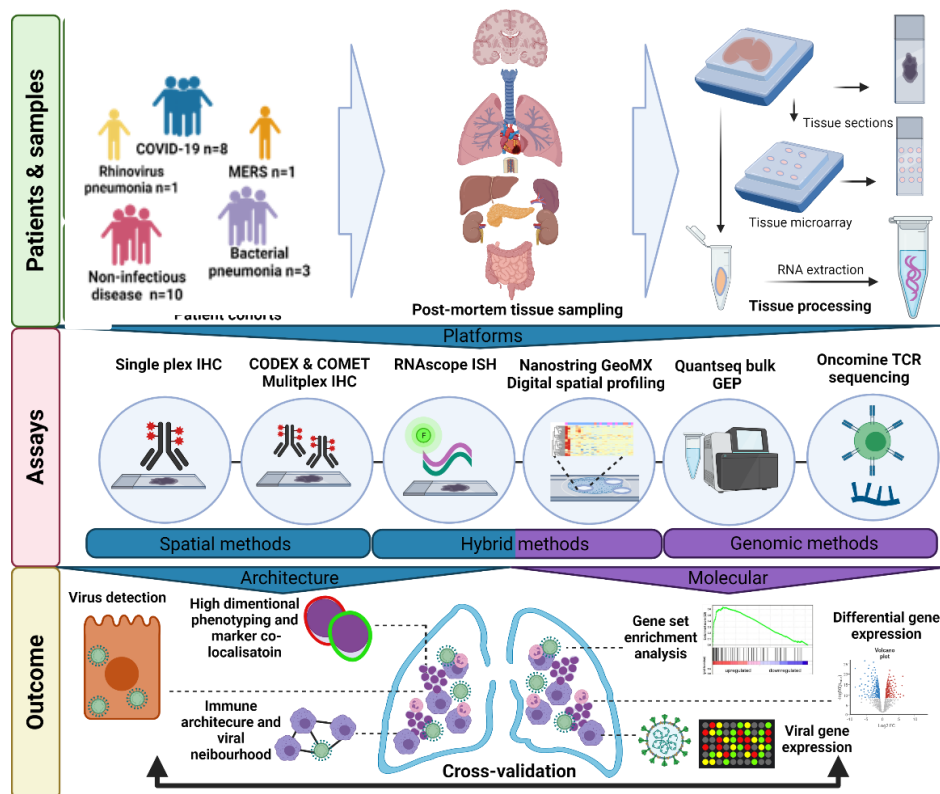


Figure 3-1. Experimental overview of the immunopathological characterisation of COVID-19 lungs, including cohorts, samples, assays and analysis. Post-mortems were performed on 8 COVID-19 patients and lung tissue samples were obtained. Control lungs included pre-pandemic cases of MERS, rhinovirus pneumonia, bacterial pneumonia and normal controls. Tissue samples underwent a multi-modality characterisation including spatial transcriptomic and proteomic techniques, enabling cross-validation of findings. Key: n=number; MERS=Middle east respiratory syndrome; IHC=immunohistochemistry; ISH=in situ hybridization; GEP=gene expression profiling; TCR=T cell receptor;

3.1. Clinicopathological characteristics

3.1.1. Clinical characteristics

The demographic details and clinical course of the patients with fatal COVID-19 who underwent post-mortem are summarised in Figure 3-2.

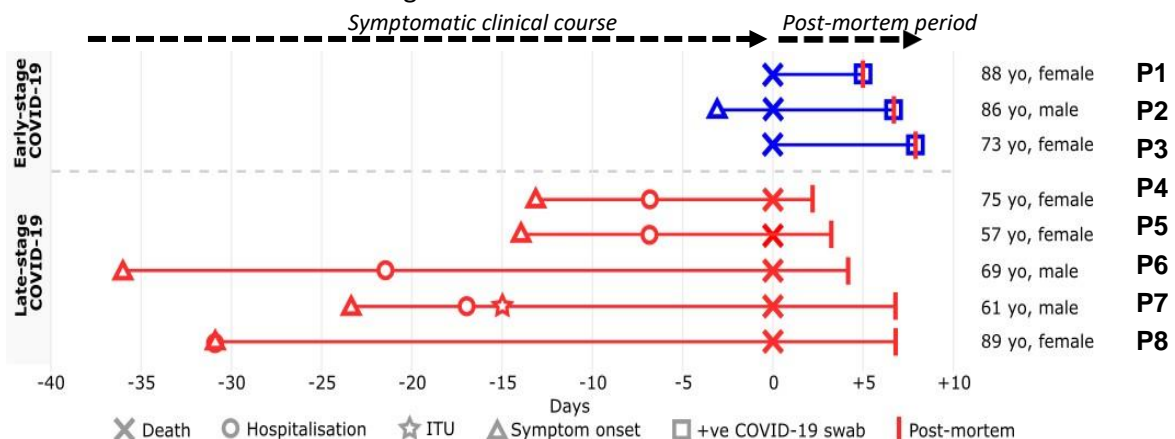


Figure 3-2. Summary of the symptomatic clinical course, demographics and pathological features of COVID-19 respiratory infection. Three patients died within 5 days of developing symptoms and five showed a more protracted course. Key: P1-P8= Patient 1 to Patient 8.

The post mortem cohort of fatal COVID-19 cases comprised 3 males and 5 females with a median age of 74 (range 57-89 years), all of which were of white British ethnicity. Three of the cohort died from COVID-19 in the community following a short clinical illness (0-3 days), whilst the others died from COVID-19 in hospital following a more protracted course (13-36 days). One patient required non-invasive ventilation and one patient underwent invasive ventilation on the intensive therapy unit. For most analyses hereafter, the cohort was divided into those who died early in the disease course (early stage (ES); 0-3 days), and those who died later in the disease course (late stage (LS); 13-36 days)

With regards to previous medical history, four of the COVID-19 cohort suffered with dementia, including the three patients who died in the community. Three suffered with hypertension, three with COPD or asthma, two with diabetes, one with congestive heart disease and one with chronic kidney disease. One patient was receiving the immunosuppressive drug methotrexate for rheumatoid arthritis.

3.1.2. Macroscopic and histopathological characteristics

On macroscopic post-mortem examination, the lung weights were heavier than normal. The median left lung weight was 777g (normal range 155-720g), and the median right lung weight was 807g (normal range 112-675g) (Matoba et al., 2017). In five cases, a mucositis (inflamed mucosa) was present in the trachea and bronchi. Seven lungs showed evidence of consolidation and oedema in at least one lung lobe. One of these cases showed features of lobar pneumonia.

Histologically, all cases of COVID-19 showed evidence of diffuse alveolar damage (DAD), the pathological manifestation of acute respiratory distress syndrome (ARDS) (Figure 1-3). Three stages of DAD are recognised: first, an early exudative phase (1-7 days of illness) characterised by a protein rich exudate in the alveoli with hyaline membranes; second, a later proliferative phase (1-3 weeks of illness) characterised by type II pneumocyte proliferation, myofibroblast proliferation and resorption of the protein rich exudate; third, a fibrotic phase (3 weeks or more of illness) characterised by

collagenous fibrosis in the alveolar space and interstitium (Cardinal-Fernández et al., 2017). Different stages of DAD co-existed in the same lung in the COVID-19 cohort but, as expected, presence of the third stage of DAD reflected the length of illness. All cases showed exudative phase changes, suggesting that DAD affects different parts of the lung in an asynchronous manner, with ongoing new onset involvement of different areas of lung occurring throughout the disease course. Six patients showed proliferative phase DAD, which included all of the late-stage disease patients and one patient who died in early stage (day 3). The presence of proliferative phase changes in a patient within three documented days of symptoms suggests that this lung pathology may precede the symptomatic manifestations in some cases. The reporting of symptoms in these patients may also have been delayed by the co-existence of dementia in a subset of patients.

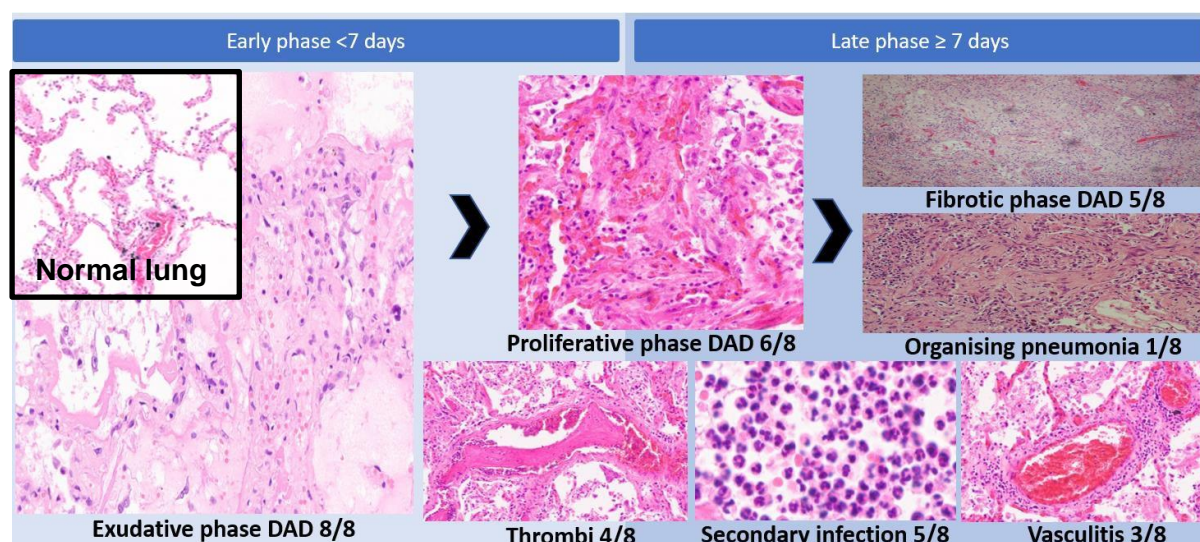


Figure 3-3. Histopathological features of COVID-19 respiratory infection across the disease timeline. Diffuse alveolar damage DAD of varying maturity is seen in all cases, whilst other pathological features such as thrombosis, secondary infection and vasculitis is enriched in late phase disease. Inset, upper left, shows normal lung for comparison, showing thin alveolar walls and open airspaces devoid of proteinaceous material and immune infiltrates.

One patient had DAD and an alternative pattern of lung injury called organising pneumonia, which comprises intra-alveolar buds of granulation tissue which progress from fibrin exudates to loose collagen-containing fibroblasts (Cordier, 2000). Additional pathologies were also present in most cases and these predominantly associated with late stage disease. Three late-stage cases and one early stage case showed evidence of thrombosis. The five late-stage COVID-19 cases showed evidence of secondary bacterial infection, which manifests histologically as aggregated collections of neutrophils in the alveolar space. In some lungs this secondary infection was widespread, and in others, there was

only very focal evidence of secondary infection. One case with secondary infection showed evidence of fungal hyphae, the morphology of which was consistent with mucormycosis. No fungal hyphae or spores were present in the remainder of the cases with secondary infection, and these were presumed to be associated with secondary bacterial infection. Three cases of COVID-19 lung showed a lymphocytic vasculitis, characterised by transmural infiltrates of lymphocytes.

Overall, in this cohort, diffuse alveolar damage was the most ubiquitous feature in the lungs with varying rates of thrombosis, secondary infection and vasculitis. These histopathological features are consistent with those previously described at post-mortem in COVID-19 lungs (Sofizan et al., 2022).

3.1.3. Assimilation of clinicopathological features.

My patient cohort could be divided into two clinically distinct cohorts: those who died early in the disease course and those who died later in the disease course. All patients showed diffuse alveolar damage but secondary pathologies were more common in the late stage patients.

3.2. Virus detection

In order to assess the presence and distribution of SARS-CoV-2 virus in COVID-19 lung, a multi-modal cross-validated approach was undertaken. Virus was detected at a transcriptomic level by Quantseq bulk sequencing, Nanostring GeoMx spatial gene expression and *in-situ* hybridisation by RNAscope using two probes targeting the spike and ORF4b genes. Proteomic detection of SARS-CoV-2 was undertaken by multiplex immunohistochemistry using antibodies specific for two protein targets: nucleocapsid and spike. SARS-CoV-2 RNAscope probes and antibodies were first validated in a SARS-CoV-2 infected Vero cell line. Infected cells were centrifuged to form a cell pellet that was then formalin fixed and paraffin embedded to match the processing of the patients' tissue samples (Appendix 3). Virus detection across the different modalities was assessed in a hierarchical fashion (Appendix 4), and cases in which virus was detected across multiple modalities were deemed to be true positive results. This obviated the potential pitfalls of false negative and positive results from using a single virus detection modality.

3.2.1. SARS-CoV-2 virus protein detection by CODEX multiplex immunohistochemistry.

Two antibodies specific to different SARS-CoV-2 proteins, spike and nucleocapsid were included in the multiplex CODEX mIHC panel. Virus detection by IHC was regarded as true positive only if dual spike and nucleocapsid staining was present (Figure 3-4). Performing qualitative assessment, positive SARS-CoV-2 virus staining was only seen in early stage COVID-19 lung. No virus staining was detected in any of the late stage COVID-19 lungs nor lungs from non-COVID-19 controls.

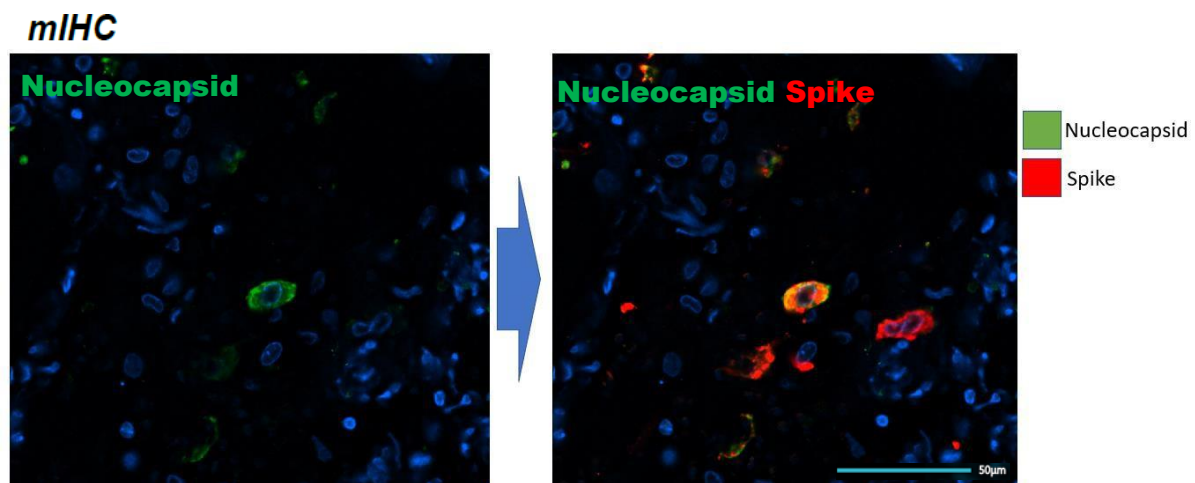


Figure 3-4. Dual spike and nucleocapsid stained COVID-19 lung tissue imaged by CODEX. The left hand panel shows the nucleocapsid channel only with strong staining in an epithelial cell. The left hand image shows the nucleocapsid and spike channel from same region of lung highlighting dual spike and nucleocapsid staining in the same epithelial cell. Note other cells showing spike-only staining which was regarded as a false positive. Key: mIHC=multiplex immunohistochemistry.

The results of quantitative assessment of mIHC images were consistent with the qualitative assessment: dual SARS-CoV-2 virus target detection was only present in the 3 early stage disease cases (Figure 3-5). No dual virus staining was detected in late stage COVID-19 lungs nor in the non-COVID-19 controls. Assessing virus staining in combination the staining of the other proteins detected by the mIHC staining showed that virus-positive cells were predominantly type II pneumocytes with a smaller number of macrophages also staining positive for virus spike and nucleocapsid proteins.

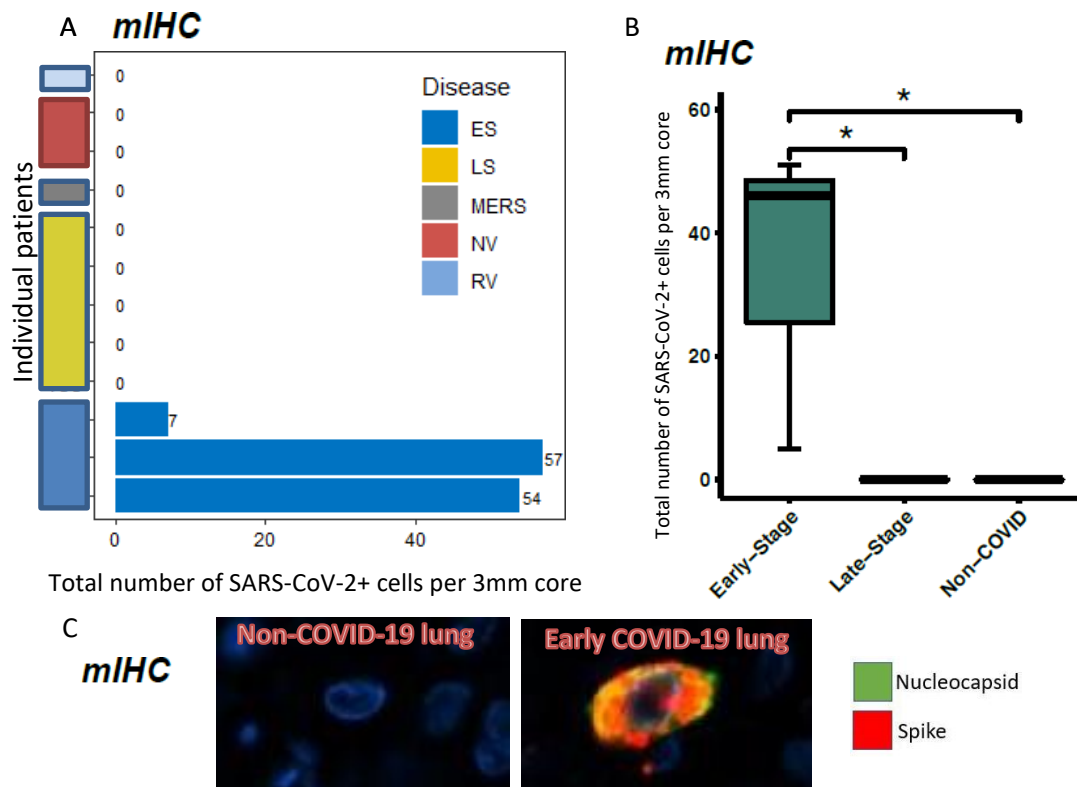


Figure 3-5. A. case-by-case plot of the number of SARS-CoV-2 virus positive cells showing double spike and nucleocapsid staining by IHC, plotted for individual cases. Only three cases of early phase COVID-19 lung showed SARS-CoV-2 protein expression. No late COVID-19 cases, or, non-COVID-19 controls. B. Summary bar and whisker plot of positive virus staining in early stage and late stage COVID-19 lung, and non-COVID-19 controls (diseased and normal included): Key: ES= early stage COVID-19; LS= late stage COVID-19 disease; MERS=middle eastern respiratory syndrome; NV=non-virus or normal controls; *= Statistically significant difference with a P-value of <0.05; **= $p < 0.01$; ***= $p < 0.001$; ****= $p < 0.0001$. (N.B. Wilcoxon statistical test performed). C. CODEX multiplex staining image showing spike and nucleocapsid staining. Left: A pneumocyte staining negative for spike and nucleocapsid. Right: Pneumocyte showing dual spike and nucleocapsid staining. Key: mIHC=multiplex immunohistochemistry.

3.2.2. SARS-CoV-2 virus detection by Quantseq bulk transcriptomic sequencing.

To assess the tissue wide presence of SARS-CoV-2 at a transcriptomic level in lung, and explore the range of viral genes expressed in infected lungs, the Quantseq bulk gene expression data was interrogated by aligning reads against the SARS-CoV-2 genome. Similar to proteomic detection of virus by mIHC, viral mRNA transcripts were detected in early stage COVID-19 lungs although smaller numbers of viral reads were present in some of the late stage cases (Figure 3-6)

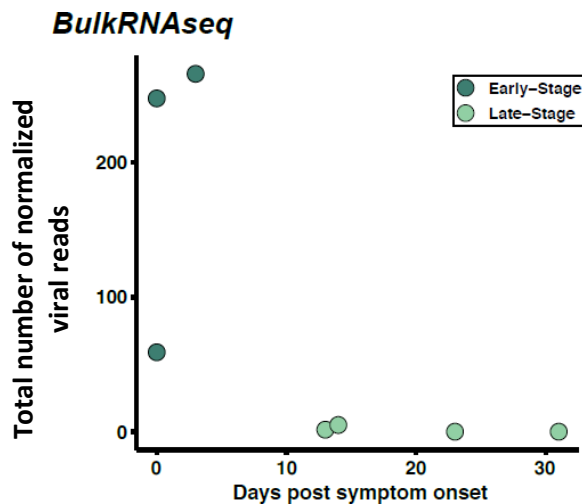


Figure 3-6. SARS-CoV-2 viral load represented by the total number of normalized viral reads in early stage and late stage COVID-19 cases, based on Quantseq bulk gene expression sequencing. In keeping with the multiplex immunohistochemistry findings, three early stage cases showed expression of SARS-CoV-2 genes, whilst three late stage cases showed little or no viral expression.

Closer examination of the viral transcriptomic data showed nucleocapsid, spike and Orf1ab were the most abundantly expressed genes (Figure 3-7) and all three transcripts were detected in all three early stage disease COVID-19 lungs. Transcripts of ORF3a, ORF7a, membrane and ORF6 were variably detected in early stage disease.

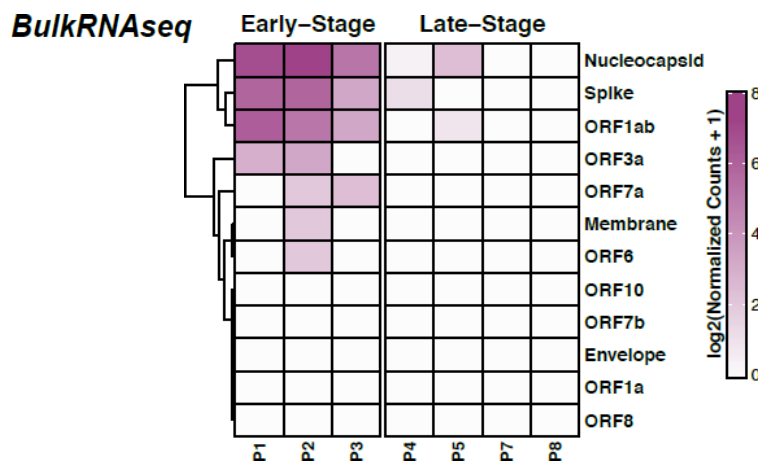


Figure 3-7. Heatmap showing expression of normalized SARS-CoV-2 viral gene reads in COVID-19 lungs, based on Quantseq bulk gene expression sequencing. Expression is predominantly seen in early stage disease with only small numbers of reads observed in late stage cases. Spike, nucleocapsid and ORF1ab were the most abundantly expressed transcript. Key: P1-P8 = Patient 1 to patient 8.

Notably, low levels of nucleocapsid, spike or ORF1ab was seen in two cases of late stage COVID-19 disease. This low-level expression in late stage COVID-19 lungs was of uncertain significance as virus was not detected at a proteomic level in these cases, or, at a transcriptomic level by other virus detection modalities. This outlier expression of COVID-19 genes by Quantseq gene expression profiling

may be due to false positive detection, the result of sample contamination, or detection of virus transcripts in the blood of viraemic COVID-19 patients, as tissue samples will also contain small amounts of patient's blood products. An alternative explanation for this discordant result is that viral mRNA is present in the lungs for prolonged periods of time. RT-PCR testing of throat swabs is known to detect viral genomic material for prolonged periods of time following infectious virus clearance. Although mRNA may be less stable than viral genomic material, the fact that Quantseq detects small fragments of mRNA may allow it to detect residual viral debris (Wölfel et al., 2020).

3.2.3. SARS-CoV-2 virus detection by Nanostring GeoMx digital spatial profiling.

To explore the location of viral RNA within lung tissues additional 'spike-in' probes to detect SARS-CoV-2 virus were included in the Nanostring GeoMx digital spatial profiling (DSP) experiment. The SARS-CoV-2 spike-in panel comprises 9 probes targeting SARS-CoV-2 virus, probes targeting the nucleocapsid and spike open reading frames of the HCoV-229E, HCoV-HKU1, HCoV-NL63 and SARS-CoV (targeting the sub-genomic positive sense strand, thus measuring gene expression), a probe targeting the negative sense genomic strand (measuring viral replication), and a probe against the human ACE2 gene. The DSP data were first interrogated to assess for the presence of virus across all regions of interest sampled in the GeoMX experiment. In line with proteomic and bulk transcriptomic data, SARS-CoV-2 virus transcripts were only detected in early stage COVID-19 lungs, whilst there was no detection above baseline for late stage COVID-19 lungs or non-COVID-19 controls (Figure 3-8).

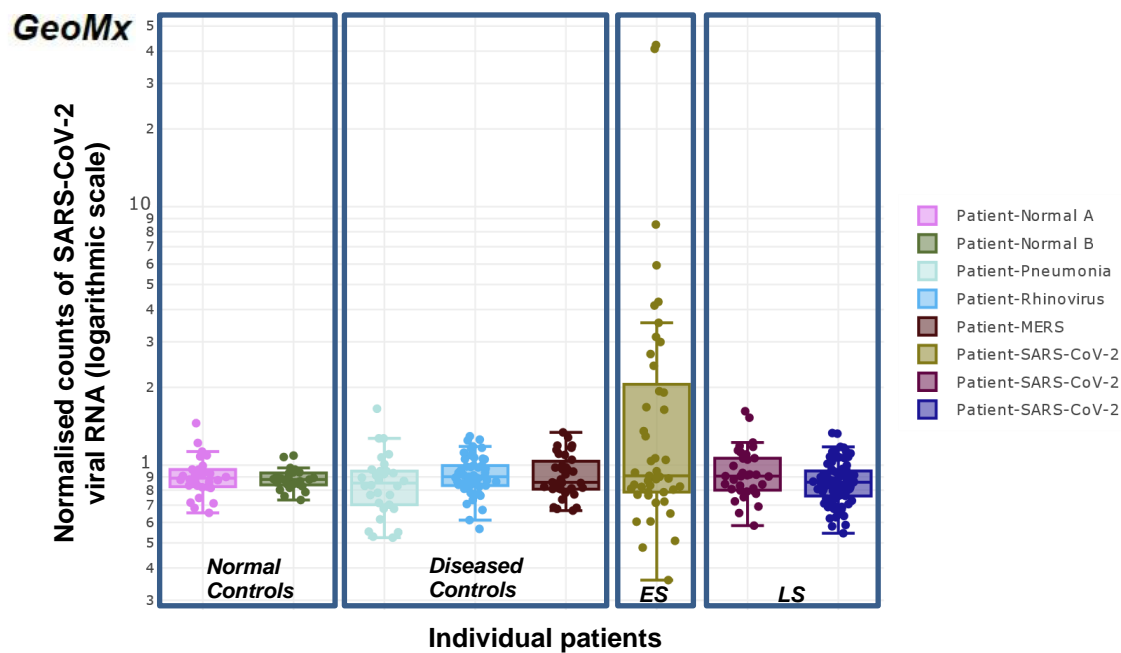


Figure 3-8. Pseudo-bulk analysis based on GeoMx data, combining all regions of interest, shows that SARS-CoV-2 gene expression was observed only in the early stage disease COVID-19 lungs. There was no evidence of increased expression in late stage COVID-19 lungs, disease controls or normal controls. Each dot represents an individual region of interest. Key: ES=early stage COVID-19 lung; LS=Late stage COVID-19 lung; MERS=Middle eastern respiratory syndrome.

To explore the location of SARS-CoV-2 viral gene expression in lung, the three compartments assessed by GeoMX DSP (alveoli, blood vessels and upper airway) were interrogated separately (Figure 3-9). All the SARS-CoV-2 virus gene expression was present with the alveolar compartment whilst no viral expression was seen in the blood vessels or upper airway. This result was consistent with the earlier proteomic assessment by mIHC that detected virus within epithelial cells and a smaller number of macrophages in the lung.

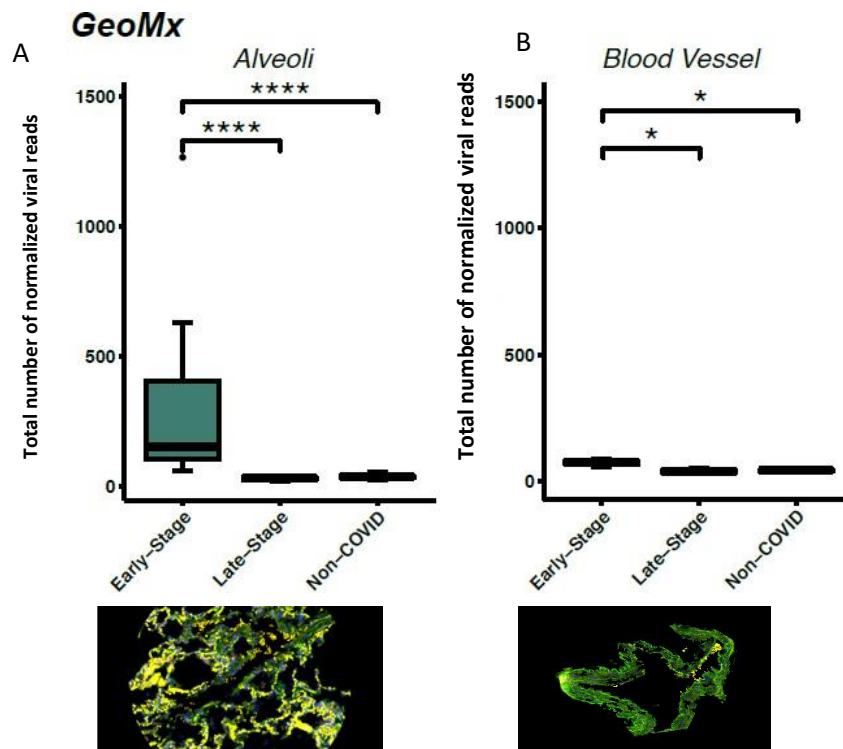


Figure 3-9. Bar and whisker plot representing an interrogation of Nanostring GeoMx SARS-CoV-2 gene expression focusing on the alveolar (A) and blood vessel (B) compartments, showed evidence of virus expression in the alveolar compartment of early stage disease COVID-19 lungs, but not late stage COVID-19 lungs, or non-COVID-19 control lungs (including diseased and normal controls). No expression was seen in the blood vessel compartment. *= Statistically significant difference with a P-value of <0.05; **= $p < 0.01$; ***= $p < 0.001$; ****= $p < 0.0001$. (N.B. Wilcoxon statistical test performed). The bottom panels show examples of alveolar (left) and blood vessel (right) ROI imaged on the GeoMX platform.

3.2.4. SARS-CoV-2 virus detection by RNAscope *in-situ* hybridisation

Lastly, *in-situ* transcriptomic detection of SARS-CoV-2 virus was performed by RNAscope, using probes against sense spike mRNA and anti-sense ORF1ab (Figure 3-10). This combination of sense and anti-sense probes allowed the detection of virus genomic RNA but also a virus mRNA transcript, thus assessing whether replicative infection was present. An AE1/AE3 antibody specific for pan-cytokeratin was also included in the experiment to detect epithelial cells.

As observed earlier using mIHC to detect viral proteins, virus RNA transcripts were predominantly detected in epithelial cells (AE1/AE3+) and in a smaller subset of non-epithelial (AE1/AE3-) cells (Figure 3-10). The non-epithelial cells which demonstrated positive viral transcript staining showed a morphology consistent with macrophages: they comprised rounded cells with abundant cytoplasm. Similarly, virus RNA was only detected by RNAscope in early stage COVID-19 lungs, no viral RNA was detected in any of the late stage COVID-19 lungs or non-COVID-19 controls.

RNAScope

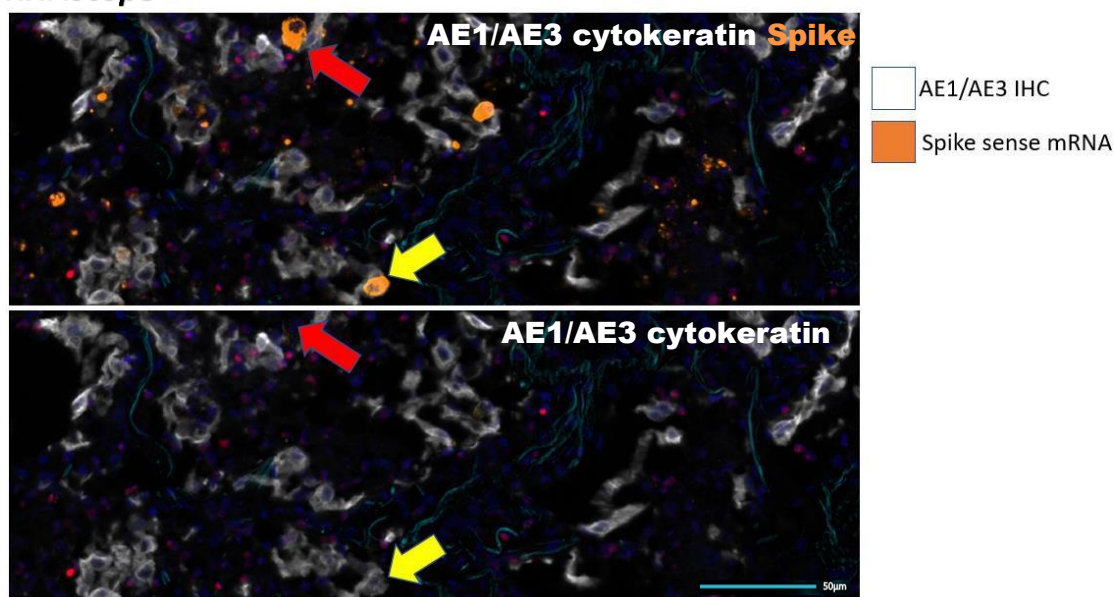


Figure 3-10. COVID-19 lung double stained for AE1/AE3 cytokeratin by IHC and spike mRNA. Upper and lower panels show the same region of lung with AE1/AE3 and spike displayed in the top panel and AE1/AE3 only in the bottom panel. Virus spike mRNA transcripts were detected by RNAscope in AE1/AE3-positive epithelial cells (yellow arrows showing virus spike in AE1/AE3+ epithelial cells) and in non-epithelial cells (red arrows showing virus spike in AE1/AE3- cells), likely macrophages based on morphology. Scale bar = 50µm.

3.2.5. Cross validation of SARS-CoV-2 virus detection.

Comparing viral loads detected across the different proteomic and transcriptomic virus detection modalities showed statistically significant correlation between each platform (Figure 3-11). Notably, of the three early stage COVID-19 lungs in which virus was detected, two cases showed a much greater viral load compared to the other virus positive case.

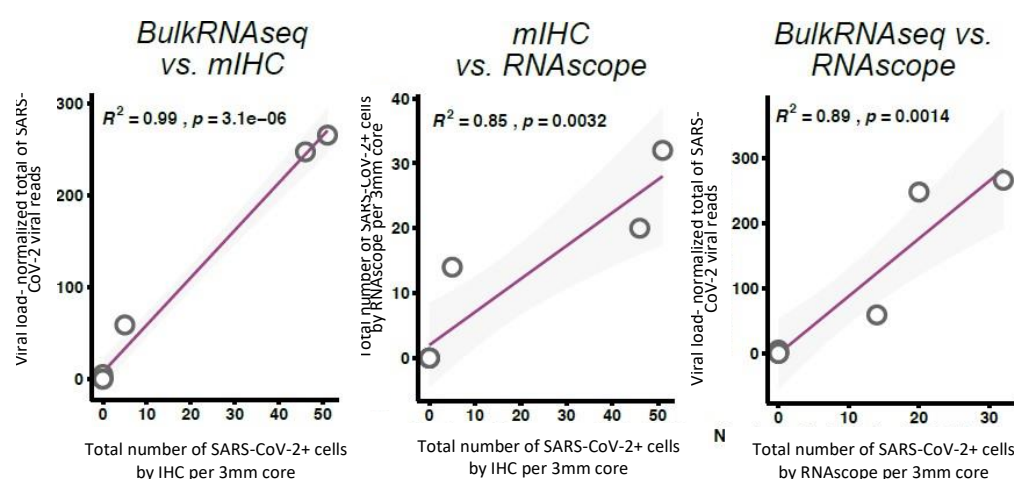


Figure 3-11. Correlation analysis of SARS-CoV-2 virus loads/virus infected cells detected across different 3 different modalities; bulk sequencing, multiplex immunohistochemistry and RNAscope. All modalities showed excellent correlation between the number of virus expressing cells and number of viral reads detected by sequencing Key: RNAseq=RNA sequencing; mIHC=multiplex immunohistochemistry.

3.3. Immune cell composition in COVID-19 lungs.

The immune cell composition in the COVID-19 lung was assessed by two methods. First, Nanostring GeoMx DSP data were deconvoluted to infer the cellular composition in the lung. Second, multiplex IHC staining of lung tissues using a panel of 38 cell lineage, immune lineage and viral markers was assessed to determine the composition and location of the immune infiltrate.

3.3.2. Estimation of cell abundance based on deconvoluted GeoMX DSP.

Utilising the Nanostring GeoMx RNA DSP data, the relative tissue cell abundances were estimated (Figure 3-12). In most lung specimens, endothelial cells were the most abundant cell type. This is in-keeping with the cellular composition of the lung which is a vascular organ primarily comprised of capillary beds for gas exchange (Khan and Lynch, 2022). In bacterial pneumonia samples, neutrophils were the most abundant immune cell type which is consistent with what is seen on histology; alveolar spaces filled with sheets of neutrophils (Jain et al., 2022). The presence of these expected features served as a useful internal control and validation. In COVID-19 lungs, there were proportional increases in both monocytes/macrophages and neutrophils compared to normal controls and rhinovirus pneumonia. Additionally, there was a proportional increase in fibroblasts in COVID-19 compared to control. Plasma cells, plasmacytoid dendritic cells and CD4+ memory cells accounted for a greater proportion of cells in late vs early stage COVID-19 lung.

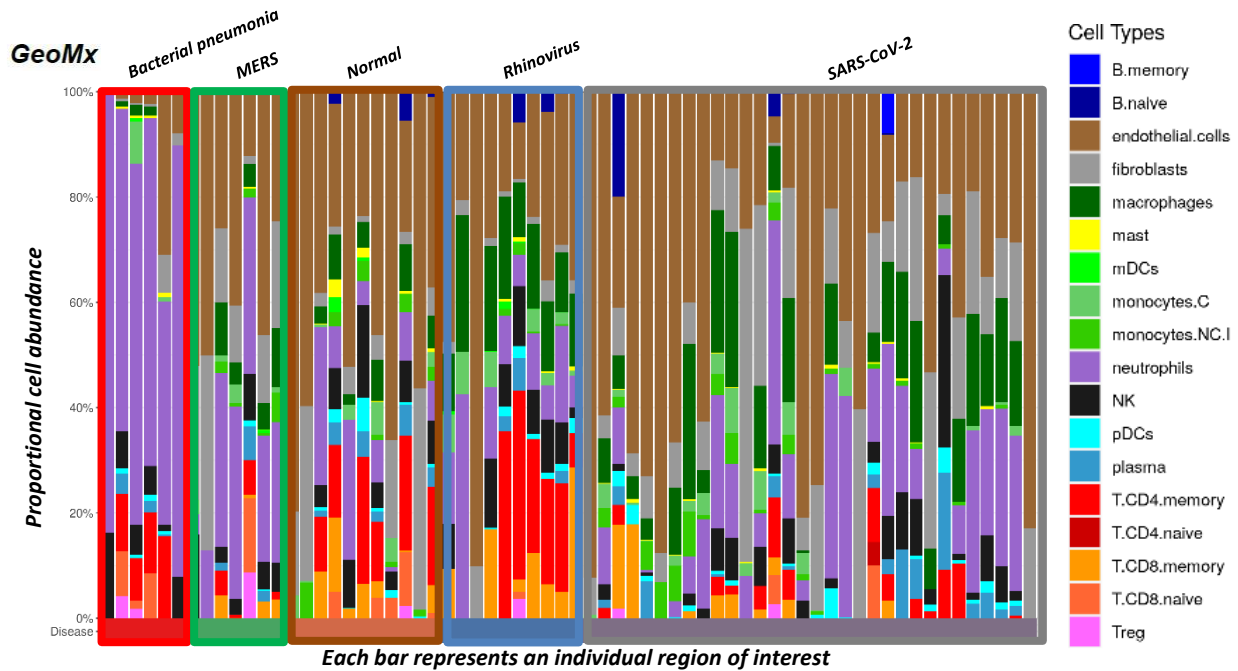


Figure 3-12. Cellular deconvolution of the Nanostring GeoMx gene expression data showing the relative abundances of various cell types in each region of interest, grouped according to disease type in COVID-19 lungs and non-COVID-19 controls. Key mast=mast cells; monocytes.C=classical monocytes; monocytes.NC.I=non-classical/intermediate monocytes; mDCs=monocytoid dendritic cells; pDCs=monocytoid dendritic cells; NK=natural killer cells; Treg=T regulatory cells; T=T-cell; B=B-cell.

3.3.3. Determination of cell composition by CODEX multiplex immunohistochemistry

The immune infiltrate in COVID-19 lungs was further assessed by CODEX mIHC, comprising a panel of 38 antibody markers. Qualitative assessment of the immune infiltrate showed macrophages were the most abundant cell type, and were present within the lumen of the alveoli (Figure 3-13). Lymphocytes were also present in a more scattered distribution, predominantly within alveolar walls and occasionally with the alveolar lumen. The most abundant lymphocyte subset was CD4+ T-cells, with fewer CD8+ T-cells and CD20+ B-cells present.

mlHC

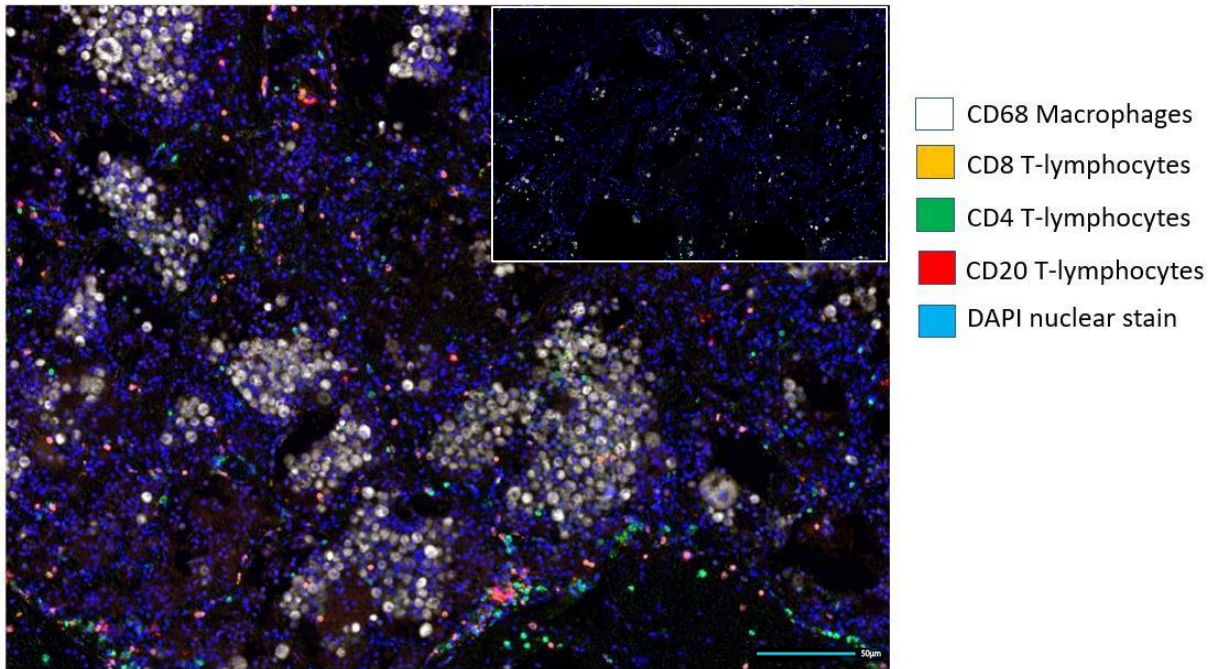
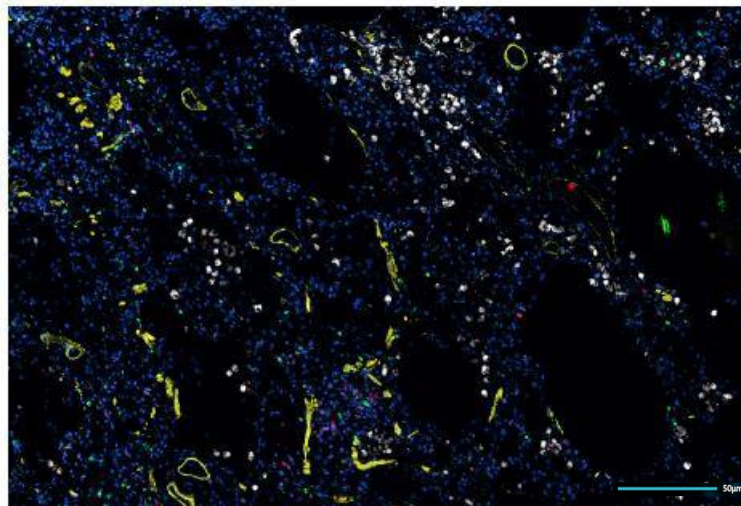


Figure 3-13. Qualitative assessment of CODEX mlHC images in COVID-19 lung showed intra-alveolar infiltrates of macrophages and sparser interstitial infiltrates of lymphocytes. Inset, normal control lung showing sparse immune cell populations. Scale bar = 50µm.

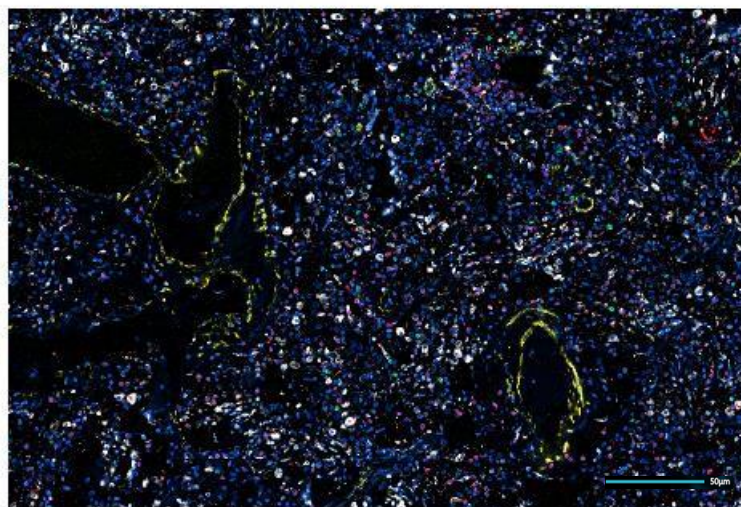
Further qualitative assessment of early stage and late stage COVID-19 lungs showed increased macrophages, CD4+ T-cells, CD8+ T-cells and B-cells in late-stage lungs.

mlHC

Early Stage



Late Stage



DAPI aSMA CD68 CD8 CD4

Figure 3-14. CODEX mlHC images showing the abundance of macrophage (CD68) and T-cell subsets (CD4 & CD8) in early stage vs late stage COVID-19 lungs. Qualitatively, the immune infiltrate is more abundant in late stage COVID-19 lung compared to early stage COVID-19 lung. Key: aSMA=alpha smooth muscle actin. Scale bar = 50µm.

To qualitatively assess the immune infiltrate in COVID-19 by mlHC, I initially focused on a subset of four COVID-19 lungs (that comprised early and late disease) and 3 controls. The multiplex images were de-arrayed and subsequently segmented using CellSeg (Lee et al., 2022). This resulted in approximately ~400,000 cells that were analysed by CELESTA. This identified four major cell types (Figure 3-15): epithelial cells (pan-cytokeratin+), endothelial cells (CD34+), immune cells (CD45+) and smooth muscle cells (SMA+) (Zhang et al., 2022).

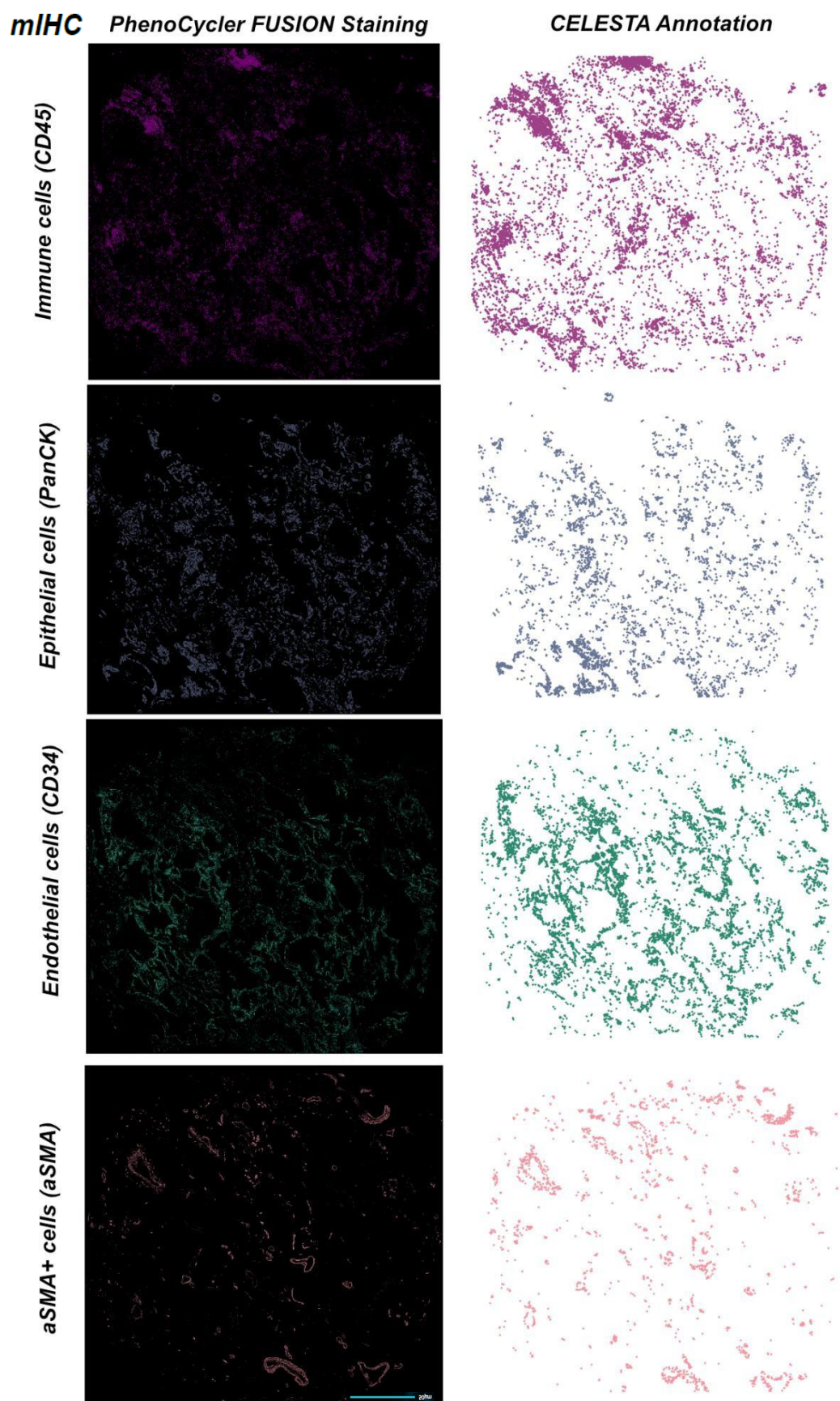


Figure 3-15. CELESTA Validation: Raw images (left) and schematic representation (right) showing CELESTA cell phenotype annotation of four phenotypes from CODEX miHC staining. CELESTA annotation accurately reflects the expected distribution of the annotated cell types based on the raw images. Key: aSMA=alpha smooth muscle actin; PanCK=pan-cytokeratin. Scale bar =50µm.

Immune cell subsets were then clustered using PhenoGraph to identify various sub-populations ((Bodenheimer et al., 2020). For ease of analysis, images were down-sampled to approximately 40,000 cells, coloured by phenotype and visualised on a tSNE plot (Figure 3-16). In keeping with the Nanostring GeoMx deconvolution data, and the qualitative assessment of COVID-19 lungs, the most abundant immune cell subset were macrophages, followed by neutrophils, CD4+ T-cells and CD8+ T-cells, with fewer NK-cells and B-cells present.

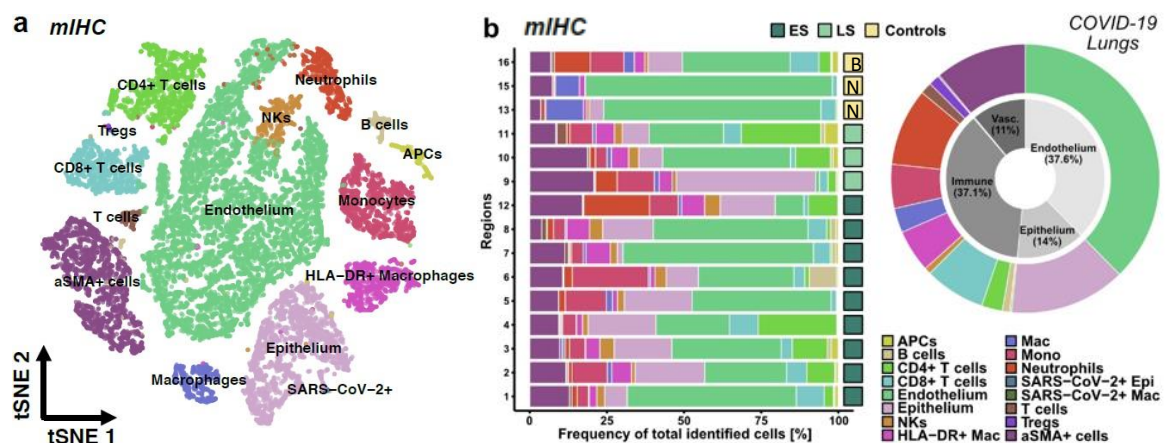


Figure 3-16. Quantitative analysis of immune cell abundance in a subset of 4 COVID-19 lungs and 3 controls, comprising 2 normal controls 1 bacterial pneumonia control. A. tSNE plot showing the abundance of immune cell subsets for all four COVID-19 cases and controls combined. B. Relative cell abundances in regions of interest in early stage (ES) COVID-19 lungs, late stage (LS) COVID-19 lungs, normal controls and bacterial pneumonia (% cell abundance of total in each region on interest). Key mac=macrophage; mono=monocytes; NK=natural killer cells; Treg=T regulatory cells; Epi=epithelium; aSMA=alpha smooth muscle actin; B=bacterial pneumonia; N=normal.

In order to quantitatively explore the differences in immune subset abundance between early stage and late stage COVID-19 lungs, I focused on a smaller panel of markers to analyse a larger cohort of COVID-19 cases. Cell abundances were plotted against symptomatic disease duration. As observed by the earlier qualitative analysis, macrophages and lymphocytes (including both CD4+ T-cells and CD8+ T-cells) were more abundant in late-stage disease compared to early stage disease (Figure 3-17).

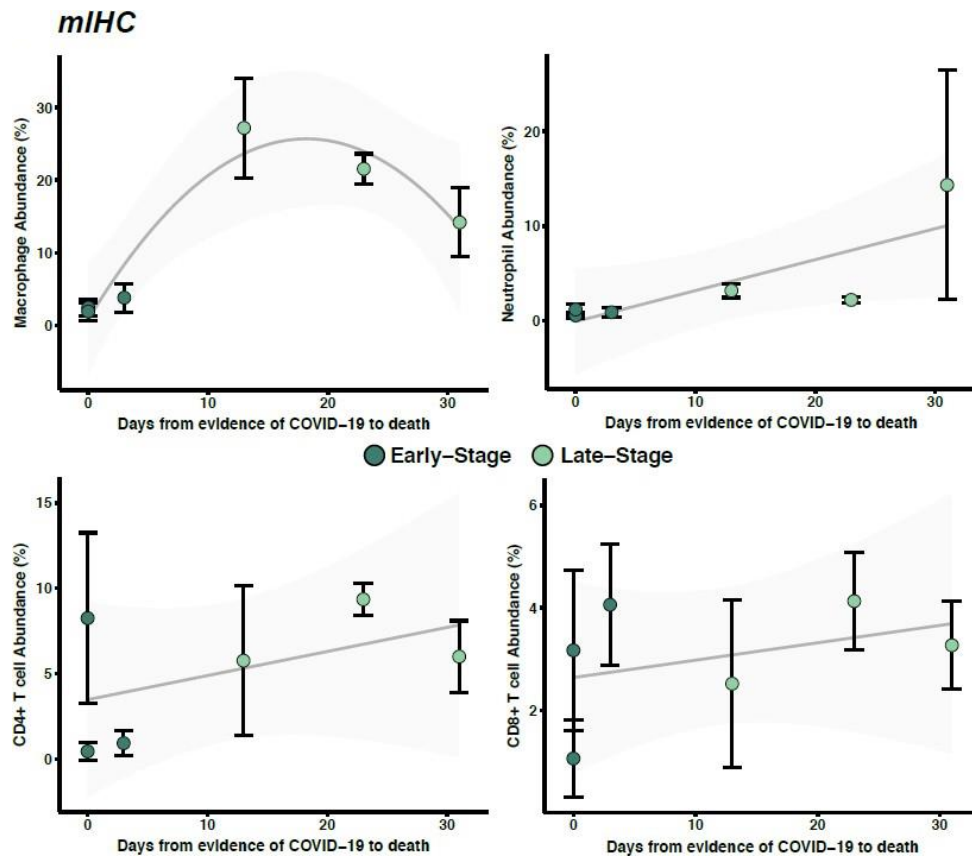


Figure 3-17. Immune subset abundances in COVID-19 lungs based on CODEX mIHC images showing cell abundance (% of total cells) of major immune subsets plotted against length of illness, defined as time from symptom onset to death. Error bars show standard deviation. Generally, innate and adaptive subsets increased with increasing duration of illness.

3.3.4. TCR sequencing

To assess whether T-cells were mounting an epitope specific response against the SARS-CoV-2 virus, TCR sequencing (TCRseq) using the Oncomine TCR Beta-SR Assay (Thermo Fisher) was performed on DNA extracted from COVID-19 lung and controls. Eight COVID-19 FFPE lung samples were sent for TCRseq, 7 non-virus controls, one case of rhinovirus, one case of bronchopneumonia and one case of MERS. The assay failed in two COVID-19 lung cases (one early, one late), and in one non-virus control due to low DNA.

First, the diversity of the TCR sequences was examined by clone count and Shannon diversity index. Shannon diversity index is a measure of biological diversity derived from ecological investigations to measure entropy in populations, and is related to the weighted geometric mean of the proportional abundances of subtypes. COVID-19 lungs showed reduced diversity by both measures (Figure 3-

18). The clone count was

significantly reduced compared to non-viral controls ($p=0.0417$, unpaired T-test), and whilst the Shannon diversity was reduced in COVID-19 lung compared to control, the difference was not statistically significant ($p=0.1997$, unpaired T-test).

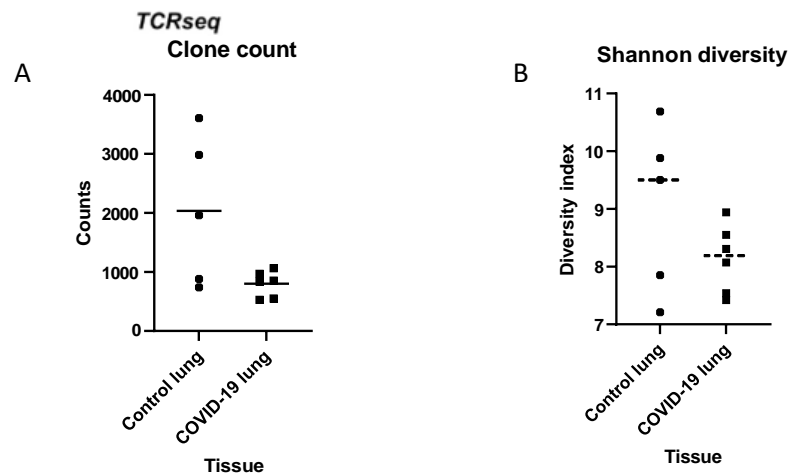


Figure 3-18. Measures of TCR diversity comparing (A) clone count and (B) Shannon diversity in COVID-19 lung vs non-COVID-19 controls (diseased and normal controls combined).

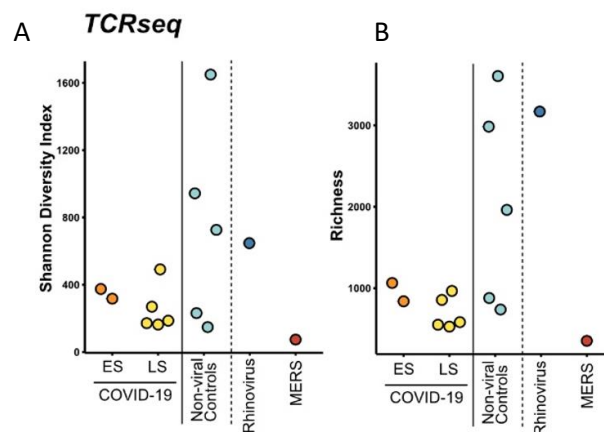


Figure 3-19. Comparison of (A) Shannon diversity and (B) richness of TCR sequences in early and late COVID-19 lungs, compared to diseased and normal controls. Key: ES=early stage; LS=late stage.

TCR clone richness and shannon diversity was assessed comparing early and late stage COVID-19 lung with diseased viral controls and non-viral controls (Figure 3-19). COVID-19 lung in early and late stages, as well as MERS lung, showed decreased Shannon diversity and richness. The findings further suggest that coronavirus related diseases are characterised by less diverse TCR repertoires in tissue compared to other viral and non-viral infectious diseases.

Next, in order to determine whether the reduced diversity was due to genuine clonal TCR expansions or reduced number of T-cells in COVID-19 lung, measures of diversity were plotted against T-cell abundance derived from CODEX multiplex IHC data (Figure 3-20).

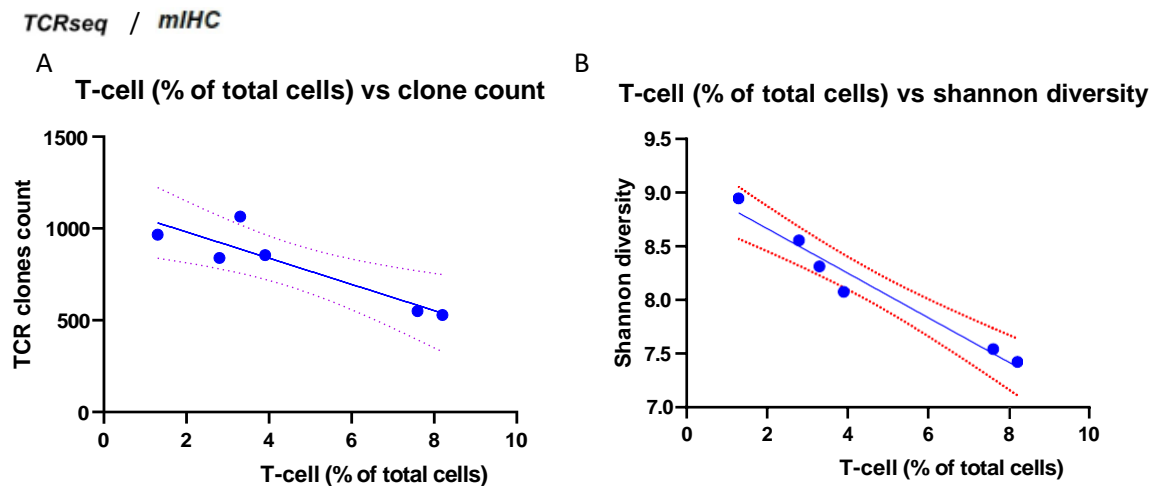


Figure 3-20. Measures of diversity in COVID-19 lungs determined by TCR sequencing plotted against T-cell abundance as determined by CODEX mIHC (A) clone count and (B) Shannon diversity, plotted against T-cell abundance (% of total cells in 3mm core).

Both the TCR clone count and the Shannon diversity showed a statistically significant negative correlation with increasing T-cell count (Pearson correlation: TCR count $r=0.9031$, $p=0.0136$; Shannon $r=0.9796$, $p=0.0006$). These findings suggest that the reduced diversity observed in COVID-19 lung compared to control lungs is due to clonal TCR expansion.

Next, the frequencies and sizes of the clonal expansions were examined (Figure 3-21). All COVID-19 and MERS lungs contained T-cell sequences that accounted for 0.1-1% and 1-10% of the total repertoire. Two late stage COVID-19 lung and the MERS lung contained sequences that accounted for 10% of the total repertoire. However, large expansions were not a specific feature of COVID-19 lungs, as large TCR expansions were also seen in bacterial pneumonia and in rhinovirus pneumonia case.

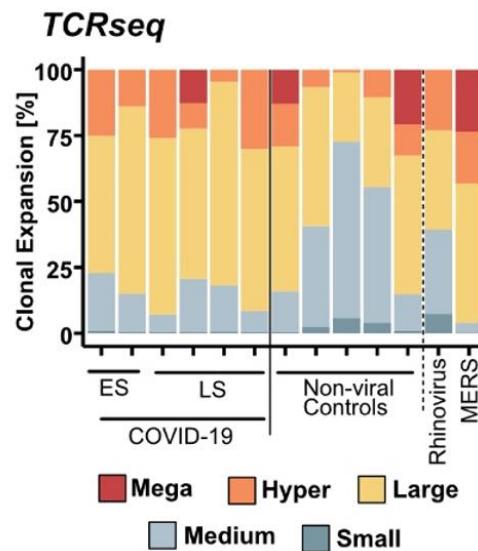


Figure 3-21. Bar plot showing the relative frequencies of the various clonal expansions in COVID-19 lungs (ES. Early stage; LS, late stage) compared to normal (non-viral) and diseased controls. Expansion were defined as follows: Mega>10% of total TCRs; hyper=1-10% of total TCR; large=0.1-1% of total TCR; medium=0.01-0.1% of total TCR; small=up to 0.01% of total TCR.

In order to determine if the TCR clonal expansions were targeting SARS-CoV-2 epitopes, TCR Beta sequences were matched to a database containing 135,000 high-confidence SARS-CoV-2 specific sequences (Nolan et al., 2020) and a further two databases containing sequences specific for SARS-CoV-2 and other viruses (Goncharov et al., 2022b; Tickotsky et al., 2017) (Figure 3-22). Overall, around 90% of TCRs from SARS-CoV-2 samples were mapped to unknown sequences, and no more than 0.5% of the repertoire was SARS-CoV-2 specific for any given COVID-19 lung. Every lung sample affected by COVID-19 contained TCR sequences reported to be specific to the SARS-CoV-2 virus, however, similar proportions of these of SARS-CoV-2 specific sequences were also seen in non-COVID-19 controls. One late stage COVID-19 lung and a MERS control showed a highly abundant TCR expansion which mapped to TCR sequences specific for Epstein Barr virus and cytomegalovirus, respectively. More detailed tree diagrams are shown in Appendix 5.

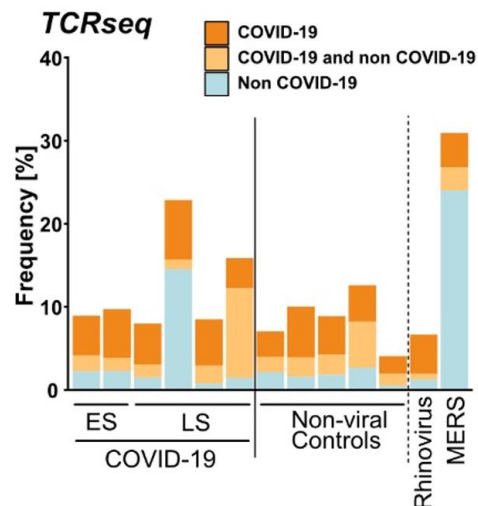


Figure 3-22. Bar plot showing frequencies of TCR sequences with known specificities for viruses (COVID-19, COVID-19 and non-COVID-19, non-COVID-19) based on cross-referencing with three databases. COVID-19 lungs showed no enrichment for SARS-CoV-2 specific TCR sequences compared to pre-pandemic diseased and normal controls. Key: ES=early stage; LS=Late stage.

3.4. SARS-CoV-2 virus microenvironment and inflammatory drivers.

To understand interactions between SARS-CoV-2 infected cells and the florid immune response, along with potential drivers of the immune response, I made use of the CODEX mIHC data and Nanostring GeoMx data I generated from the same set of patients in which I had consistently detected virus across multiple platforms. In this analysis, for each patient I compared the immediate immune SARS-CoV-2 virus niche in virus-positive regions of the lung to virus negative regions from the same lung.

3.4.1. Characterisation of the virus niche by CODEX mIHC.

CODEX mIHC data was interrogated by measuring immune cell abundances of the 100 cells closest to SARS-CoV-2 infected epithelial cells compared to non-virus infected epithelial cells within the same cases. Generally, immune cells (identified broadly by CD45 positivity using CELESTA) were significantly reduced in the immediate SARS-CoV-2 microenvironment (Figure 3-23).

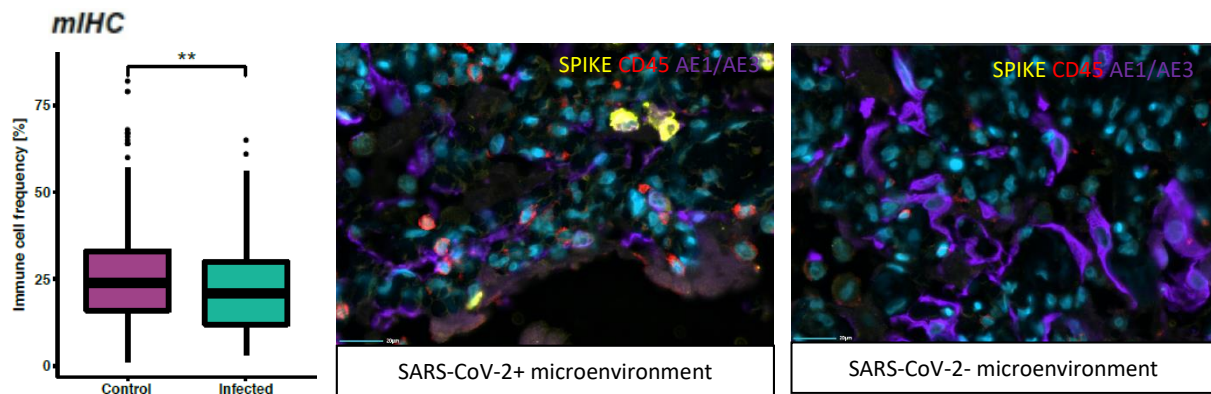


Figure 3-23. Quantification of Immune cells identified by CD45 positivity by multiplex immunohistochemistry images in the immediate microenvironment (nearest 100 cells) of SARS-CoV-2 infected epithelial cells compared to the microenvironment of non-infected epithelium from the same patients. By Wilcoxon statistical test, the microenvironment of non-infected cells epithelial cells showed a statistically significant increase in immune cells. * = Statistically significant difference with a P-value of <0.05; **= $p<0.01$; ***= $p<0.001$; ****= $p<0.0001$. Scale bar = 20µm. The left COMET image shows an enrichment of CD45+ cells (red) in the immediate vicinity of SARS-CoV-2 positive epithelial cells (purple and yellow), compared to the right COMET image, showing a depletion of CD45 cells in the vicinity of SARS-CoV-2 negative epithelial cells (purple).

In contrast to the overall reduction in immune cells in the COVID-19 microenvironment, macrophages were increased significantly within the SARS-CoV-2 viral niche (Figures 3-24, 3-25). The majority of these macrophages expressed PDL1 and IDO immune checkpoint ligands. In contrast, neutrophils were significantly depleted in the immediate microenvironment of SARS-CoV-2 infected epithelial cells compared to non-infected epithelial cells. Similarly, B-cells, CD4+ T-cells and CD8+ T-cells subsets, including PD1 expressing T-cells, were also depleted from virus microenvironment.

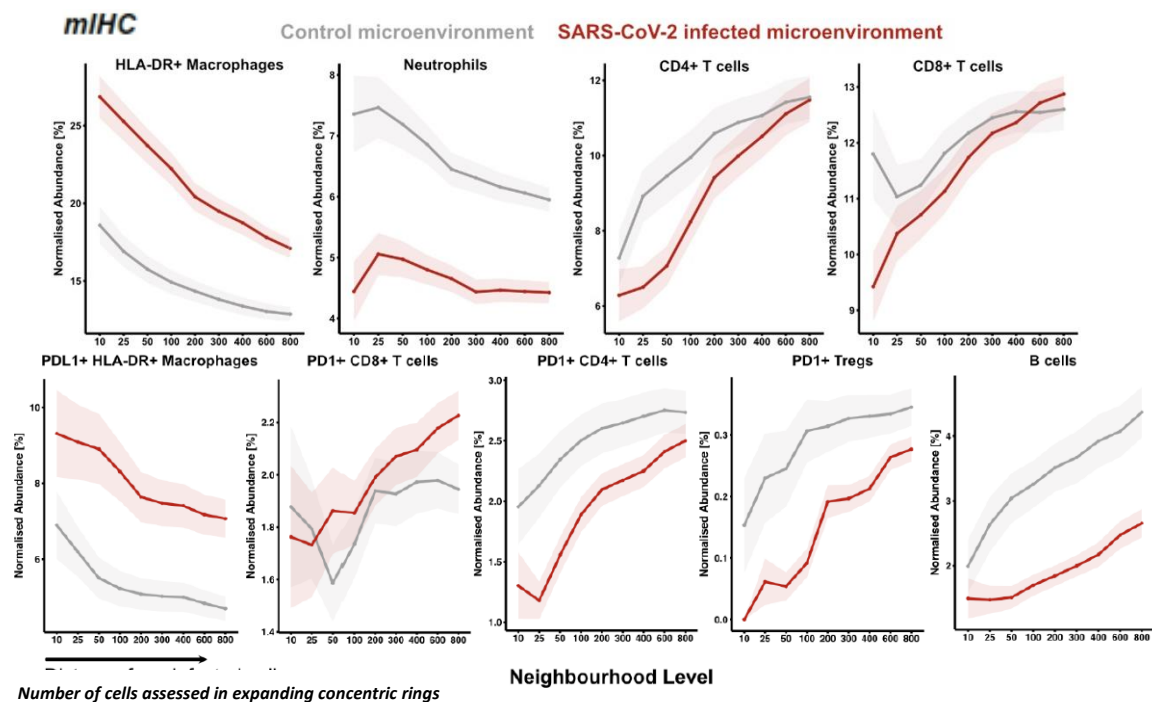


Figure 3-24. Immune cell abundances in the immediate virus positive and negative microenvironment of COVID-19 lung epithelial cells based on multiplex immunohistochemistry. Normalised abundance is plotted against number of cells assessed in expanding concentric rings away from the cell of interest. Normalised abundance is cell number normalised by the number of cells in the microenvironment per neighbourhood level.

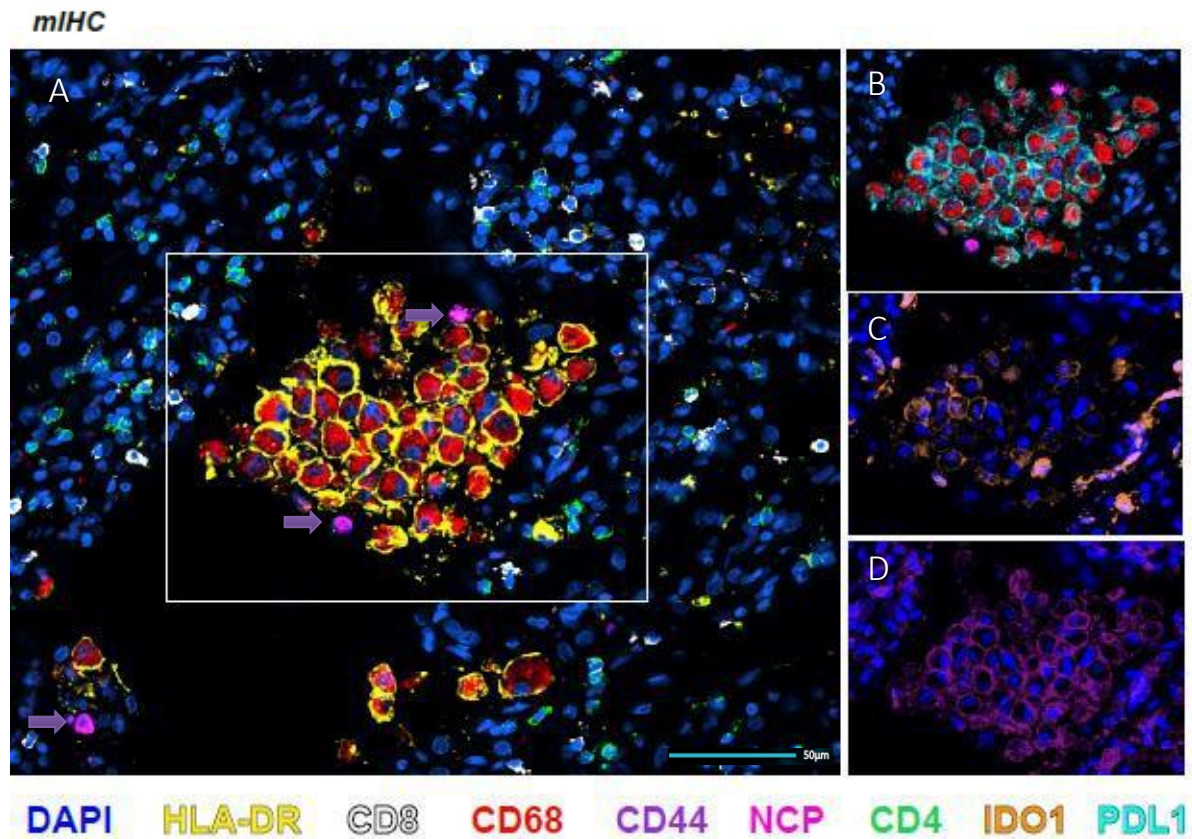


Figure 3-25. CODEX mIHC image showing aggregates of HLA-DR (A), PDL1 (B), IDO (C), and CD44 (D) expressing macrophages adjacent to SARS-CoV-2 virus (nucleocapsid) infected epithelial cells (purple arrow). Scale bar =50µm.

3.4.2. Tissue wide virus-associated changes by bulk sequencing

To understand the influence of the SARS-CoV-2 virus on the wider tissue microenvironment, Quantseq bulk sequencing was interrogated to look at tissue wide changes in SARS-CoV-2 positive COVID-19 lung compared to SARS-CoV-2 negative COVID-19 lung (Figure 3-26). The most notable differences were mRNAs associated with interferon-related changes, including upregulation of interferon inducible antiviral genes MX1 and ISG15 (Braun et al., 2015; Perng and Lenschow, 2018).

BulkRNAseq

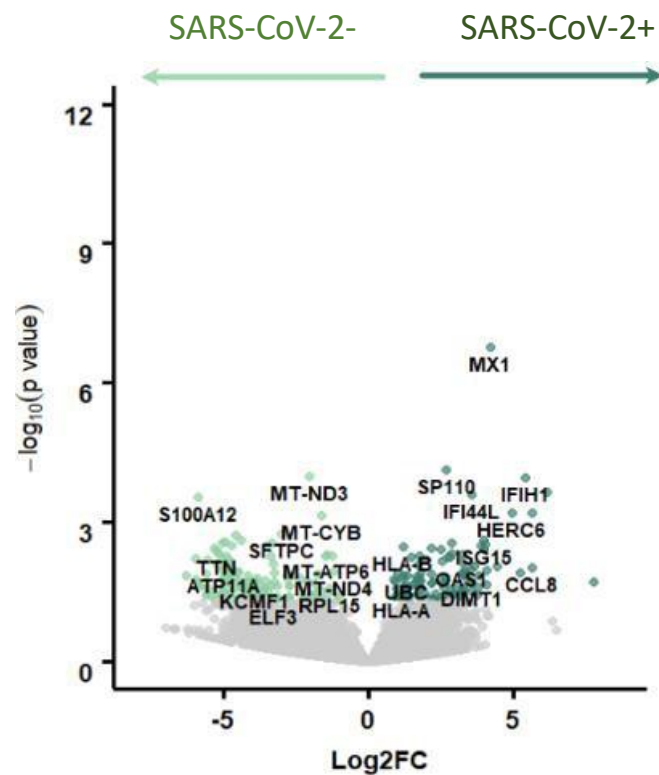


Figure 3-26. Volcano plot of Quantseq bulk sequencing comparing tissue wide normalized gene expression in SARS-CoV-2 infected lungs vs non-infected (normal) control lungs. Genes which were upregulated at statistically significant level following compensation for multiple comparisons are highlighted in green. The cut off for significance was $p < 0.05$. Genes of biological interest named on figure.

3.4.2. Characterisation of virus niche by Nanostring GeoMx

To explore localised changes in association with the virus niche and understand the mechanistic basis for observed immune cellular changes, Nanostring GeoMx gene expression data were interrogated, comparing alveolar regions that were high in virus with alveolar regions low in virus from the same lung (1800 gene analysed – CTA panel). Alveolar virus status was determined by level of spike and ORF1ab mRNA from each region. Alveolar regions with over 250 virus-specific transcripts were regarded as 'virus high' and regions with less than 250 were regarded as 'virus low' (Figure 3-27).

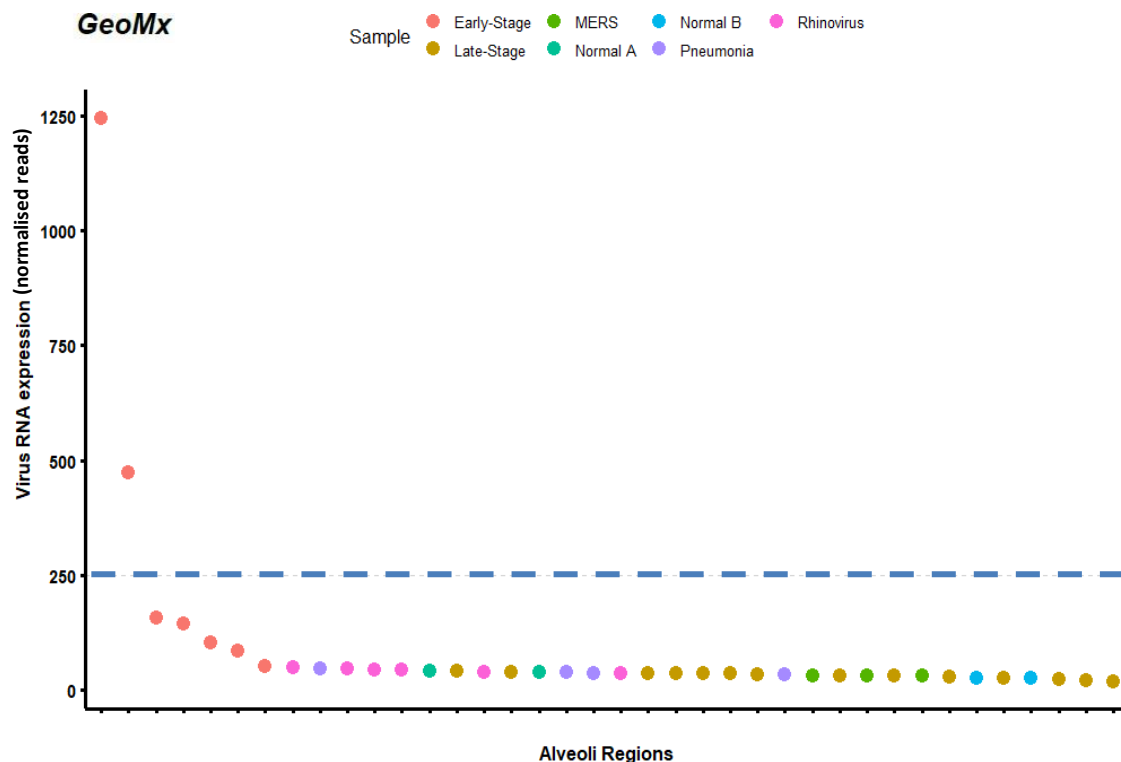


Figure 3-27. Virus RNA gene expression determined by Nanostring GeoMx for each region of interest analysed in lungs of SARS-CoV-2 patients and controls, ordered from highest expression regions to lowest expressing regions. Alveolar regions with virus expression over 250 were regarded as virus high, and regions with expression below 250 virus low. For subsequent virus high vs virus low analyses, regions above 250 normalised reads were considered virus-high.

Virus-high alveolar regions showed increased expression of various chemokines and chemokine receptors including interferon alpha, interferon regulatory factors such as IRF8 and IRF1, as well as CCL5, CXCL13, CXCR4, CCL19, CCL2 and CXCL11 (Figure 3-28a). Analysis of the pathways upregulated in virus high regions demonstrated an enrichment of chemokine-cytokine pathways and lymphocyte recruitment pathways (Figure 3-28b).

3.4.3. IL6 expression in the viral niche by RNAscope

Given that IL6 is known to play an important role in the systemic response to SARS-CoV-2, and is involved in the recruitment of immune cells locally in response to pathogens, a probe for cytokine IL6 was included in the RNAscope experiment along with the SARS-CoV-2 viral probes (Santa Cruz et al., 2021; Tanaka et al., 2014). Regions from adjacent to virus infected epithelium were compared to regions devoid of infected epithelium. *IL-6* expressing cells were markedly enriched in the viral niche compared to regions without infected cells within the same lung tissues.

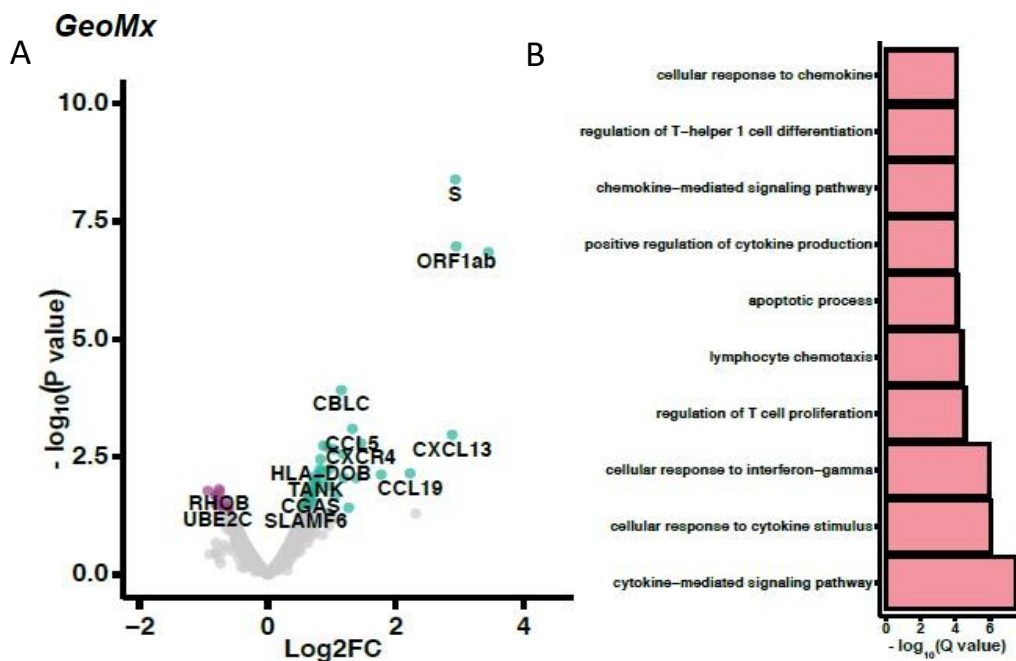


Figure 3-28. (A) Differential gene expression by GeoMx comparing virus-high and virus-low alveolar lung regions from the lungs COVID-19 patients. 1800 genes were assessed. Genes which were upregulated at statistically significant level following compensation for multiple comparisons are highlighted in green and purple. (B) Pathway analysis (gene set enrichment analysis) of gene upregulated in virus-high regions of lung.

RNASeScope

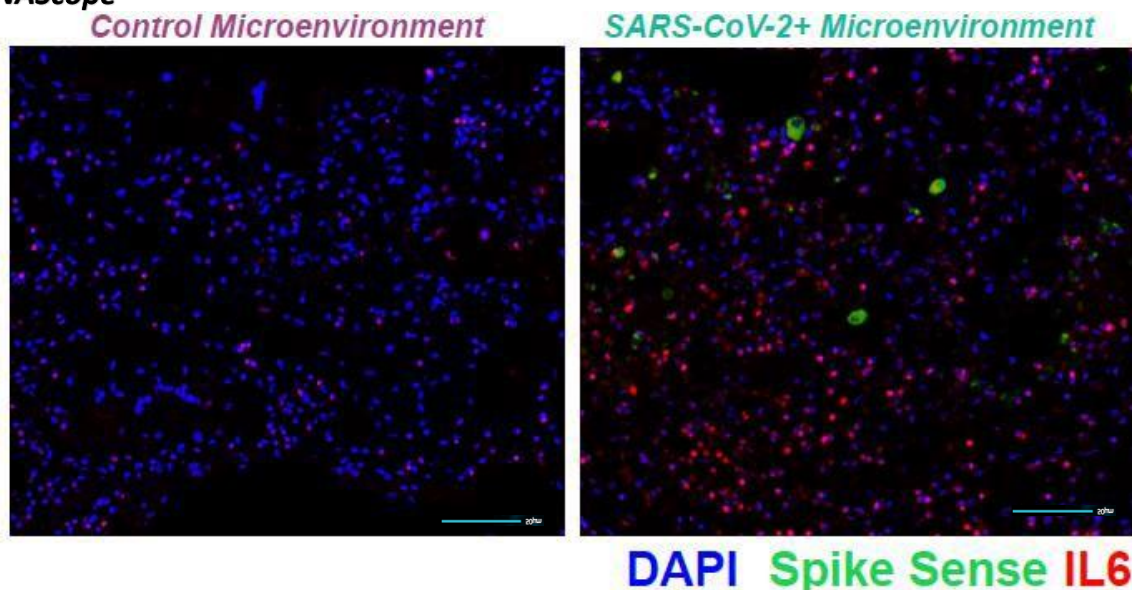


Figure 3-29. IL6 expression on RNASeScope comparing SARS-CoV-2 infected regions with non-infected regions from the same lungs. IL6 is upregulated in virus high regions. Scale bar = 50µm.

3.4.4. Assimilation of SARS-CoV-2 microenvironment data

Overall, the wider changes in the lung as observed on bulk sequencing were that of an interferon induced anti-viral response. Interferon responses are well characterised and known to have anti-viral activity (Katze et al., 2002). In contrast, the localised SARS-CoV-2 immune niche showed an immune-

suppressive phenotype, favouring persistence of the virus (figure 3-30) (Schönrich and Raftery, 2019). This includes expression of immune checkpoint ligands (e.g. PDL1) and exclusion of T-cells and B-cells from the immediate viral vicinity. This immune cell exclusion was maintained despite high levels of immune cell chemoattractants such as IL6.

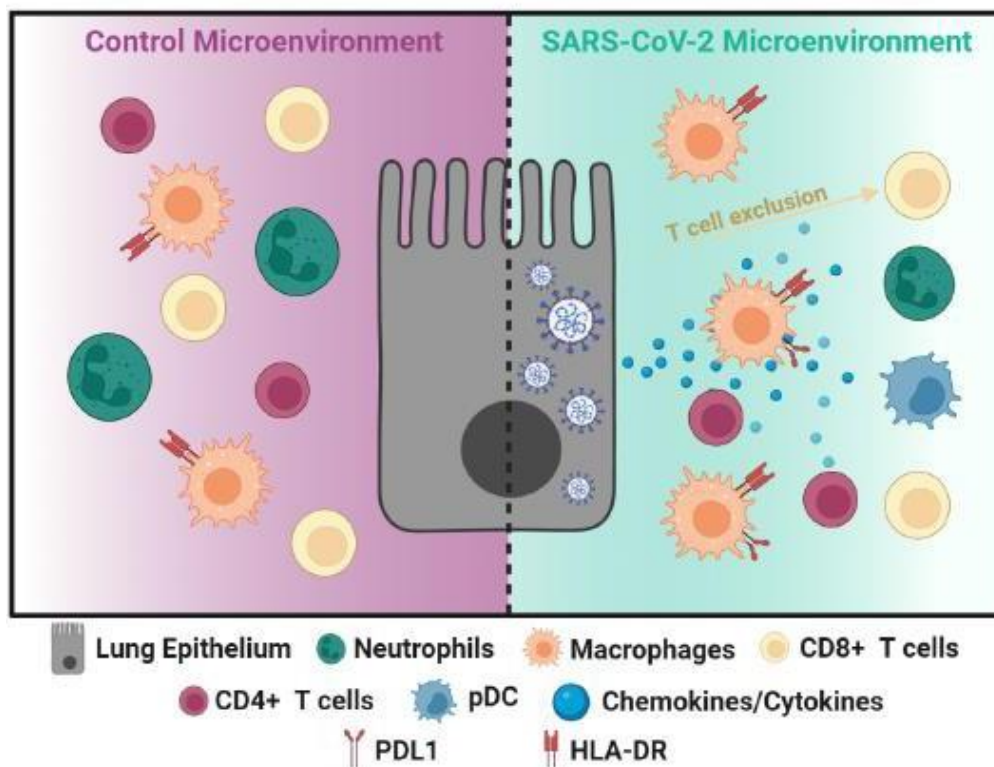


Figure 3-30. Summary of the immune microenvironmental changes observed within the SARS-CoV-2 positive niche compared to virus negative lung regions.

3.5. Discussion and conclusions

There have been numerous studies examining the systemic response to COVID-19 infection. Far fewer studies have examined the immune response in tissue (Babal et al., 2021; Ekstedt et al., 2022). Furthermore, most post-mortem studies which have focused on COVID-19 have been in patients with later stage disease. Very few studies have included patients who died early in the disease course and there are no subgroup analyses looking specifically at the immunological features in these cases. Therefore, my study afforded a unique opportunity to examine the changes seen in early disease. This early-stage disease likely represents a uniquely aggressive phenotype which kills the patient early in the disease course before the virus is cleared.

Using a multi-modal, cross-platform approach with orthologous methodologies, SARS-CoV-2 virus was predominantly detected in early stage COVID-19 (≤ 3 days) with little detection in late-stage disease (≥ 13 days). No virus was detected in non-COVID-19 controls. This pattern was consistent across all modalities of proteomic and transcriptomic virus detection and there was good correlation in virus quantity measured either by transcript count or infected cells count. This result is consistent with previous reports suggesting that the virus is cleared from the lung early in the disease course (Caniego-Casas et al., 2022; Desai et al., 2020). Given that virus was detected by PCR testing of nasopharyngeal swabs sampled earlier in time 'in-life' from the late stage COVID-19 cases, the absence of virus in their post mortem lungs could be due to two possible explanations. First, the virus is eventually cleared from the lungs but is still present in the upper respiratory tract. Second, PCR testing is sensitive and throat swabs yield positive results even when contemporaneous viral culture assays are no longer positive (Wölfel et al., 2020), which has been ascribed to viral nucleic acid being present in residual cellular 'debris' resulting from the initial infection. Despite the absence of virus in these late-stage cases, the pathological changes were severe and widespread. The findings indicate that immunopathological changes continue to develop and affect lung function even in the absence of viral infection. This result is consistent with the cytokine mediated systemic inflammatory changes described in COVID-19 (Ekstedt et al., 2022).

In virus positive COVID-19 lungs, replicative virus was detected predominantly in type II pneumocyte epithelial cells. A smaller subset of macrophages also showed evidence of replicative virus infection. These results are consistent with a number of studies which also showed evidence of SARS-CoV-2 virus in epithelium and macrophages (Caniego-Casas et al., 2022; Desai et al., 2020). In contrast, other studies have also shown evidence of virus in in endothelium and fibroblasts (Liu et al., 2021). Many of these studies reporting virus in a wider range of cell types typically only detected virus by one modality, or detected only one target. In my study, the robustness of virus detection was ensured by using multiple modalities at different '-omic' levels directed at multiple targets. I saw no evidence of

Page 80 of 261

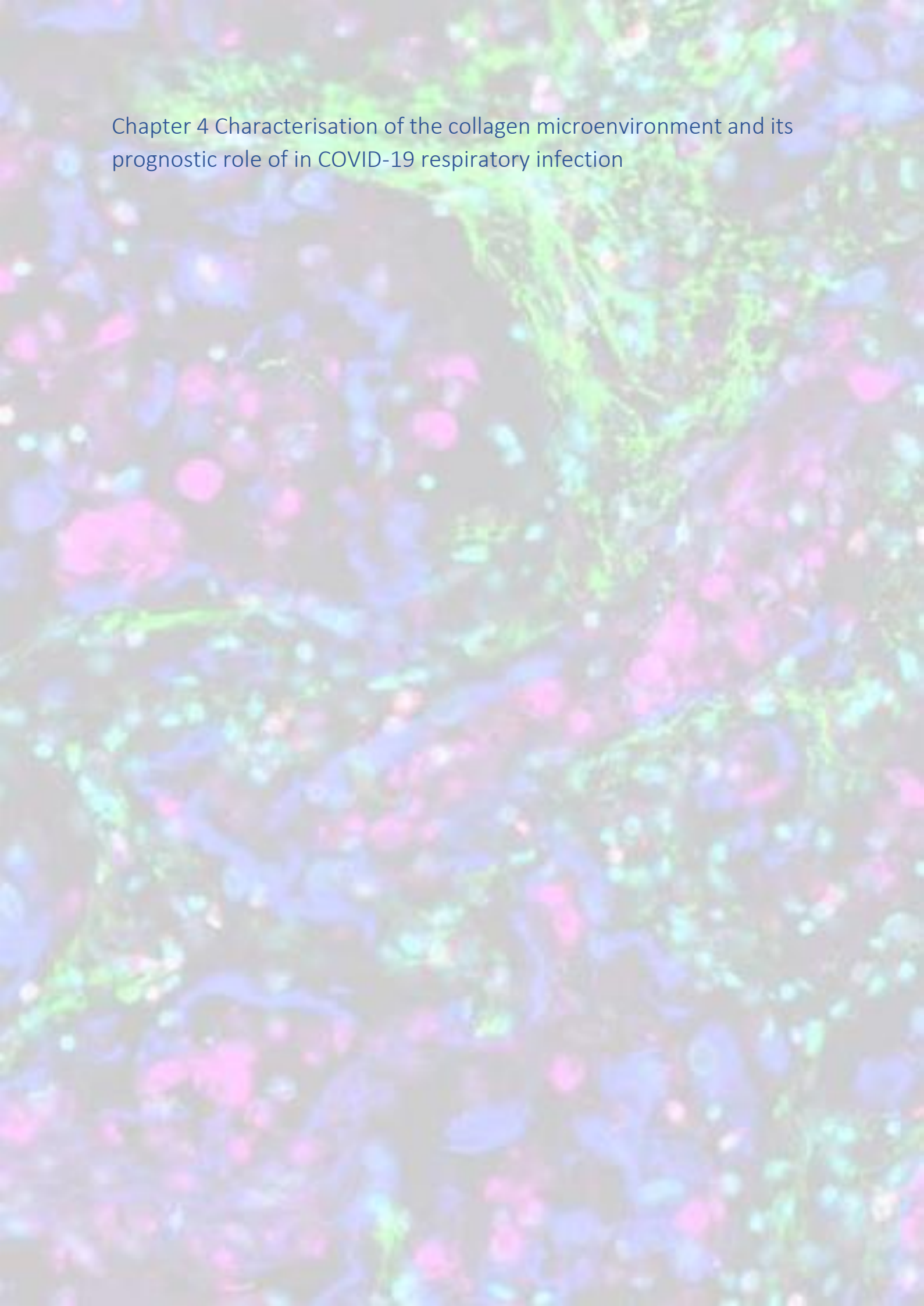
virus in T-cells and fibroblasts, as observed by other studies (Rendeiro et al., 2021). The presence of virus in macrophages may reflect primary infection, but could also reflect phagocytosed material within macrophages.

Regarding the immune infiltrate, macrophages were the most abundant immune cell in COVID-19 lungs, but there were also increases in T-cells, B-cell and neutrophil frequency. These immune subtypes increased in late-stage disease, despite the absence of virus in these cases. Analysis of TCR showed reduced diversity and increased clonal expansions of T-cells, however, there was no apparent increase in SARS-CoV-2 specific T-cells compared to controls. It is therefore unclear if the T-cell compartment was mounting a specific response to SARS-CoV-2, against the lung or another antigen. The absence of SARS-CoV-2 specific TCR sequences could reflect the inadequacy of the current TCR databases and the complexities of HLA specific epitope recognition. Furthermore, the TCR sequencing assay employed β TCR chain only, and specificity also depends on the sequence of the α chain. Additionally, TCRs specific for particular antigens can be private to specific individuals, and will not be captured on public databases. The presence of SARS-CoV-2 specific TCR sequences in pre-pandemic controls could suggest that some of the viral specific sequences detected may be cross-reactive TCR sequences specific for other viruses, such as circulating seasonal coronaviruses, as suggested by Kundu et al., 2022.

My investigation also revealed competing anti-viral and pro-viral signatures in the immune microenvironment of SARS-CoV-2 lung. It is the first study to describe the immediate SARS-CoV-2 viral niche, which comprised numerous immune escape and evasive mechanisms, including checkpoint expression of IDO1 and PDL1 on macrophages. This checkpoint expression is likely, in turn, induced by antiviral interferon responses (Garcia-Diaz et al., 2017). Additional immune evasive mechanisms observed included T-cell exclusion from the viral niche. This T-cell exclusion in the SARS-CoV-2 niche was present despite the global increase in lymphocyte chemoattractant in COVID-19 lungs.

Conclusions:

1. Lungs from fatal COVID-19 infection invariably show diffuse alveolar damage and variable thrombosis, secondary infection and lymphocytic vasculitis.
2. Detectable virus is seen in early stage disease but is cleared from late stage disease.
3. The immune composition in COVID-19 lung comprises predominantly macrophages, and fewer T-cells, B-cells and neutrophils. The infiltrating T-cells show no enrichment of SARS-CoV-2 specific TCRs.
4. The viral niche shows competing anti-viral and pro-viral mechanisms; the former includes immune checkpoint expression of neighbouring macrophages and the latter includes interferon responses.



Chapter 4 Characterisation of the collagen microenvironment and its prognostic role of in COVID-19 respiratory infection

4. Characterisation of the collagen microenvironment and its prognostic role in COVID-19 respiratory infection

During my pathological assessment of COVID-19 lungs I observed several features, in particular thickening of the alveolar wall and altered architecture, that suggested fibrosis and collagen deposition might play an important role in the pathological development of COVID-19. Furthermore, the prominent recruitment of macrophages I observed in COVID-19 lung, reported to mediate fibrosis, suggested fibrosis could be contributing to alveolar thickening (Gomez-Rial et al., 2020; Wang et al., 2020a). The associated widening of the alveolar wall due to fibrosis could impede gas exchange and lung function. Most tissue studies have focused on the immune cellular changes in COVID-19 infection with few studies examining the role of fibrosis and collagens in pathogenesis. Therefore, I used the molecular data generated by my earlier work characterising the immune and cellular microenvironment of COVID-19 lungs to explore the non-cellular microenvironment.

My strategy was as follows. First, I would use my spatial sequencing data to explore whether specific collagens were upregulated in COVID-19 lung (Figure 4-1). The most significantly upregulated collagens would then be validated at a proteomic level by immunohistochemistry. In order to determine the clinical significance of the changes in the collagen microenvironment, collagen metabolism would be assessed in serum taken from additional cohorts of patients with mild and severe COVID-19 disease. Finally, any differences observed in collagen metabolism would then be used as basis to form a novel biomarker of outcome in hospitalised patients.

The aims of this investigation were:

- i. Describe the spatial characteristics of altered collagen metabolism in COVID-19 lung tissue.
- ii. Determine whether changes in collagen metabolism can be detected in blood and, if so, explore their association with patient outcome

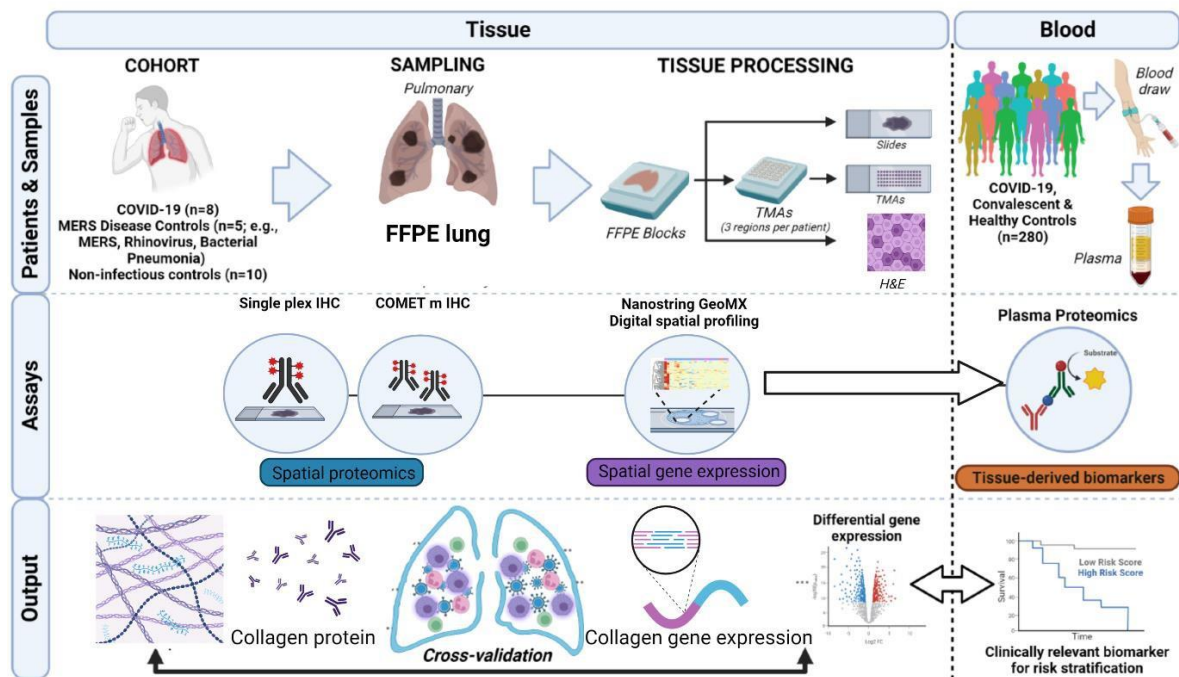


Figure 4-1. Schematic overview of the collagen characterisation experimental workplan and clinical validation in COVID-19 lung.

4.1. Spatial gene expression of collagen genes in COVID-19 post-mortem lung

First, the Nanostring GeoMx digital spatial profiling (DSP) data was utilised to explore whether specific collagens were upregulated in COVID-19 lung.

4.1.1. Bulk Quantseq and pseudo-bulk gene expression of collagen genes

I performed a Quantseq bulk sequencing and pseudo-bulk analysis of GeoMx digital DSP data, comparing collagen gene expression SARS-CoV-2 positive lung tissues to controls. In the GeoMX DSP pseudo-bulk analysis, all regions of the lung were included in the analysis. The most upregulated genes included inflammatory, thrombosis and fibrosis related genes (Figure 4-2). Specifically, genes associated with collagen 1, 3 and 6 were upregulated in SARS-CoV-2. Interestingly, these collagen genes are also implicated in idiopathic pulmonary fibrosis (IPF) and upregulation of these collagens is associated with progressive fibrosis (Organ et al., 2019a). In keeping with pseudo-bulk analysis, bulk sequencing analysis showed upregulation of collagens 1A1, 1A2, 3A1 and 6A1.

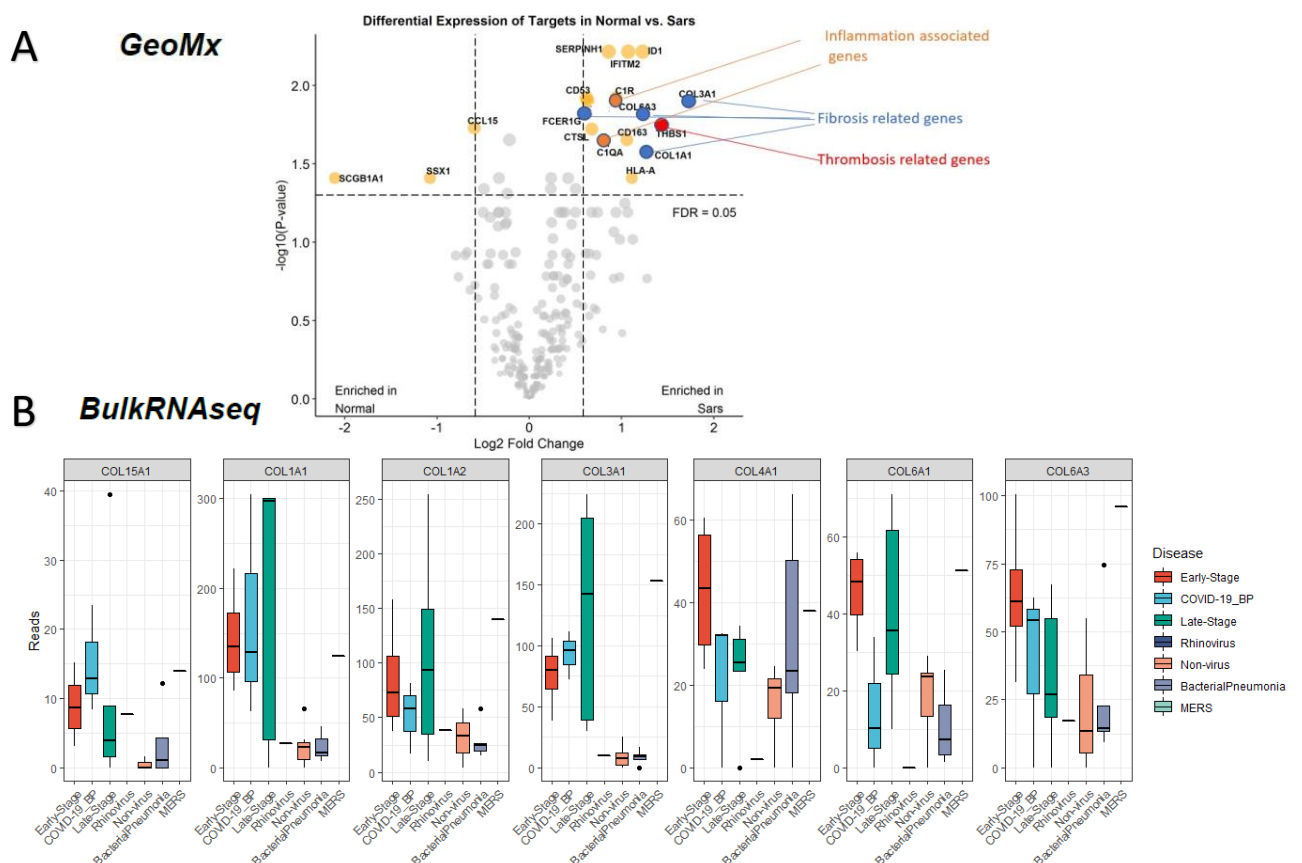


Figure 4-2. (A) Volcano plot showing differential gene expression of a pseudo-bulk GeoMx analysis (all regions of interest combined) comparing COVID-19 lung with normal lung. Genes differentially expressed at a statistically significant level following adjustment for multiple comparisons are highlighted. Of note, key collagen genes are upregulated in COVID-19 lung. (B) Quantseq bulk gene expression sequencing shows upregulation of 1A1, 1A2, 3A1 and 6A1.

4.1.2. Spatial analysis of collagen gene expression by Nanostring GeoMx

In order to understand whether collagen deposition might be contributing to the thickened alveolar walls, collagen gene expression in the alveolar walls of COVID-19 lungs was examined. The SARS-CoV-2 lungs and the MERS lung showed upregulation of collagens in the alveolar compartment compared to normal and disease controls (figure 4-3) (Ramadan and Shaib, 2019). Further pan-collagen analysis examining late and early stage COVID-19 lungs, showed that collagens were upregulated more in late stage compared to early stage disease (figure 4-4). Next, gene expression of specific collagens was examined, comparing early and late stage COVID-19 lungs to non-COVID-19 lung (Figure 4-5, 4-6). Late stage disease COVID-19 lungs showed a statistically significant upregulation of collagen 1A, 3A, 4A and 6A in the alveolar compartment. By contrast, in the blood vessel compartment, only collagen 4 was significantly upregulated in early COVID-19 compared to non-COVID-19 controls, whilst collagen 1A, 3A and 6A showed no significant upregulation (Appendix 6).

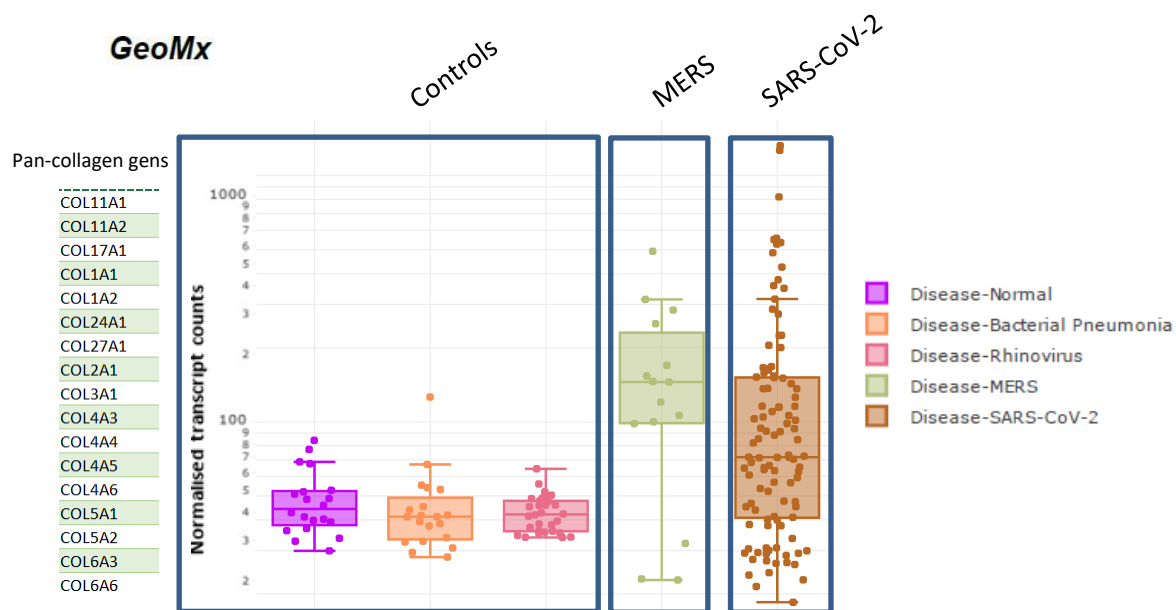


Figure 4-4. Pan-collagen gene expression (normalised transcript count per area of interest) in the alveolar compartment by GeoMx DSP (1800 gene CTA assay) shows upregulation of collagens in SARS-CoV-2 and MERS but not control cases. Pan-collagen genes shows in table.

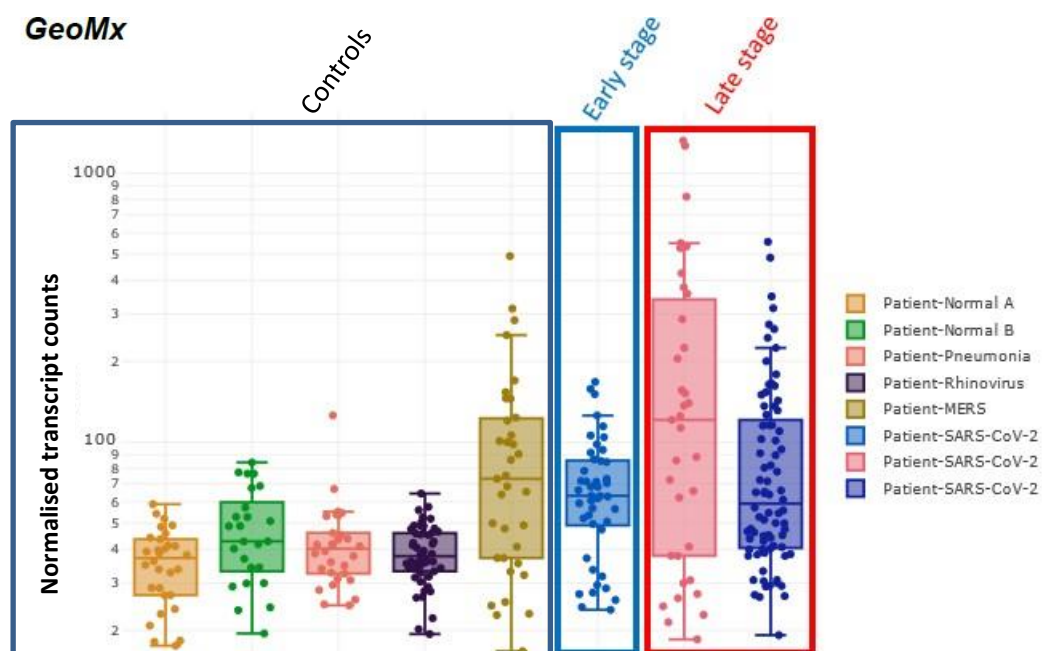


Figure 4-5. Pan-collagen gene expression (normalised transcript count per area of interest) in the alveolar compartment by GeoMx DSP shows upregulation of collagens in late stage COVID-19 lungs compared to early stage disease.

GeoMx

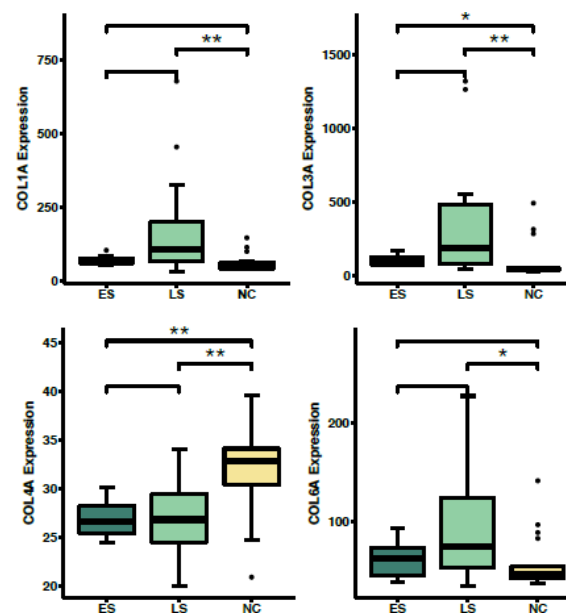


Figure 4-6. Bar and whisker plot showing expression of specific collagen in the alveolus based on GeoMx DSP gene expression. *= Statistically significant difference with a P-value of <0.05; **= $p < 0.01$; ***= $p < 0.001$; ****= $p < 0.0001$. Key: ES=early stage; LS=Late stage; NC=normal control.

Given the proposed role of macrophages in mediating fibroblast driven collagen deposition and fibrosis, the alveolar GeoMx DSP data were further interrogated to determine if macrophage activation markers correlated with collagen expression (Figure 4-7). Macrophage activation markers showed a statistically significant positive correlation with collagen expression. These findings suggested that macrophages may be a major contributor to the development of fibrosis.

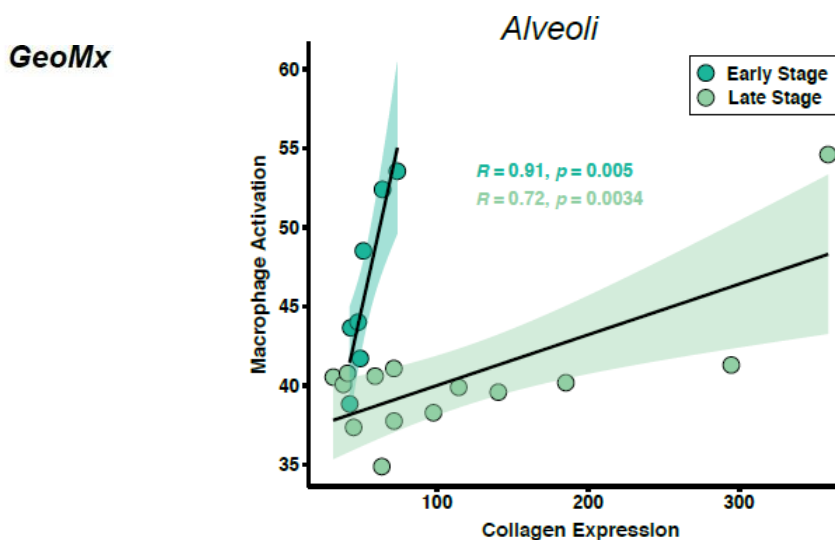


Figure 4-7. Correlation analysis of macrophage activation (based on GSEA) markers and collagen genes (COL1A, COL3A, COL4A and COL6A) in the alveolar space based on GeoMX DSP (CTA 1800 gene assay). Macrophage activation is associated with collagen deposition in both early stage and late stage COVID-19 lungs. The correlation is strongest in early stage disease.

4.1.3. Temporal analysis of collagen gene expression by Quantseq bulk sequencing.

To assess the temporal relationship of length of illness with collagen gene expression, Quantseq bulk sequencing data was interrogated, as there were a greater number of COVID-19 lung cases included in this dataset.

BulkRNAseq

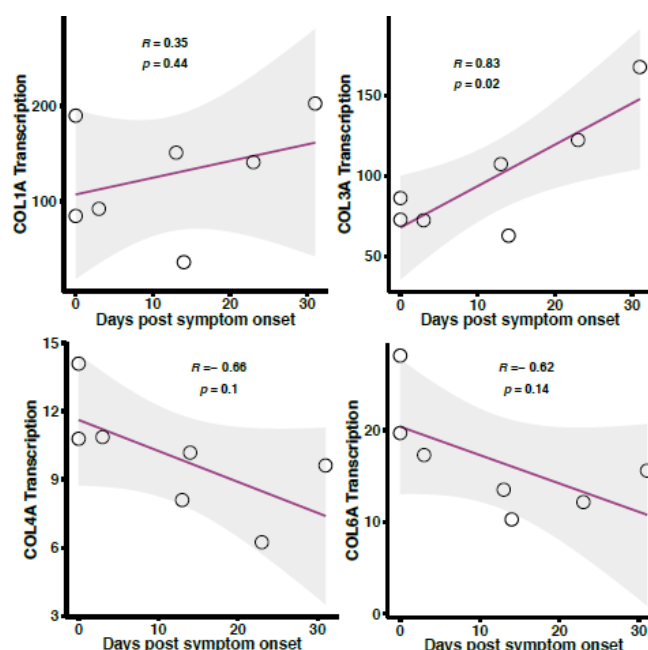


Figure 4-8. Association with length of illness and collagen gene expression based on Quantseq bulk gene expression data.

Collagens 1A and 3A showed a trend towards increasing expression with increasing length of illness, whilst collagens 4A and 6A showed a trend for decreasing expression with greater length of illness.

4.1.4. Assimilation of collagen gene expression data.

COVID-19 and MERS lungs both showed increases in pan-collagen gene expression. Both of these respiratory illnesses are caused by coronaviruses, suggesting that there is a common underlying cause for the observed increase in collagens caused by this class of virus. Crucially, the observed increases in collagen gene expression were more pronounced in the alveolar compartment by spatial transcriptomics, indicating that collagen deposition might be contributing to the thickened alveolar walls observed in COVID-19 lungs, which in turn impedes gas exchange and lung function. The temporal relationship of increased collagen expression showed conflicting results between GeoMX DSP data compared to Quantseq bulk sequencing. In the GeoMX DSP analysis, collagens 1, 3 and 6

were upregulated to a greater degree in late stage COVID-19 compared to late stage COVID-19. In contrast, analysis of bulk Quansseq data showed a negative correlation with increasing length of illness. The contrasting relationship of collagen VI expression with disease length may reflect the compartmentalised nature of GeoMx sequencing, compared to the tissue wide analysis of Quantseq bulk sequencing. Alternatively, the small numbers of cases in the GeoMx DSP experiment (1 vs 3) compared with Quantseq sequencing (3 vs 5) may have affected the results and the Quantseq experiment may be more reliable with more cases.

4.2. Characterisation of collagen protein in COVID-19 post-mortem lung

In order to validate whether increased expression of collagen genes equated to increased collagen deposition at a proteomic level, both single-plex chromogenic and multiplex fluorescence assays were employed. This analysis focused mostly on collagen VI as this collagen was associated with COVID-19 lungs for several analyses and had previously been shown to be a notable biomarker for progressive lung disease in idiopathic pulmonary fibrosis (Organ et al., 2019a).

4.2.1. Chromogenic single plex

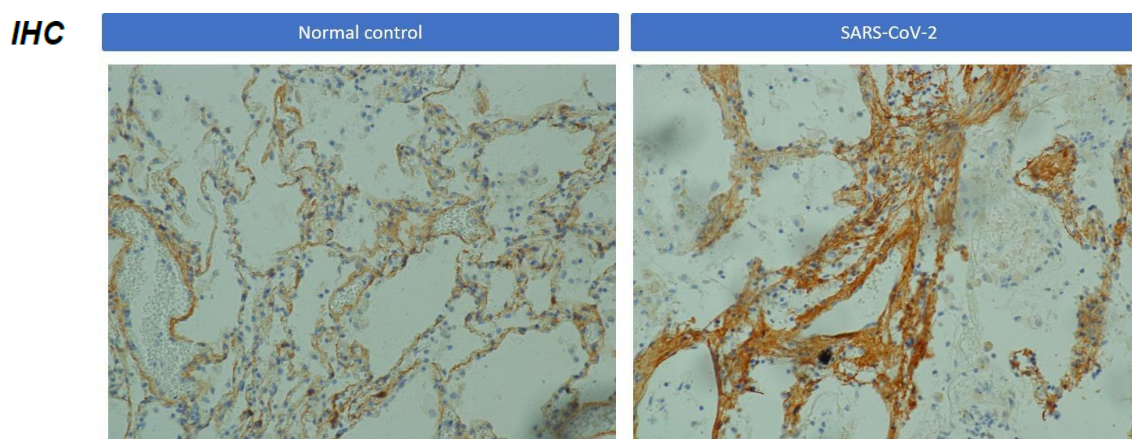


Figure 4-9. Single-plex chromogenic staining for collagen VI showed increased collagen deposition in the alveolar wall of COVID-19 lungs compared to a normal control.

Chromogenic single-plex immunohistochemistry for collagen VI showed increased deposition in COVID-19 lungs compared to controls (figure 4-9). The distribution of this increased deposition was primarily in the interstitium of the alveolar wall and showed a fine fibrillar pattern, in keeping with

new deposition rather than the coarse deposition expected for long term collagen deposition. In contrast the normal control lungs showed a thin bi-layer of collagen VI in the alveolar wall in a ‘tram-track distribution’.

4.2.2. COMET multiplex immunohistochemistry of collagen deposition.

To further assess and quantify collagen deposition in lung, a multiplex immunohistochemistry panel comprising 18 markers was employed comparing COVID-19 lungs to normal controls. The panel included antibodies against collagen VI, collagen IV and broad cell lineage markers. As observed by chromogenic staining, COVID-19 lungs showed increased collagen VI deposition in the alveolar wall in a fine fibrillar pattern, likely contributing to thickening of the alveolar wall (Figures 4-10, 4-11).

mIHC

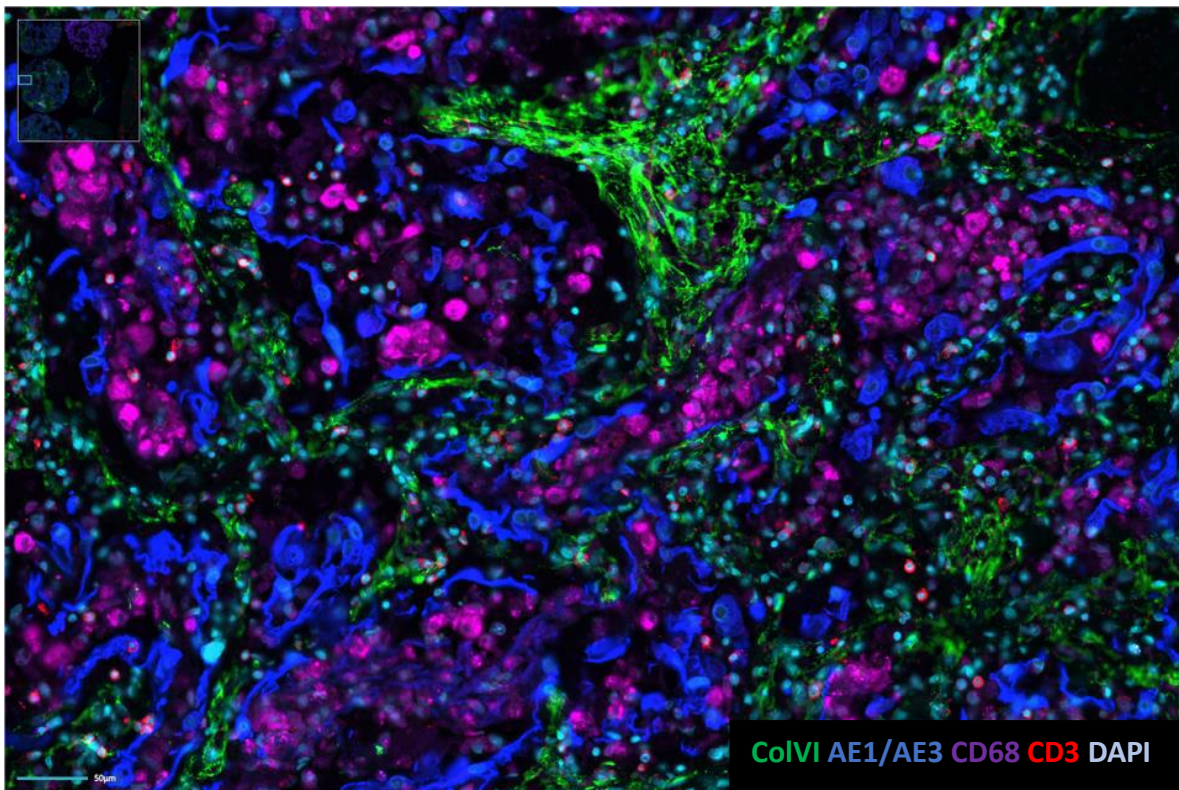


Figure 4-10. COMET multiplex immunohistochemistry showed increased collagen VI deposition in the alveolar wall associated with expansion of the alveolar wall.

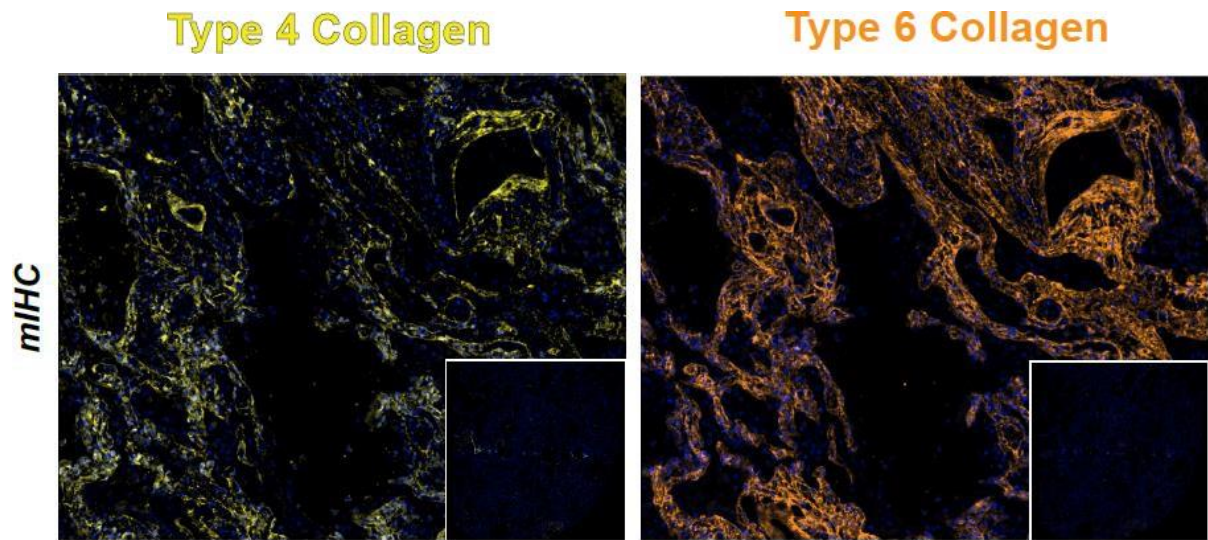


Figure 4-11. Fluorescent mIHC images showing increased collagen IV and VI in the alveolar walls of COVID-19 lung compared to normal control lungs (inset).

Quantitative analysis of the COMET mIHC images by Otsu thresholding, measuring the percentage of collagen per unit of area, showed increased collagen IV and VI deposition in early stage COVID-19 lung compared to late stage COVID-19 lungs and normal control lungs.

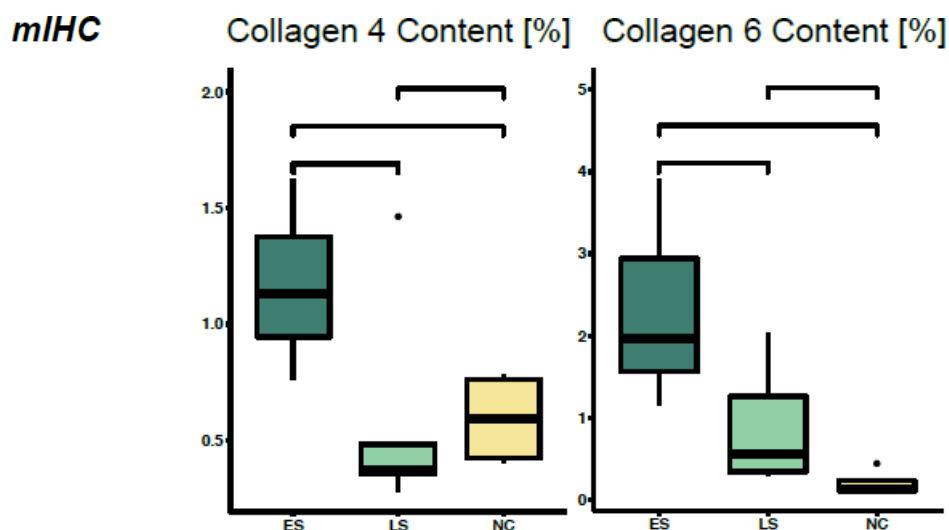


Figure 4-12. Quantitative analysis of collagen VI and VI deposition showed increased collagen content (% of total pixels showing positive collagen staining) in early stage COVID-19 lungs compared to late stage COVID-19 lungs and normal controls. *= Statistically significant difference with a P-value of <0.05; **= $p < 0.01$; ***= $p < 0.001$; ****= $p < 0.0001$. Y-axis

4.3. Serum collagen VI is increased in hospitalised COVID-19 patients and is a biomarker for mortality

To understand the clinical significance of increased collagen deposition in COVID-19 lungs, and whether increased collagen was associated with poor outcome, serological measures of collagen metabolism were measured in the blood of a separate cohort of COVID-19 patients. This cohort

included acute hospitalised (non-ITU) patients, acute ITU patients, convalescent ITU patients, patients with acute mild/asymptomatic disease, convalescent mild/asymptomatic disease, and comparison healthy volunteer controls (Figure 4-10).

ELISA assays were performed by my collaborator (Nordic Bioscience) on serum samples from this cohort, measuring markers of collagen synthesis (pro-collagens 20, 3, 3X, 4 & 6) and collagen breakdown (collagens 1, 3 & 6). Serum markers for neutrophil activity and thrombosis were also assessed by ELISA (Appendix 7).

ELISA

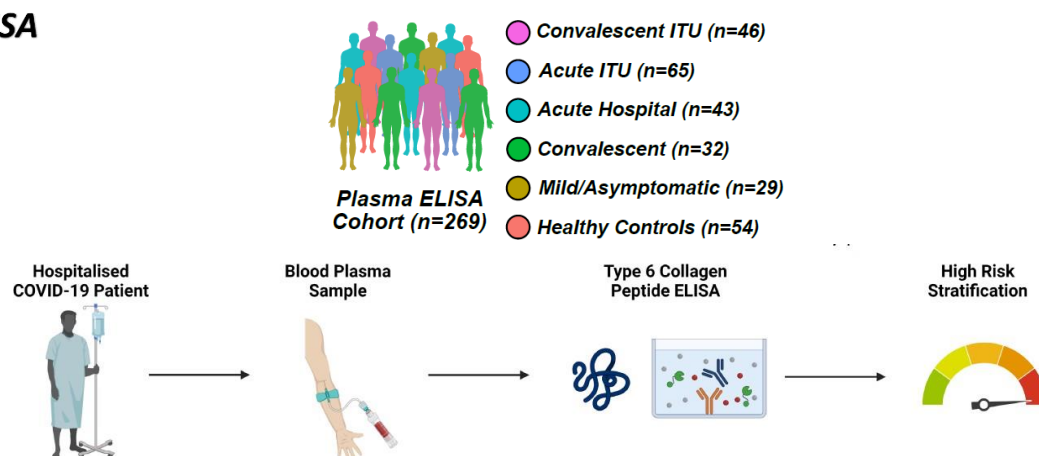


Figure 4-13. Schematic overview of the serum measurement of collagen metabolism in COVID-19 patients.

To first assess the results from all of the ELISA assays, a principle component analysis was performed. This showed that acute hospital (non-ITU) and acute ITU patients separated from each other and also the other cohorts based on serum markers of collagen metabolism, neutrophil activity and thrombosis characteristics (figure 4-11).

ELISA

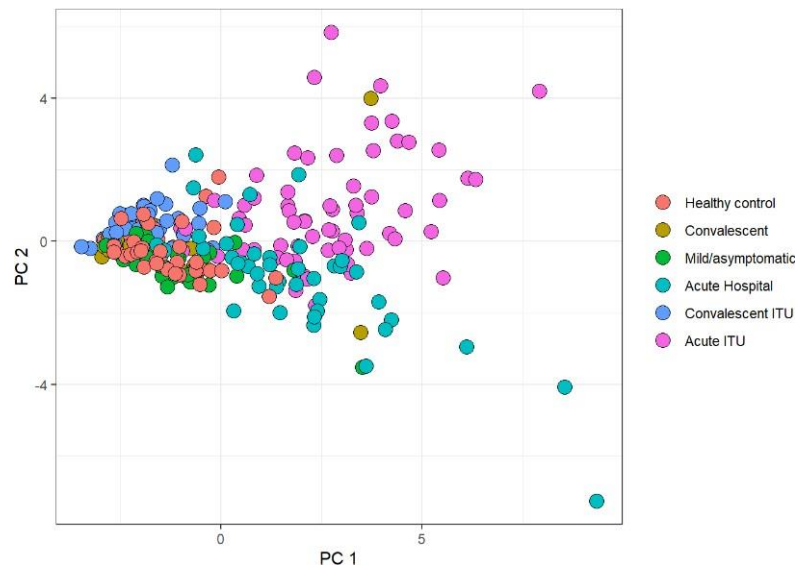


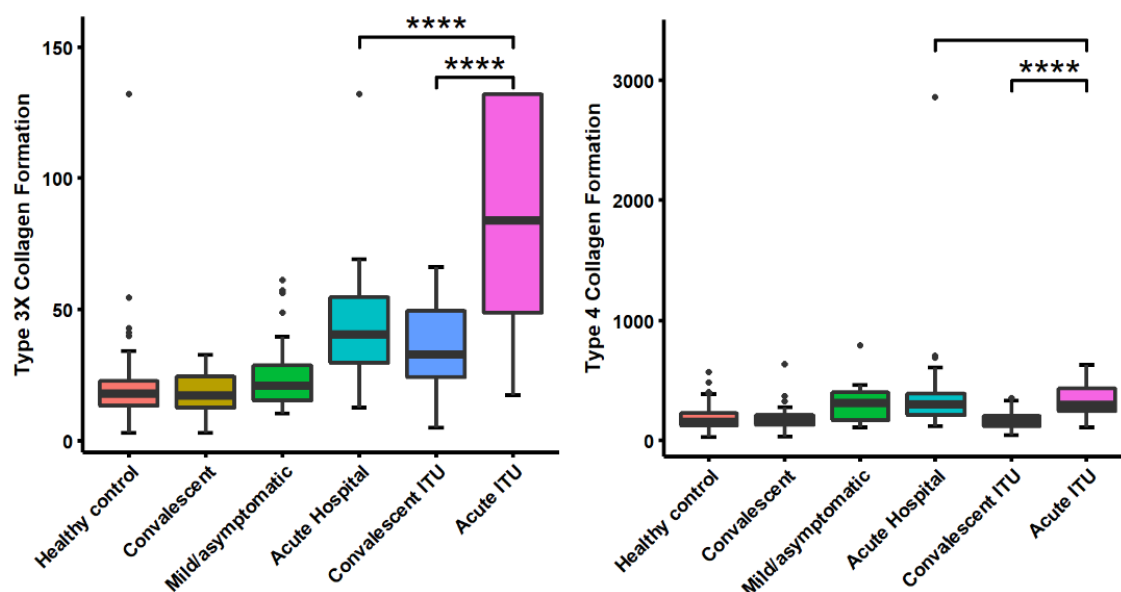
Figure 4-14. Principle component analysis shows acute hospitalised and acute ITU patients form separate clusters based on ELISA analysis of serum markers of collagen, neutrophil and thrombosis data.

4.3.1. Serum ELISA measurements of collagen breakdown and synthesis

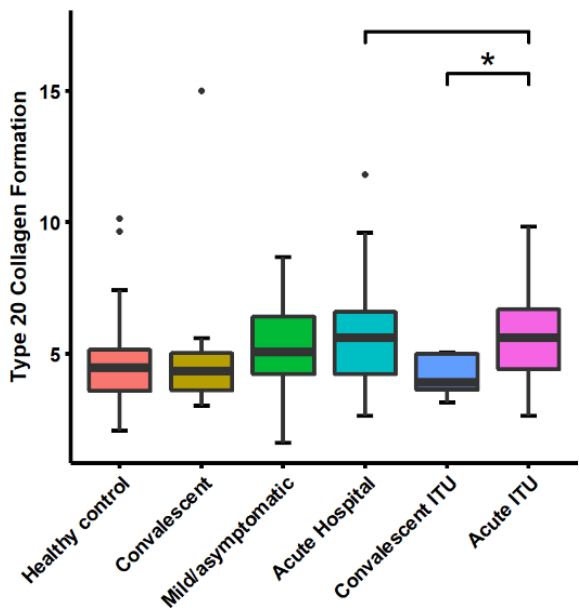
First, the serum levels of collagen synthesis and degradation in cohorts of patients with varying severity of COVID-19 disease and healthy volunteer controls were compared. Acute hospital ITU patients and acute hospitalised (non-ITU) patients showed increased serum markers of collagen synthesis and breakdown, particularly collagens 1, 3 and 6 (Figure 4-12). Levels of collagen biomarkers were generally higher in acute disease compared to convalescent patients.

ELISA

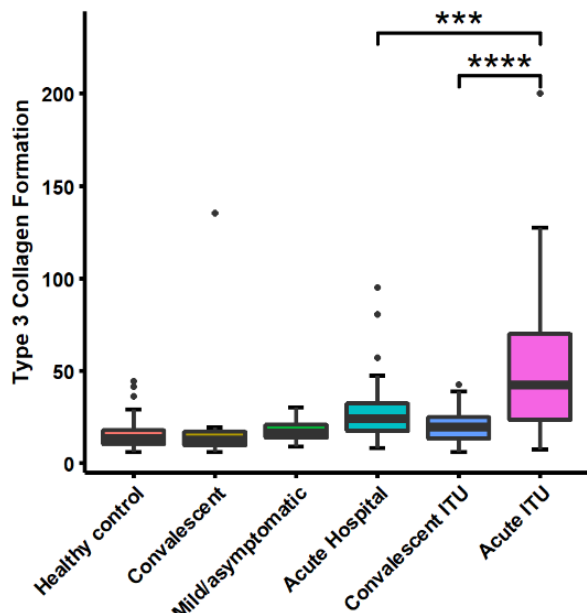
PRO-C3X - Type 3X collagen formation PRO-C4 - Type 4 collagen formation



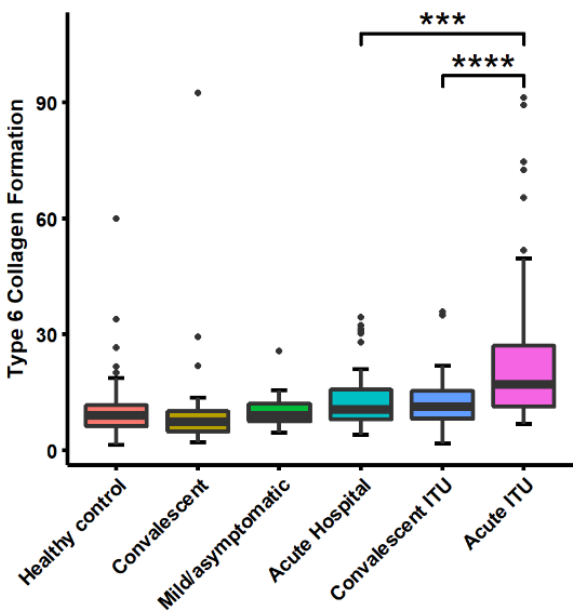
PRO-C20 - FACIT Collagen formation



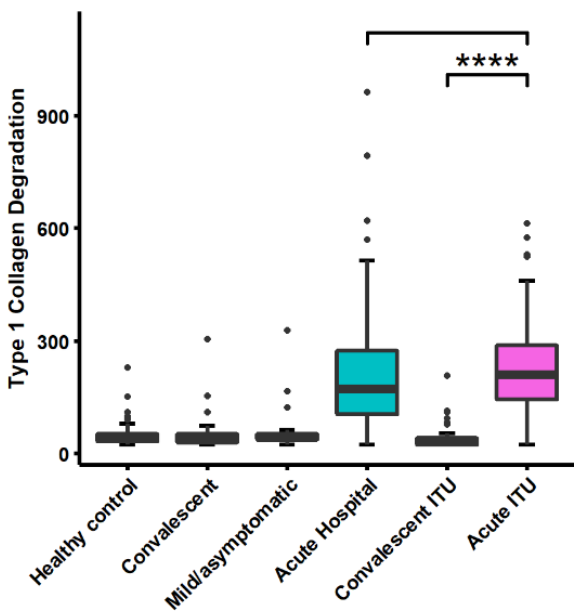
PRO-C3 - Type 3 collagen formation



PRO-C6 - Type 6 collagen formation



RE-C1M - Type 1 Collagen Degradation



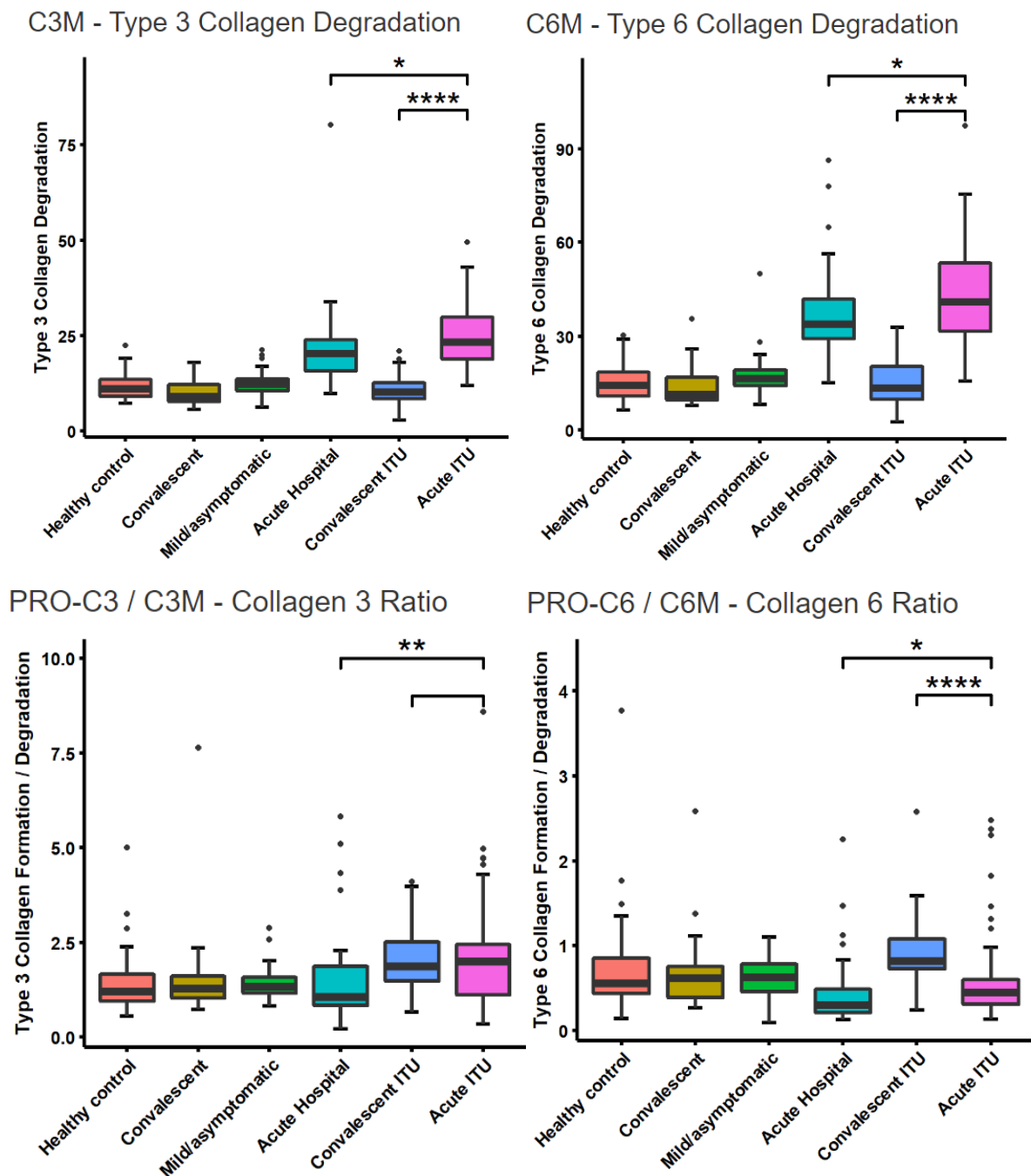


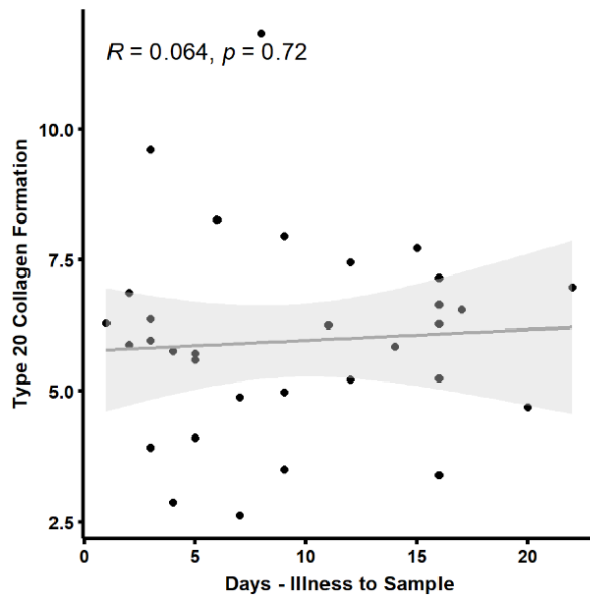
Figure 4-15. Comparative levels of serum biomarkers of collagen synthesis and breakdown across the cohorts. * = Statistically significant difference with a P-value of <0.05; **=p<0.01; ***p<0.001; ****p<0.0001.

4.3.2. Temporal changes in serum collagen

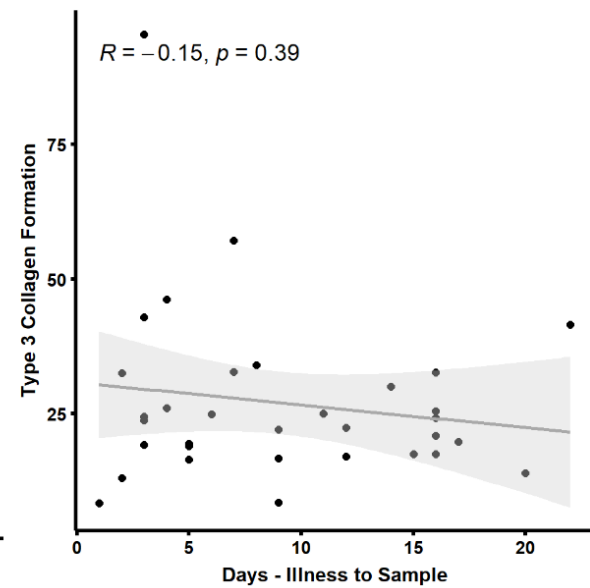
The acute hospital COVID-19 cases included information of length of illness, allowing temporal changes in collagen metabolism during COVID-19 to be assessed. Length of illness (time between symptoms arising to time of blood sampling) was plotted against the serum level of the various biomarkers (Figure 4-13).

ELISA

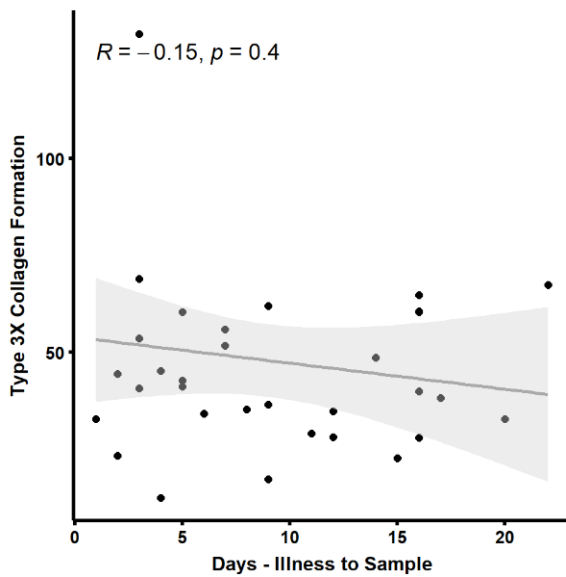
PRO-C20 - FACIT Collagen formation



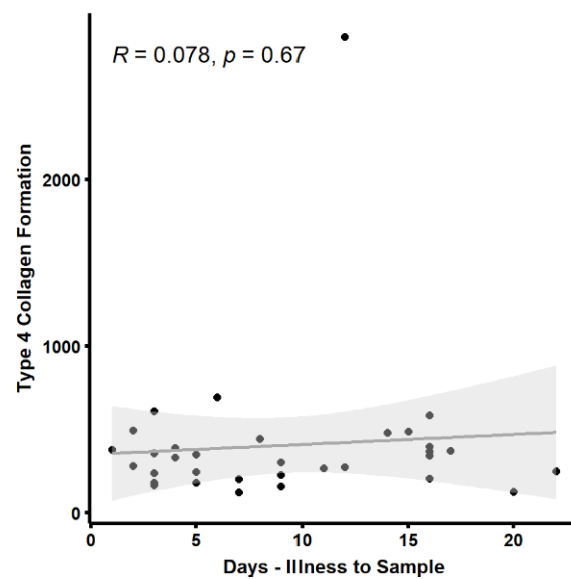
PRO-C3 - Type 3 collagen formation



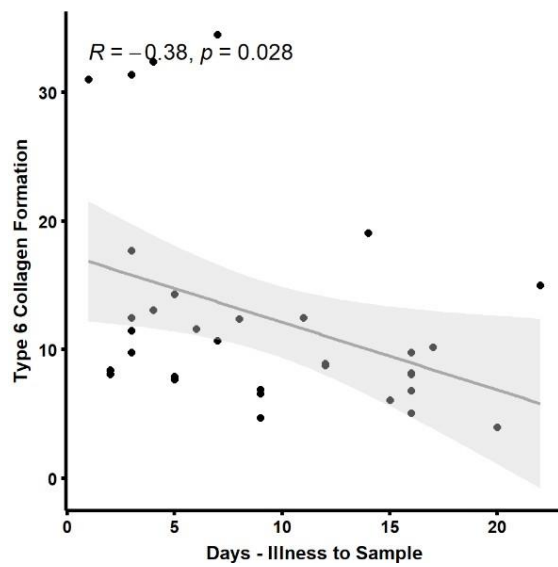
PRO-C3X - Type 3X collagen formation



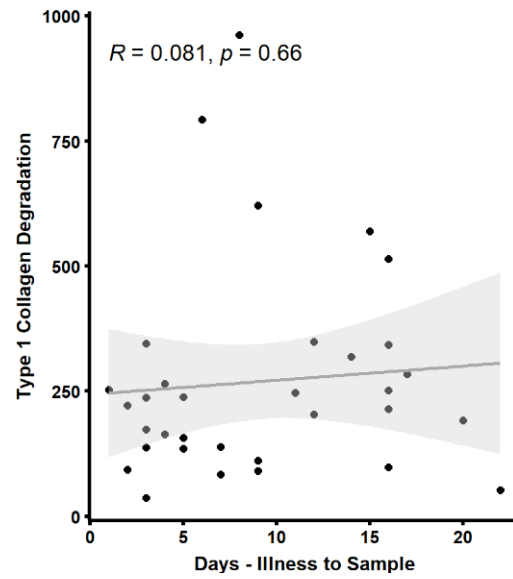
PRO-C4 - Type 4 collagen formation



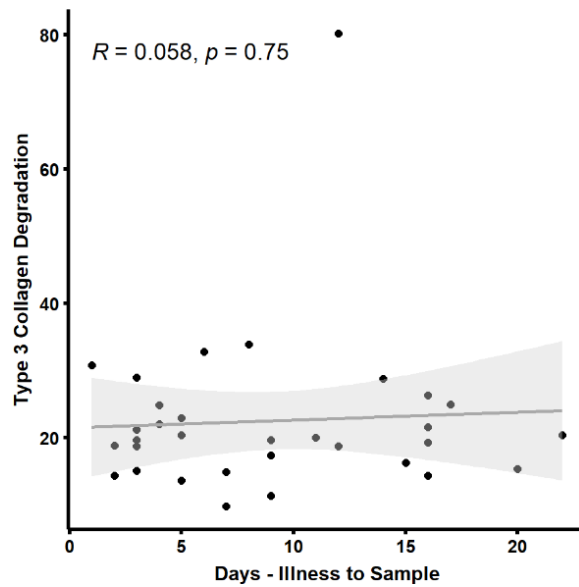
PRO-C6 - Type 6 collagen formation



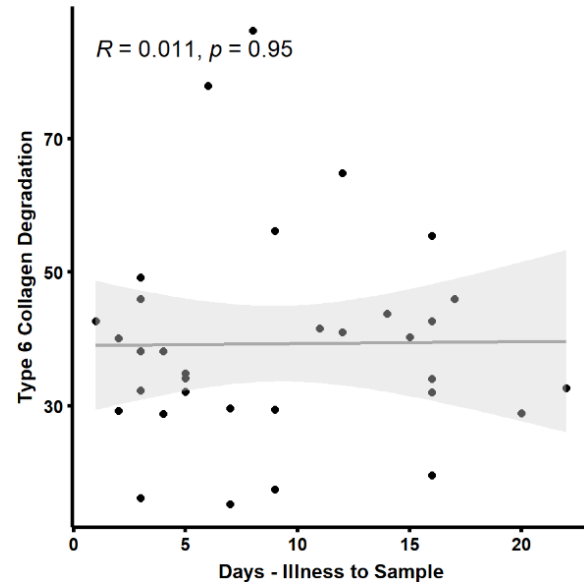
RE-C1M - Type 1 Collagen Degradation



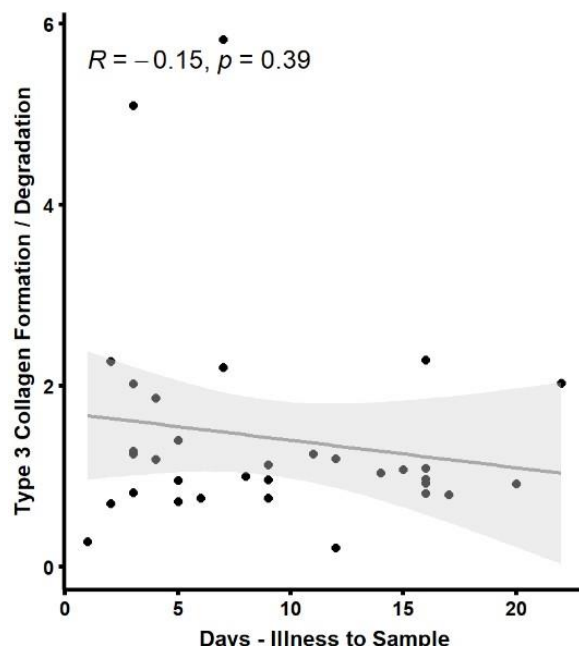
C3M - Type 3 Collagen Degradation



C6M - Type 6 Collagen Degradation



PRO-C3 / C3M - Collagen 3 Ratio



PRO-C6 / C6M - Collagen 6 Ratio

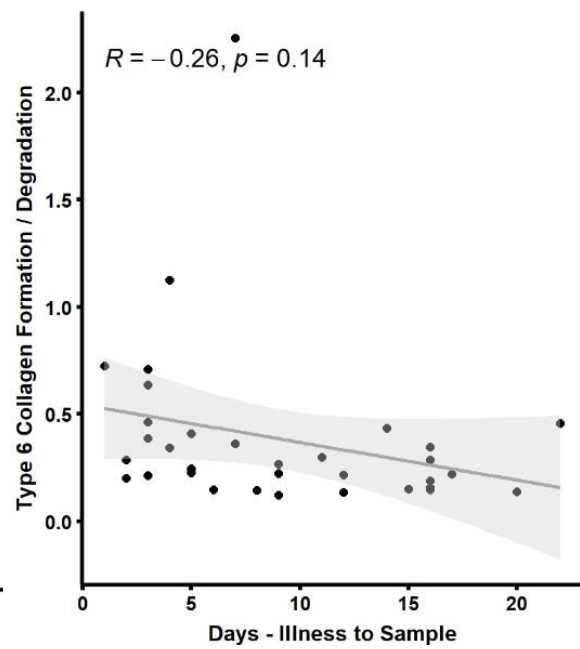


Figure 4-16. Temporal association between duration of illness and collagen biomarkers of synthesis and degradation measured in serum.

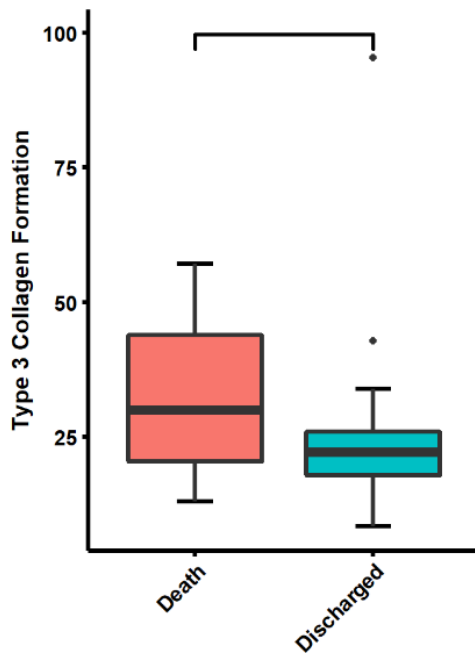
Only pro-collagen VI synthesis showed a statistically significant negative correlation with length of illness. This result suggests that collagen VI synthesis was most active during the more acute phases of the disease, a finding consistent with the trends observed in the bulk Quantseq and COMET multiplex immunohistochemistry data.

4.3.3. Serum collagen markers and outcome

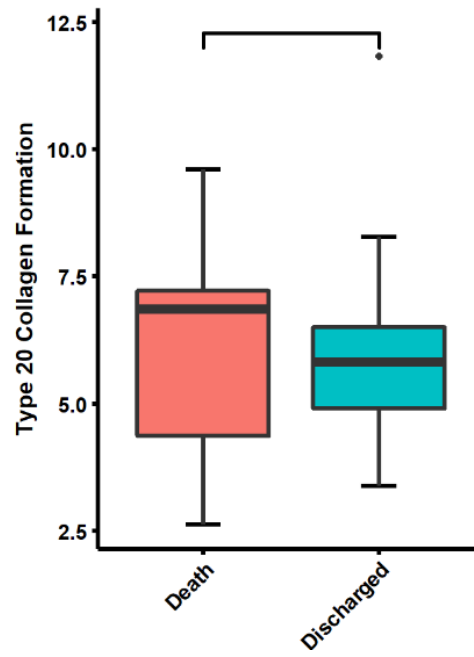
Finally, the association of serum collagen biomarkers of synthesis and degradation with outcome was assessed, combining acute hospitalised (non-ITU) patients and ITU patients. Levels of the various markers of collagen synthesis and degradation were plotted, comparing patients who died from COVID-19 to those who survived (Figure 4-14).

ELISA

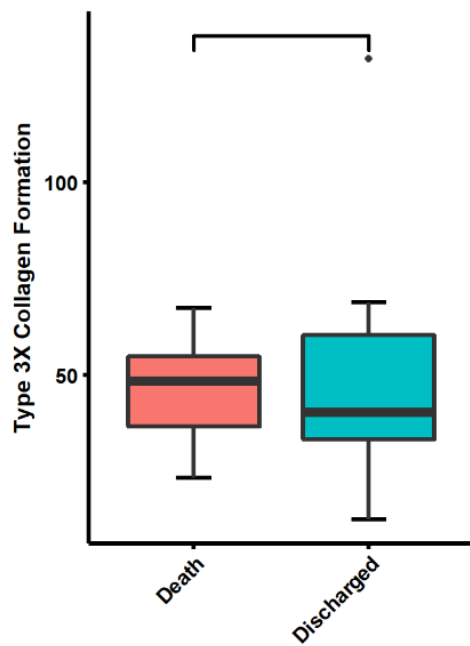
PRO-C3 - Type 3 collagen formation



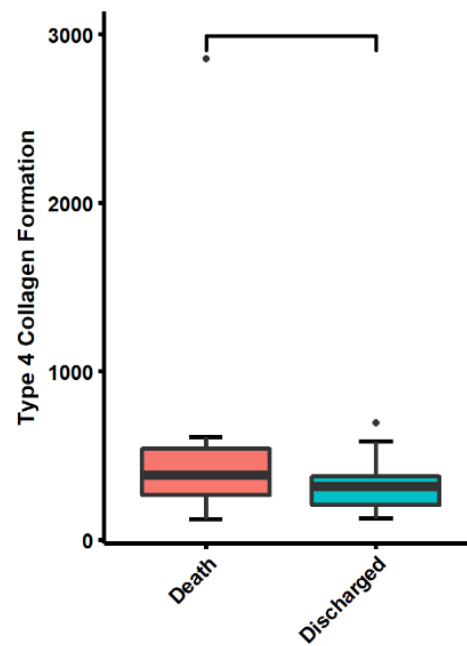
PRO-C20 - FACIT Collagen formation



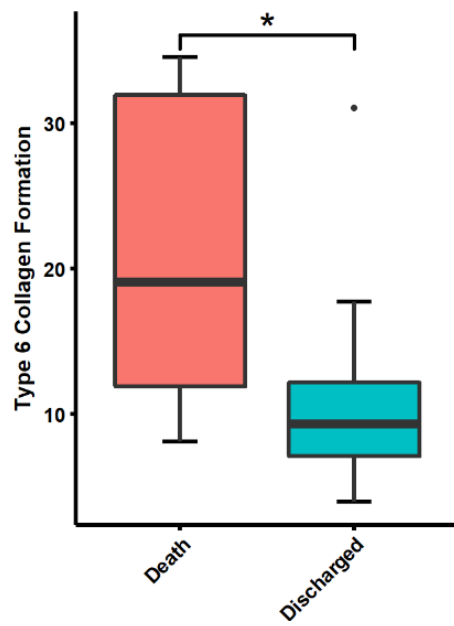
PRO-C3X - Type 3X collagen formation



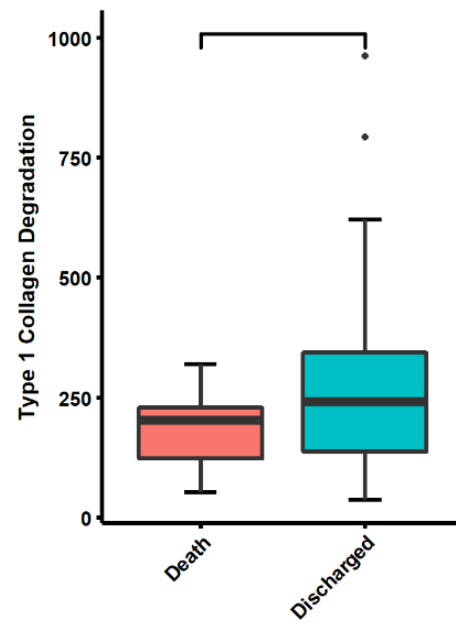
PRO-C4 - Type 4 collagen formation



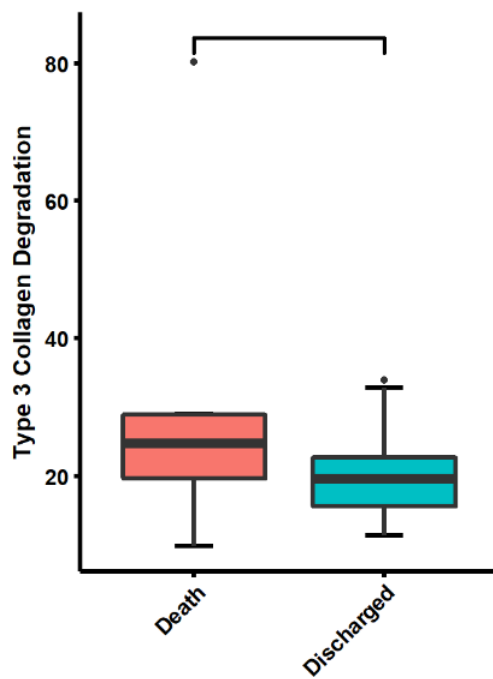
PRO-C6 - Type 6 collagen formation



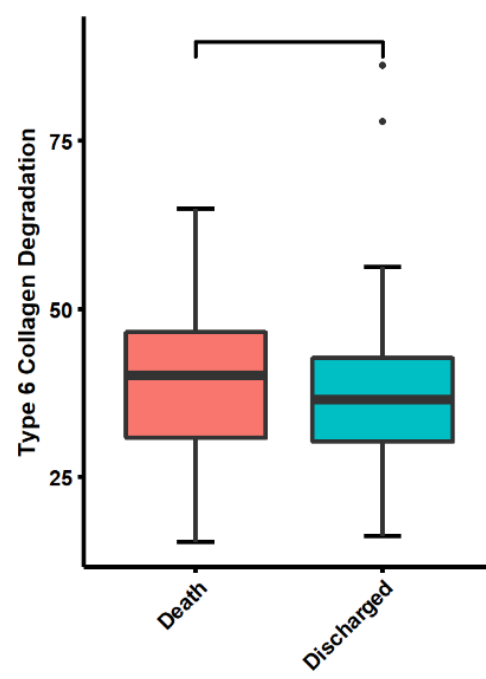
RE-C1M - Type 1 Collagen Degradation



C3M - Type 3 Collagen Degradation



C6M - Type 6 Collagen Degradation



PRO-C3 / C3M - Collagen 3 Ratio

PRO-C6 / C6M - Collagen 6 Ratio

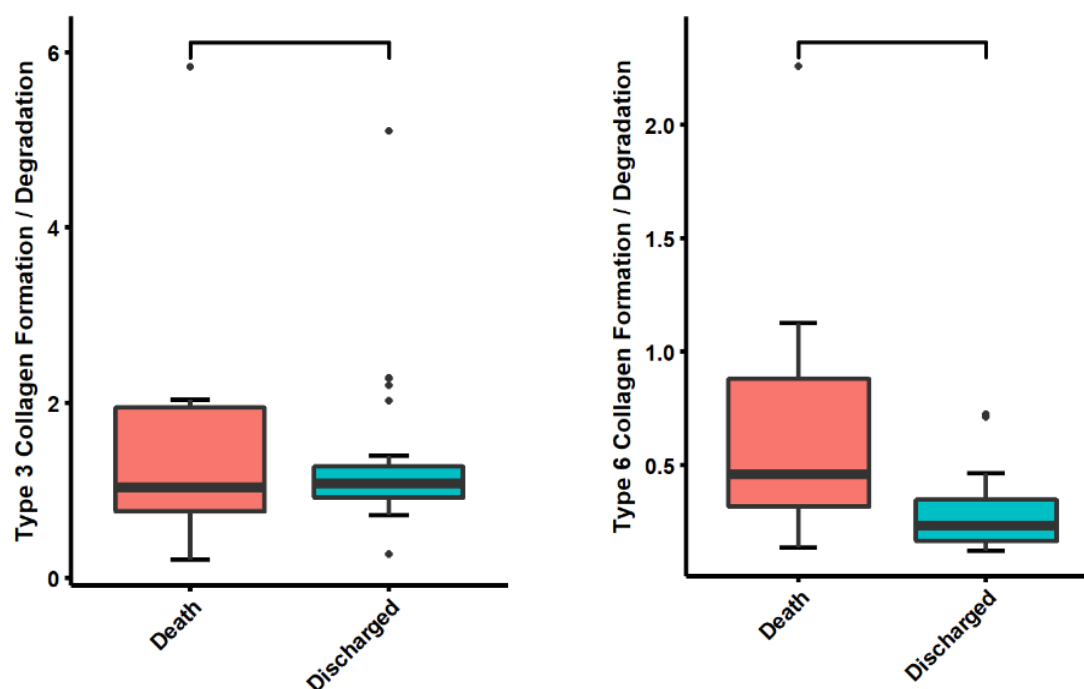


Figure 4-17. Bar and whisker plot showing collagen biomarker levels in serum comparing acute hospitalised and ITU patients who died with those that survived. *= Statistically significant difference with a P-value of <0.05; **= $p < 0.01$; ***= $p < 0.001$; ****= $p < 0.0001$.

Only the serum marker of collagen VI synthesis showed a statistically significant increase in patients who died of COVID-19 compared to those that survived, indicating that higher levels of collagen VI deposition in the lung is associated with poorer outcome.

Finally, as collagen VI synthesis showed the strongest association with death from COVID-19 in ITU and non-ITU hospitalised patients, survival curves was plotted for all hospitalised patients, dividing the combined cohort into collagen VI high and low cases. The mean value of collagen VI synthesis (figure 4-15) was used to divide the cohort. Hospitalised COVID-19 patients with low levels of collagen VI synthesis, as measured by ELISA of serum samples, had a statistically significant better survival compared to patients with high levels (Figure 4-18, $p < 0.0001$).

ELISA

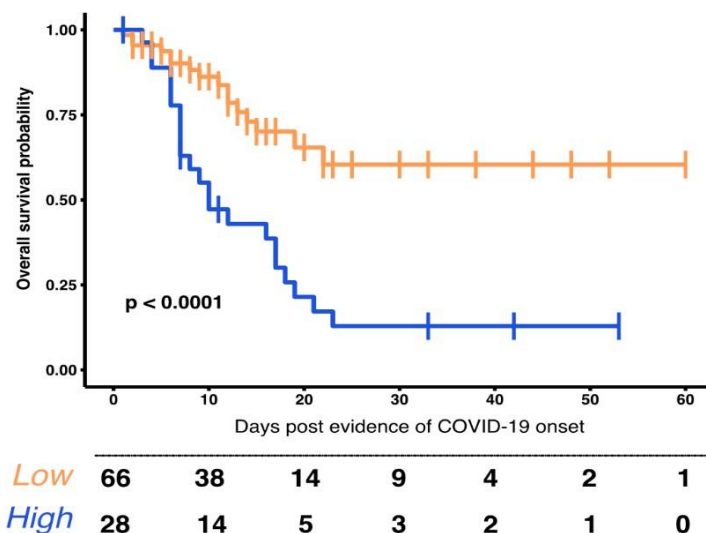


Figure 4-18. Survival curve for all ITU and non-ITU hospital patients combined, divided into serum collagen VI synthesis high vs low groups.

Next, the association between serum collagen VI synthesis and survival was considered for hospitalised non-ITU patients and the hospitalised ITU patient groups. For both groups, serum collagen VI high status was significantly associated with poor survival (hospitalised non-ITU, $p=0.027$, Figure 4-19; hospitalised ITU, $p=0.065$, Figure 4-20).

ELISA

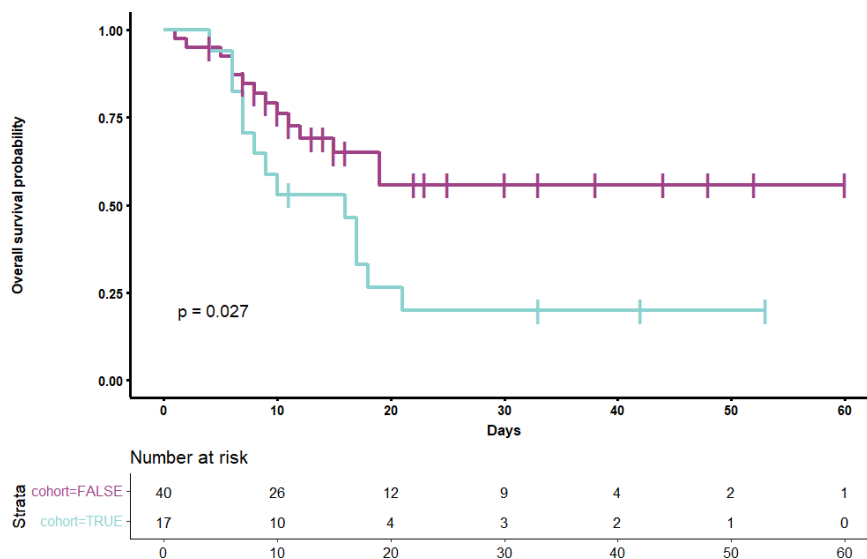


Figure 4-19. Survival curve for ITU COVID-19 patients comparing collagen VI high vs low serum levels.

ELISA

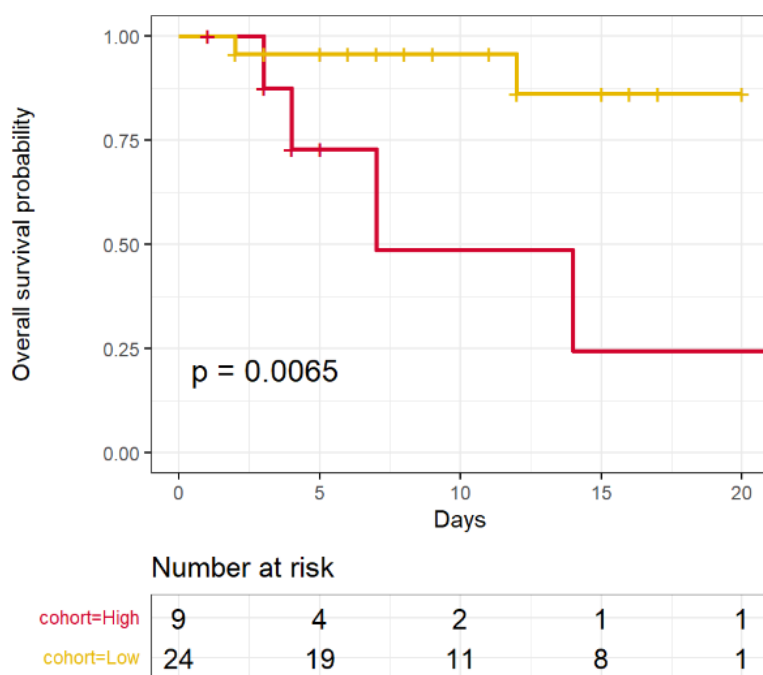


Figure 4-20. Survival curve for non-ITU hospital patients combined comparing collagen VI high vs low

4.4. Discussion and conclusions

Examining post-mortem lung samples using transcriptomic and proteomic methods I have shown increased expression and deposition of collagens 1, 3, 4 and 6 in COVID-19. Spatially-resolved analysis also showed these changes occurred in the alveolar walls, particularly for collagen VI. Quantitative analysis of this data showed both collagen IV and VI proteins showed increased deposition in early stage COVID-19 disease compared to late stage, suggesting that the temporal Quantseq bulk data was more reliable than the GeoMX data. Critically, extending this work, using blood samples from a separate cohort of patients with varying disease severity, I showed increased levels of a marker of collagen VI synthesis in the serum is a predictive biomarker of outcome.

The role of lung fibrosis and remodeling in mediating the fatal course of COVID-19 has previously been described. However, this work focused more generally on fibrosis rather than specific collagens (Ackermann et al., 2022; Borczuk, 2021; George et al., 2020; Yao et al., 2021). Whilst serum pro-collagen 3 was noted to be associated with outcome, these studies did not measure collagen 6. It is unclear why collagen deposition was apparently increased in early stage disease more than late stage

disease. It is unlikely that collagen is resorbed in later disease, and more likely that patients who die rapidly and early in the disease course have increased collagen deposition compared to those who suffer a more protracted course. This would also fit with the increased levels of collagen VI seen in the serum of patients who died from COVID-19.

The surrogate detection of altered collagen deposition in serum, reflecting altered collagen in the lung, is important clinically, as lungs are rarely biopsied during the course of the disease. Therefore, the detection of a biomarker of outcome in blood is an extremely convenient and cost-effective means of measuring collagen fibrosis compared to lung biopsy, which exposes patients to much greater risk. Notably, serum collagen VI is already used as a predictor for progressive fibrosis in other fibrotic lung diseases, such as idiopathic pulmonary fibrosis (Organ et al., 2019a). My identification of a serum biomarker predictive for mortality in severe COVID-19 is of particular value to clinicians, as it could help identify patients who require more intensive therapy. It will have particular relevance for resource poor or stretched medical settings and is especially important in the context of ITU, where beds and resources are limited, and patient stratification is imperative.

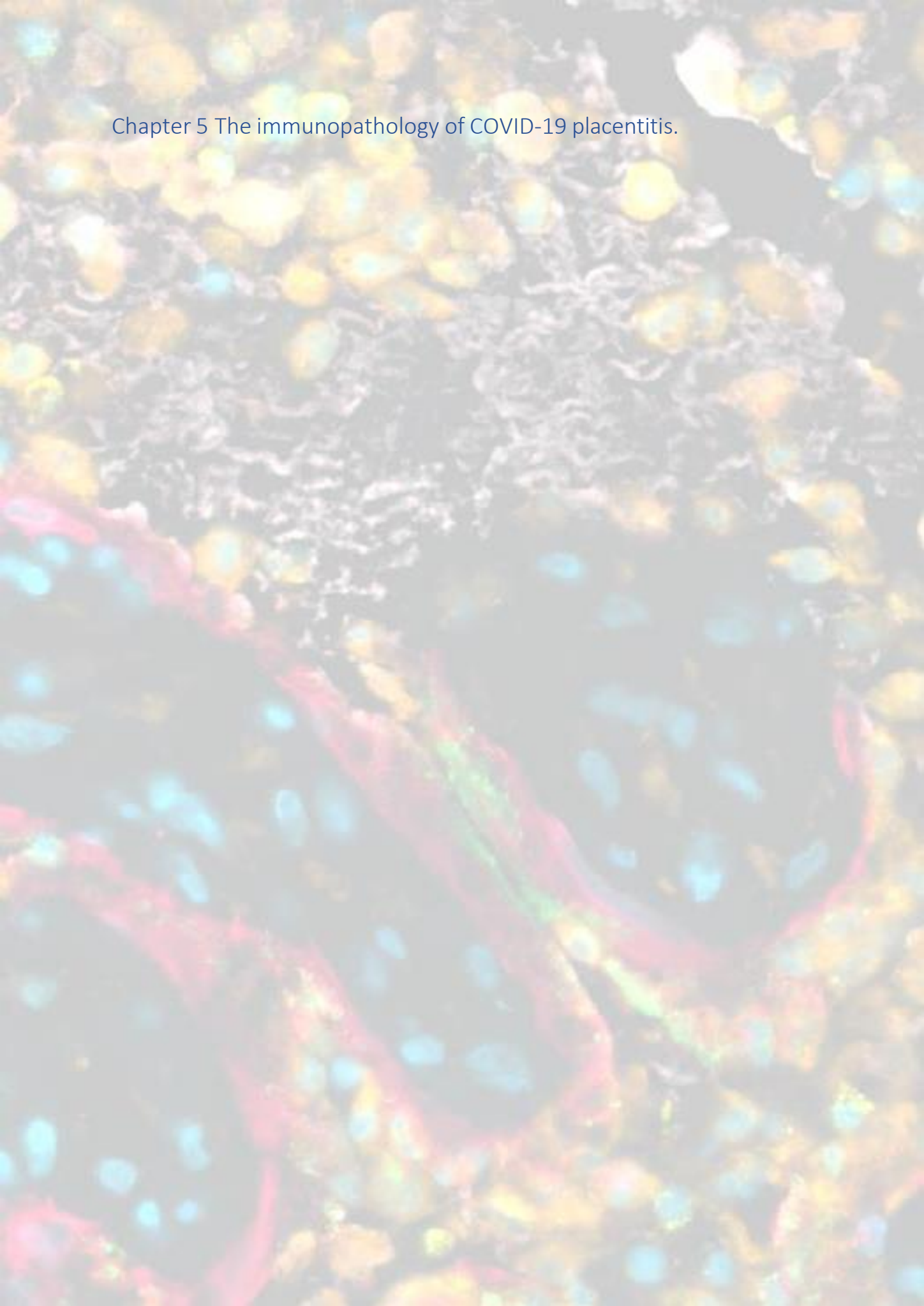
Whilst collagen VI is shown here to be a predictor of outcome in acute COVID-19 disease, it is yet unclear whether it predicts the development of long-term progressive fibrosis, which is seen in a minority of COVID-19 patients (Doane et al., 2021). Fibrosis has previously been noted in COVID-19 lung, and in some cases, the progressive fibrosis following the acute illness has led to lung failure and death (Schwensen et al., 2021). Predicting this progressive fibrosis should be the subject of further work as such a biomarker could help clinicians stratify patients for anti-fibrotic therapy, some forms of which are capable of targeting collagen VI synthesis specifically (Jessen et al., 2021; Organ et al., 2019b).

Conclusions:

1. Lungs from fatal COVID-19 patients show increased levels of collagens in the alveolar wall which likely contribute to alveolar wall thickening, and associated reduced lung function.

2. Macrophages may play an important role in mediating collagen fibrosis.
3. Serum collagen VI is novel biomarker for mortality in severe COVID-19 including hospitalised and ITU patients.

Chapter 5 The immunopathology of COVID-19 placentitis.



5. The immunopathology of COVID-19 placentitis.

Although the respiratory tract is the primary site of SARS-CoV-2 infection, the virus can infect other tissues. Having established a reliable means to detect the virus and characterise its microenvironment in the lung, I sought to extend my work to elucidate the immunopathology of extrapulmonary COVID-19 infection. I chose to study COVID-19-associated placental disease. COVID-19 placentitis is a rare, but potentially devastating, complication of maternal COVID-19 infection (Stenton et al., 2022). It is strongly associated with intra-uterine death (IUD) and characterised by three key histopathological features; chronic histiocytic intervillitis (CHI), trophoblast necrosis (TN) and massive perivillous fibrin deposition (MPVFD) (Schwartz et al., 2022b). The exact role of the virus in mediating the immune pathology, and the nature of the immunopathology, of COVID-19 placentitis were both unclear. Although COVID-19 placentitis is clearly associated with maternal SARS-CoV-2 infection, reports from some groups that not all cases have direct SARS-CoV-2 placental infection has raised a key question in the field: is SARS-CoV-2 infection of the placenta directly involved in the pathogenesis of COVID-19 placentitis? An alternative explanation is that placental SARS-CoV-2 virus is present only as a passenger, in those cases where it is present, and COVID-19 placentitis arises solely as a complication of the mother's respiratory infection (Argueta et al., 2022; Linehan et al., 2021; Schwartz et al., 2022a).

I examined placental tissue from SARS-CoV-2 infected mothers (n=13) with obstetric complications using a multi-modal spatial approach (Figure 5-1). Cases were compared to diseased, non-viral, pre-pandemic placental tissue controls (n=6; three cases of chronic histiocytic intervillitis (CHI) & three cases of villitis of unknown aetiology (VUE)) and normal placental tissue controls (n=5). Tissue samples underwent clinicopathological assessment followed by: i) Tissue-wide whole-transcriptome analysis using bulk Quantseq 3' RNA sequencing; ii) Spatially-resolved whole transcriptome profiling, targeting the trophoblast, immune, stromal and decidual compartments, by Nanostring GeoMx digital spatial profiling (DSP); iii) Targeted cellular-level expression of specific viral and cytokine genes by multiplex

RNAscope in conjunction with TSA-based immunohistochemistry; and iv) tissue-based spatial proteomics using multiplex immunohistochemistry (mIHC) on the Lunaphore COMET platform.

The overall aims were to:

- i. Describe the clinicopathological features of COVID-19 placentitis.
- ii. Determine the presence and extent of placental SARS-CoV-2 infection
- iii. Characterise the immune infiltrate in COVID-19 placentitis
- iv. Reveal the virus immune microenvironment
- v. Elucidate key inflammatory pathways that mediate the immune response

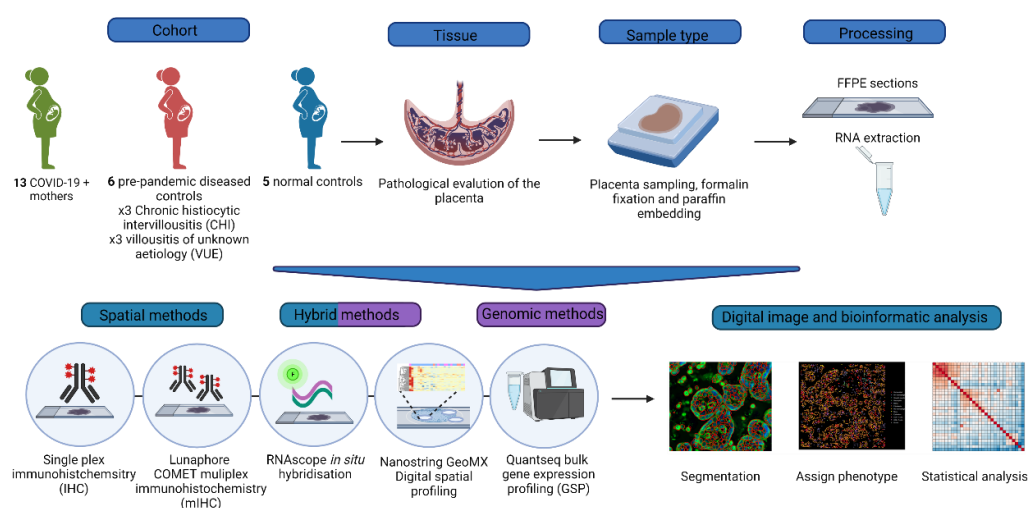


Figure 5-1. Experimental overview of the multi-modal characterisation of COVID-19 placentitis.

5.1. Clinicopathological characteristics

5.1.1. Clinical characteristics

Placental Formalin fixed paraffin embedded (FFPE) tissue samples from 13 mothers with SARS-CoV-2 respiratory infection suffering obstetric complications were obtained from Birmingham Women's Hospital, a regional centre serving the West Midlands County. Placentas from SARS-CoV-2 infected mothers will be denoted as 'Cov19' for the remainder of the chapter. Respiratory SARS-CoV-2 infection was confirmed by routine nasopharyngeal swab and PCR test in 12/13 (92%) cases. One mother tested negative by respiratory PCR but was subsequently identified as virus positive based on SARS-CoV-2

detection in her placenta. Eleven pre-pandemic non-virus associated control placentas were also collated, comprising 4 CHI controls (Control^{CHI}), 2 CV controls (Control^{CV}) and 5 normal controls (Normal).

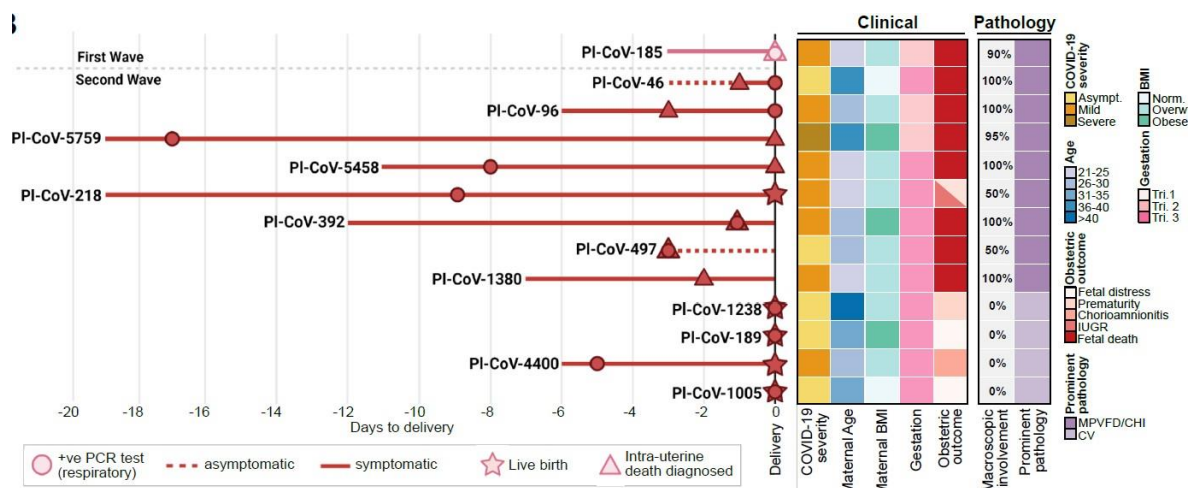


Figure 5-2. Summary of the clinic-pathological features of 13 SARS-CoV-2 infected mothers with obstetric complications.

The clinical characteristics are summarised in Table 5-1. The cohort was enriched for mothers with a raised BMI (9/13 - 69%), a known risk factor for severe respiratory COVID-19 infection (Mahase, 2020). Most of the mothers delivered the baby in the third trimester (10/13 - 76%) and the remainder in the second trimester. Only one mother had severe concomitant respiratory COVID-19, whilst the others had mild or asymptomatic infection. Intriguingly, in spite of the mild respiratory illness experienced by most mothers, obstetric complications were severe. Most of the mothers (8/13 - 62%), suffered an intra-uterine death (IUD) leading to still-birth. The remainder were complicated by intra-uterine growth restriction (IUGR), prematurity, or fetal distress. Prematurity and IUGR frequently co-occurred.

<i>COVID-19 status</i> <i>Pathology</i> <i>Sample size</i>	Maternal respiratory SARS-CoV-2+				Pre-pandemic controls		
	All	M+P+	M+P-	M+P-	NA	NA	NA
	All	CHI	CHI	CV	CHI	CV	Norm
	n=13	n=6	n=3	n=4	n=4	n=2	n=5
Clinical characteristics n (%)							
Age							
18-25	4	3 (50)	1 (33)	0 (0)	0 (0)	0 (0)	2 (40)
26-35	6	2 (33)	1 (33)	3 (75)	2 (50)	1 (50)	3 (60)
36+	3	1 (17)	1 (33)	1 (25)	2 (50)	1 (50)	0 (0)
Fetal Sex							
Male	6	2 (33)	2 (67)	2 (50)	1 (25)*	1 (50)	4 (80)
Female	6	4 (67)	1 (33)	1 (25)	2 (50)	1 (50)	1 (20)
Male/female twin	1	0 (0)	0 (0)	1 (25)	0 (0)	0 (0)	0 (0)
Ethnicity							
Caucasian	5	3 (50)	1 (33)	1 (1)	2 (50)	2 (100)	3 (60)
Black	2	2 (33)	0 (0)	0 (0)	0 (0)	0 (0)	1 (20)
Asian	4	1 (17)	1 (33)	2 (50)	1 (25)	0 (0)	1 (20)
Middle eastern	2	0 (0)	1 (33)	1 (25)	1 (25)	0 (0)	0 (0)
Body mass index							
Normal	2	1 (17)	0 (0)	1 (25)	1 (25)*	NA*	NA*
Overweight	8	4 (67)	2 (67)	2 (50)	0 (0)	NA	NA
Obese	3	1 (17)	1 (33)	1 (25)	2 (50)	NA	NA
Gestation							
Second trimester	3	2 (33)	1 (33)	0 (0)	1 (25)	0 (0)	0 (0)
Third trimester	10	4 (67)	2 (67)	4 (100)	3 (75)	2 (100)	5 (100)
COVID-19 Respiratory illness							
Severe	1	0 (0)	1 (33)	0 (0)	NA	NA	NA
Mild	7	5 (83)	1 (33)	1 (25)	NA	NA	NA
Asymptomatic	5	1 (17)	1 (33)	3 (75)	NA	NA	NA
Obstetric outcome							
Intra uterine death	8	6 (100)	2 (67)	0 (0)	1 (25)	0 (0)	0 (0)
Prematurity	2	0 (0)	1 (33)	1 (25)	1 (25)	2 (100)	0 (0)
Intra-uterine growth restriction	2	0 (0)	1 (33)	1 (25)	2 (50)	1 (50)	0 (0)

Table 5-1. Clinical characteristics of the COVID-19 cohort and controls.

5.1.2. Histopathological characteristics

The histopathological features of the cohort were assessed on haematoxylin and eosin (H&E) stained FFPE sections and by standard diagnostic single-plex chromogenic immunohistochemistry (CD68) performed by Birmingham Women's Hospital paediatric pathology department. The results are summarised in Table 5-2.

COVID-19 status Pathology Sample size	Maternal respiratory SARS-CoV-2+				Pre-pandemic controls		
	All	M+P+	M+P-	M+P-	NA	NA	NA
	All	CHI	CHI	CV	CHI	CV	Norm
	n=13	n=6	n=3	n=4	n=4	n=2	n=5
Pathological features n (%)							
Macroscopic findings							
MPVFD	9	6 (100)	3 (100)	0 (0)	2 (50)	0 (0)	0 (0)
Abruption	1	0 (0)	1 (33)	0 (0)	0 (0)	1 (50)	0 (0)
Membrane opacity	7	3 (50)	1 (33)	3 (75)	1 (25)	1 (50)	0 (0)
Microscopic findings							
Chronic histiocytic Intervillositis	10	6 (100)	3 (100)	1 (25) ⁺	4 (100)	0 (0)	0 (0)
Chronic villitis	9	4 (67)	3 (67)	3 (75)	1 (25)	2 (100)	0 (0)
Basal villitis	6	2 (33)	1 (33)	3 (75)	1 (25)	2 (100)	0 (0)
Acute chorioamnionitis	5	1 (17)	2 (67)	2 (50)	0 (0)	0 (0)	0 (0)
Chronic chorioamnionitis	7	5 (83)	1 (33)	1 (25)	1 (25)	2 (100)	0 (0)
Chronic deciduitis	9	4 (67)	2 (67)	3 (75)	2 (50)	2 (100)	0 (0)
Secondary bacterial infection	1	0 (0)	0 (0)	1 (25)	0 (0)	0 (0)	0 (0)
Funisitis	2	0 (0)	0 (0)	2 (50)	0 (0)	0 (0)	0 (0)
Sub-chorionic microabscesses	1	0 (0)	1 (33)	0 (0)	0 (0)	0 (0)	0 (0)

Table 5-2. Pathological characteristics of the COVID-19 placentitis cohort and controls. *one case with predominant chronic villitis pattern pathology showed focal CHI.

Overall, two broad patterns of pathology were observed in placentas from obstetrically complicated SARS-CoV-2+ infection. The most common pattern (9/13 - 69%), comprised widespread fibrin deposition macroscopically (Figure 5-3), associated with three distinct histopathological features: chronic histiocytic intervillitis (CHI), massive perivillous fibrin deposition (MPVFD), and prominent trophoblast necrosis (TN) (Figure 5-4). These three features have previously been proposed as the defining pathological characteristics of COVID-19 placentitis in the correct clinical context. Whilst this combination of pathological features is seen in control^{CHI} placentas, the necrosis in Cov19^{CHI} placentas often affected the full circumference of the placental villi (Figure 5-5).



Figure 5-3. Macroscopic assessment of placentas from SARS-CoV-2 positive mothers showed widespread lesional involvement in 9/13 cases with extensive fibrin deposition in a 'lace-like' pattern.

The second pattern of pathology, observed in 4/13 (31%) SARS-CoV-2 infected mothers, was that of chronic villitis, predominantly comprising lymphocytic infiltrates within the villous stroma. One case with prominent chronic villitis showed very focal CHI. There was no evidence of extensive fibrin deposition in any of Cov19^{CV} placenta.

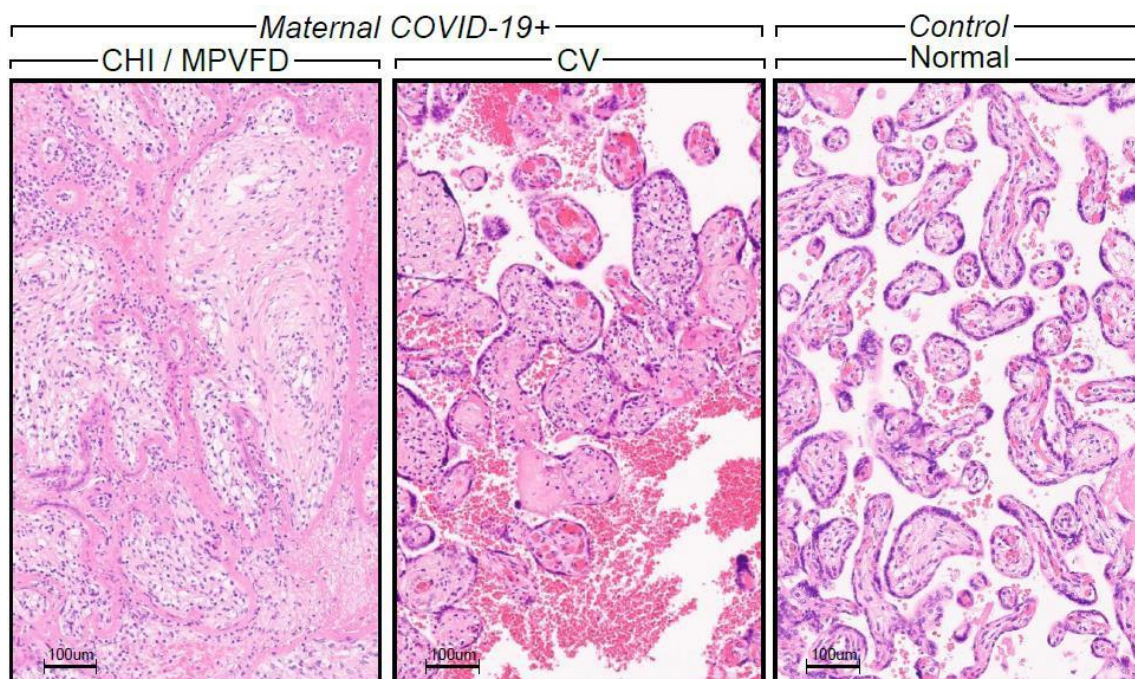


Figure 5-4. Two patterns of pathology were observed amongst SARS-CoV-2 infected mothers- CHI/MPVFD and CV predominant.

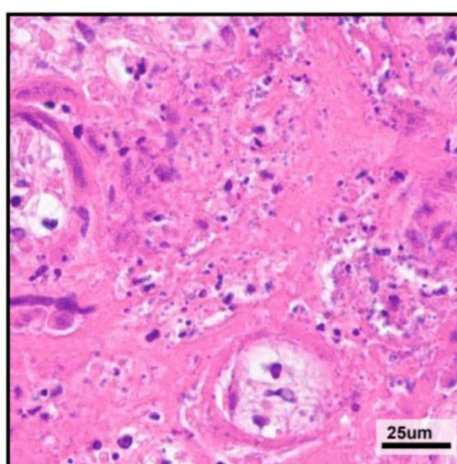


Figure 5-5. Trophoblast necrosis in COV19^{CHI} showing circumferential involvement of the placental trophoblast.

As part of routine diagnosis, CD68 immunohistochemistry is typically performed in the context of CHI to confirm the presence of macrophages. Diagnostic CD68 staining was examined across the cohort.

CoV19^{CHI} placentas showed a unique macrophage distribution compared to control^{CHI}. Macrophages in Cov19^{CHI} were palisading around the circumference of the placental villi, abutting the trophoblast. In contrast, pre-pandemic control^{CHI} placentas, macrophages were predominantly in the middle of the intervillous space.

IHC

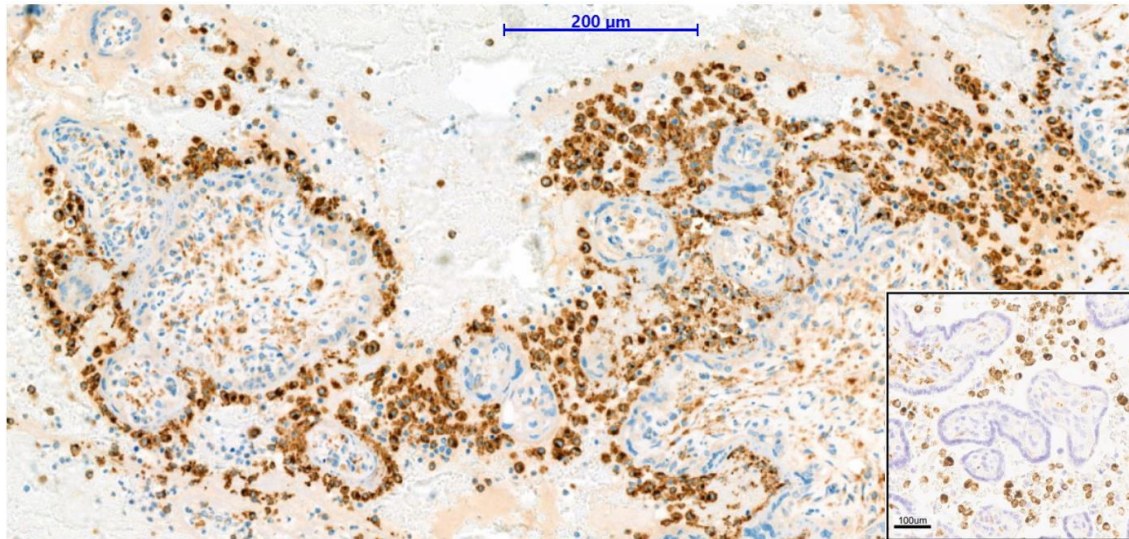


Figure 5-6. Single-plex chromogenic immunohistochemistry showing macrophages (CD68+) palisading and closely abutting the placental villi compared to (inset) control^{CHI} which has macrophages in the middle of the maternal space.

5.1.3. Clinicopathological correlation

Next, the pathological features were examined in association with the clinical features. It was noted all intra-uterine deaths occurred in association with CHI/MFVPD pathology, whilst no intrauterine deaths were seen in placentas shows chronic villitis predominant morphology. Notably, none of the mothers had a previous history of CHI or villitis of unknown origin.

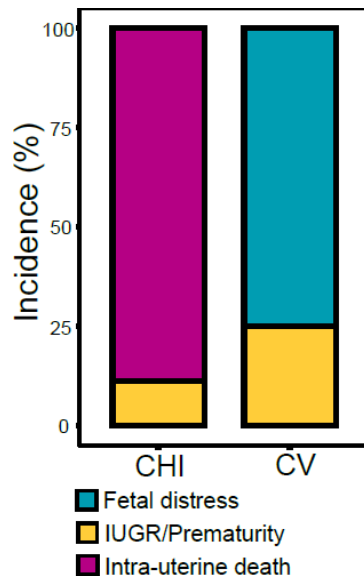


Figure 5-7. Comparison of complications associated with CHI and CV predominant pathologies shows that IUD is strongly associated with CHI pathology.

5.2. Virus detection

To robustly determine the presence and extent of placental SARS-CoV-2 infection in COVID-19 placentitis, a multi-modal, well validated (Appendix 3) approach to virus detection was undertaken at an RNA and proteomic level. Virus RNA was detected by means of Quantseq bulk RNA sequencing and by RNAscope, whilst virus proteins were detected as part of a wider multiplex immunohistochemistry panel. Overall, virus was deemed to infect the trophoblasts in 6/13 (%) Cov19 placentas and was absent from disease and normal controls.

5.2.1. Virus RNA detection by Quantseq bulk RNA sequencing

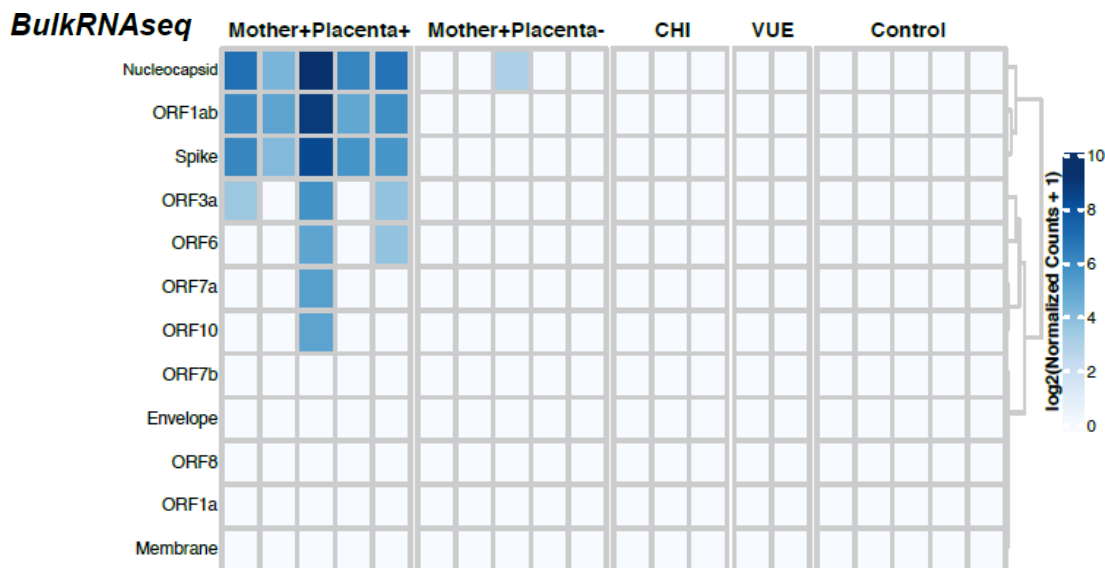


Figure 5-8. Quantseq bulk RNA sequencing showing SARS-CoV-2 gene expression in placentas from SARS-CoV-2 positive mothers and controls.

To detect viral RNA, and to define which viral genes were expressed in CoV-19 placentas, Quantseq gene expression data were aligned to the SARS-CoV-2 genome. Of the 10 cases of Cov19 placentas assessed, 5 showed convincing evidence of SARS-CoV-2 gene expression (Figure 5-8). All of the cases in which virus was detected were Cov19^{CHI}. Only a small number of nucleocapsid reads were detected in one Cov19^{CV} case; as virus was not detected by any other modality this case was scored as virus negative. This low-level detection of virus could represent the remnants of earlier infection, false positive detection or reflect circulating virus in the mothers blood passing through the vascular-rich placenta.

For the five cases positive for SARS-CoV-2, nucleocapsid, ORF1ab and spike were the most commonly detected transcripts and were present in all cases; ORF3a, ORF6, ORF7a and ORF 10 were variably detected in a subset of cases.

5.2.2. Virus RNA detection by RNA scope

To explore virus distribution and whether replicative infection was present, RNAscope with probes against orf1ab sense and spike antisense transcripts was employed (Figure 5-9).

Spike and orf1ab were detected in the placental trophoblast in 6/13 (46%) cases with a patchy, tissue distribution with detection by both probes indicating replicative infection of the trophoblast. Consistent with the Quantseq bulk gene expression data, virus was only detected only in Cov19^{CHI} cases.

RNAScope

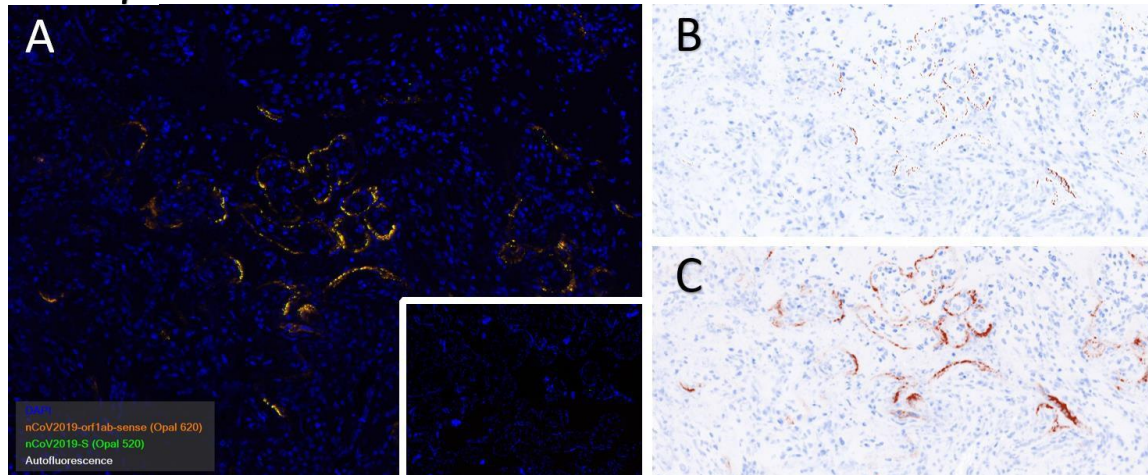


Figure 5-9 . Dual RNAScope against 'orf1ab' sense and 'spike' anti-sense RNA showed co-localisation of expression in the syncytiotrophoblast in 6/13 Cov19 placentas (A). Pseudo-chromogenic image processing shows isolated spike (B) and more abundant orf1ab (C) expression, consistent with active viral replication

5.2.3. Virus detection by chromogenic single-plex immunohistochemistry

First, placentas were stained for SARS-CoV-2 spike by single-plex chromogenic immunohistochemistry on the Leica Bond-Max (Figure 5-10). Positive virus staining was seen in 6/13 (46%) cases; these were the same Cov19^{CHI} cases which showed positive virus staining by RNAScope. The virus protein also showed a similar distribution to that observed by RNAScope, with patchy positivity in the syncytiotrophoblast.

IHC

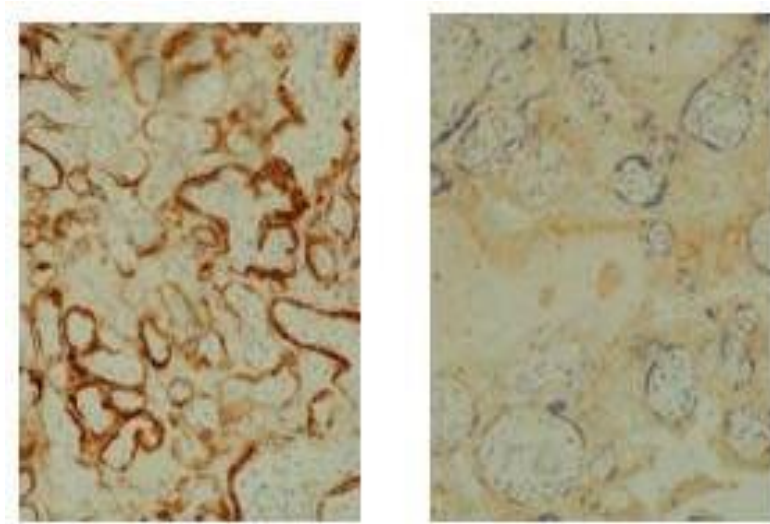


Figure 5-10. Chromogenic immunohistochemistry for SARS-CoV-2 spike showed virus protein expression in the trophoblast of 6 placentas (left panel), the remainder were negative (right panel)

5.2.4. Virus protein detection by multiplex immunohistochemistry

The two antibodies specific for SARS-CoV-2 spike and nucleocapsid proteins were included in a larger panel of antibodies for the Lunaphore COMET multiplex IHC platform. Detection of virus protein by mIHC matched the previous detection of virus by chromogenic staining and RNAscope: co-expression of both spike and nucleocapsid proteins in the syncytiotrophoblast with a patchy distribution (Figure 5-11). Virus protein was detected in the same six Cov19^{CHI} cases that had tested positive for SARS-CoV-2 by RNAscope and Quantseq bulk gene expression.

Quantitative analysis of COMET mIHC images confirmed that virus was present predominantly in the trophoblast cells, but also a smaller proportion of macrophages (Figure 5-12). COMET mIHC images were therefore further inspected for evidence of virus protein staining in macrophages (Figure 1-13).

mlHC

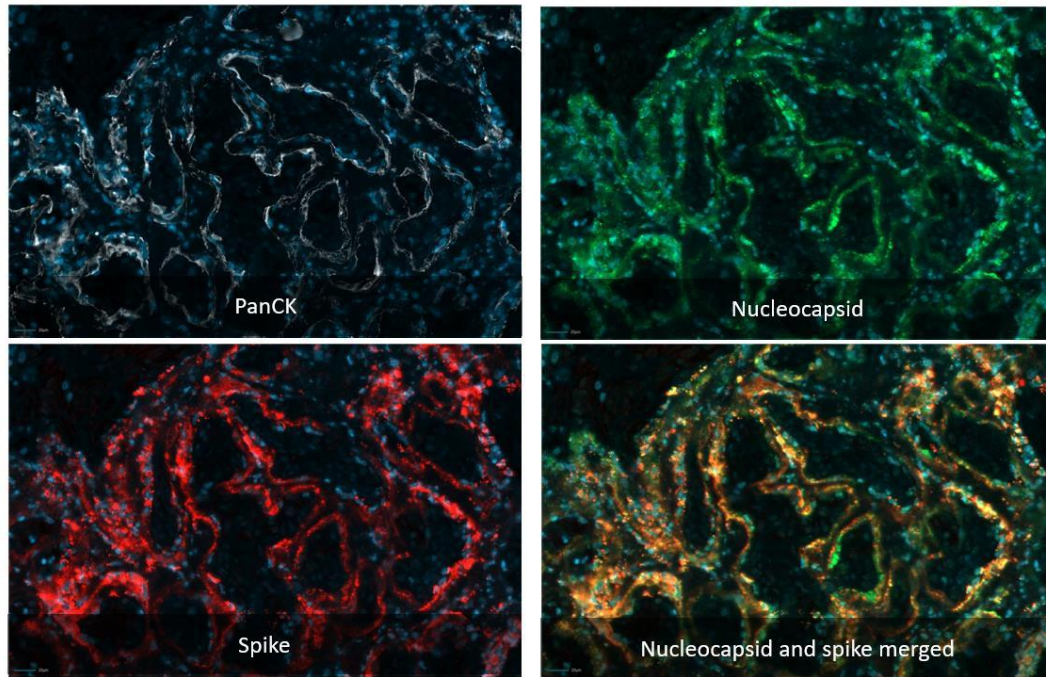


Figure 5-11. COMET mlHC image showing co-expression of spike and nucleocapsid proteins in the cytochrome (AE1/AE3) positive trophoblast layer.

mlHC

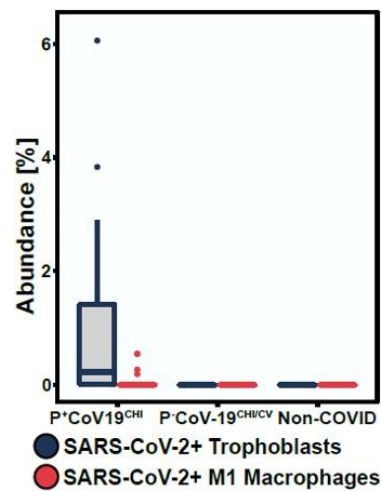


Figure 5-12. Quantitative analysis of the COMET mlHC images shows that virus protein is present mostly in the trophoblast layer, and in a small proportion of macrophages.

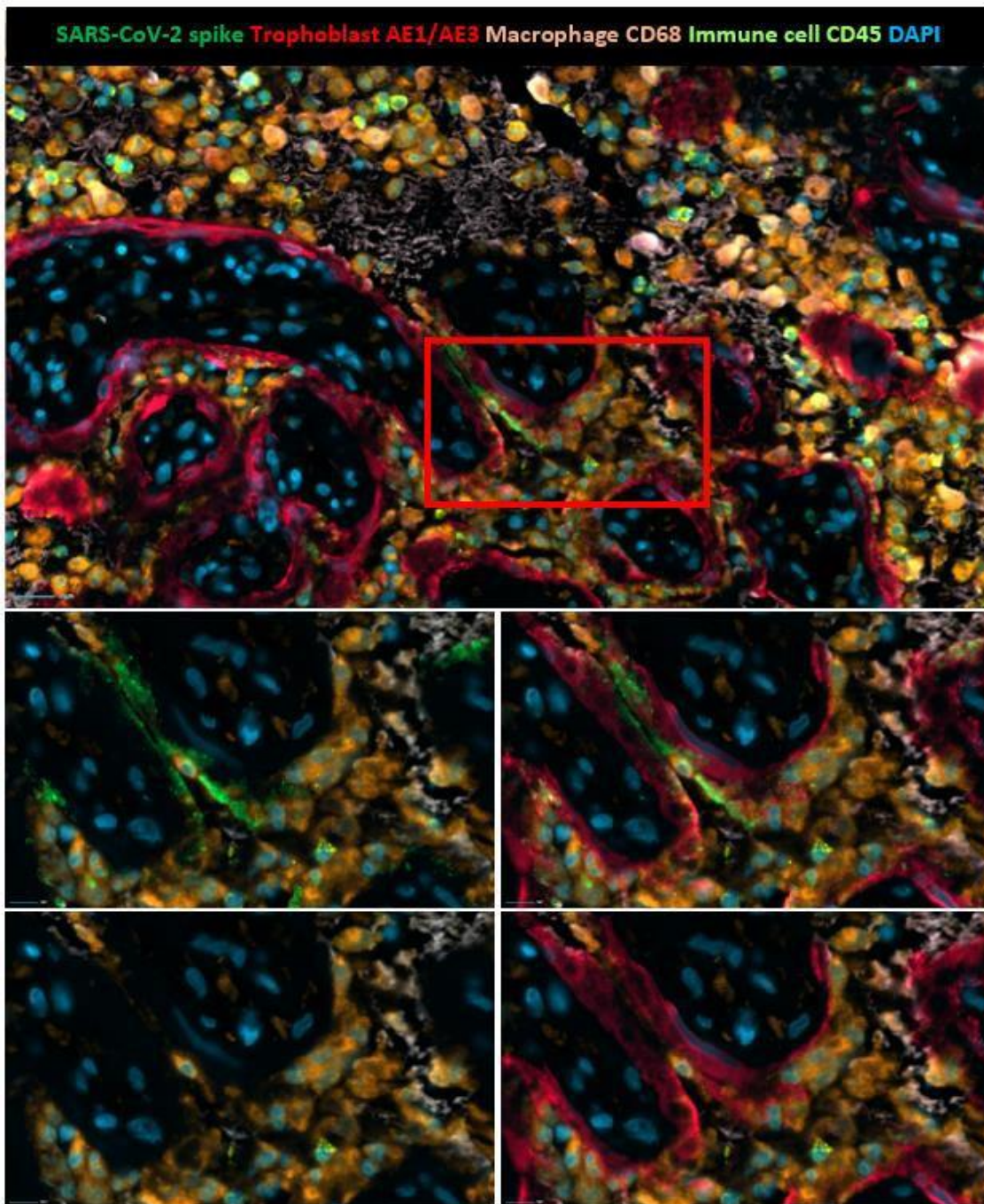


Figure 5-13. COMET miHC images showing expression of virus protein in macrophages abutting the virus infected trophoblast.

SARS-CoV-2 virus staining was present in a subset of macrophages abutting the virus infected trophoblast. Unlike virus staining of the trophoblast, which showed virus proteins to be widely distributed in the cytoplasm of the infected trophoblast cells, macrophage virus staining showed punctate, granular staining. This staining was reminiscent of phagosome staining, suggestive of the virus being phagocytosed by macrophages at the fetomaternal interface.

5.2.4. Determination of virus strain

To determine whether particular virus strains were associated with placental infection, two placentas were selected for determination of virus strain by RT-PCR and sanger sequencing. The detected virus strain reflected the most prevalent circulating strains at the time of sampling these were the ancestral hCoV-19/Wuhan/WIV04 and the alpha variant (Figure 5-14).

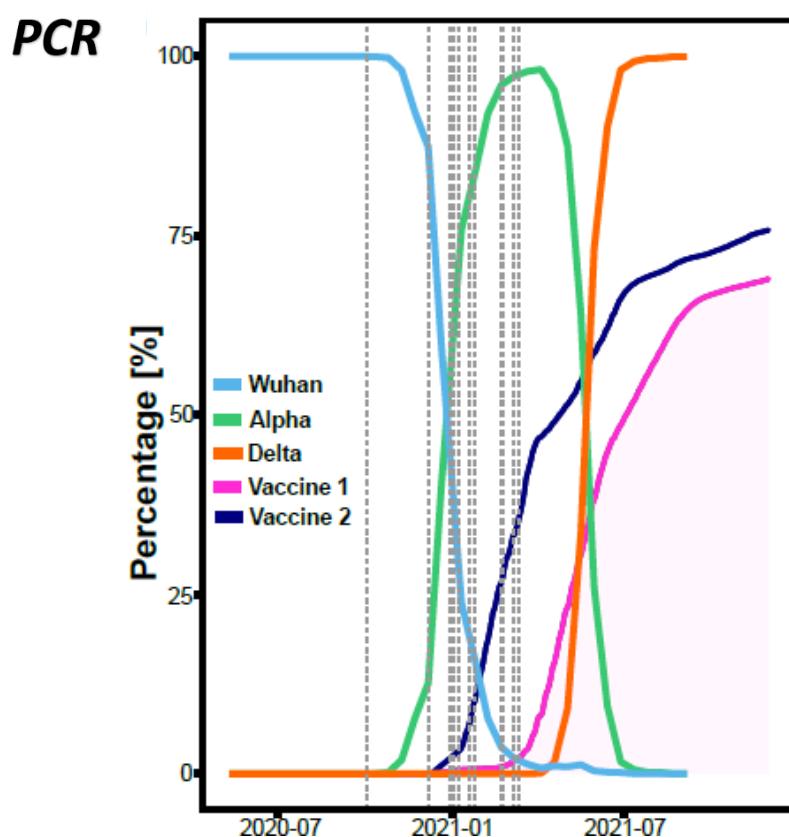


Figure 5-14. Predominant SARS-CoV-2 viral strains in the community at the time of placental sampling.

5.2.5. Virus entry receptors expression

SARS-CoV-2 enters host cells via the ACE2 cell surface receptor with additional proteins acting as host entry factors (Jackson et al., 2022). ACE2 is commonly expressed on the placental trophoblast (Azinheira Nobrega Cruz et al., 2021) raising the question of why only a minority of mothers with respiratory SARS-CoV-2 infection show placental SARS-CoV-2 infection and placentitis. To address this question I interrogated the Nanostring GeoMx DSP and COMET mIHC data to look for differences in viral receptor and entry factor expression.

Analysis of the trophoblast layer by GeoMx DSP did not detect any major differences in levels of ACE2, BSG, NRP1 or TMPRSS2 transcripts between cases of COVID-19 placentitis compared to controls (Figure 5-15).

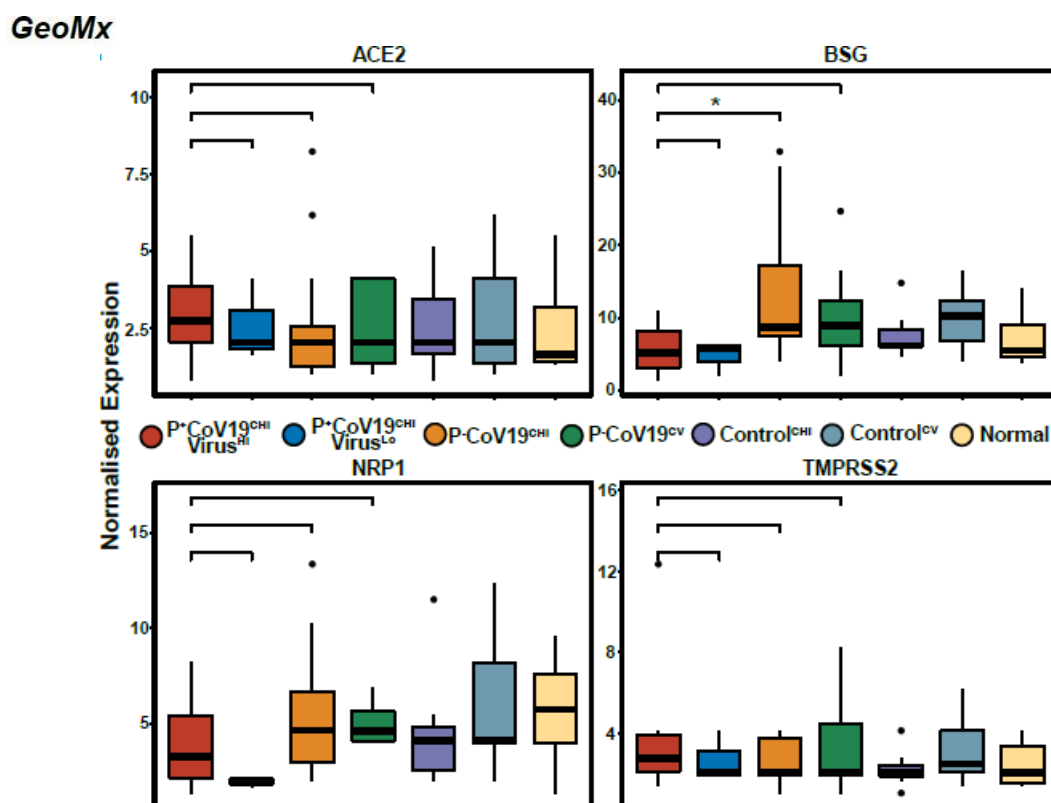


Figure 5-15. SARS-CoV-2 viral entry receptor expression by Nanostring GeoMx DSP. *= Statistically significant difference with a P-value of <0.05; **= $p < 0.01$; ***= $p < 0.001$; ****= $p < 0.0001$.

Analysis of the COMET mIHC images showed ACE2 was expressed on approximately the same number of trophoblasts in placentas from SARS-CoV-2 infected mothers compared to controls. However, 12/13 (92%) placentas from SARS-CoV-2 infected mothers showed an atypical distribution of expression compared to controls (Figure 5-16). Most CoV-19 placentas showed expression of ACE2 on the maternal surface as well as the ante-luminal surface, in a tram-track distribution. In contrast, the control placentas only showed ACE2 expression on the ante-luminal surface. As the maternal surface of the trophoblast is exposed to maternal blood, this provides a plausible mechanistic basis of why some placentas are differentially infected with SARS-CoV-2 following maternal respiratory infection. However, these data cannot exclude the possibility that this unusual distribution of ACE2 is an incidental response to respiratory viral infection.

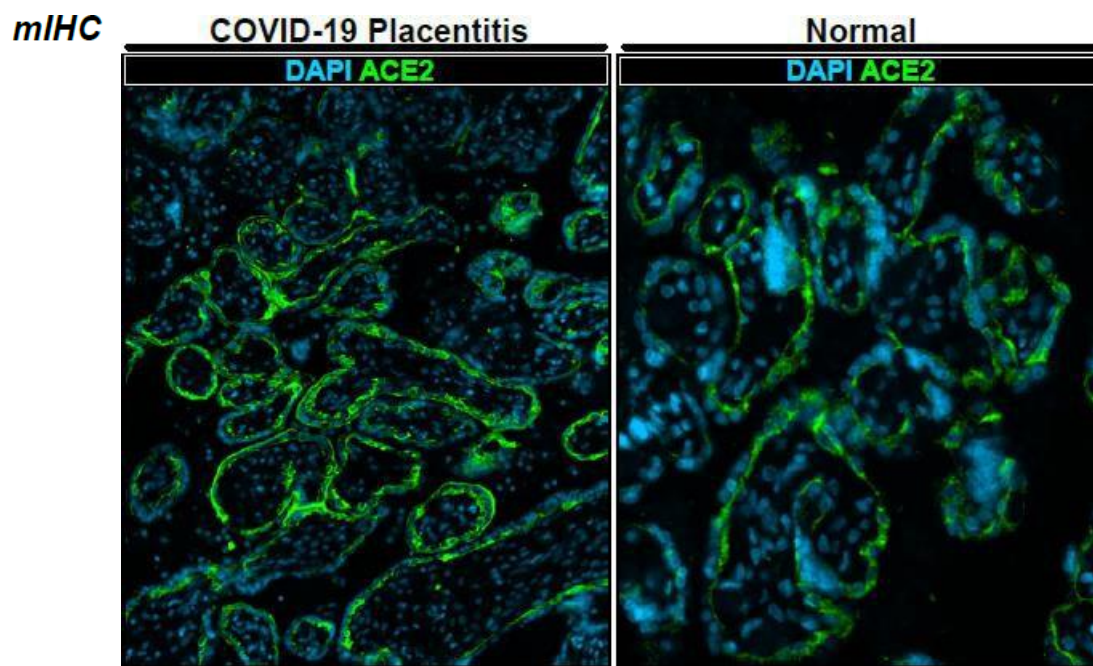


Figure 5-16. COMET mIHC images showing an altered tram-track maternal and ante-luminal distribution of ACE2 expression in a representative Cov19 placenta compared to the ante-luminal ACE2 expression present in a control placenta.

5.3. Immune infiltrate

The immune composition of placentas from cases of COVID-19 placentitis was assessed by mIHC staining of tissue samples on the Lunaphore COMET. The mIHC antibody panel comprised immune cell lineage, immune checkpoint, viral and structural protein specific antibodies. Images first underwent qualitative assessment followed by quantification of the immune infiltrate. More detailed analyses of macrophages was undertaken by interrogation of Nanostring GeoMx DSP data.

5.3.1. Qualitative assessment of the immune infiltrate

Architectural assessment of mIHC images confirmed the pathological findings, showing MPFD, and prominent macrophage infiltrates abutting the virus infected placenta (Figure 5-17).

mIHC

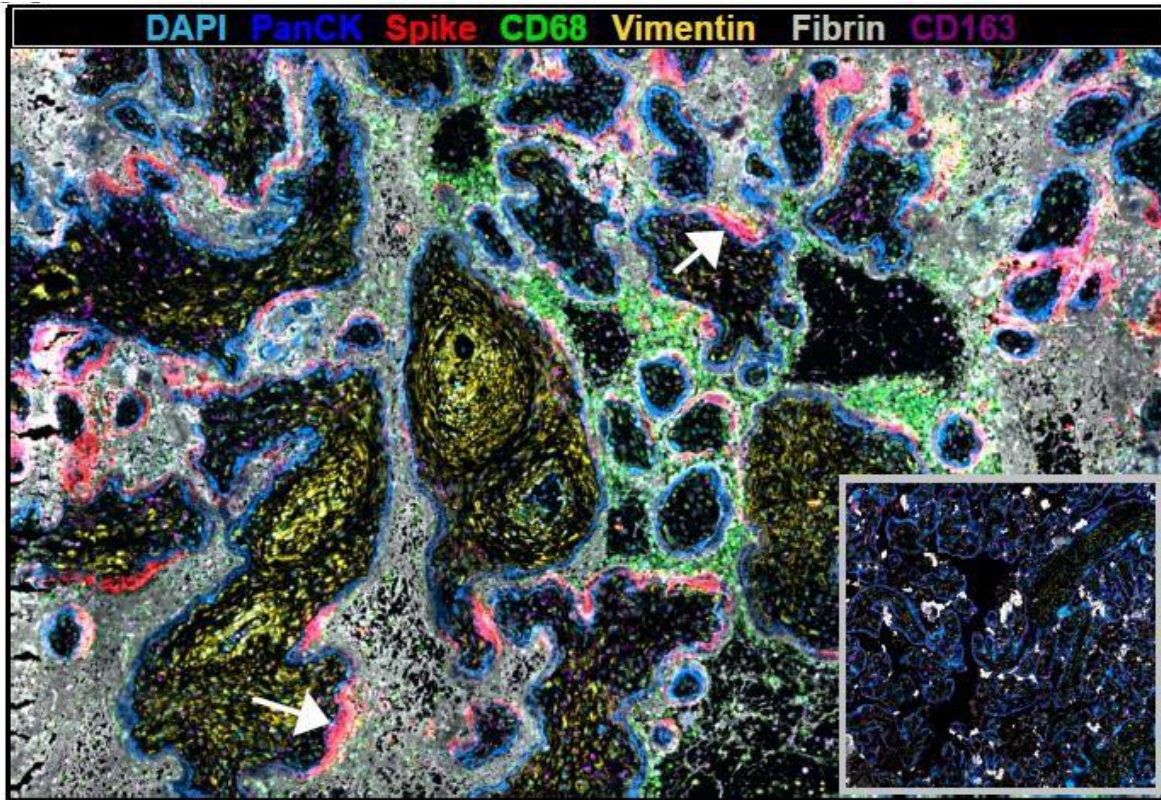


Figure 5-17. COMET mIHC image showing massive perivillous fibrin and macrophages abutting virus infection trophoblast (white arrow). Control placenta inset.

Further inspection of mIHC images showed the immune infiltrate comprised predominantly macrophages, with smaller populations of T-cells, B-cells and neutrophils (Figure 5-18). These immune cells were mostly present in the maternal intervillous space. Some macrophages were present within the villous stroma.

mIHC

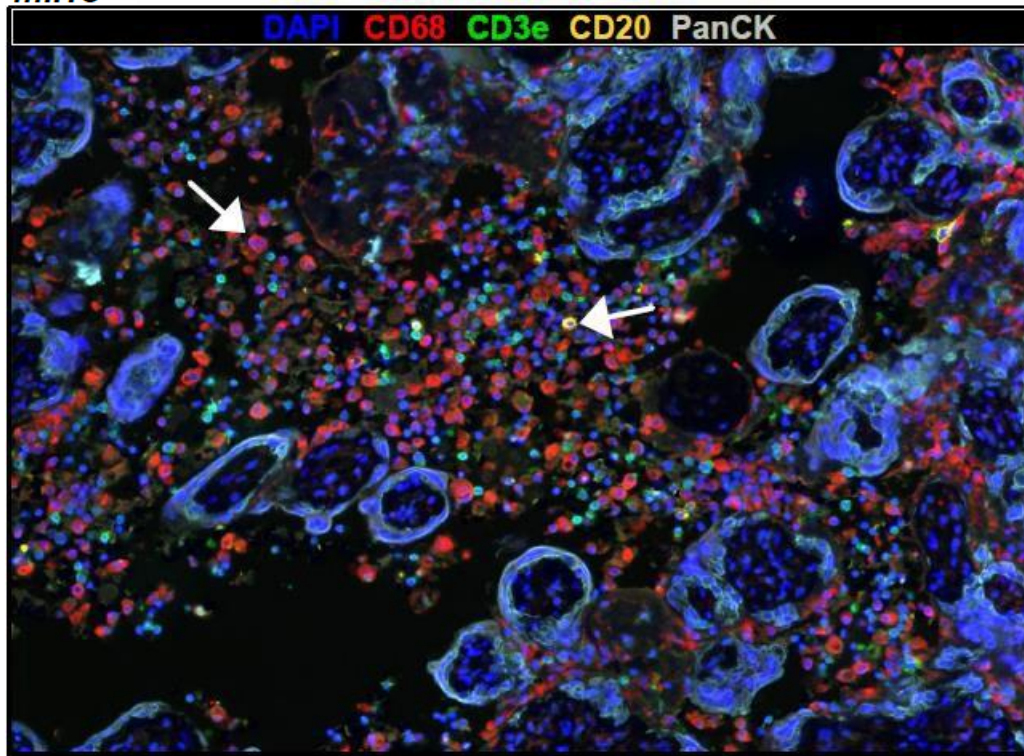


Figure 5-18. COVID-19 placentitis showing a mixed population of macrophages and lymphocytes (white arrows).

5.3.2. Quantitative assessment of the immune composition

In order to quantify the immune cell abundances in COVID-19 placentitis compared to controls, mIHC images were segmented into regions via deep learning-based segmentation. From across all images, three million cells were segmented with DeepCell. These cells were then clustered with PhenoGraph (Bodenheimer et al., 2020). Forty-one clusters were initially generated, which were subsequently merged into 10 meta clusters (figure 5-19, 5-20). These metaclusters were then validated using the mIHC images (Figures 5-19, 5-20) projected onto a tSNE plot (figure 5-21).

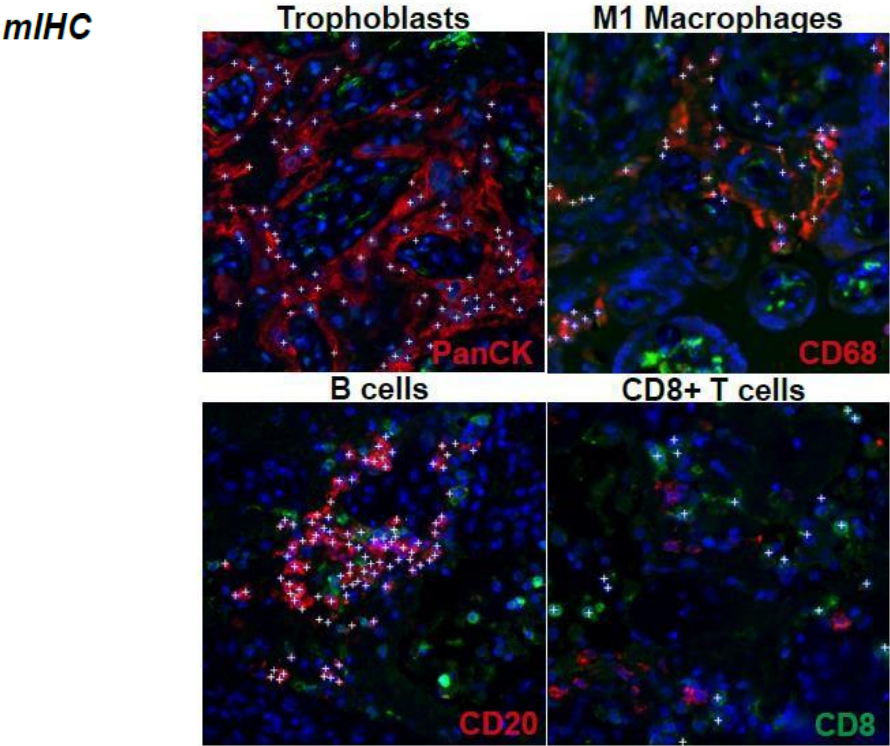


Figure 5-19. Validation of metaclusters using the mIHC images.

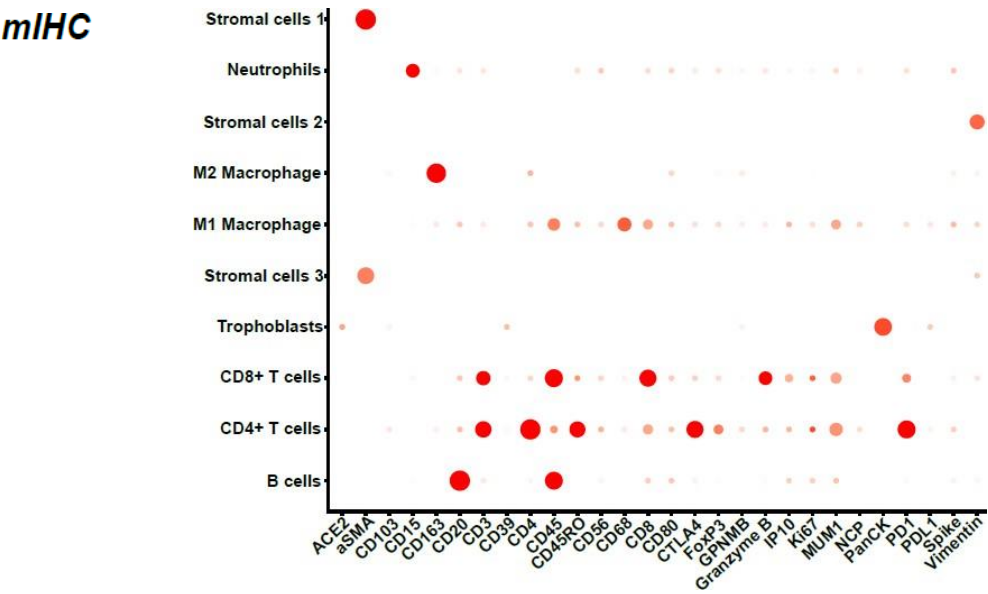


Figure 5-20. Metaclusters identified on quantitative assessment of mIHC images.

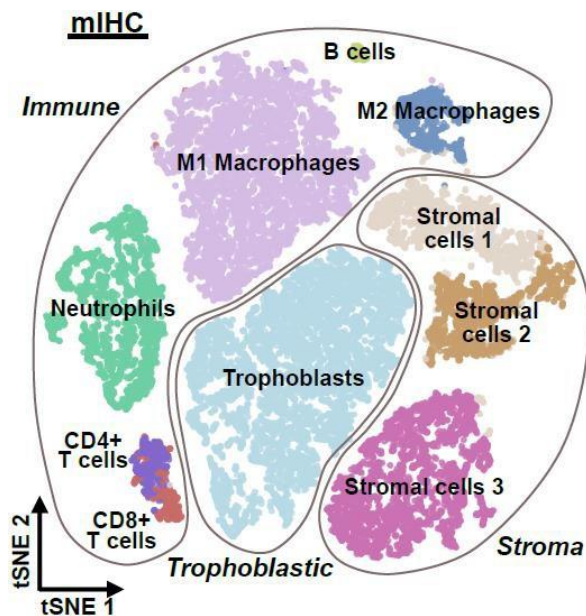
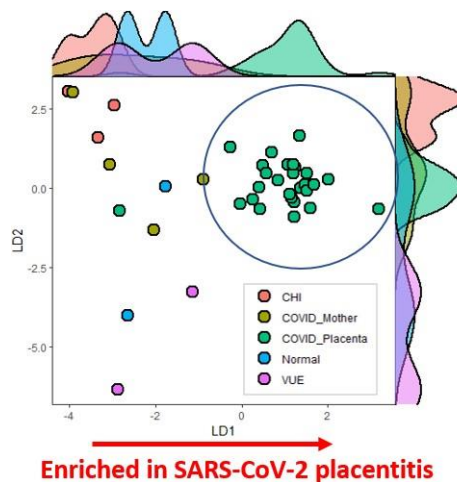


Figure 5-21. tSNE plot representing the 10 metaclusters identified on quantitative analysis of mIHC images.

Next, a principal component analysis (PCA) was undertaken based on the abundances of each metacluster to identify the most distinguishing features for each disease state (Figure 5-22). SARS-CoV-2+ CoV19^{CHI} cases clustered together on the PCA and were distinct from SARS-CoV-2 negative CoV19^{CHI} and controls, suggesting that SARS-CoV-2 virus positivity is associated with a unique immunological state in COVID-19 placentitis. Consequently, SARS-CoV-2+ CoV19^{CHI} placentas (denoted P+Cov19^{CHI}) were analysed separately in subsequent analyses.

mIHC

A



B

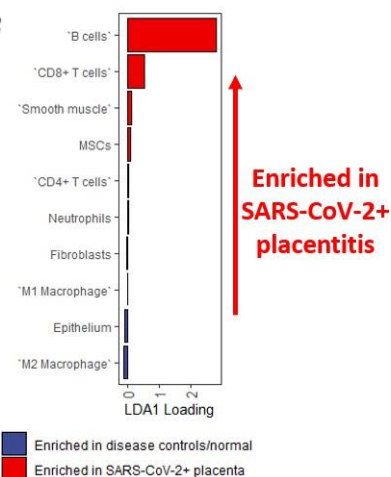


Figure 5-22. (A) PCA showing SARS-CoV-2 placentas forming a unique cluster compared to normal and diseased controls. Abundances of each disease is plotted on the upper X and right Y axis. (B) Loadings contributing most to LD1, show features responsible for the unique clustering on the X-axis. B-cell contribute most to the variance of LD1.

Inspection of the PCA loading revealed that the presence of B-cells and CD8+ T-cells were the factors that contributed most to the unique clustering of SARS-CoV-2+ CoV19^{CHI}.

Next, the abundances of the key immune subsets were plotted across the Cov19 placentas and controls (Figure 5-23). The abundance of the epithelial cells were markedly reduced in P+CoV19^{CHI} placentas, most likely reflecting the extensive necrosis in the trophoblast layer. Notably, the extent of fibrin deposition was also greater in P+CoV19^{CHI} placentas, even compared to P-Cov19^{CHI} placentas, implying that the presence of virus contributes to fibrin deposition. P+CoV19^{CHI} placentas were also enriched for a number of immune subtypes, including B-cells, CD4+ T-cells, M1 macrophages and neutrophils.

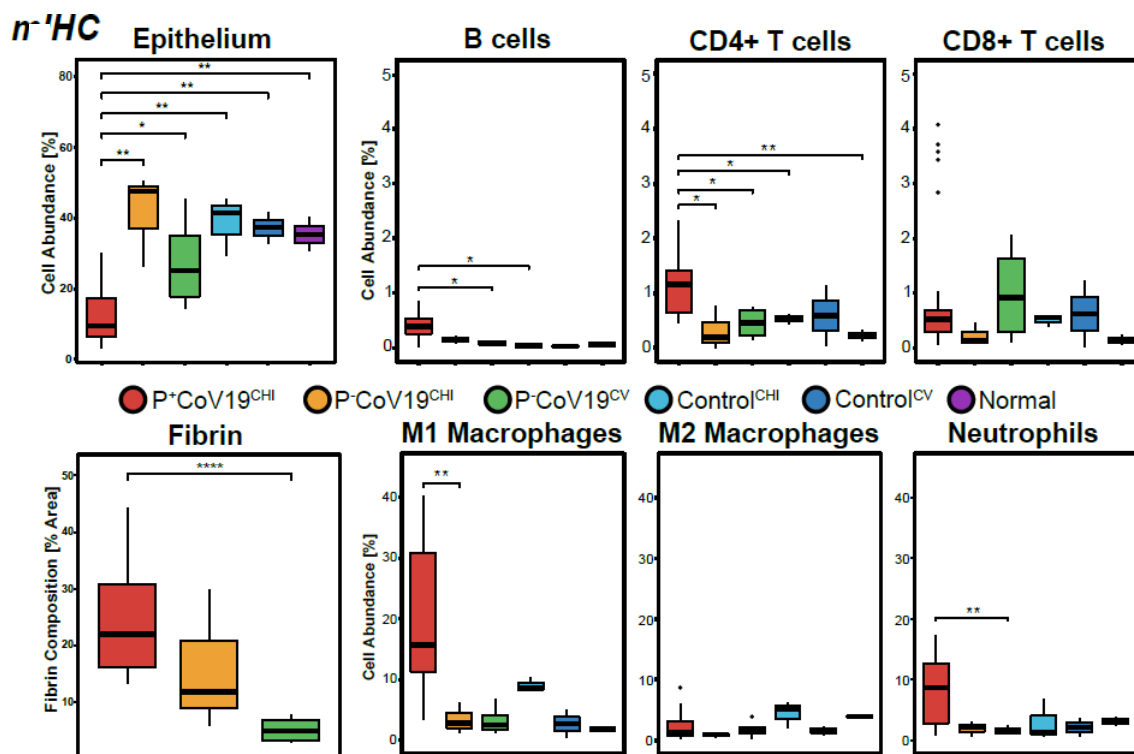


Figure 5-23. Abundances of the key cell and immune subtypes based on COMET mIHC images. Key: CHI=Chronic histiocytic intervillitis; CV=chronic villitis. P+CoV19 = Covid-19+ placenta; P-Cov19=Covid-19 negative placenta. *= Statistically significant difference with a P-value of <0.05; **= $p < 0.01$; ***= $p < 0.001$; ****= $p < 0.0001$.

5.2.3. Detailed quantitative analysis of T-cells

A more detailed phenotypic analysis of CD4+ and CD8+ T-cells was performed to investigate differences in immune cell status across disease states (Figure 5-24). CD4+ T-cells in P+CoV19^{CHI} placentas had a distinct phenotype compared to other placenta samples; increased co-expression of CD45RO, Ki-67, CTLA4 and PD1, suggesting antigen-experienced T-cells were present in P+CoV19^{CHI}.

CD8⁺ T-cells showed a similar increase in CD45RO, CTLA-4 and Ki-67 expression in P+CoV19^{CHI}. The increased expression of granzyme-B in these T-cells suggested they were cytotoxic effector T-cells. In normal placentas, CD4⁺ and CD8⁺ T-cells were low in number and enriched in CD103, suggesting they were resident memory T-cells (Schenkel and Masopust, 2014) .

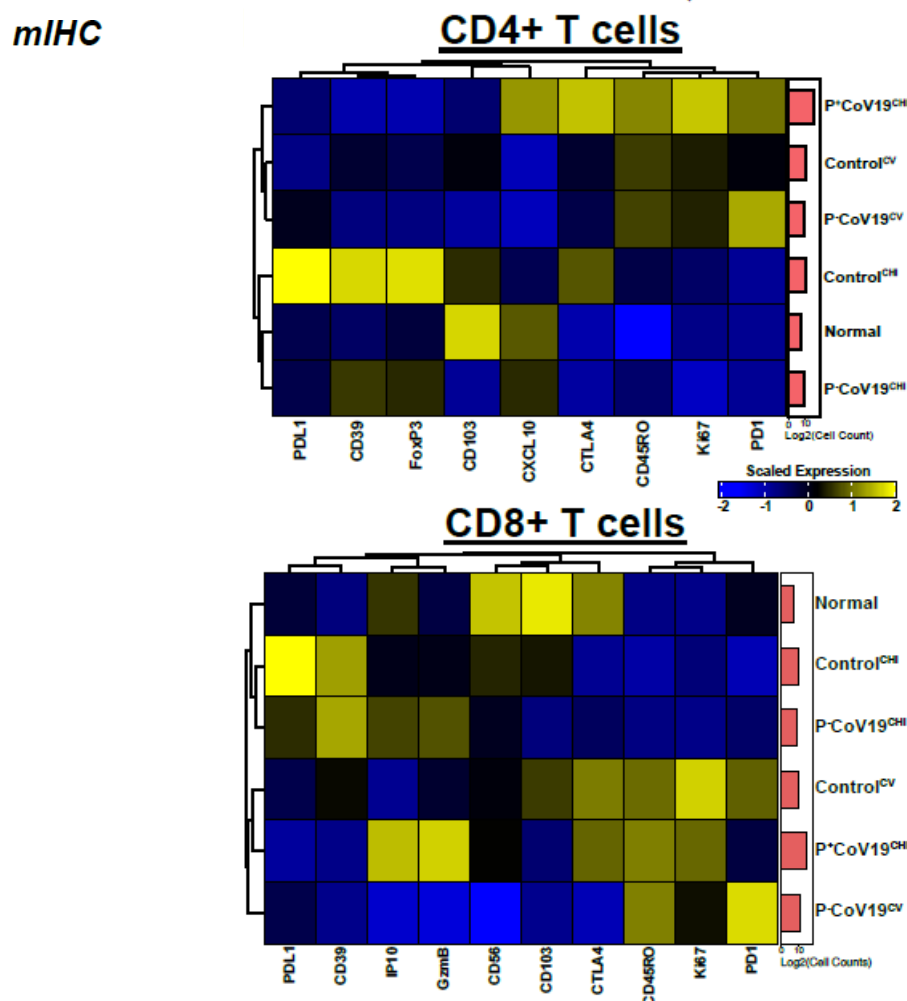


Figure 5-24. Co-expression of immune markers in CD4⁺ and CD8⁺ placental T-cells based on COMET mIHC images. Key: CHI=Chronic histiocytic intervillitis; CV=chronic villitis. P+CoV19 = Covid-19+ placenta; P-CoV19=Covid-19 negative placenta.

5.2.4. Detailed quantitative analysis of macrophages

Finally, given that macrophages were the most abundant immune cell in COVID-19 placentitis, a more detailed phenotypic analysis was undertaken, utilising COMET mIHC data and Nanostring GeoMx DSP data. Plotting the M1:M2 ratio, based on mIHC images, across the placental cohorts showed that M1 macrophages were proportionally increased in P+CoV19^{CHI}, even compared to P+CoV19^{CHI} placentas

(Figure 5-25). The median M1:M2 ratio for P+CoV19^{CHI} placentas was 14.8 (range 0.86-81.2), whilst normal controls showed a predominance of M2 polarised macrophages (median M1:M2 ratio 0.48, range 0.47-0.49); these cells are likely resident M2 polarised Hofbauer cells.

mIHC

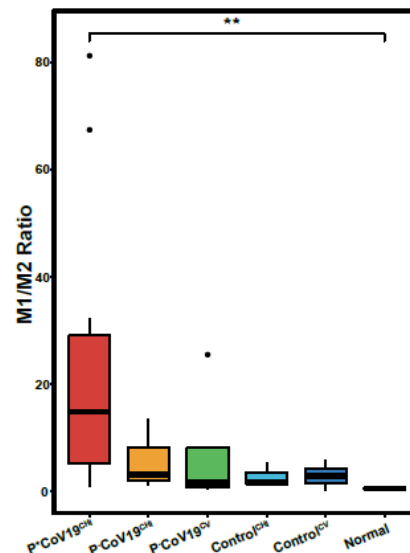


Figure 5-25. M1:M2 macrophage ratio based on COMET mIHC imaging. Key: CHI=Chronic histiocytic intervillitis; CV=chronic villitis. P+Cov19 = Covid-19+ placenta; P-Cov19=Covid-19 negative placenta. *= Statistically significant difference with a P-value of <0.05; **= $p<0.01$; ***= $p<0.001$; ****= $p<0.0001$.

On inspection of the mIHC images, stromal macrophages were invariably M2 polarised (CD163+), compared to more mixed populations of M1 and M2 polarised macrophages in the intervillous space (Figure 5-26). To test whether the stromal M2 macrophages were indeed Hoffbauer cells, and not maternal macrophages infiltrating the fetal stroma, DNA FISH for X and Y chromosomes was conducted in cases in which the fetus was male. As expected, the stromal M2 macrophages were fetal derived XY Hoffbauer cells and the intervillous macrophages were maternal derived XX cells indicating a lack of cell mixing in the diseased placentas (Figure 1-27)

mIHC

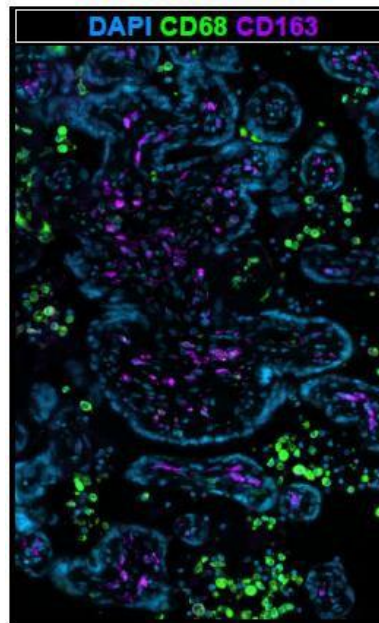


Figure 5-26. COMET mIHC image showing M1 polarised (CD68+) macrophages in the intervillous space and M2 macrophages (CD163+) in the villous stroma.

DNA FISH

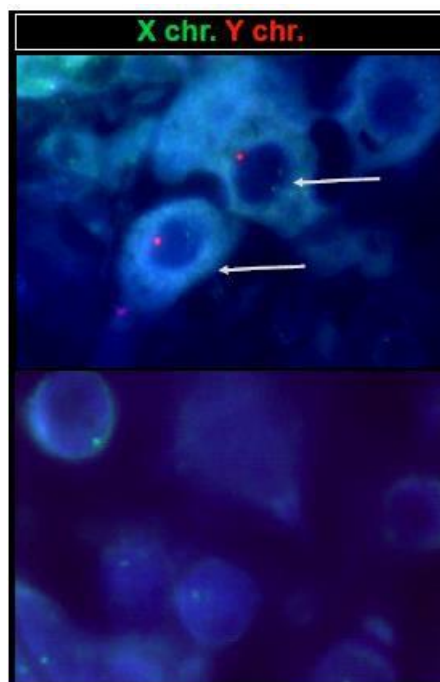


Figure 5-27. Upper panel: Stromal macrophages showing an XY complement of chromosomes. Lower panel: Intervillous macrophages showing an XY complement of chromosomes.

Next, mIHC images were interrogated to assess the co-expression of immune markers on M1 and M2 macrophages in COVID-19 placentas and controls (Figure 5-28).

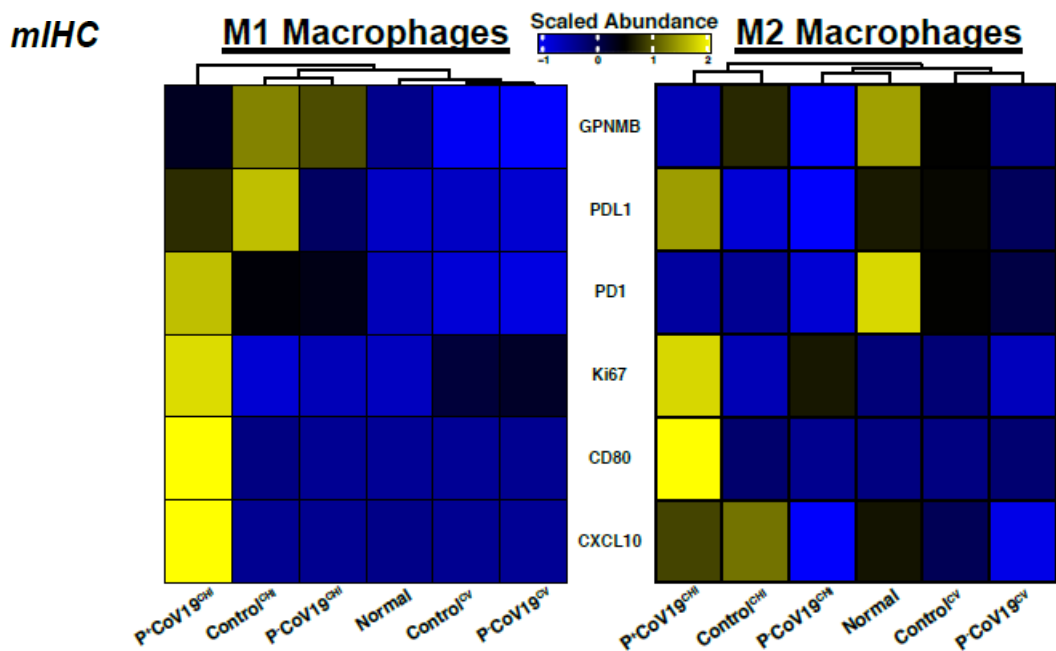


Figure 5-28. Marker co-expression on M1 and M2 macrophages in diseased and control placentas based on mIHC images. Key: CHI=Chronic histiocytic intervillitis; CV=chronic villitis. P+CoV19 = Covid-19+ placenta; P-CoV19=Covid-19 negative placenta.

M1 macrophages from all disease placentas with CHI morphology showed increased expression of GPNMB, PDL1 and PD1. In addition, M1 macrophages from P+CoV19^{CHI} cases uniquely expressed CD80, Ki-67 and chemokine CXCL10. PDL1, CD80 and Ki-67 were also upregulated by M2 macrophages from P+CoV19^{CHI} cases. Therefore, both M1 and M2 macrophages in P+CoV19^{CHI} placentas show a distinct phenotype compared to other diseased and normal placentas.

CXCL10 is an important chemoattractant for macrophages and neutrophils, and was noted to be enriched on M1 and M2 macrophages by mIHC (Petrovic-Djergovic et al., 2015). To further assess the expression of CXCL10 along with other important cytokines known to be released by macrophages, RNAscope for CXCL10, IL6 and IL8 was performed in conjunction with CD68 immunohistochemistry (Figure 5-29).

RNAScope

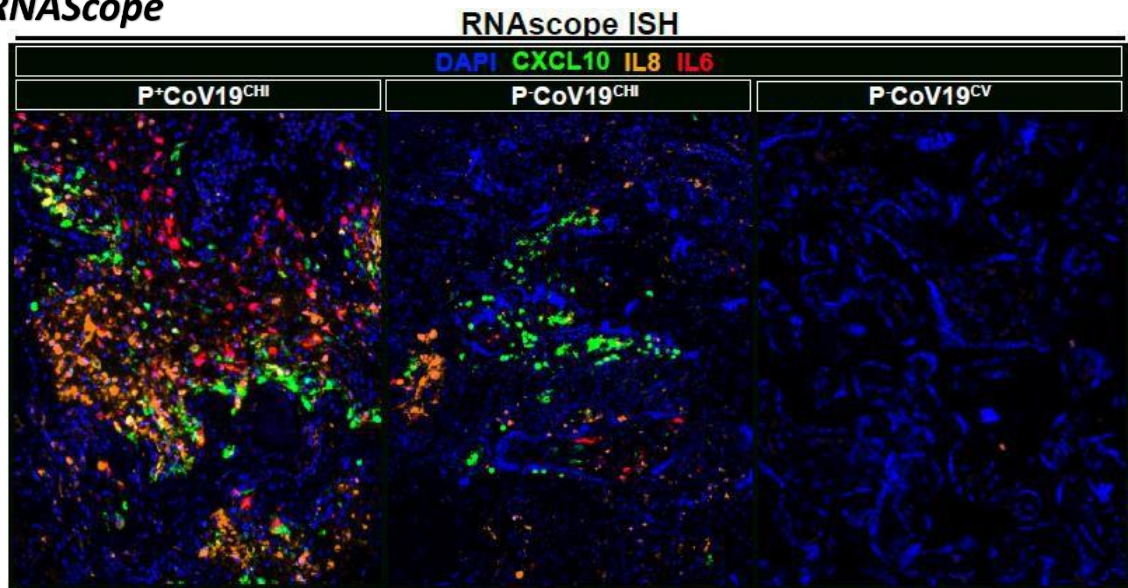


Figure 5-29. RNAscope showing highly upregulated expression of CXCL10, IL6 and IL8 in P+COV19^{CHI} compared to controls.

All three cytokines showed marked upregulation in the P+Cov19^{CHI} placentas compared to virus negative COVID-19 associated placentitis. Quantification of this expression in the context of CD68 IHC showed that macrophages were the main sources of CXCL10 and IL8.

RNAScope

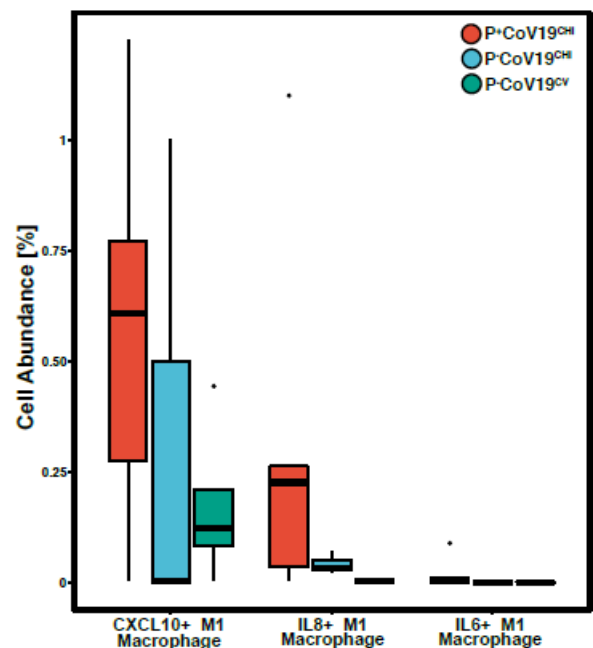


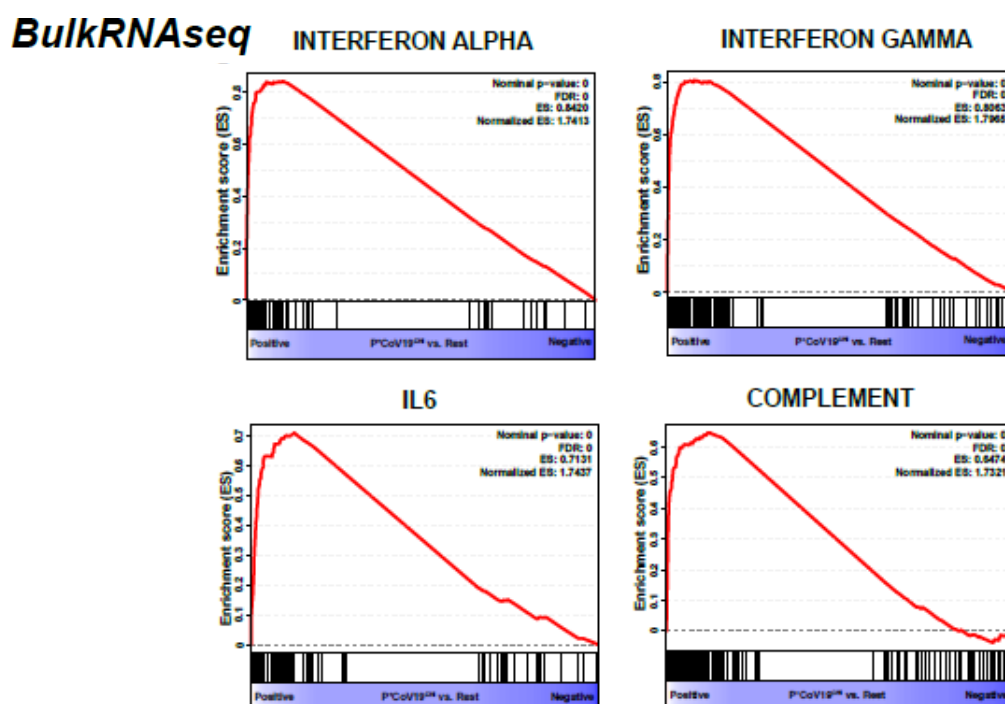
Figure 5-30. Bar and whisker plot RNAscope for CXCL10 combined with CD68 IHC shows that CXCL10 and IL8 are abundantly expressed in macrophages. Key: CHI=Chronic histiocytic intervillitis; CV=chronic villitis. P+Cov19 = Covid-19+ placenta; P-Cov19=Covid-19 negative placenta.

5.4. Inflammatory pathways

To further characterise the inflammatory mediators and pathways that were driving recruitment of immune cells in COVID-19 placentitis, bulk and spatially resolved transcriptomic data were analysed.

5.4.1. Gene set enrichment analysis and interferon stimulated genes.

A gene set enrichment analysis of Quantseq bulk sequencing data, comparing P+Cov19^{CHI} cases with all other groups, revealed upregulation of IL-6/JAK-STAT signaling in keeping with the upregulation of IL-6 observed by RNAscope in macrophages (Figure 5-31). Allograft rejection pathways were also upregulated in P+Cov19^{CHI} cases suggesting a loss of maternal immune tolerance to the placenta (Sun et al., 2021). Genes associated with complement activation, coagulation and hypoxia related pathways were also upregulated. The former has already been reported to play a role in COVID-19 placentitis (Watkins et al., 2021). The latter two pathways are consistent with the extensive malperfusion caused by extensive fibrin deposition. As interferon alpha and gamma responses exert antiviral activity, and were upregulated on gene set enrichment analysis, expression of interferon stimulated genes (ISGs) was assessed (Samuel, 2001). ISGs were markedly enriched in P+Cov19^{CHI} placentas compared to all other groups (Figure 5-32). Notably, a subset of 37 ISGs shown experimentally to act as viral restriction factors and limit viral replication (Martin-Sancho et al., 2021) was also markedly upregulated in P+Cov19^{CHI} placentas (Figure 5-33).



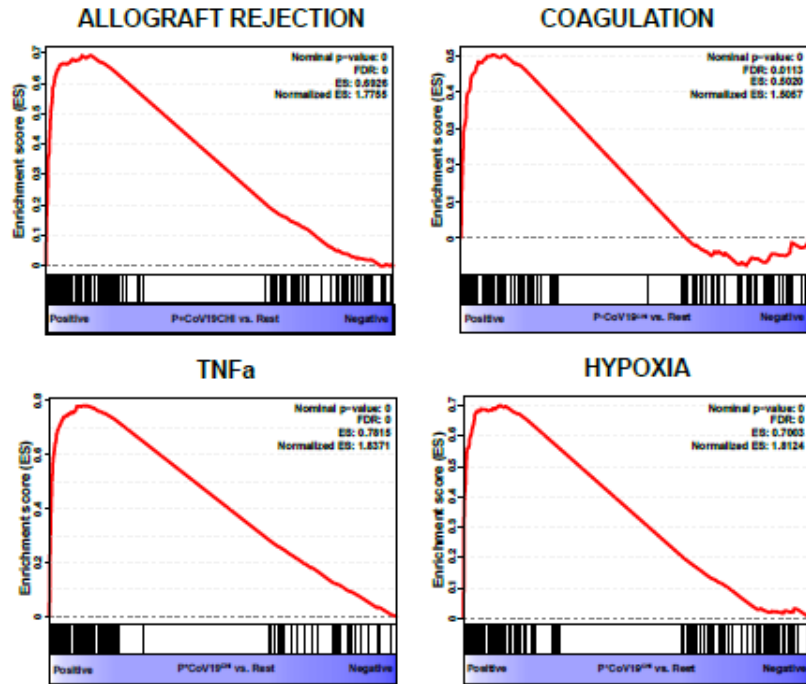


Figure 5-31. Gene set enrichment analysis showing pathways upregulated in P+COV19CHI placentas compared to all other groups.

BulkRNAseq

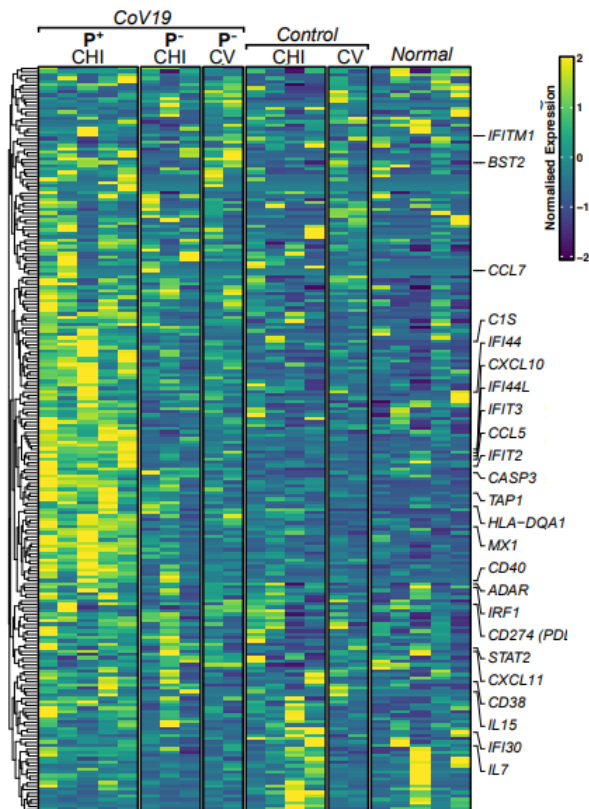


Figure 5-32. Heatmap demonstrating ISGs showing enriched expression in P+Cov19 placentas compared to control placentas by Quantseq bulk RNAsequencing. .Key: CHI=Chronic histiocytic intervillitis; CV=chronic villitis.P+Cov19 = Covid-19+ placenta; P-Cov19=Covid-19 negative placenta.

BulkRNAseq

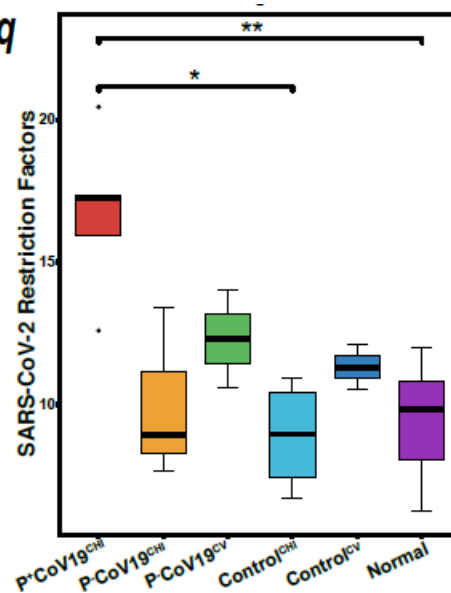


Figure 5-33. Bar and whisker plot showing comparing normalized gene expression of SARS-CoV-2 restriction factors by Quantseq bulk sequencing in COVID-19 positive placentas and controls. Key: CHI=Chronic histiocytic intervillitis; CV=chronic villitis. P+CoV19 = Covid-19+ placenta; P-CoV19=Covid-19 negative placenta. * = Statistically significant difference with a P-value of <0.05; **= $p < 0.01$; ***= $p < 0.001$; ****= $p < 0.0001$.

5.4.2. Spatially resolved expression of interferon genes

Given the known anti-viral properties of type I and II interferons, their expression was assessed spatially using the GeoMx DSP data (figure 5-34). Intriguingly, whilst bulk sequencing demonstrated strong upregulation of interferon genes, spatial DSP showed this upregulation occurred only in virus-low areas of the placenta; virus high areas showed minimal interferon gene expression. This result implies that localised interferon blunting is present in SARS-CoV-2 positive regions of the placenta, which could serve as a novel immune evasive mechanism.

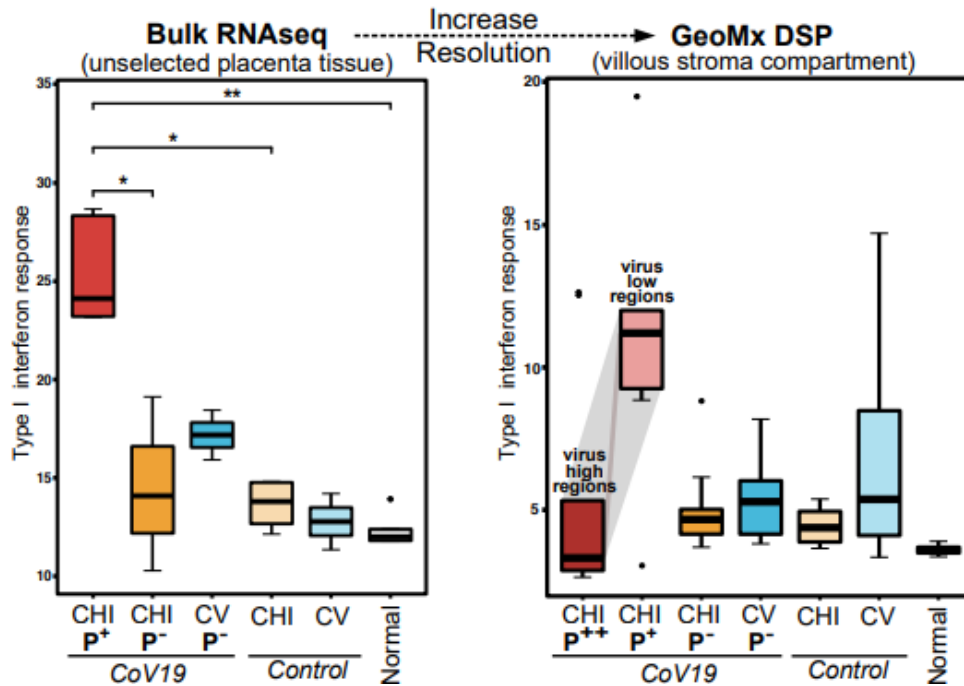


Figure 5-34. Comparison of bulk sequencing expression of interferon genes compared to spatially resolved expression by GeoMX, showing pan-tissue upregulation of interferons on bulk sequencing, but interferon blunting in virus high regions from the same placentas. Key: CHI=Chronic histiocytic intervillitis; CV=chronic villitis. P+Cov19 = Covid-19+ placenta; P-Cov19=Covid-19 negative placenta. *= Statistically significant difference with a P-value of <0.05; **= $p < 0.01$; ***= $p < 0.001$; ****= $p < 0.0001$.

5.5. SARS-CoV-2 virus niche in COVID-19 placentitis.

To explore whether there were additional mechanisms of immune escape and evasion which could help the SARS-CoV-2 virus replicate in the normally interferon-rich anti-viral microenvironment of the placenta, GeoMx DSP and COMET mIHC data were analysed to explore the immune cells and phenotype of the SARS-CoV-2 infected cell niche.

5.5.1. SARS-CoV-2 virus niche analysis by COMET mIHC

The abundance of each immune subtype was calculated according to its distance from the infected SARS-CoV-2+ trophoblast (Figure 5-35). Compared to non-infected trophoblast from the same placenta, the virus infected trophoblast was enriched for PDL1+ M1 macrophages, neutrophils and CD4+PD1+ T-cells, and depleted of CD8+ T-cells and CD20+ B-cells.

mIHC

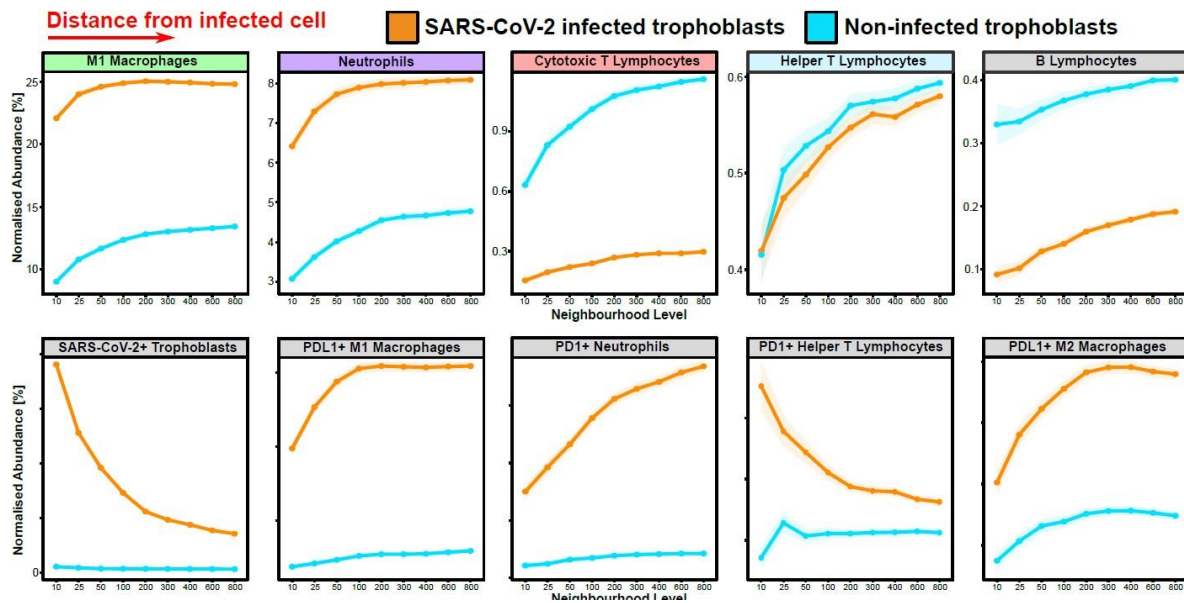


Figure 5-35. Assessment of the viral immune niche by COMET mIHC. Immune cell abundances in the immediate virus positive and negative microenvironment of COVID-19 placentitis trophoblast cells based on multiplex immunohistochemistry. Normalised abundance is plotted against number of cells assessed in expanding concentric rings away from the cell of interest.

These findings were confirmed by visual inspection of the P+Cov19^{CHI} images (figure 5-36). Overall, the enrichment of immune checkpoints and exclusion of cytotoxic T-cells from virus-infected cell regions are consistent with an immune evasive viral niche.

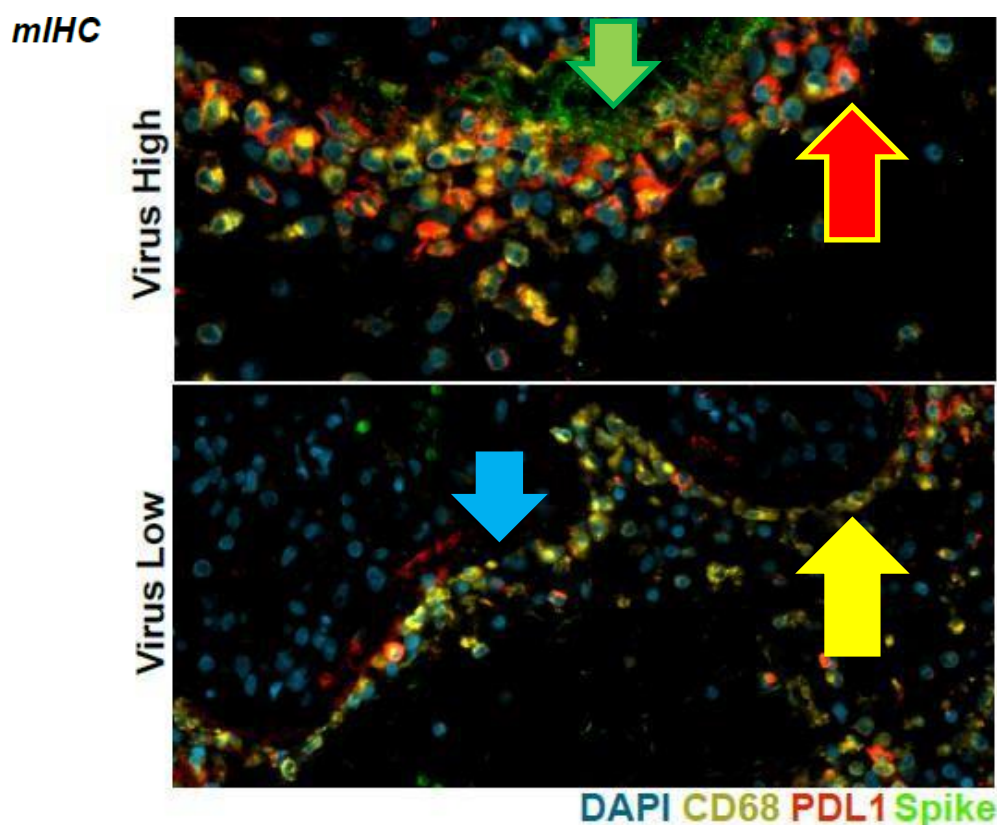


Figure 5-36. COMET miHC image showing enrichment of PDL1+ macrophages (red and yellow highlighted by red arrow) in the vicinity of SARS-CoV-2 infected trophoblast (green, highlighted by green arrow) (top panel). Fewer macrophages express PDL1 (yellow arrow) adjacent to the virus low trophoblast (blue arrow) (bottom panel).

5.5.2. SARS-CoV-2 virus niche analysis by GeoMx DSP

Finally, GeoMx DSP data were analysed, comparing gene expression in virus high to virus low areas from the same placenta (Figure 5-37). Gene ontology analysis of differentially expressed genes demonstrated upregulation of MHC class I and II antigen presentation genes in virus-high regions, as well as increased VSIG8, which binds to the potential immune checkpoint molecule VISTA; CCR1, a chemotactic molecule for macrophages, granulocytes and T-lymphocytes was also increased. Collectively, upregulation of these genes could lead to sensitisation of the non-self placenta to the maternal immune system.

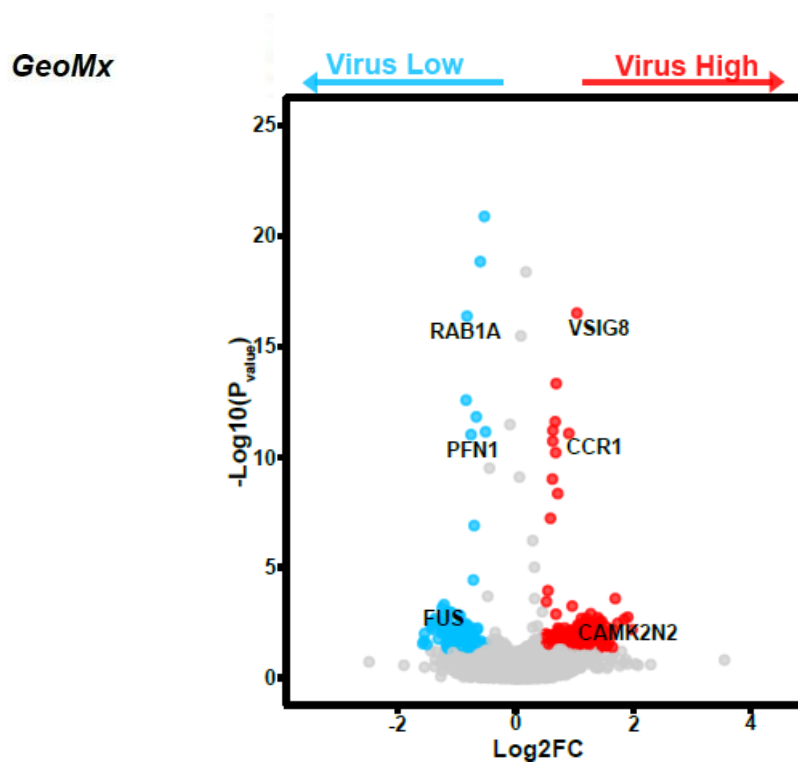


Figure 5-37. Differential gene expression in virus high vs virus low region of the same placenta by GeoMx DSP by whole transcriptome assay. Genes upregulated at a statistically significant level ($FDR < 0.05$) after compensation for multiple comparisons are shown in red and blue.

Discussion and conclusions

COVID-19 placentitis has been associated with poor obstetric outcome. However, the role SARS-CoV-2 plays in mediating the pathological changes is controversial. Using a robust multi-modal, cross platform approach, my investigation reveals inflammatory mediators and competing anti-viral and immune escape mechanisms are present in SARS-CoV-2 infected placentas (Figure 5-38). These findings confirm a central role for the SARS-CoV-2 virus in driving the devastating pathogenic consequences of COVID-19 placentitis.

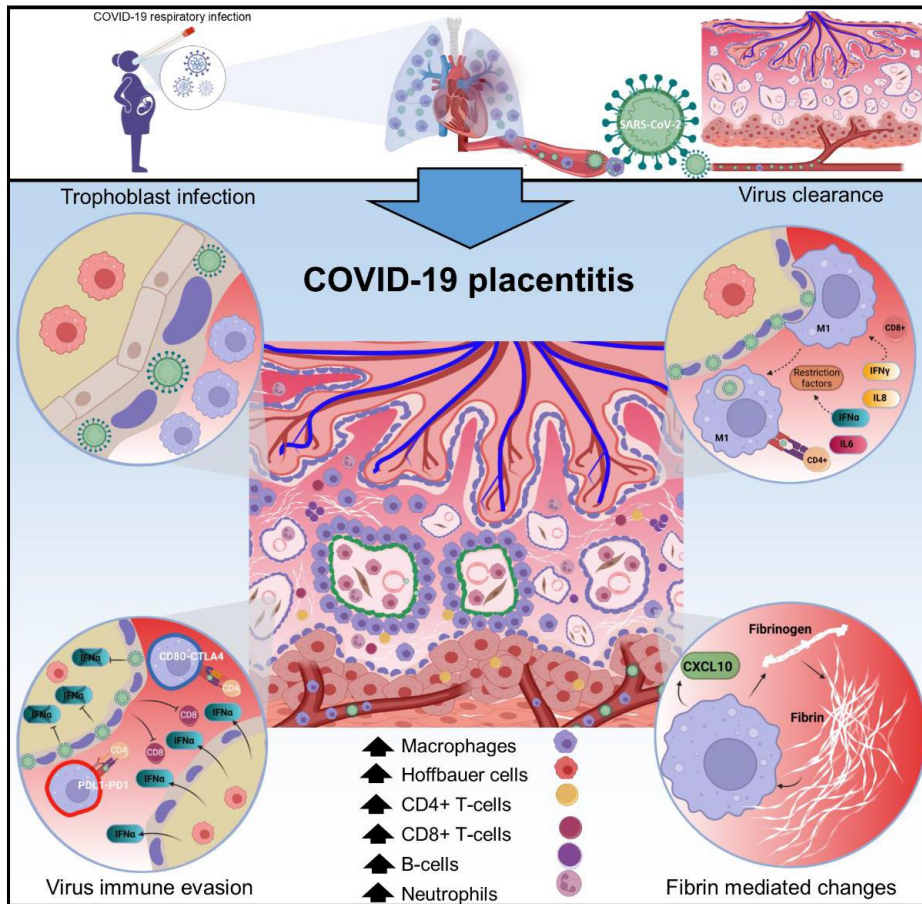


Figure 5-38. Summary of the main findings in COVID-19 placentitis

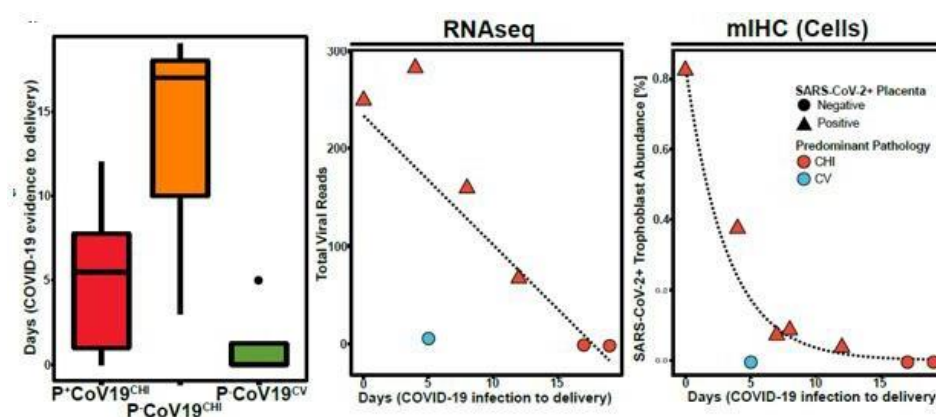
Two predominant placental pathologies were observed in Cov19 placentas: CHI with MPVFD or chronic villitis. The most serious complications, such as intrauterine death, all occurred in the context of placental CHI and MPVFD. Some pathological features set Cov19 CHI/MPVFD apart from pre-pandemic CHI cases. These include circumferential trophoblast necrosis and macrophages tightly abutting the trophoblast layer. CHI, MPVFD and TN are the hallmarks of COVID-19 placentitis in the previously published literature and are the predominant pathology associated with adverse outcome in maternal SARS-CoV-2 infection(Schwartz et al., 2022a).

Adopting a multi-modal, cross validated approach, SARS-CoV-2 was robustly detected in a subset (6/13 46%) of placentas from SARS-CoV-2 mothers with obstetric complications. This result is consistent

with the variable detection rates reported in the literature (Argueta et al., 2022; Linehan et al., 2021; Schwartz et al., 2022a). The presence of virus in the placenta was always associated with CHI/MPVFD pathology, and no virus was detected in the CoV19^{CV} cases. It is unclear whether cases that show chronic villitis pathology are incidental pathologies unrelated to the maternal SARS-CoV-2 infection, or, whether SARS-CoV-2 is mediating the pathological changes via indirect mechanisms, such as systemic cytokine release.

It has been unclear why only a subset of placentas with CHI/MPVFD pathology from SARS-CoV-2 infected mothers show evidence of placental infection. However, upon analysis of the viral load determined by bulk sequencing and mIHC, in association with length of illness, a reduction in viral load is seen over time. Furthermore, those Cov19^{CHI} cases which are virus negative show an increased duration of illness. This implies that virus is cleared over time and that virus negative cases may have previously been positive and cleared the virus. This is analogous to what is seen in COVID-19 lung.

Figure 5-39. Analysis of the temporal relationship between length of symptomatic illness in COVID-19 placentitis and viral load.



Left panel shows that symptomatic illness is increased in virus negative placentas compared to virus positive placentas. Middle and right panel show a trend towards decreasing virus load by gene expression and mIHC with increasing length of symptomatic illness. Key: CHI=Chronic histiocytic intervillitis; CV=chronic villitis. P+CoV19 = Covid-19+ placenta; P-CoV19=Covid-19 negative placenta.

Whilst the trophoblast was predominantly found to harbour SARS-CoV-2, mIHC showed some punctate viral staining suggestive of phagocytosis. This was further evidenced by the absence of macrophage staining by ORF1ab on RNAscope, indicating a lack of replicative infection and favouring phagocytosis. Macrophages phagocytosing virus at the maternal interface could also explain the unique distribution of macrophages in COVID-19 placentitis compared to cases of non- viral CHI.

Analysis of the inflammatory mediators and viral immune niche reveals competing anti-viral responses with counteracting pro-viral immune evasive mechanisms. Both of these processes contribute to the observed placental pathology. The antiviral responses included upregulation of anti-viral type I interferons and interferon-stimulated genes (ISG) and restriction factors (Martin-Sancho et al., 2021). Despite these anti-viral activities, type I interferons are known to cause placental damage in the context of Zika placental infection (Yockey et al., 2018). Secondly, classical MHC class-I and II were upregulated in the trophoblast layer, which normally lacks these molecules. This could represent a pragmatic but problematic adaption to eliminate virus, especially with the observed upregulation of allograft rejection-type response. These features suggest a loss of maternal immune tolerance to the fetal placenta. Such allograft rejection responses have been suggested to play a role in non-virus associated CHI, as there are similarities with transplant-type rejection (Brady et al., 2021). Lastly, phagocytic M1 macrophages were enriched adjacent to the virus infected trophoblast. These macrophages also showed upregulation of CXCL10, a chemoattractant for neutrophils and macrophages. Thus macrophage CXCL10 could form positive feedback loop for further macrophage recruitment (Zhang et al., 2021; Zhang et al., 1995). CXCL10 has also been suggested as a potential druggable target in the context of other alphaviruses, and should be explored as a potential target in SARS-CoV-2 infection (Lin et al., 2020). Statins are a widely available class of drug that are known to target CXCL10 release and are safe in the later stages of pregnancy (Mauricio and Khera, 2022).

The observed immune evasive mechanisms were present in the immediate viral immune niche, and included increased PDL1+ M1 macrophages and PD1+ T-cells, and exclusion of CD8+ T-cells. There was also apparent interferon blunting in virus high regions, in contrast to the global upregulation of interferons in the placenta. The mechanism of interferon blunting is currently unclear and this remains a priority for future work.

Despite the devastating clinical consequences of COVID-19 placentitis, only a minority of SARS-CoV-2 mothers develop inflammation of the placenta. Regardless, most of the severe complications of

maternal SARS-CoV-2 infection are concentrated in mothers who develop COVID-19 placentitis (Thomas et al., 2021). Interestingly, the severity of the respiratory disease does not correlate with the severity of the obstetric complication, with most stillbirths in mild or asymptomatic disease. One might expect a greater rate of placental infection, as most placentas express ACE2 (Hikmet et al., 2020). This investigation reveals how the distribution of the ACE2 expression on the maternal surface exposed to maternal blood, could provide a mechanistic explanation as to why a minority of mothers are infected. Non-virus associated CHI/MPVFD was known to occur at low incidence in pregnancy prior to the pandemic, and is associated with a risk of recurrence in subsequent pregnancies (Brady et al., 2021). Mothers in our cohort had no prior history of CHI, further arguing against a passive role for the virus in placentas destined to develop CHI regardless of maternal COVID-19 status. Akin to non-virus associated CHI, COVID-19 placentitis showed evidence of loss of maternal tolerance to placenta. This provides a mechanistic basis for recurrence in subsequent pregnancies, necessitating close obstetric follow-up and monitoring to enable appropriate counselling of patients and record the true risk of recurrence.

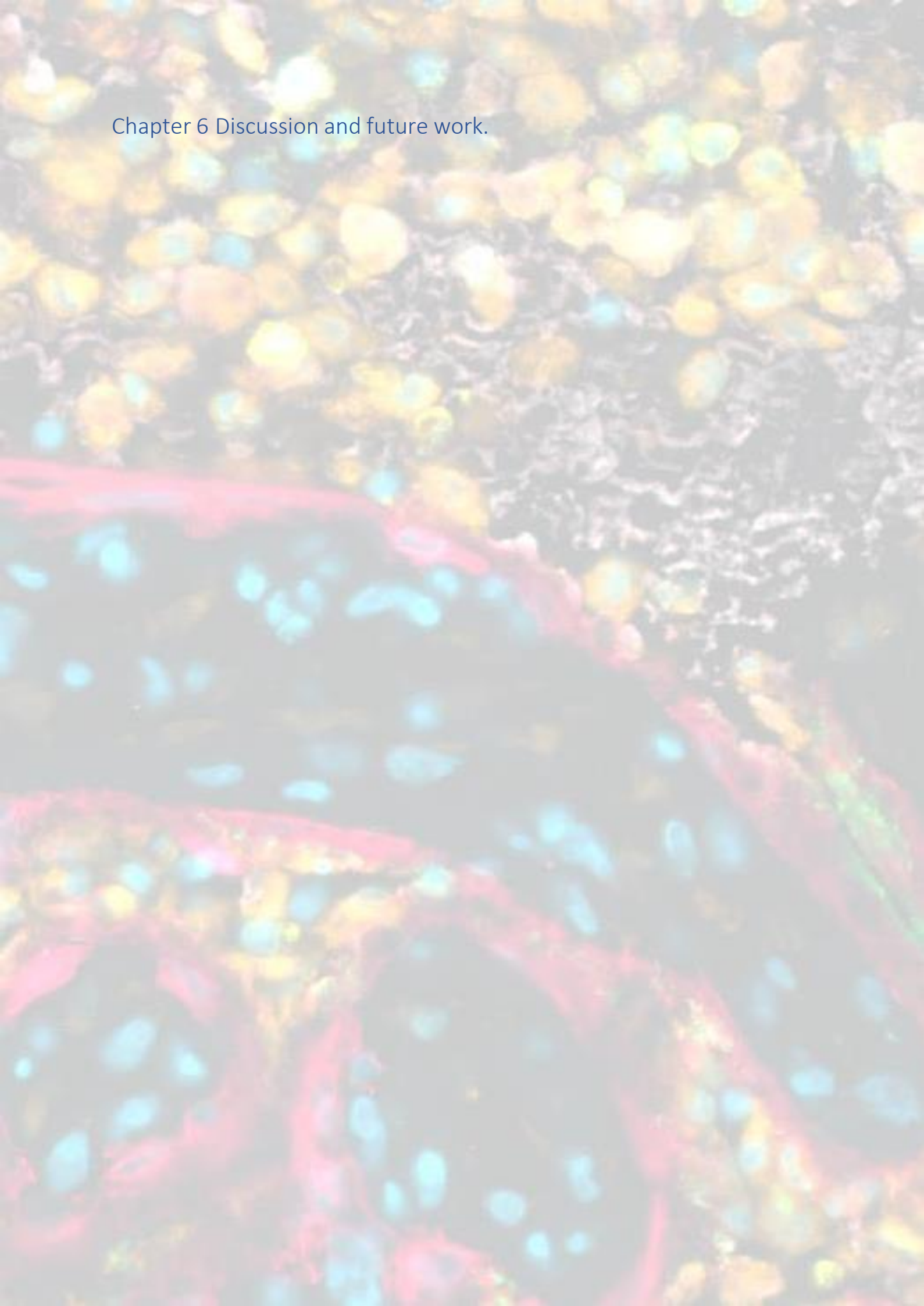
Conclusions:

1. SARS-CoV-2 infects the placenta and is associated with severe inflammation, which is immunologically distinct from other pre-pandemic placental inflammatory conditions.
2. Competing anti-viral and immune evasive responses are observed in SARS-CoV-2 infected placentas. Anti-viral responses include the tissue-wide up-regulation of type I interferon response genes, expression of restriction factors and infiltration of phagocytic macrophages. Immune evasive mechanisms include local virus-associated interferon blunting, over-expression of immune checkpoints, and CD4+ and CD8+ T-cell depletion from the microenvironment of virus-infected trophoblasts.

3. Absence of the virus in the placentas of mothers testing positive for SARS-CoV-2 with associated pathologies, likely represents temporal advancement of the disease following virus clearance by the immune system.

4. ACE2 re-localisation to the maternal circulatory side of the trophoblast layer in 12/13 cases of mothers with COVID-19 experiencing obstetric complications may explain why some women are more susceptible to direct placental infection by SARS-CoV-2.

Chapter 6 Discussion and future work.



6.1. Comparison of the tissue immune response to SARS-CoV-2 in lung and placenta

The immune response to SARS-CoV-2 infection in lung and placenta showed significant overlap. In both settings, patients who were sampled early in the disease course showed evidence of active viral infection, whereas in patients sampled after a more prolonged course, there was no detectable virus.

Whilst we can infer that there is a temporal progression from active viral infection to viral clearance, the findings also suggest that there are two disease phenotypes. Patients who progress quickly due to more aggressive disease, leading to either death or miscarriage, and those whose course is tempered allowing for viral clearance before death or miscarriage. It is unclear what factors influence the aggressiveness of the disease course. In respiratory COVID-19 infection, the three patients who died early in the disease course were from care homes and suffered dementia. It is likely they were frail and may have succumbed to the disease for these reasons. It is less clear why some cases of COVID-19 placentitis progress so quickly.

Both COVID-19 lung and placenta showed florid inflammation with stark structural changes in the underlying tissue. Competing anti-viral and immune evasive mechanisms were influential in driving the disease course in both settings. These mechanisms were much the same in both tissues. Anti-viral mechanisms were mediated through strong interferon responses in both tissues along with influxes of immune cells which typically aid the clearance of virus. Macrophages were particularly prominent in both diseases and there was strong evidence of phagocytosis in COVID-19 placentitis. It is less clear whether there is active infection of macrophages in the lung but some authors have suggested that the inflammasome of infected macrophages drives the pulmonary pathology of COVID-19 (Sefik et al., 2022). Regardless of whether macrophages are infected in COVID-19 lung or not, it is clear they play a pivotal role in driving the immune response in SARS-CoV-2 infection (Kosyreva et al., 2021). I detected upregulation of CXCL10 in the macrophages infiltrating COVID-19 placentitis which likely leads to further recruitment of macrophages and other inflammatory cells. CXCL10 measured in

blood has already been shown to predict outcome in COVID-19 respiratory disease (Lorè et al., 2021). Here I postulated that CXCL10 could be a therapeutic target in COVID-19 placentitis as has already been suggested in COVID-19 lung disease (Julian et al., 2021). Statins, a commonly prescribed drug for high cholesterol can selectively inhibit CXCL10. This emphasises the complexity of the immune changes in SARS-CoV-2 tissue infection, as the responses aimed at eliminating the virus often lead to harm in the host tissue. It also emphasises the importance of understanding these changes with a view to developing novel treatment strategies.

The immune evasive strategies employed by the virus in lung and placenta were numerous, and included expression of immune checkpoint ligands and exclusion of cytotoxic T-cells from the immediate viral niche. It was unclear how some evasive mechanism, such as interferon blunting, was mediated. Regardless of the biological basis of the observed changes in lung and placenta, it is likely that both the anti-viral mechanisms designed to control the virus, and pro-virus mechanisms favouring the persistence the virus, contribute to the overall pathological changes.

6.2. Role of the autopsy, archival specimens and spatial profiling.

This study emphasises the role autopsy and archival pathology specimens can play in understanding disease. During the pandemic, the autopsy rate declined significantly (Bhatt et al., 2022). This was largely due to staffing shortages and unfounded concerns over safety. Consequently, there has been little COVID-19 tissue available for research. This is further cofounded by the lack of COVID-19 biopsy tissue available.

With the growth of spatial profiling platform such as COMET, CODEX and GeoMx, the potential for such post-mortem tissue and archival surgical tissue to yield novel biological insights into disease has never been greater. As I demonstrate here, these techniques work in even the most degraded post-mortem lung tissue, which traditionally would have been regarded as inappropriate for molecular analyses. Here, these tissues have not only yielded novel biological insight, but have led to potentially clinically relevant discoveries such as the prognostic value of collagen VI in respiratory COVID-19.

6.3. Limitations of the study

One of the major limitations of the study is the low case numbers used in the spatial profiling component. This again, largely relates to the unavailability of the tissue, or, in the case of COVID-19 placentitis, the rarity of the disease. Regardless, through adopting a multi-modal, cross-platform approach, I was able to validate my most significant findings. Furthermore, findings such as the upregulation of collagen VI, held true even in a larger clinical cohort.

Another limitation of this study is the lack of broader control tissues. It would be interesting to compare COVID-19 lung disease with a wider range of viral lung diseases. Similarly, there are a number of other causes of virus driven inflammation in the placenta, such as Zika and CMV (Rabelo et al., 2020). Comparing COVID-19 placentitis with these placentitides would be informative.

Lastly, as most of the work was conducted on fixed tissue samples, the study lacks true mechanistic insight into phenomena observed in the tissue. Future work should include validation of the observations in model systems.

6.4. Future work

There are a number of areas in which I would like to continue work into COVID-19 associated infections.

1. Understanding of the mechanisms of interferon blunting: Understanding exactly how the virus blunts the interferon response in the immediate microenvironment could lead to potential therapeutic approaches. Understanding these interactions will require mechanistic work on cell lines and animal models in collaboration with others.
2. Explore the role of CXCL10 as therapeutic target in COVID-19 placentitis: Whilst many new therapeutic avenues are being explored in COVID-19 respiratory disease, there is little work in COVID-19 placentitis. CXCL10 represents a potential target in this settings and requires further validation in tissue and models.

3. Understanding the risk of recurrence in COVID-19 placentitis: Non-viral CHI is a recurrent disease, but it is currently unclear whether COVID-19 CHI is associated with disease recurrence. This is a cause of anxiety for many parents and could be addressed with simple follow-up studies.

4. Role of collagen VI in predicting long term fibrosis or long COVID-19: this study demonstrated that serum collagen VI levels predict outcome in acutely hospitalised COVID-19 patients. I would like to extend this work to understand whether the assay can predict more progressive long term fibrosis or long COVID-19 symptoms. Cohorts with long term follow-up are available and could be used for this purpose.

Chapter 7 References

- Ackermann, M., Kamp, J.C., Werlein, C., Walsh, C.L., Stark, H., Prade, V., Surabattula, R., Wagner, W.L., Disney, C., Bodey, A.J., *et al.* (2022). The fatal trajectory of pulmonary COVID- 19 is driven by lobular ischemia and fibrotic remodelling. *EBioMedicine* 85, 104296.
- Ahmed SF, Quadeer AA, McKay MR. Preliminary Identification of Potential Vaccine Targets for the COVID-19 Coronavirus (SARS-CoV-2) Based on SARS-CoV Immunological Studies. *Viruses*. 2020;12(3)
- Allotey, J., Stallings, E., Bonet, M., Yap, M., Chatterjee, S., Kew, T., Debenham, L., Llavall, A.C., Dixit, A., Zhou, D., *et al.* (2020). Clinical manifestations, risk factors, and maternal and perinatal outcomes of coronavirus disease 2019 in pregnancy: living systematic review and meta-analysis. *Bmj* 370, m3320.
- Anders, S., Pyl, P.T., and Huber, W. (2015). HTSeq--a Python framework to work with high-throughput sequencing data. *Bioinformatics* 31, 166-169.
- Andrews, S. (2010). FastQC: A Quality Control Tool for High Throughput Sequence Data.
- Argueta, L.B., Lacko, L.A., Bram, Y., Tada, T., Carrau, L., Rendeiro, A.F., Zhang, T., Uhl, S., Lubor, B.C., Chandar, V., *et al.* (2022). Inflammatory responses in the placenta upon SARS- CoV-2 infection late in pregnancy. *iScience* 25, 104223.
- Azinheira Nobrega Cruz, N., Stoll, D., Casarini, D.E., and Bertagnolli, M. (2021). Role of ACE2 in pregnancy and potential implications for COVID-19 susceptibility. *Clin Sci (Lond)* 135, 1805-1824.
- Babal, P., Krivosikova, L., Sarvaicova, L., Deckov, I., Szemes, T., Sedlackova, T., Palkovic, M., Kalinakova, A., and Janega, P. (2021). Intrauterine Fetal Demise After Uncomplicated COVID- 19: What Can We Learn from the Case? *Viruses* 13.
- Babiker, A., Immergluck, K., Stampfer, S.D., Rao, A., Bassit, L., Su, M., Nguyen, V., Stittleburg, V., Ingersoll, J.M., Bradley, H.L., *et al.* (2021). Single-Amplicon Multiplex Real-Time Reverse Transcription-PCR with Tiled Probes To Detect SARS-CoV-2 spike Mutations Associated with Variants of Concern. *J Clin Microbiol* 59, e0144621.
- Bankhead, P., Loughrey, M.B., Fernandez, J.A., Dombrowski, Y., McArt, D.G., Dunne, P.D., McQuaid, S., Gray, R.T., Murray, L.J., Coleman, H.G., *et al.* (2017). QuPath: Open source software for digital pathology image analysis. *Sci Rep* 7, 16878.
- Barton, L.M., Duval, E.J., Stroberg, E., Ghosh, S., and Mukhopadhyay, S. (2020). COVID-19 Autopsies, Oklahoma, USA. *Am J Clin Pathol* 153, 725-733.

- Belitski, M., Guenther, C., Kritikos, A.S., and Thurik, R. Economic effects of the COVID-19 pandemic on entrepreneurship and small businesses (*Small Bus Econ.* 2022;58(2):593-609. doi: 10.1007/s11187-021-00544-y. Epub 2021 Sep 12.).
- Bhatt, M., MovaseghiGargari, M., and Chand, M.T. (2022). The importance of autopsies despite the declining number amidst the COVID-19 pandemic. *Autops Case Rep* 12, e2021371.
- Bodenheimer, T., Halappanavar, M., Jefferys, S., Gibson, R., Liu, S., Mucha, P.J., Stanley, N., Parker, J.S., and Selitsky, S.R. (2020). FastPG: fast clustering of millions of single cells. *BioRxiv*.
- Borczuk, A.C. (2021). Pulmonary pathology of COVID-19: a review of autopsy studies. *Curr Opin Pulm Med* 27, 184-192.
- Brady, C.A., Williams, C., Sharps, M.C., Shelleh, A., Batra, G., Heazell, A.E.P., and Crocker, I.P. (2021). Chronic histiocytic intervillitis: A breakdown in immune tolerance comparable to allograft rejection? *American Journal of Reproductive Immunology* 85, e13373.
- Braun, B.A., Marcovitz, A., Camp, J.G., Jia, R., and Bejerano, G. (2015). Mx1 and Mx2 key antiviral proteins are surprisingly lost in toothed whales. *Proceedings of the National Academy of Sciences* 112, 8036-8040.
- Bushnell, B. (2014). BBMap: A Fast, Accurate, Splice-Aware Aligner. LBNL Report.
- Caniego-Casas, T., Martinez-Garcia, L., Alonso-Riano, M., Pizarro, D., Carretero-Barrio, I., Martinez-de-Castro, N., Ruz-Caracuel, I., de Pablo, R., Saiz, A., Royo, R.N., *et al.* (2022). RNA SARS-CoV-2 Persistence in the Lung of Severe COVID-19 Patients: A Case Series of Autopsies. *Front Microbiol* 13, 824967.
- Cao, X. (2020). COVID-19: immunopathology and its implications for therapy. *Nature Reviews Immunology* 20, 269-270.
- Cardinal-Fernández, P., Lorente, J.A., Ballén-Barragán, A., and Matute-Bello, G. (2017). Acute Respiratory Distress Syndrome and Diffuse Alveolar Damage. New Insights on a Complex Relationship. *Ann Am Thorac Soc* 14, 844-850.
- Chen, E.Y., Tan, C.M., Kou, Y., Duan, Q., Wang, Z., Meirelles, G.V., Clark, N.R., and Ma'ayan, A. (2013). Enrichr: interactive and collaborative HTML5 gene list enrichment analysis tool. *BMC Bioinformatics* 14, 128.
- Cordier, J.-F. (2000). Organising pneumonia. *Thorax* 55, 318.
- Delahoy, M.J., Whitaker, M., O'Halloran, A., Chai, S.J., Kirley, P.D., Alden, N., Kawasaki, B., Meek, J., Yousey-Hindes, K., Anderson, E.J., *et al.* (2020). Characteristics and Maternal and Birth Outcomes of Hospitalized Pregnant Women with Laboratory-Confirmed COVID-19 -COVID-NET, 13 States, March 1-August 22, 2020. *MMWR Morb Mortal Wkly Rep* 69, 1347-1354.

- Desai, N., Neyaz, A., Szabolcs, A., Shih, A.R., Chen, J.H., Thapar, V., Nieman, L.T., Solovyov, A., Mehta, A., Lieb, D.J., *et al.* (2020). Temporal and spatial heterogeneity of host response to SARS-CoV-2 pulmonary infection. *Nat Commun* 11, 6319.
- Doane, J.J., Hirsch, K.S., Baldwin, J.O., Wurfel, M.M., Pipavath, S.N., and West, T.E. (2021). Progressive Pulmonary Fibrosis After Non-Critical COVID-19: A Case Report. *Am J Case Rep* 22, e933458.
- Dobin, A., Davis, C.A., Schlesinger, F., Drenkow, J., Zaleski, C., Jha, S., Batut, P., Chaisson, M., and Gingeras, T.R. (2013). STAR: ultrafast universal RNA-seq aligner. *Bioinformatics* 29, 15- 21.
- Ekstedt, S., Piersiala, K., Petro, M., Karlsson, A., Kågedal, Å., Kumlien Georén, S., and Cardell, L.O. (2022). A prolonged innate systemic immune response in COVID-19. *Sci Rep* 12, 9915.
- Garcia-Diaz, A., Shin, D.S., Moreno, B.H., Saco, J., Escuin-Ordinas, H., Rodriguez, G.A., Zaretsky, J.M., Sun, L., Hugo, W., Wang, X., *et al.* (2017). Interferon Receptor Signaling Pathways Regulating PD-L1 and PD-L2 Expression. *Cell Rep* 19, 1189-1201.
- George, P.M., Wells, A.U., and Jenkins, R.G. (2020). Pulmonary fibrosis and COVID-19: the potential role for antifibrotic therapy. *Lancet Respir Med* 8, 807-815.
- Gomez-Rial, J., Rivero-Calle, I., Salas, A., and Martinon-Torres, F. (2020). Role of Monocytes/Macrophages in Covid-19 Pathogenesis: Implications for Therapy. *Infect Drug Resist* 13, 2485-2493.
- Goncharov, M., Bagaev, D., Shcherbinin, D., Zvyagin, I., Bolotin, D., Thomas, P.G., Minervina, A.A., Pogorelyy, M.V., Ladell, K., McLaren, J.E., *et al.* (2022). VDJdb in the pandemic era: a compendium of T cell receptors specific for SARS-CoV-2. *Nature Methods* 19, 1017-1019.
- Greenwald, N.F., Miller, G., Moen, E., Kong, A., Kagel, A., Dougherty, T., Fullaway, C.C., McIntosh, B.J., Leow, K.X., Schwartz, M.S., *et al.* (2022). Whole-cell segmentation of tissue images with human-level performance using large-scale data annotation and deep learning. *Nat Biotechnol* 40, 555-565.
- Gu, Z., Eils, R., and Schlesner, M. (2016). Complex heatmaps reveal patterns and correlations in multidimensional genomic data. *Bioinformatics* 32, 2847-2849.
- Han, R., Huang, L., Jiang, H., Dong, J., Peng, H., and Zhang, D. (2020). Early Clinical and CT Manifestations of Coronavirus Disease 2019 (COVID-19) Pneumonia. *AJR Am J Roentgenol* 215, 338-343.
- Herold, T., Jurinovic, V., Arnreich, C., Lipworth, B.J., Hellmuth, J.C., von Bergwelt-Baildon, M., Klein, M., and Weinberger, T. (2020). Elevated levels of IL-6 and CRP predict the need for mechanical ventilation in COVID-19. *Journal of Allergy and Clinical Immunology* 146, 128-136. e124.

- Hikmet, F., Mear, L., Edvinsson, A., Micke, P., Uhlen, M., and Lindskog, C. (2020). The protein expression profile of ACE2 in human tissues. *Mol Syst Biol* 16, e9610.
- Hoo, R., Nakimuli, A., and Vento-Tormo, R. (2020). Innate Immune Mechanisms to Protect Against Infection at the Human Decidual-Placental Interface. *Frontiers in Immunology* 11.
- Jackson, C.B., Farzan, M., Chen, B., and Choe, H. (2022). Mechanisms of SARS-CoV-2 entry into cells. *Nature Reviews Molecular Cell Biology* 23, 3-20.
- Jain, V., Vashisht, R., Yilmaz, G., and Bhardwaj, A. (2022). Pneumonia Pathology. In *StatPearls* (Treasure Island (FL): StatPearls Publishing.
- Jessen, H., Hoyer, N., Prior, T.S., Frederiksen, P., Ronnow, S.R., Karsdal, M.A., Leeming, D.J., Bendstrup, E., Sand, J.M.B., and Shaker, S.B. (2021). Longitudinal serological assessment of type VI collagen turnover is related to progression in a real-world cohort of idiopathic pulmonary fibrosis. *BMC Pulm Med* 21, 382.
- Jiang, S., Chan, C.N., Rovira-Clave, X., Chen, H., Bai, Y., Zhu, B., McCaffrey, E., Greenwald, N.F., Liu, C., Barlow, G.L., *et al.* (2022). Combined protein and nucleic acid imaging reveals virus-dependent B cell and macrophage immunosuppression of tissue microenvironments. *Immunity* 55, 1118-1134 e1118.
- Julian, D.R., Kazakoff, M.A., Patel, A., Jaynes, J., Willis, M.S., and Yates, C.C. (2021). Chemokine-Based Therapeutics for the Treatment of Inflammatory and Fibrotic Convergent Pathways in COVID-19. *Current Pathobiology Reports* 9, 93-105.
- Karlinsky, A. (2021). National Excess Mortality from Sub-National data: Method and Application for Argentina. *medRxiv*, 2021.2008.2030.21262814.
- Katze, M.G., He, Y., and Gale, M. (2002). Viruses and interferon: a fight for supremacy. *Nature Reviews Immunology* 2, 675-687.
- Khan, S., Siddique, R., Shereen, M.A., Ali, A., Liu, J., Bai, Q., Bashir, N., and Xue, M. (2020). Emergence of a Novel Coronavirus, Severe Acute Respiratory Syndrome Coronavirus 2: Biology and Therapeutic Options. *J Clin Microbiol* 58.
- Khan, Y.S., and Lynch, D.T. (2022). Histology, Lung. In *StatPearls* (Treasure Island (FL): StatPearls Publishing
- Kosyreva, A., Dzhililova, D., Lokhonina, A., Vishnyakova, P., and Fatkhudinov, T. (2021). The Role of Macrophages in the Pathogenesis of SARS-CoV-2-Associated Acute Respiratory Distress Syndrome. *Front Immunol* 12, 682871.
- Kundu, R., Narean, J.S., Wang, L., Fenn, J., Pillay, T., Fernandez, N.D., Conibear, E., Koycheva, A., Davies, M., Tolosa-Wright, M., *et al.* (2022). Cross-reactive memory T cells associate with protection against SARS-CoV-2 infection in COVID-19 contacts. *Nat Commun* 13, 80.
- Lee, M.Y., Bedia, J.S., Bhate, S.S., Barlow, G.L., Phillips, D., Fantl, W.J., Nolan, G.P., and Schurch, C.M. (2022). CellSeg: a robust, pre-trained nucleus segmentation and pixel

quantification software for highly multiplexed fluorescence images. *BMC Bioinformatics* 23, 46.

- Levin AT, Hanage WP, Owusu-Boaitey N, Cochran KB, Walsh SP, Meyerowitz-Katz G. Assessing the age specificity of infection fatality rates for COVID-19: systematic review, meta-analysis, and public policy implications. *Eur J Epidemiol*. 2020 Dec;35(12):1123-1138.
- Levin, A.T., Owusu-Boaitey, N., Pugh, S., Fosdick, B.K., Zwi, A.B., Malani, A., Soman, S., Besançon, L., Kashnitsky, I., Ganesh, S., *et al.* (2022). Assessing the burden of COVID-19 in developing countries: systematic review, meta-analysis and public policy implications. *BMJ Global Health* 7, e008477.
- Li, H., Handsaker, B., Wysoker, A., Fennell, T., Ruan, J., Homer, N., Marth, G., Abecasis, G., Durbin, R., and Genome Project Data Processing, S. (2009). The Sequence Alignment/Map format and SAMtools. *Bioinformatics* 25, 2078-2079.
- Lin, T., Geng, T., Harrison, A.G., Yang, D., Vella, A.T., Fikrig, E., and Wang, P. (2020). CXCL10 Signaling Contributes to the Pathogenesis of Arthritogenic Alphaviruses. In *Viruses*.
- Linehan, L., O'Donoghue, K., Dineen, S., White, J., Higgins, J.R., and Fitzgerald, B. (2021). SARS-CoV-2 placentitis: An uncommon complication of maternal COVID-19. *Placenta* 104, 261-266.
- Liu, F., Han, K., Blair, R., Kenst, K., Qin, Z., Upcin, B., Wörsdörfer, P., Midkiff, C.C., Mudd, J., Belyaeva, E., *et al.* (2021). SARS-CoV-2 Infects Endothelial Cells In Vivo and In Vitro. *Front Cell Infect Microbiol* 11, 701278.
- Liu, Z., Li, J., Chen, D., Gao, R., Zeng, W., Chen, S., Huang, Y., Huang, J., Long, W., and Li, M. (2020). Dynamic interleukin-6 level changes as a prognostic indicator in patients with COVID-19. *Frontiers in Pharmacology* 11, 1093.
- Lorè, N.I., De Lorenzo, R., Rancoita, P.M.V., Cugnata, F., Agresti, A., Benedetti, F., Bianchi, M.E., Bonini, C., Capobianco, A., Conte, C., *et al.* (2021). CXCL10 levels at hospital admission predict COVID-19 outcome: hierarchical assessment of 53 putative inflammatory biomarkers in an observational study. *Molecular Medicine* 27, 129.
- Love, M.I., Huber, W., and Anders, S. (2014). Moderated estimation of fold change and dispersion for RNA-seq data with DESeq2. *Genome Biol* 15, 550.
- Mahase, E. (2020). Covid-19: Why are age and obesity risk factors for serious disease? *BMJ* 371, m4130.
- Mariano, G., Farthing, R.J., Lale-Farjat, S.L.M., and Bergeron, J.R.C. (2020). Structural Characterization of SARS-CoV-2: Where We Are, and Where We Need to Be. *Frontiers in Molecular Biosciences* 7.

- Martin-Sancho, L., Lewinski, M.K., Pache, L., Stoneham, C.A., Yin, X., Becker, M.E., Pratt, D., Churas, C., Rosenthal, S.B., and Liu, S. (2021). Functional landscape of SARS-CoV-2 cellular restriction. *Molecular cell* *81*, 2656-2668. e2658.
- Matoba, K., Hyodoh, H., Murakami, M., Saito, A., Matoba, T., Ishida, L., Fujita, E., Yamase, M., and Jin, S. (2017). Estimating normal lung weight measurement using postmortem CT in forensic cases. *Legal Medicine* *29*, 77-81.
- Mauricio, R., and Khera, A. (2022). Statin Use in Pregnancy: Is It Time For a Paradigm Shift? *Circulation* *145*, 496-498.
- Menter, T., Mertz, K.D., Jiang, S., Chen, H., Monod, C., Tzankov, A., Waldvogel, S., Schulzke, S.M., Hösli, I., and Bruder, E. (2021). Placental Pathology Findings during and after SARS- CoV-2 Infection: Features of Villitis and Malperfusion. *Pathobiology* *88*, 69-77.
- Mootha, V.K., Lindgren, C.M., Eriksson, K.F., Subramanian, A., Sihag, S., Lehar, J., Puigserver, P., Carlsson, E., Ridderstrale, M., Laurila, E., *et al.* (2003). PGC-1alpha-responsive genes involved in oxidative phosphorylation are coordinately downregulated in human diabetes. *Nat Genet* *34*, 267-273.
- Myles Lewi, K.G., Elisabetta Sciacca, Cankut Cubuk, Anna Surace (2022). glmmSeq: General Linear Mixed Models for Gene-level Differential Expression.
- Nolan, S., Vignali, M., Klinger, M., Dines, J.N., Kaplan, I.M., Svejnoha, E., Craft, T., Boland, K., Pesesky, M., Gittelman, R.M., *et al.* (2020). A large-scale database of T-cell receptor beta (TCR β) sequences and binding associations from natural and synthetic exposure to SARS- CoV-2. *Res Sq.*
- Organ, L.A., Duggan, A.-M.R., Oballa, E., Taggart, S.C., Simpson, J.K., Kang'ombe, A.R., Braybrooke, R., Molyneaux, P.L., North, B., Karkera, Y., *et al.* (2019a). Biomarkers of collagen synthesis predict progression in the PROFILE idiopathic pulmonary fibrosis cohort. *Respiratory Research* *20*, 148.
- Peng, H., Yang, L.T., Wang, L.Y., Li, J., Huang, J., Lu, Z.Q., Koup, R.A., Bailer, R.T., and Wu, C.Y. (2006). Long-lived memory T lymphocyte responses against SARS coronavirus nucleocapsid protein in SARS-recovered patients. *Virology* *351*, 466-475.
- Perng, Y.-C., and Lenschow, D.J. (2018). ISG15 in antiviral immunity and beyond. *Nature Reviews Microbiology* *16*, 423-439.
- Petrovic-Djergovic, D., Popovic, M., Chittiprol, S., Cortado, H., Ransom, R.F., and Partida- Sánchez, S. (2015). CXCL10 induces the recruitment of monocyte-derived macrophages into kidney, which aggravate puromycin aminonucleoside nephrosis. *Clin Exp Immunol* *180*, 305-315.
- Putri, G.H., Anders, S., Pyl, P.T., Pimanda, J.E., and Zanini, F. (2022). Analysing high-throughput sequencing data in Python with HTSeq 2.0. *Bioinformatics* *38*, 2943-2945.

- Rabelo, K., de Souza, L.J., Salomão, N.G., Machado, L.N., Pereira, P.G., Portari, E.A., Basílio- de-Oliveira, R., Dos Santos, F.B., Neves, L.D., Morgade, L.F., *et al.* (2020). Zika Induces Human Placental Damage and Inflammation. *Front Immunol* 11, 2146.
- Ramadan, N., and Shaib, H. (2019). Middle East respiratory syndrome coronavirus (MERS- CoV): A review. *Germs* 9, 35-42.
- Rendeiro, A.F., Ravichandran, H., Bram, Y., Chandar, V., Kim, J., Meydan, C., Park, J., Foox, J., Hether, T., Warren, S., *et al.* (2021). The spatial landscape of lung pathology during COVID- 19 progression. *Nature* 593, 564-569.
- Retamozo S, Brito-Zerón P, Sisó-Almirall A, Flores-Chávez A, Soto-Cárdenas MJ, Ramos-Casals M. Haemophagocytic syndrome and COVID-19. *Clin Rheumatol.* 2021 Apr;40(4):1233-1244.
- Samuel, C.E. (2001). Antiviral actions of interferons. *Clin Microbiol Rev* 14, 778-809, table of contents.
- Santa Cruz, A., Mendes-Frias, A., Oliveira, A.I., Dias, L., Matos, A.R., Carvalho, A., Capela, C., Pedrosa, J., Castro, A.G., and Silvestre, R. (2021). Interleukin-6 Is a Biomarker for the Development of Fatal Severe Acute Respiratory Syndrome Coronavirus 2 Pneumonia. *Frontiers in Immunology* 12.
- Schenkel, J.M., and Masopust, D. (2014). Tissue-resident memory T cells. *Immunity* 41, 886- 897.
- Scherger, S., Henao-Martínez, A., Franco-Paredes, C., and Shapiro, L. (2020). Rethinking interleukin-6 blockade for treatment of COVID-19. *Medical hypotheses* 144, 110053.
- Schönrich, G., and Raftery, M.J. (2019). The PD-1/PD-L1 Axis and Virus Infections: A Delicate Balance. *Frontiers in Cellular and Infection Microbiology* 9.
- Schurch, C.M., Bhate, S.S., Barlow, G.L., Phillips, D.J., Noti, L., Zlobec, I., Chu, P., Black, S., Demeter, J., McIlwain, D.R., *et al.* (2020). Coordinated Cellular Neighborhoods Orchestrate Antitumoral Immunity at the Colorectal Cancer Invasive Front. *Cell* 182, 1341-1359 e1319.
- Schwartz, D.A. (2020). An Analysis of 38 Pregnant Women With COVID-19, Their Newborn Infants, and Maternal-Fetal Transmission of SARS-CoV-2: Maternal Coronavirus Infections and Pregnancy Outcomes. *Arch Pathol Lab Med* 144, 799-805.
- Schwartz, D.A., Avvad-Portari, E., Babál, P., Baldewijns, M., Blomberg, M., Bouachba, A., Camacho, J., Collardeau-Frachon, S., Colson, A., Dehaene, I., *et al.* (2022b). Placental Tissue Destruction and Insufficiency From COVID-19 Causes Stillbirth and Neonatal Death From Hypoxic-Ischemic Injury: A Study of 68 Cases With SARS-CoV-2 Placentitis From 12 Countries. *Archives of Pathology & Laboratory Medicine* 146, 660-676.

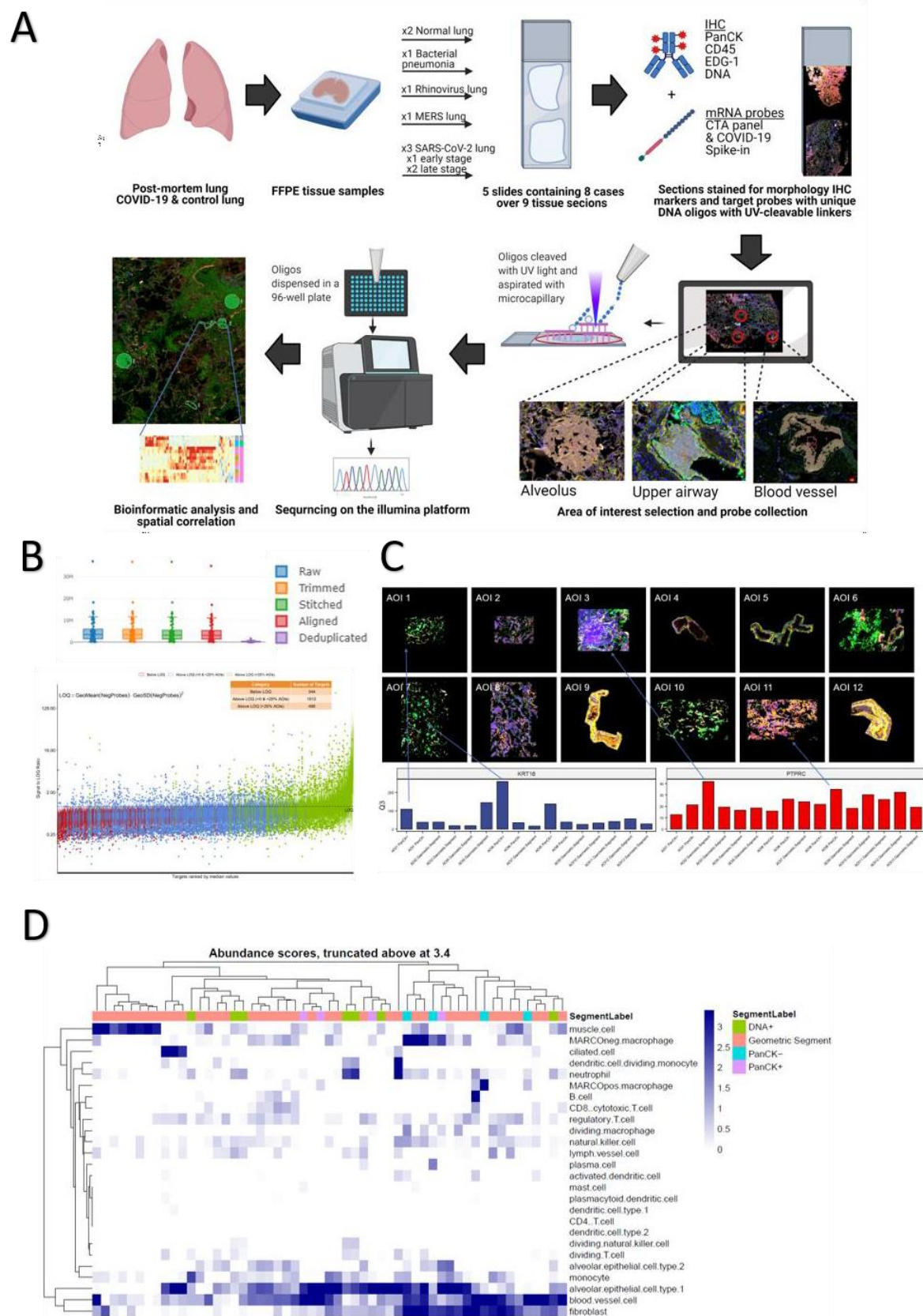
- Schwensen, H.F., Borreschmidt, L.K., Storgaard, M., Redsted, S., Christensen, S., and Madsen, L.B. (2021). Fatal pulmonary fibrosis: a post-COVID-19 autopsy case. *Journal of Clinical Pathology* 74, 400.
- Sefik, E., Qu, R., Junqueira, C., Kaffe, E., Mirza, H., Zhao, J., Brewer, J.R., Han, A., Steach, H.R., Israelow, B., *et al.* (2022). Inflammasome activation in infected macrophages drives COVID- 19 pathology. *Nature* 606, 585-593.
- Senegas, A., Villard, O., Neuville, A., Marcellin, L., Pfaff, A.W., Steinmetz, T., Mousli, M., Klein, J.P., and Candolfi, E. (2009). Toxoplasma gondii-induced foetal resorption in mice involves interferon-gamma-induced apoptosis and spiral artery dilation at the maternofetal interface. *Int J Parasitol* 39, 481-487.
- Sofizan, N., Rahman, A., Soon, L.P., Ly, C.K., and Abdullah, N.Z.B. (2022). Autopsy findings in COVID-19 infection-related death: a systematic review. *Egypt J Forensic Sci* 12, 22.
- Stenton, S., McPartland, J., Shukla, R., Turner, K., Marton, T., Hargitai, B., Bamber, A., Pryce, J., Peres, C.L., Burgess, N., *et al.* (2022). SARS-COV2 placentitis and pregnancy outcome: A multicentre experience during the Alpha and early Delta waves of coronavirus pandemic in England. *EClinicalMedicine* 47, 101389.
- Subramanian, A., Tamayo, P., Mootha, V.K., Mukherjee, S., Ebert, B.L., Gillette, M.A., Paulovich, A., Pomeroy, S.L., Golub, T.R., Lander, E.S., *et al.* (2005). Gene set enrichment analysis: a knowledge-based approach for interpreting genome-wide expression profiles. *Proc Natl Acad Sci U S A* 102, 15545-15550.
- Sun, J.-Y., Wu, R., Xu, J., Xue, H.-Y., Lu, X.-J., and Ji, J. (2021). Placental Immune Tolerance and Organ Transplantation: Underlying Interconnections and Clinical Implications. *Frontiers in Immunology* 12.
- Sun, P., Lu, X., Xu, C., Sun, W., and Pan, B. (2020). Understanding of COVID-19 based on current evidence. *J Med Virol* 92, 548-551.
- Tanaka, T., Narazaki, M., and Kishimoto, T. (2014). IL-6 in inflammation, immunity, and disease. *Cold Spring Harb Perspect Biol* 6, a016295.
- Thomas, J., Sun, Y., and Debelenko, L. (2021). Infrequent Placental and Fetal Involvement in SARS-CoV-2 Infection: Pathology Data from a Large Medical Center. *J Dev Biol* 9.
- Tickotsky, N., Sagiv, T., Prilusky, J., Shifrut, E., and Friedman, N. (2017). McPAS-TCR: a manually curated catalogue of pathology-associated T cell receptor sequences. *Bioinformatics* 33, 2924-2929.
- Urra JM, Cabrera CM, Porras L, Ródenas I. Selective CD8 cell reduction by SARS-CoV-2 is associated with a worse prognosis and systemic inflammation in COVID-19 patients. *Clin Immunol*. 2020 Aug;217:108486.

- Wang, C., Xie, J., Zhao, L., Fei, X., Zhang, H., Tan, Y., Nie, X., Zhou, L., Liu, Z., Ren, Y., *et al.* (2020). Alveolar macrophage dysfunction and cytokine storm in the pathogenesis of two severe COVID-19 patients. *EBioMedicine* 57, 102833.
- Wang, M.-Y., Zhao, R., Gao, L.-J., Gao, X.-F., Wang, D.-P., and Cao, J.-M. (2020b). SARS-CoV-2: Structure, Biology, and Structure-Based Therapeutics Development. *Frontiers in Cellular and Infection Microbiology* 10.
- Watkins, J.C., Torous, V.F., and Roberts, D.J. (2021). Defining Severe Acute Respiratory Syndrome Coronavirus 2 (SARS-CoV-2) Placentitis. *Arch Pathol Lab Med* 145, 1341-1349.
- Watkins, J.C., Torous, V.F., and Roberts, D.J. (2021). Defining Severe Acute Respiratory Syndrome Coronavirus 2 (SARS-CoV-2) Placentitis. *Arch Pathol Lab Med* 145, 1341-1349.
- Wells, A.I., and Coyne, C.B. (2018). Type III Interferons in Antiviral Defenses at Barrier Surfaces. *Trends Immunol* 39, 848-858.
- Wölfel, R., Corman, V.M., Guggemos, W., Seilmaier, M., Zange, S., Müller, M.A., Niemeyer, D., Jones, T.C., Vollmar, P., Rothe, C., *et al.* (2020). Virological assessment of hospitalized patients with COVID-2019. *Nature* 581, 465-469.
- Xu, Z., Shi, L., Wang, Y., Zhang, J., Huang, L., Zhang, C., Liu, S., Zhao, P., Liu, H., Zhu, L., *et al.* (2020). Pathological findings of COVID-19 associated with acute respiratory distress syndrome. *Lancet Respir Med* 8, 420-422.
- Yao, X.H., Luo, T., Shi, Y., He, Z.C., Tang, R., Zhang, P.P., Cai, J., Zhou, X.D., Jiang, D.P., Fei, X.C., *et al.* (2021). A cohort autopsy study defines COVID-19 systemic pathogenesis. *Cell Res* 31, 836-846.
- Yockey, L.J., Jurado, K.A., Arora, N., Millet, A., Rakib, T., Milano, K.M., Hastings, A.K., Fikrig, E., Kong, Y., Horvath, T.L., *et al.* (2018). Type I interferons instigate fetal demise after Zika virus infection. *Sci Immunol* 3.
- Zhang, F., Mears, J.R., Shakib, L., Beynor, J.I., Shanaj, S., Korsunsky, I., Nathan, A., Donlin, L.T., Raychaudhuri, S., Accelerating Medicines Partnership Rheumatoid, A., *et al.* (2021). IFN- γ and TNF- α drive a CXCL10+ CCL2+ macrophage phenotype expanded in severe COVID-19 lungs and inflammatory diseases with tissue inflammation. *Genome Medicine* 13, 64.
- Zhang, J.J., Dong, X., Cao, Y.Y., Yuan, Y.D., Yang, Y.B., Yan, Y.Q., Akdis, C.A., and Gao, Y.D. (2020). Clinical characteristics of 140 patients infected with SARS-CoV-2 in Wuhan, China. *Allergy* 75, 1730-1741.
- Zhang, W., Li, I., Reticker-Flynn, N.E., Good, Z., Chang, S., Samusik, N., Saumyaa, S., Li, Y., Zhou, X., Liang, R., *et al.* (2022). Identification of cell types in multiplexed in situ images by combining protein expression and spatial information using CELESTA. *Nat Methods* 19, 759- 769.

- Zhang, W., Li, I., Reticker-Flynn, N.E., Good, Z., Chang, S., Samusik, N., Saumyaa, S., Li, Y., Zhou, X., Liang, R., *et al.* (2022). Identification of cell types in multiplexed in situ images by combining protein expression and spatial information using CELESTA. *Nat Methods* 19, 759- 769.
- Zhang, Y., Broser, M., Cohen, H., Bodkin, M., Law, K., Reibman, J., and Rom, W.N. (1995). Enhanced interleukin-8 release and gene expression in macrophages after exposure to *Mycobacterium tuberculosis* and its components. *The Journal of Clinical Investigation* 95, 586-592.
- Zimmerman, S.M., Fropf, R., Kulasekara, B.R., Griswold, M., Appelbe, O., Bahrami, A., Boykin, R., Buhr, D.L., Fuhrman, K., Hoang, M.L., *et al.* (2022). Spatially resolved whole transcriptome profiling in human and mouse tissue using Digital Spatial Profiling. *Genome Res.*

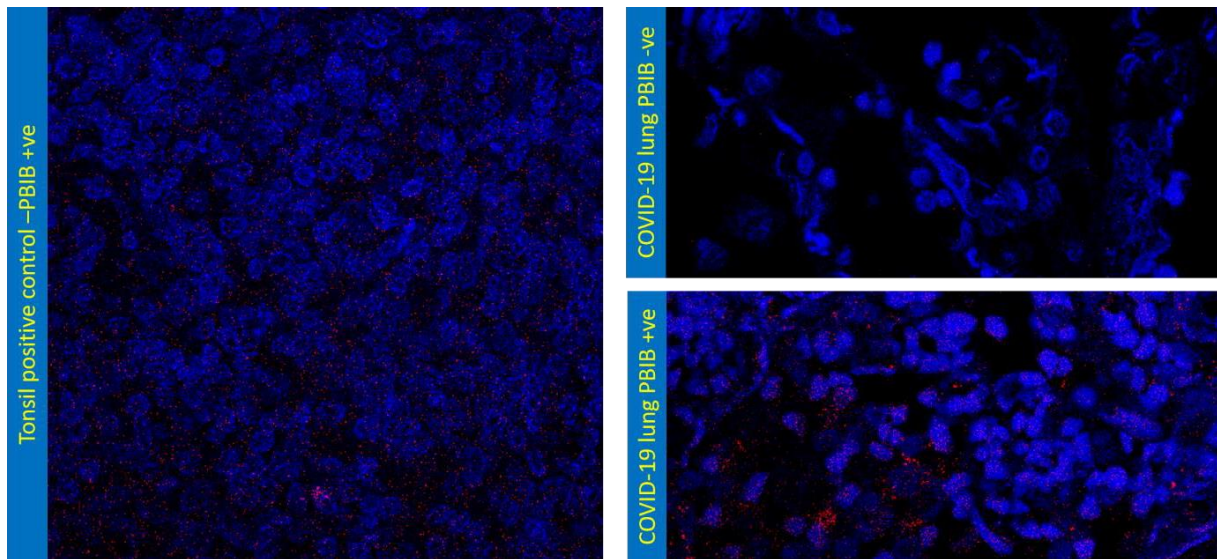
Chapter 8 Appendices

Appendix 1: Nanostring GeoMx lung experiment design and validation.



Appendix 1. A. Experimental overview of GeoMx experiment. B. Number of reads analysed for GeoMx lung experiment. C. Validation of regions of interest based on CD45 and cytokeratin expression. D. Cellular deconvolution of lung GeoMx data.

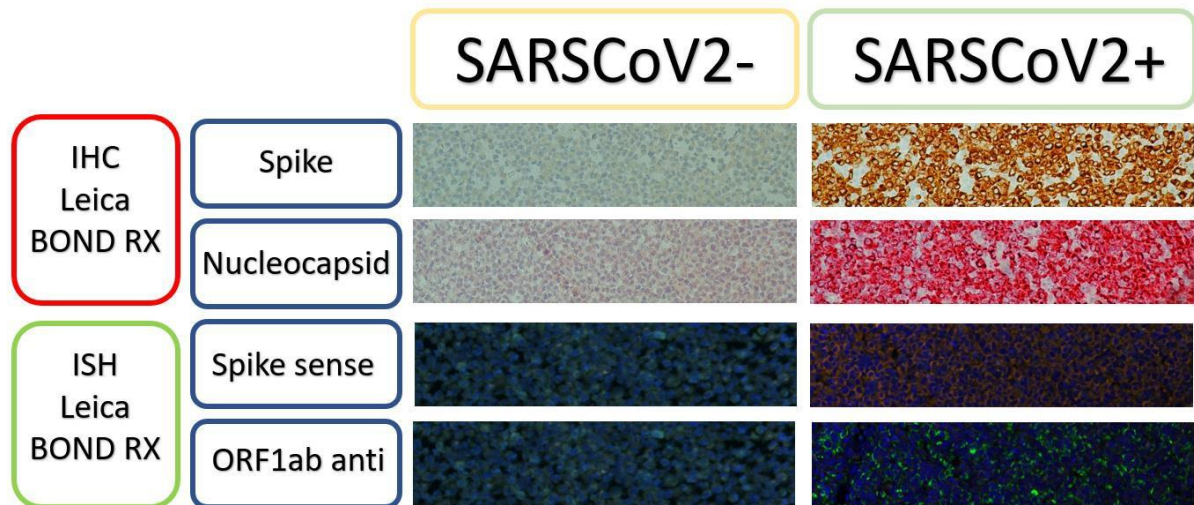
Appendix 2: RNAscope QC



Case	Treatment	RNAscope PBIB probe detection
1 Lung	8 min AR, 15 protease 8 min AR, 15 protease	Poor Negative
2 Lung	8 min AR, 15 protease 15 min AR, 15 protease	Good Poor
3 Lung	8 min AR, 15 protease 15 min AR, 15 protease	Poor Negative
4 Lung	8 min AR, 15 protease 15 min AR, 15 protease	Very good Good
5 Lung	8 min AR, 15 protease 15 min AR, 15 protease	Very good Very good
6 Lung	8 min AR, 15 protease 15 min AR, 15 protease	Very good Good
7 Lung	8 min AR, 15 protease 15 min AR, 15 protease	Good Poor
8 Lung	8 min AR, 15 protease 15 min AR, 15 protease	Very good Very good

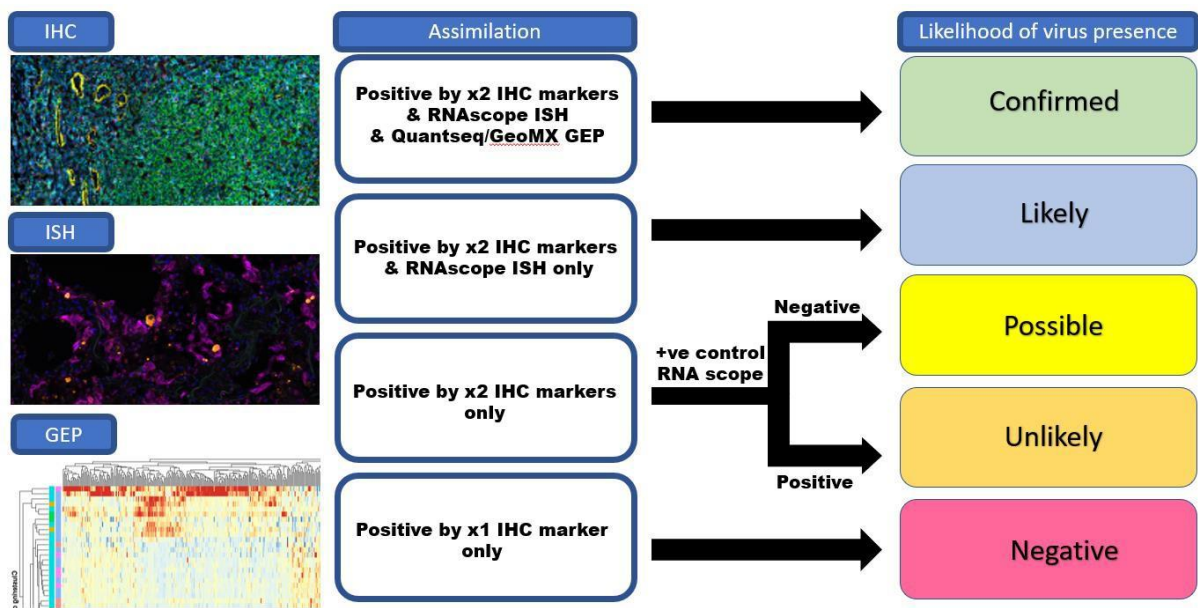
Appendix 2. Quality control of lung tissue using RNAscope PBIB housekeeping control prob. Results for each COVID-19 tissue is shown

Appendix 3: Validation of SARS-CoV-2 antibodies and probes



Appendix 3. A. Validation of SARS-CoV-2 antibodies and RNAscope probes using a SARS-CoV-2 infected cell line which was pelleted into FFPE.

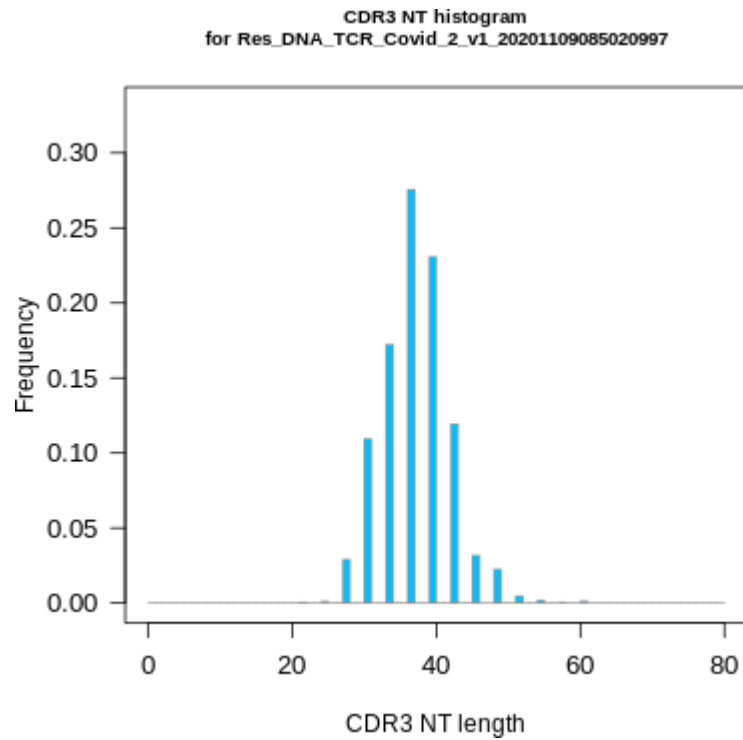
Appendix 4: Assimilation of virus detection data.



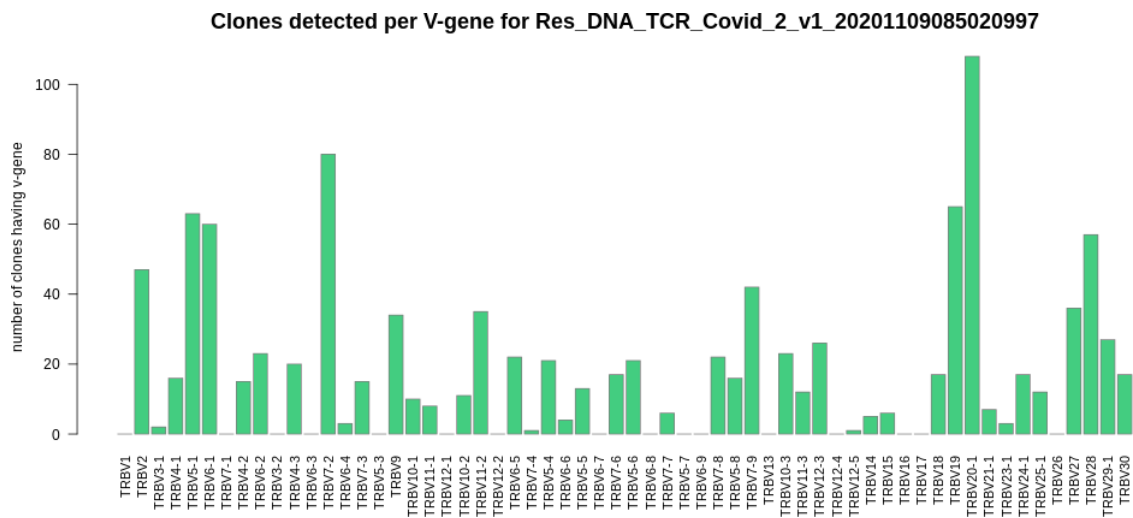
Appendix 4. Hierarchy of importance of viral detection methodologies.

Appendix 5: Detailed TCR data.

COVID-19 Lung early stage case 1

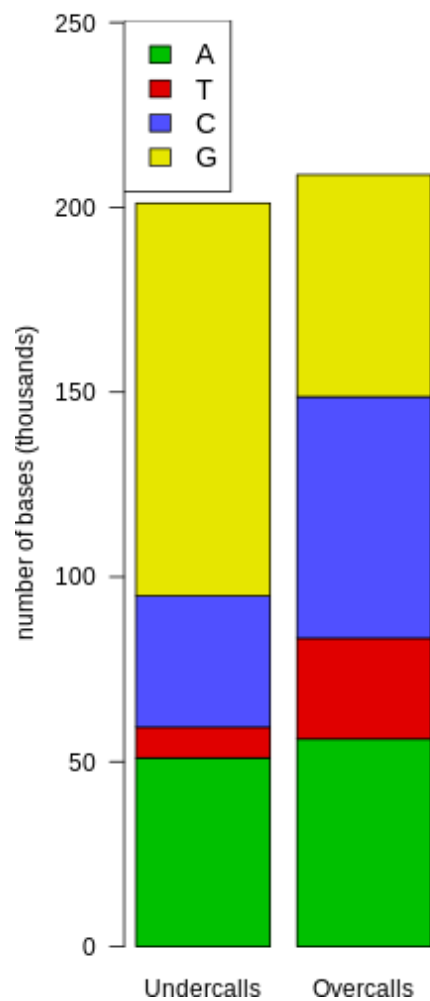


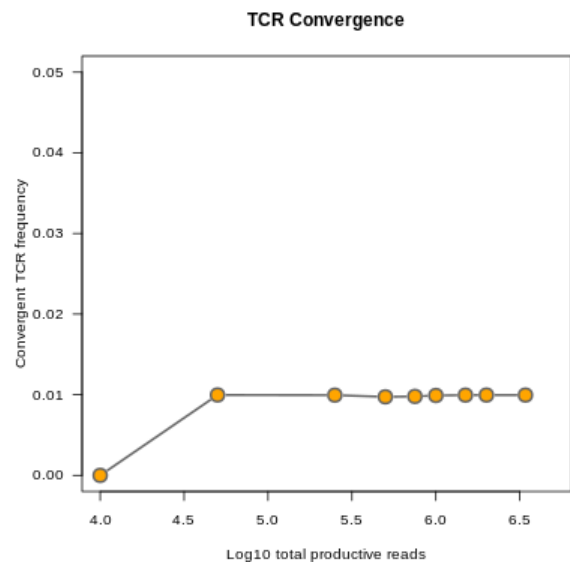
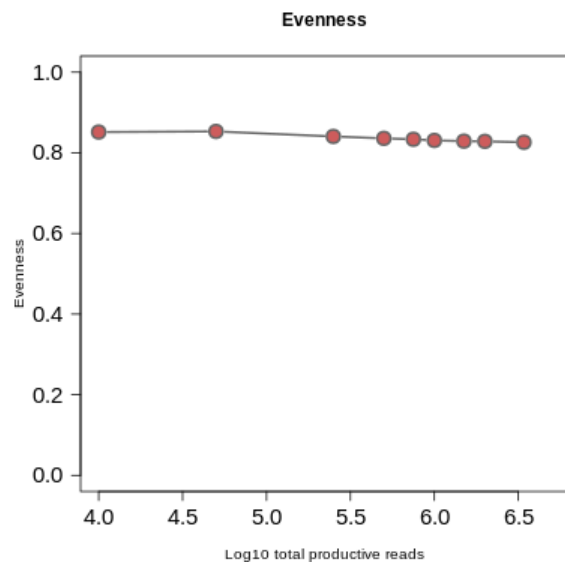
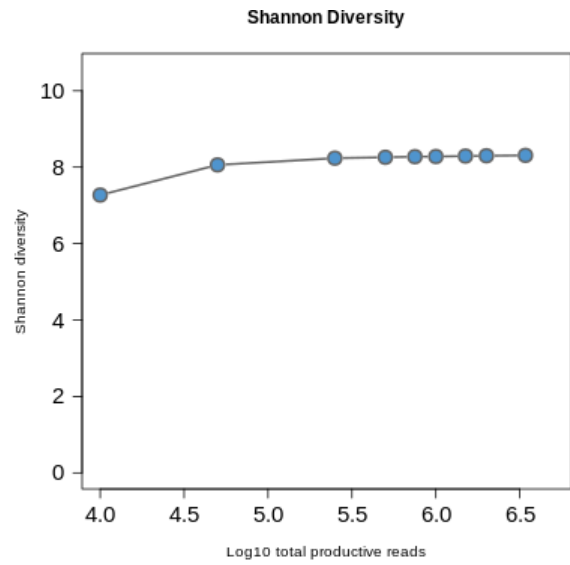
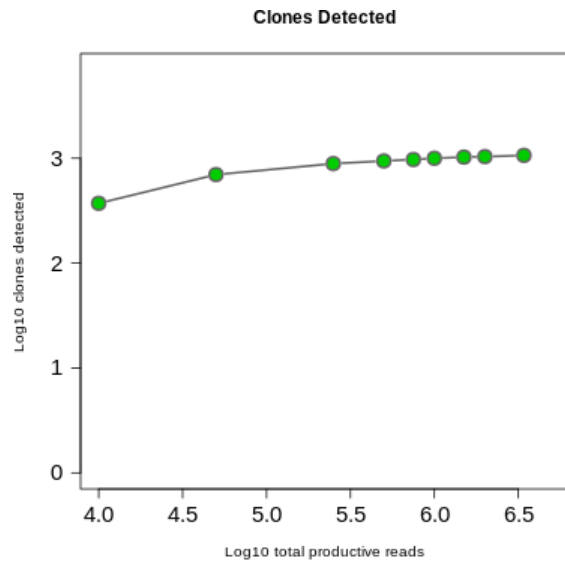
Histogram of CDR3 nucleotide length showing a normal distribution

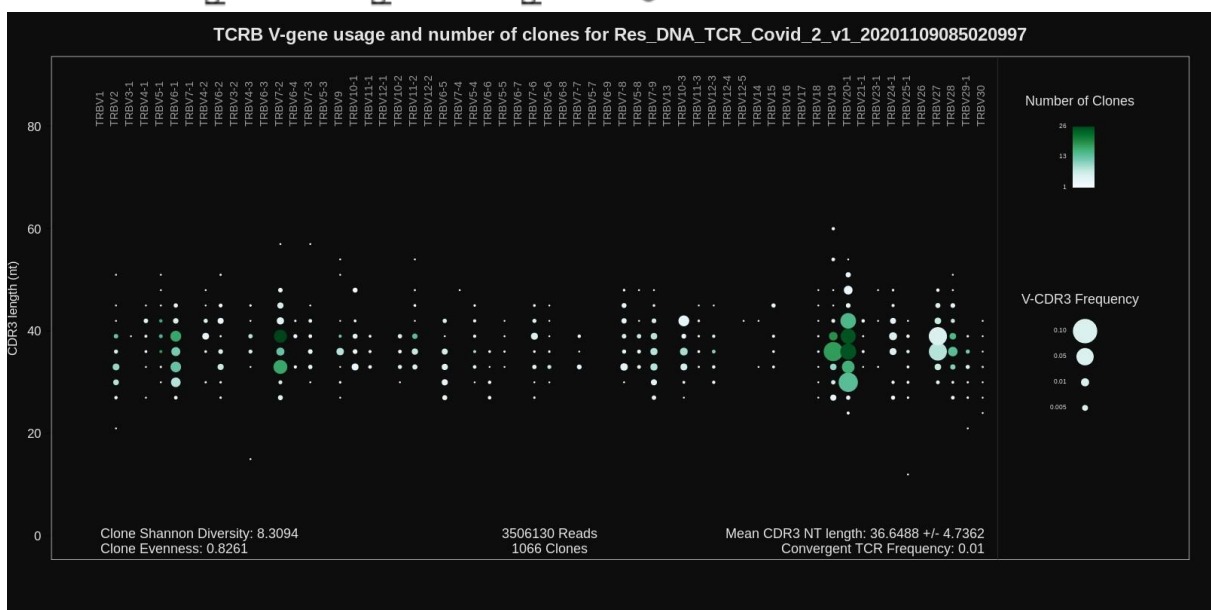
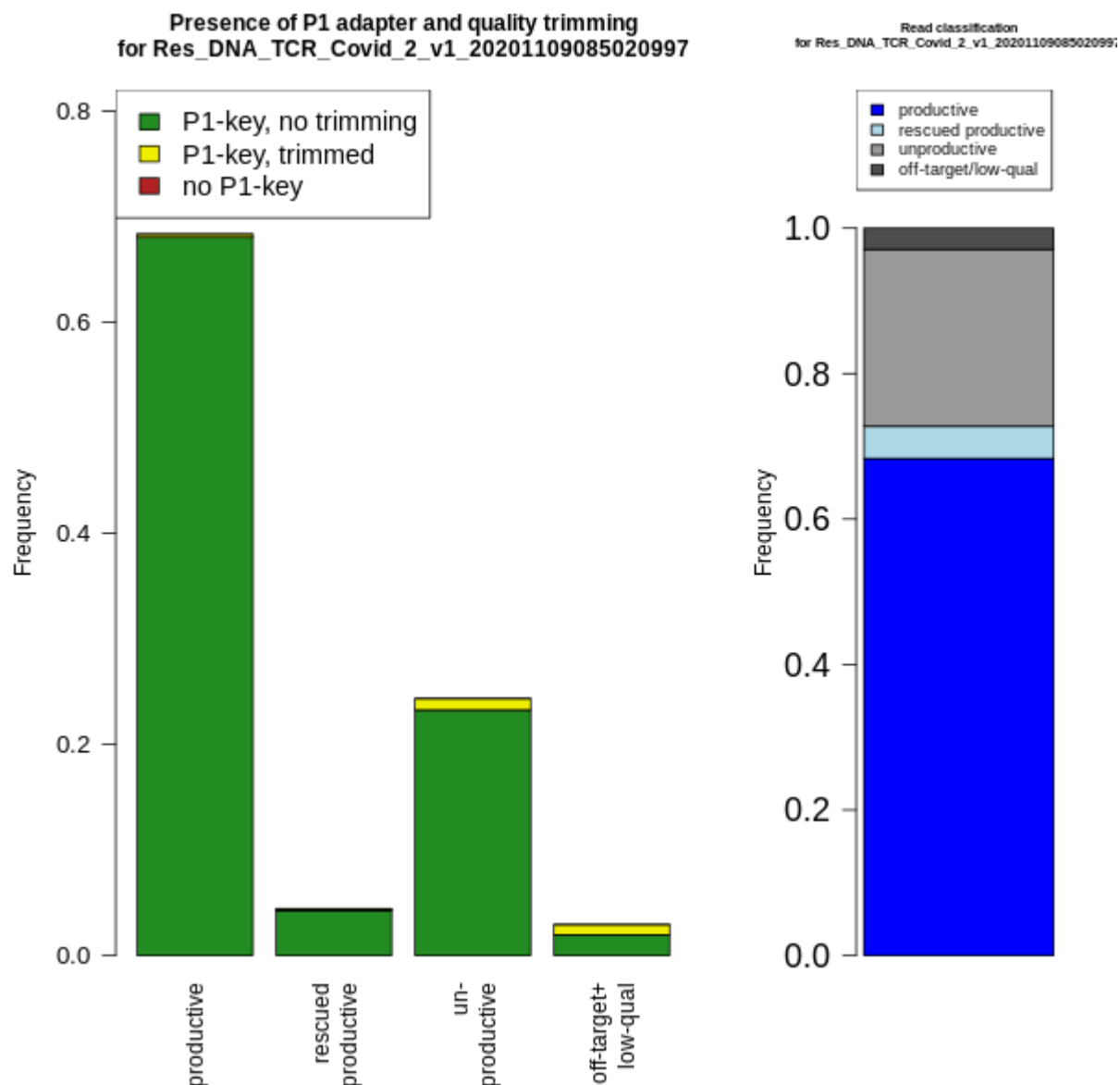


Number of clones per V-gene

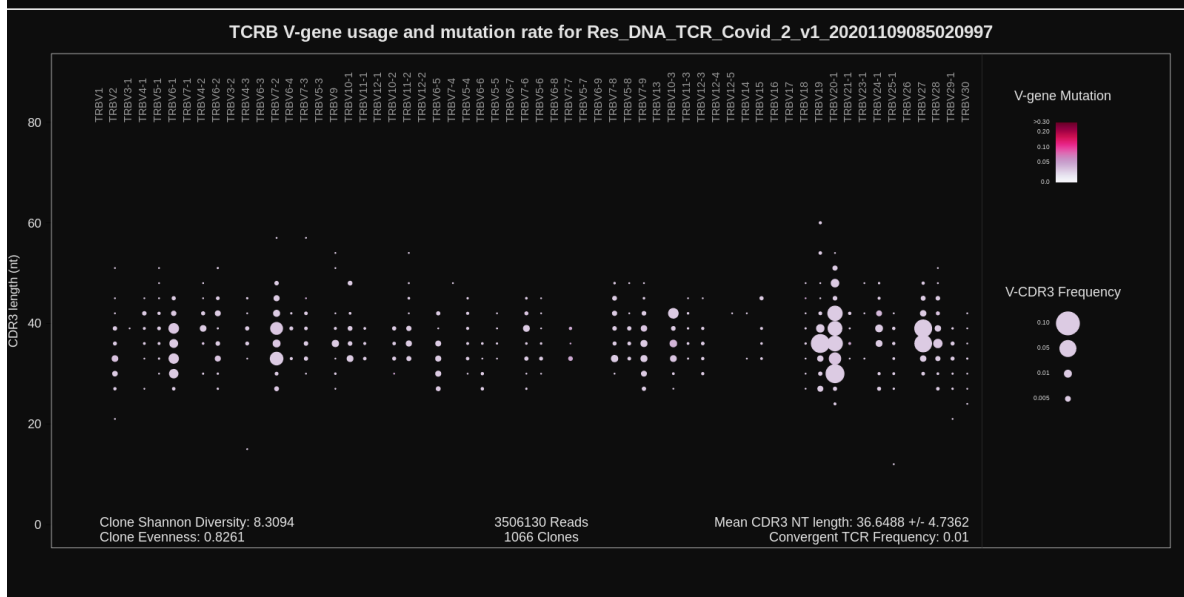
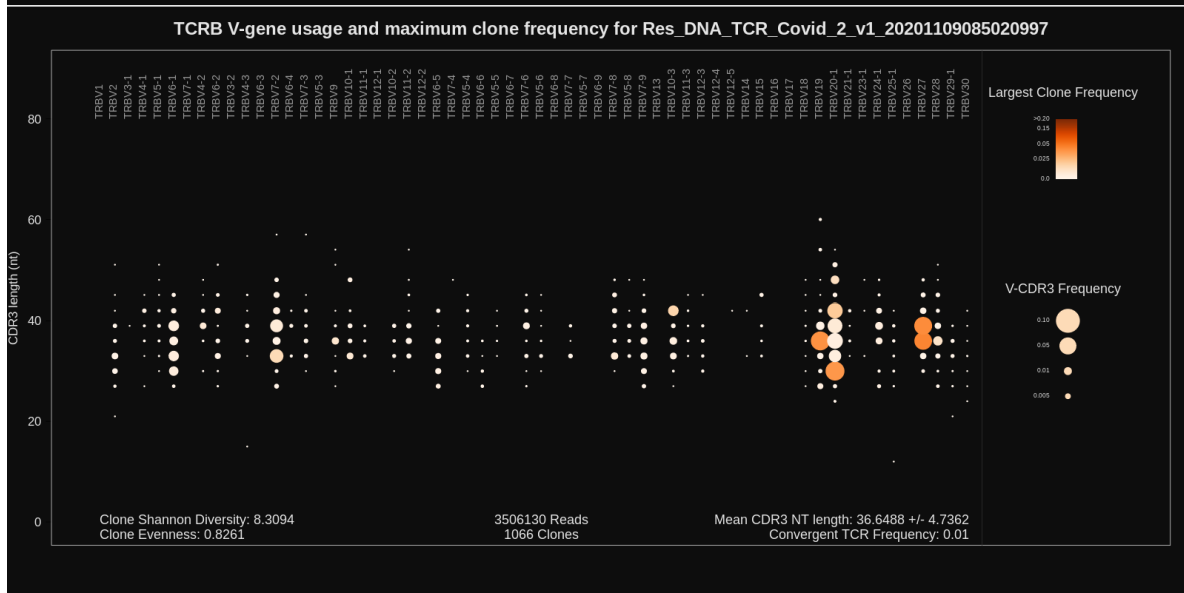
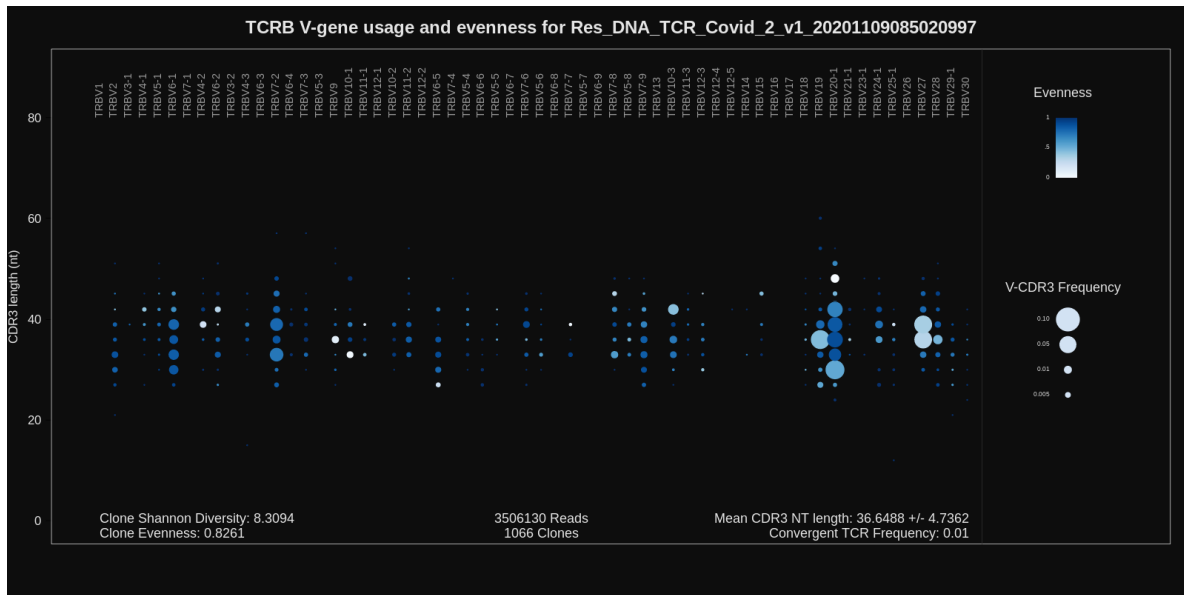
Repaired base composition
for Res_DNA_TCR_Covid_2_v1_2020110908502099



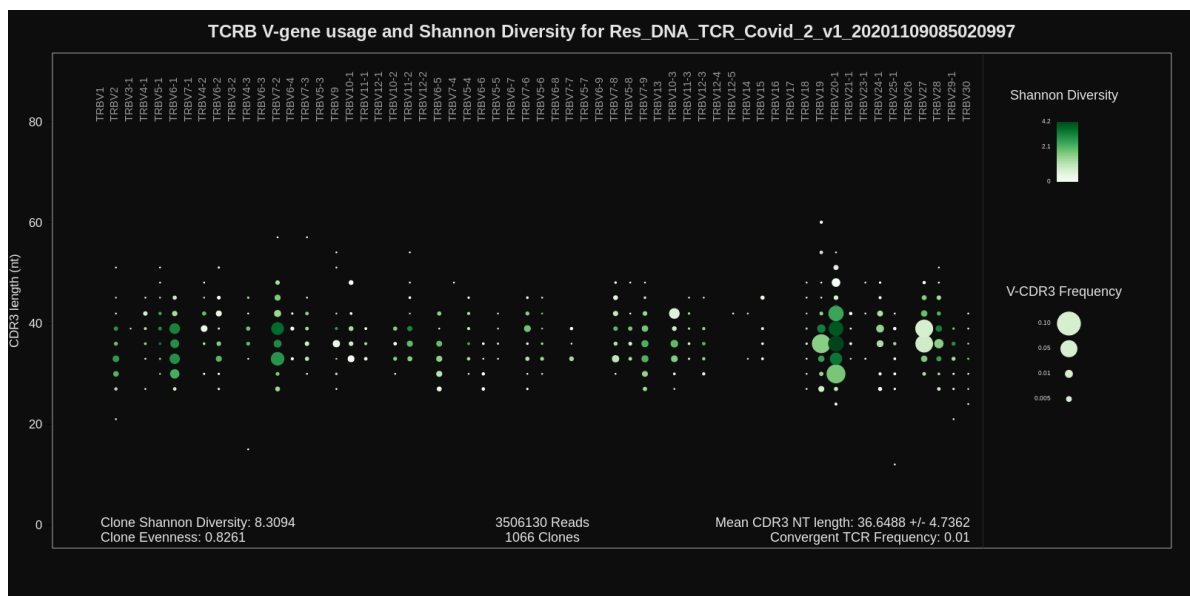




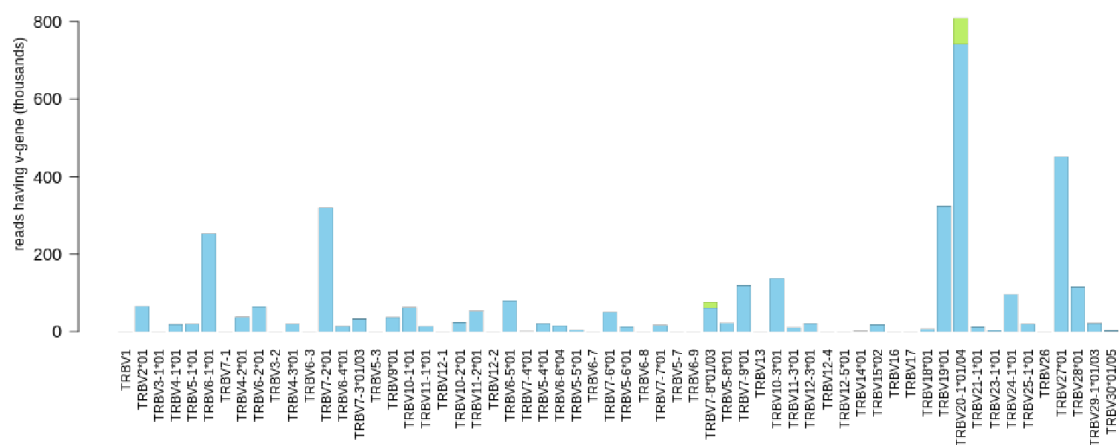
TCRB V-gene usage



TCRB V-gene usage

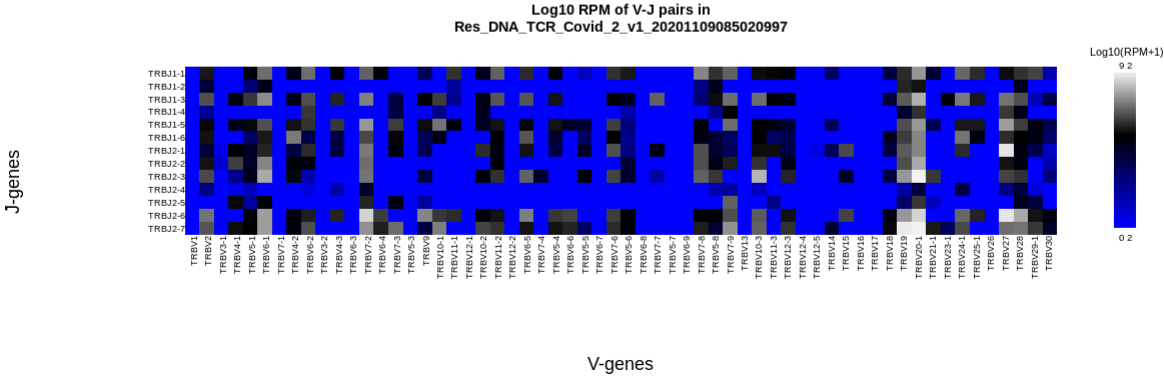
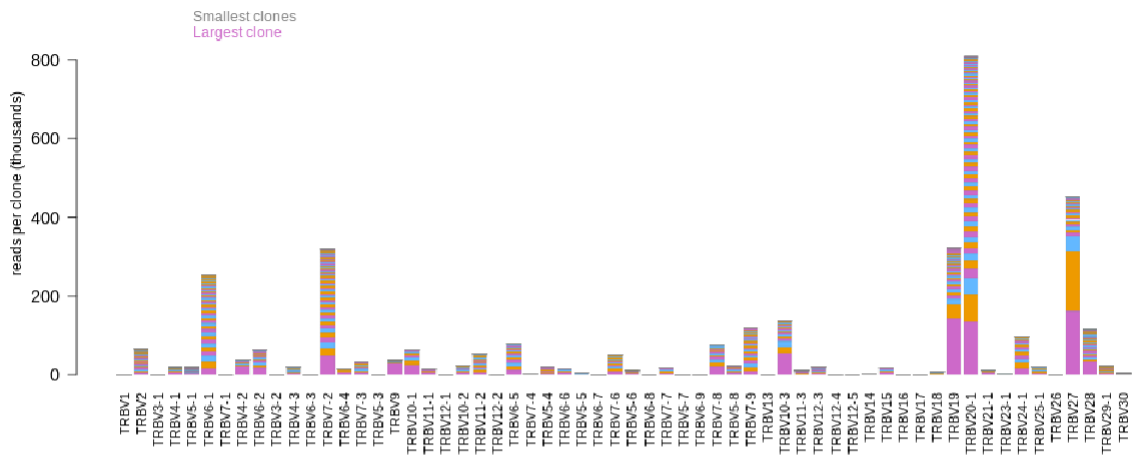


V-gene usage, colored by allele for Res_DNA_TCR_Covid_2_v1_20201109085020997

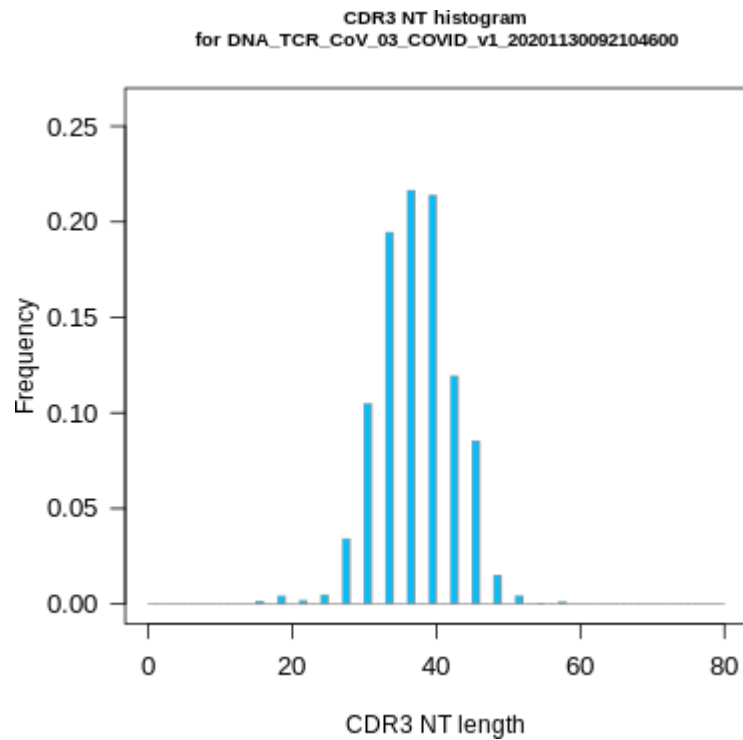


TCRB V-gene usage

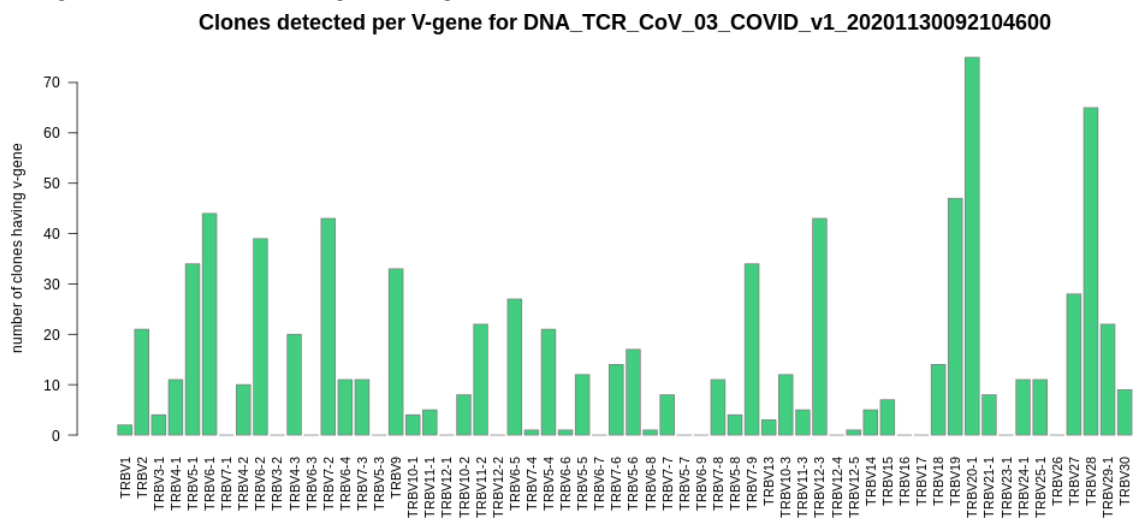
V-gene usage, colored by clone size for Res_DNA_TCR_Covid_2_v1_20201109085020997



COVID-19 lung early stage case 2

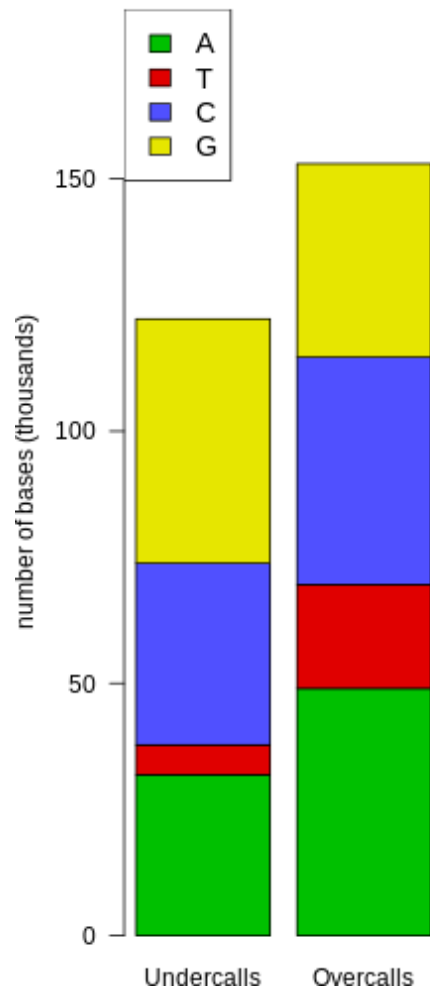


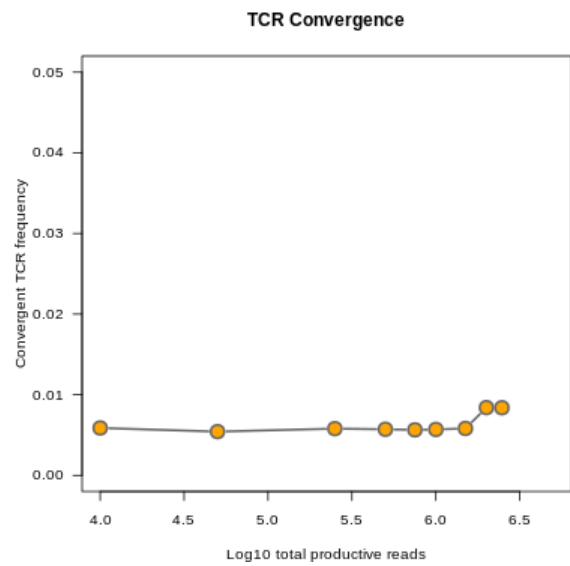
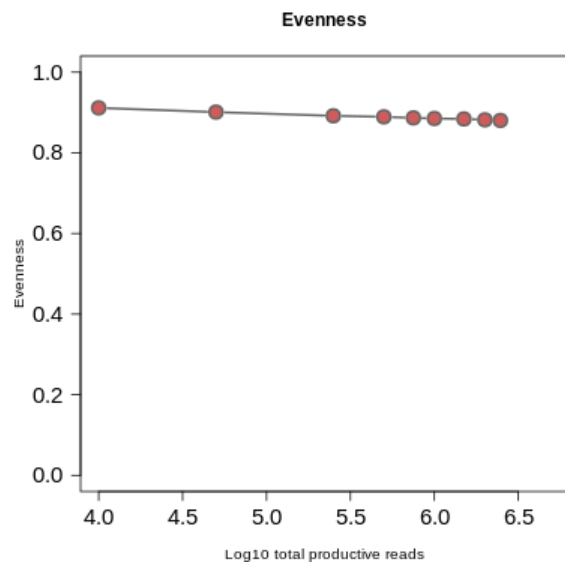
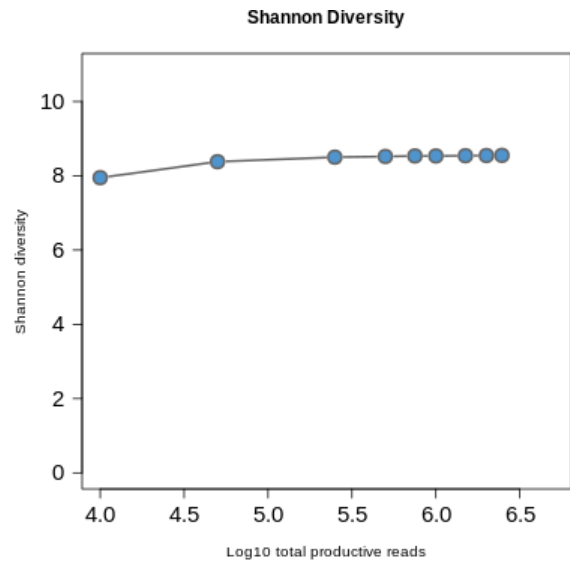
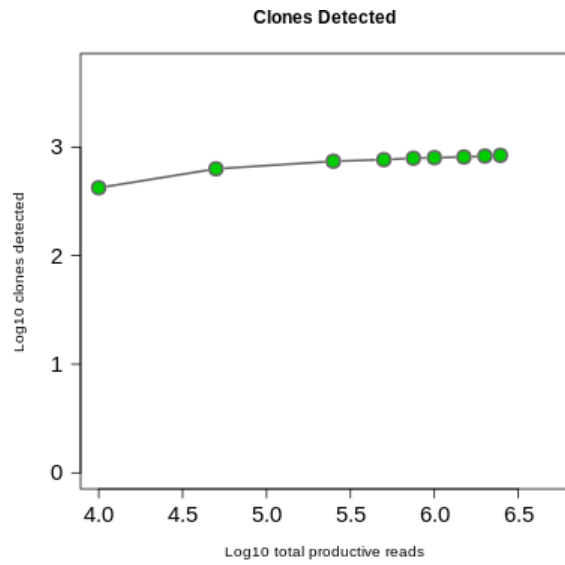
Histogram of CDR3 nucleotide length showing a normal distribution



Number of clones per V-gene

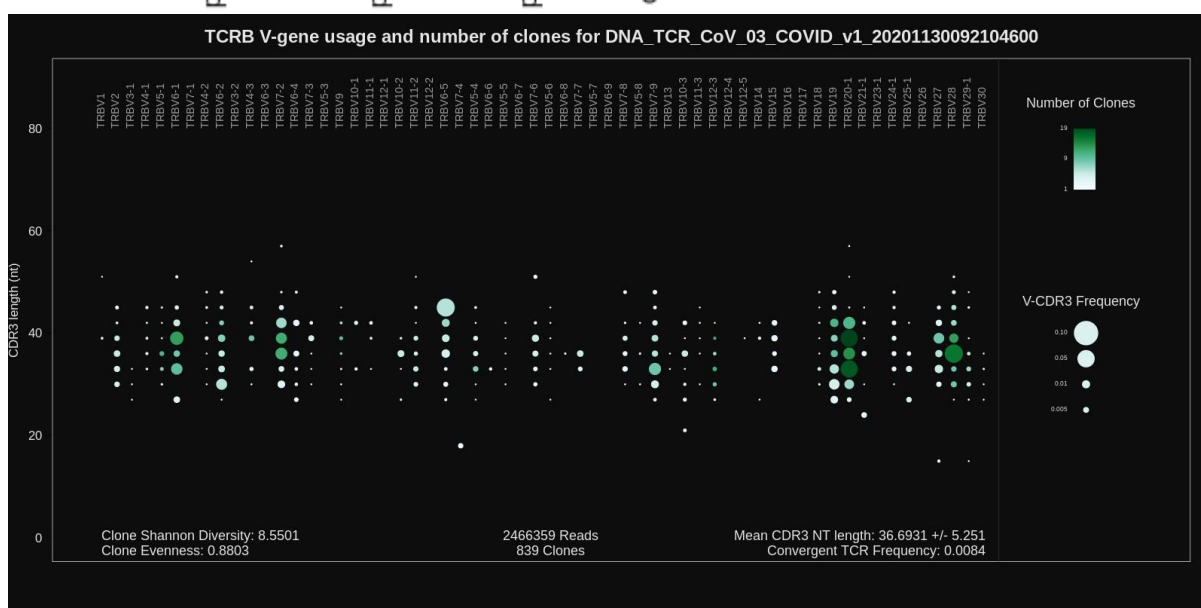
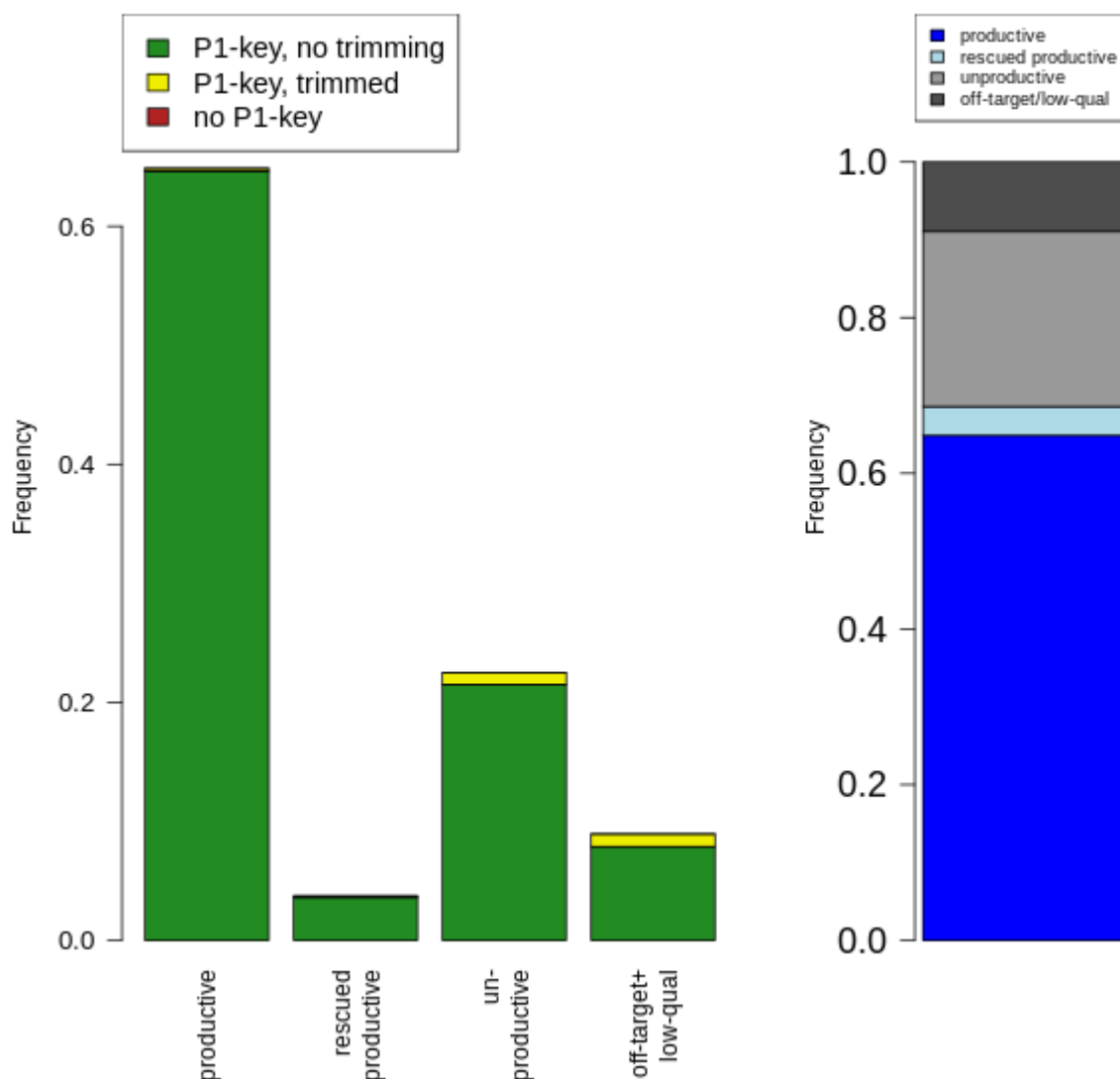
Repaired base composition
for DNA_TCR_CoV_03_COVID_v1_202011300921046



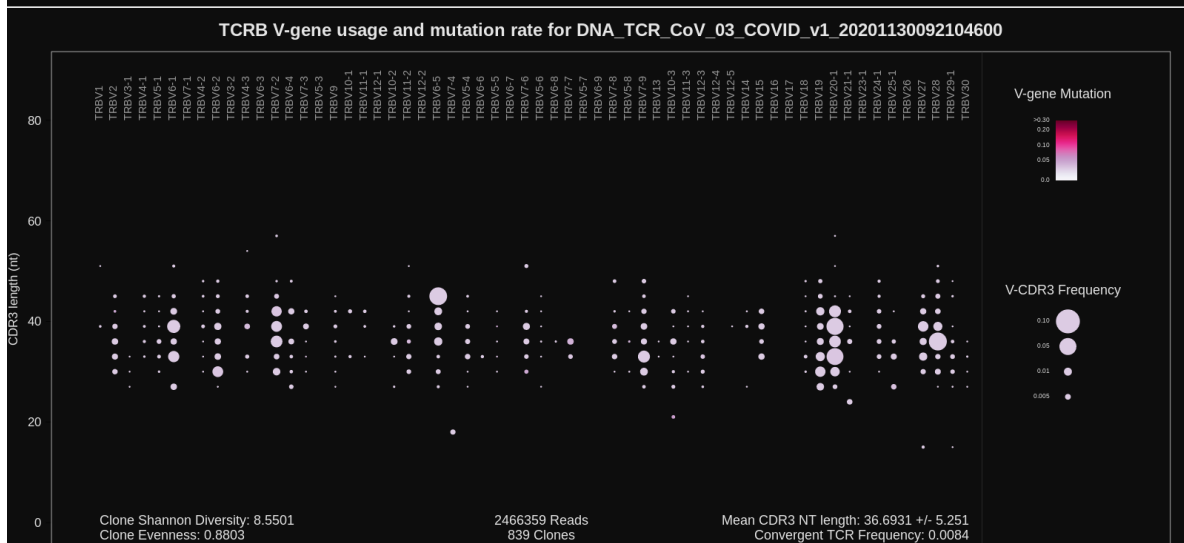
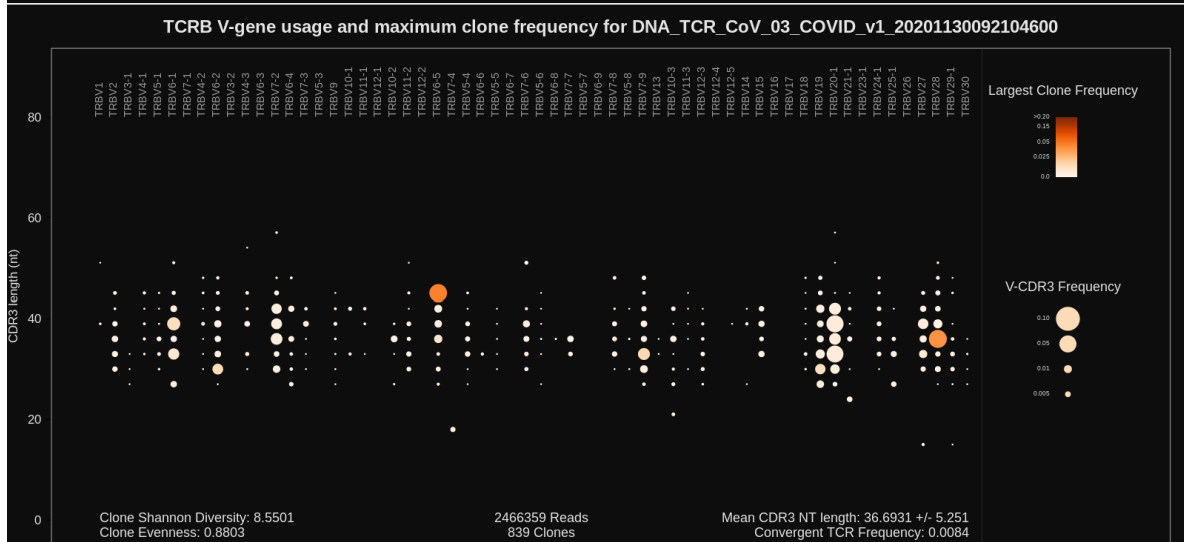
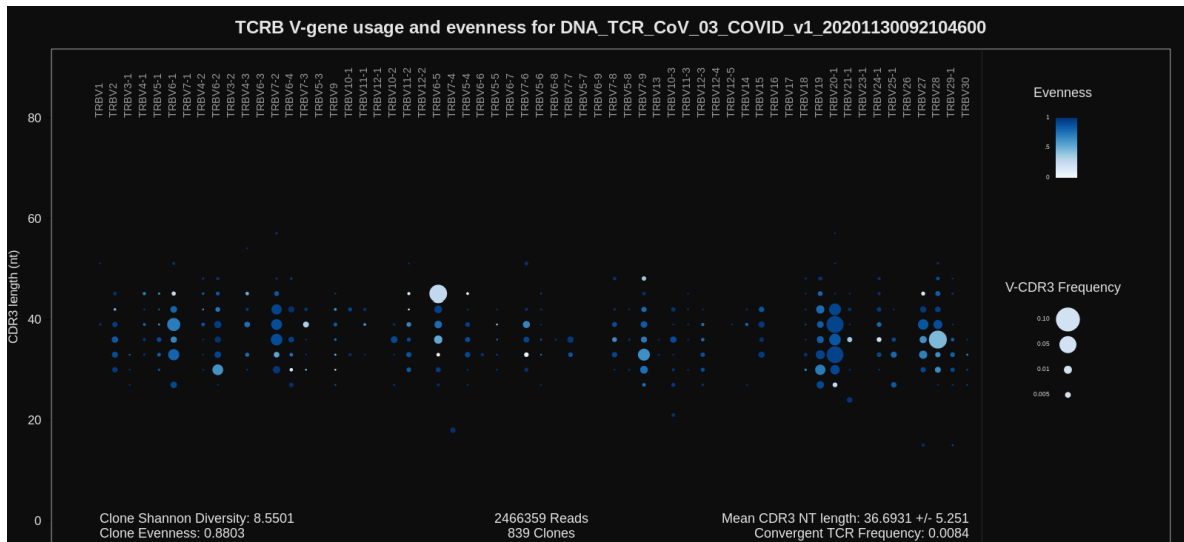


Presence of P1 adapter and quality trimming for DNA_TCR_CoV_03_COVID_v1_20201130092104600

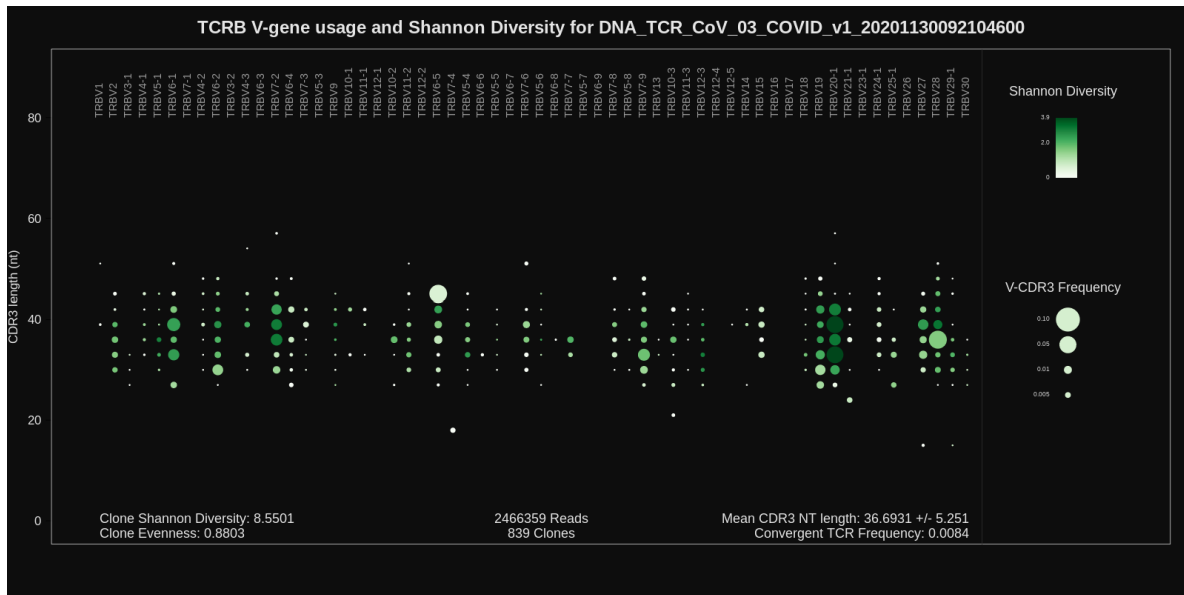
Read classification
for DNA_TCR_CoV_03_COVID_v1_20201130092104600



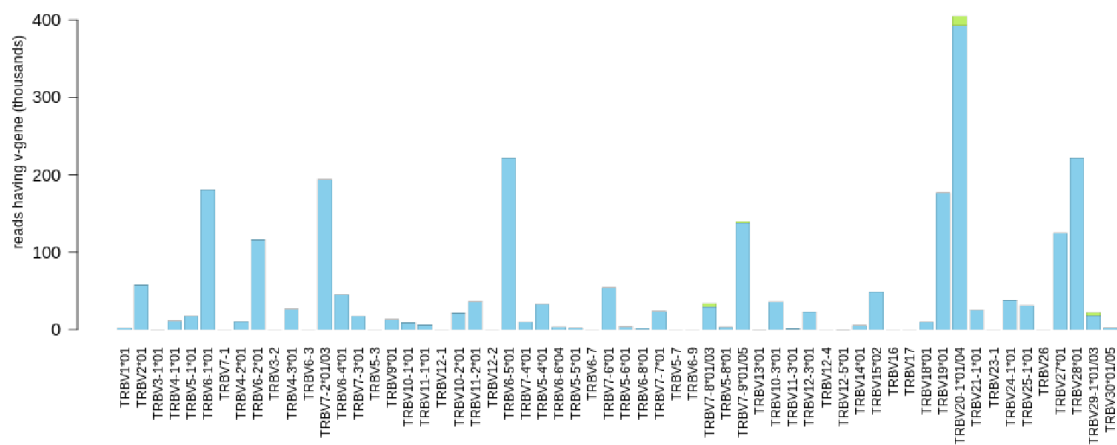
TCRB V-gene usage



TCRB V-gene usage

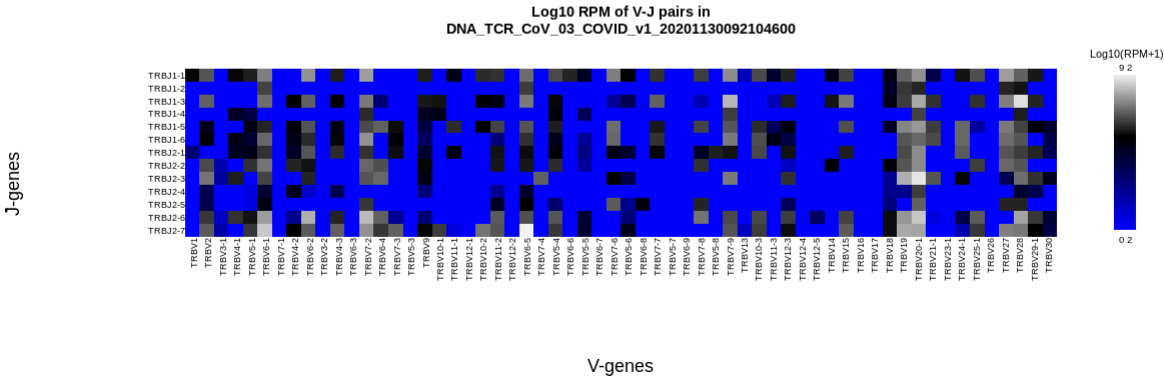
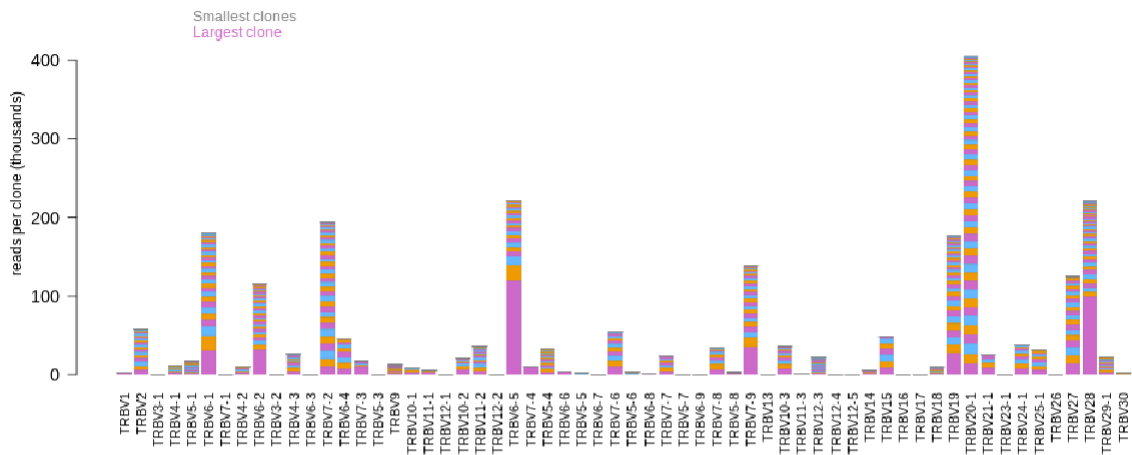


V-gene usage, colored by allele for DNA_TCR_CoV_03_COVID_v1_20201130092104600

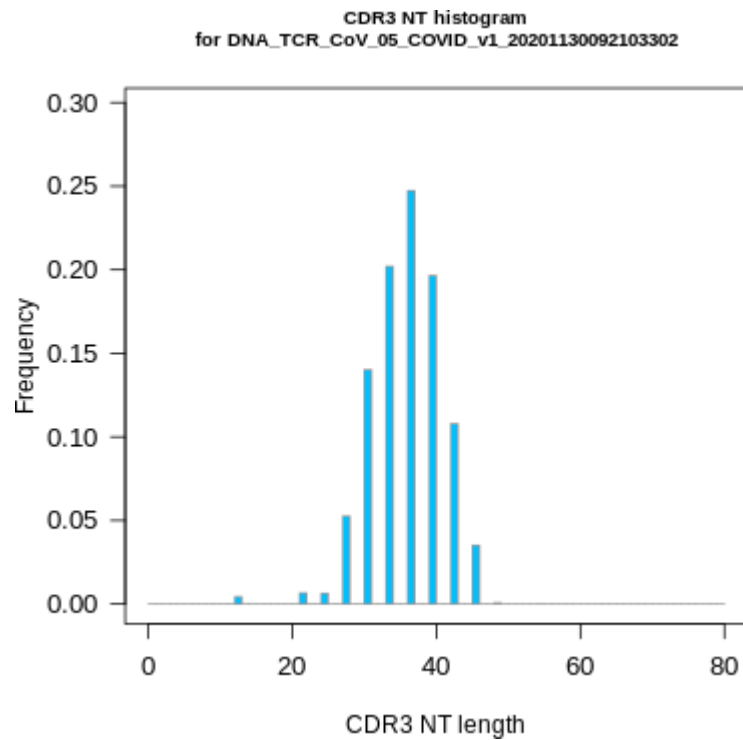


TCRB V-gene usage

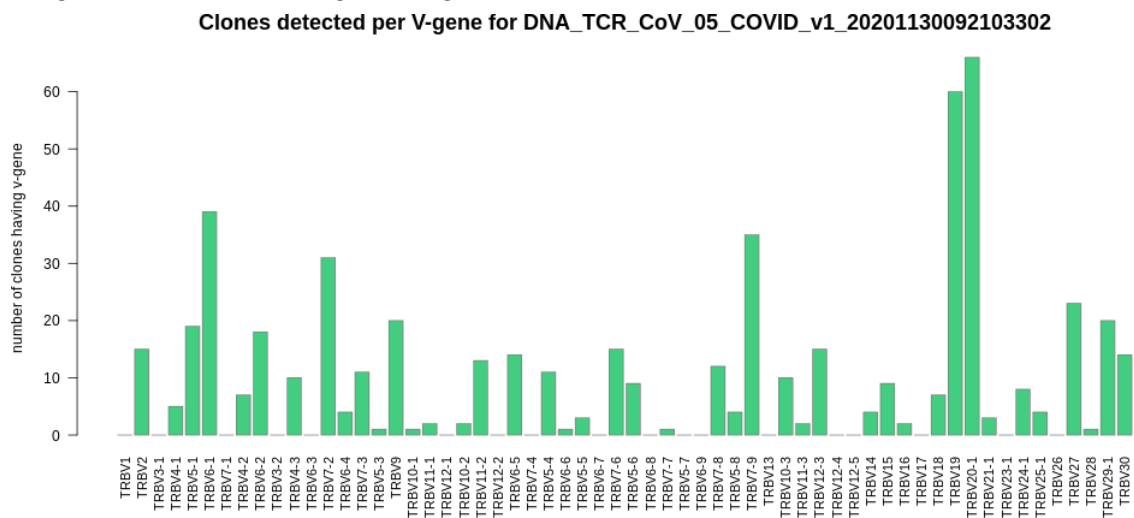
V-gene usage, colored by clone size for DNA_TCR_CoV_03_COVID_v1_20201130092104600



COVID-19 lung late stage case 1

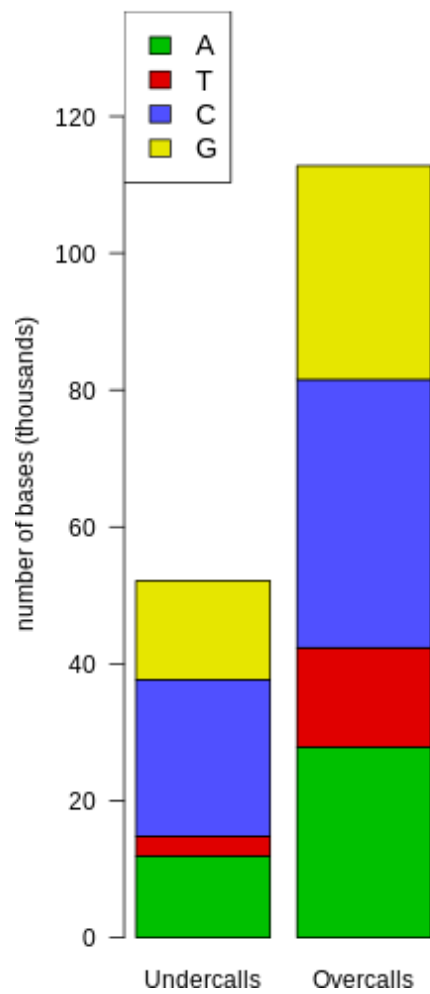


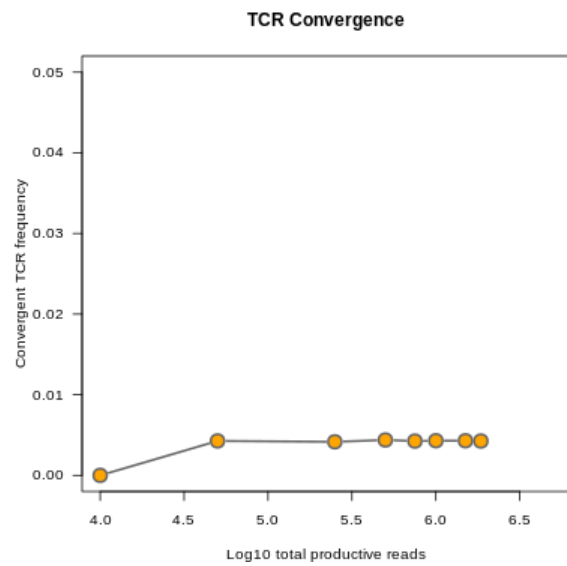
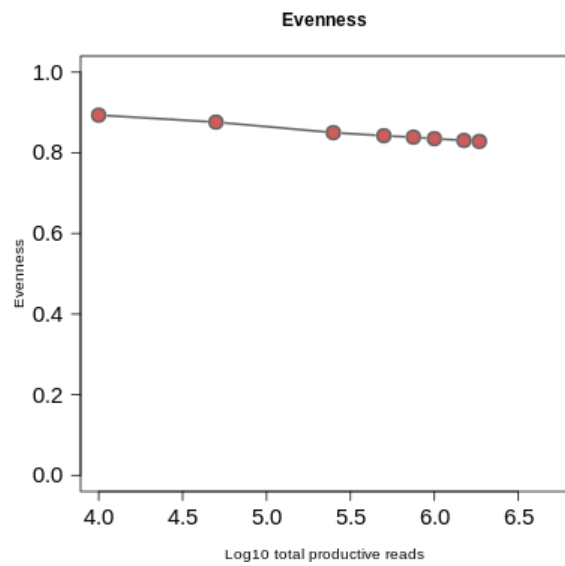
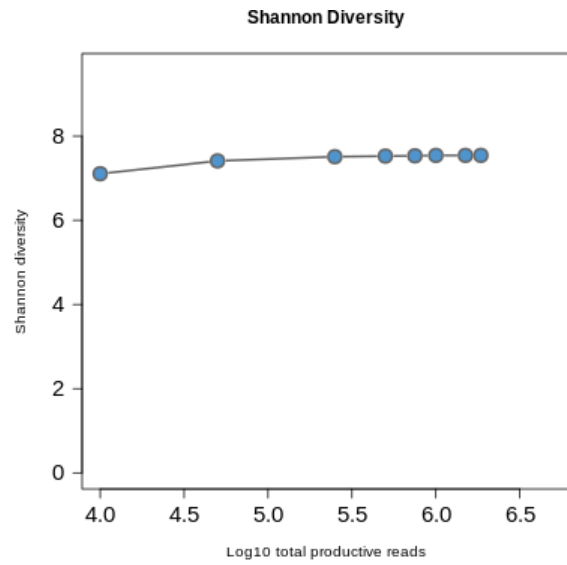
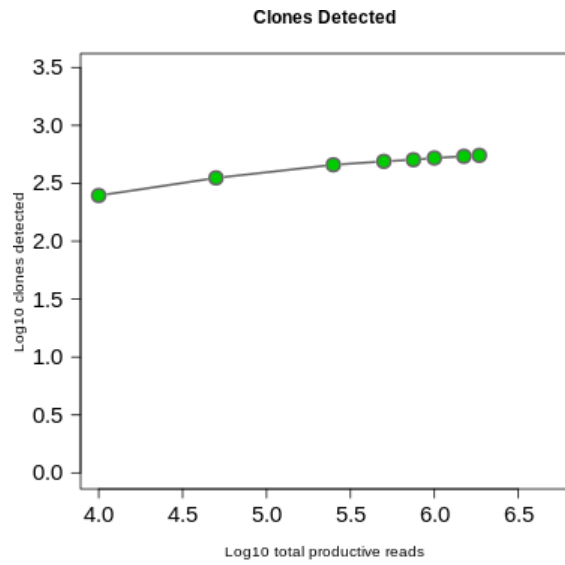
Histogram of CDR3 nucleotide length showing a normal distribution

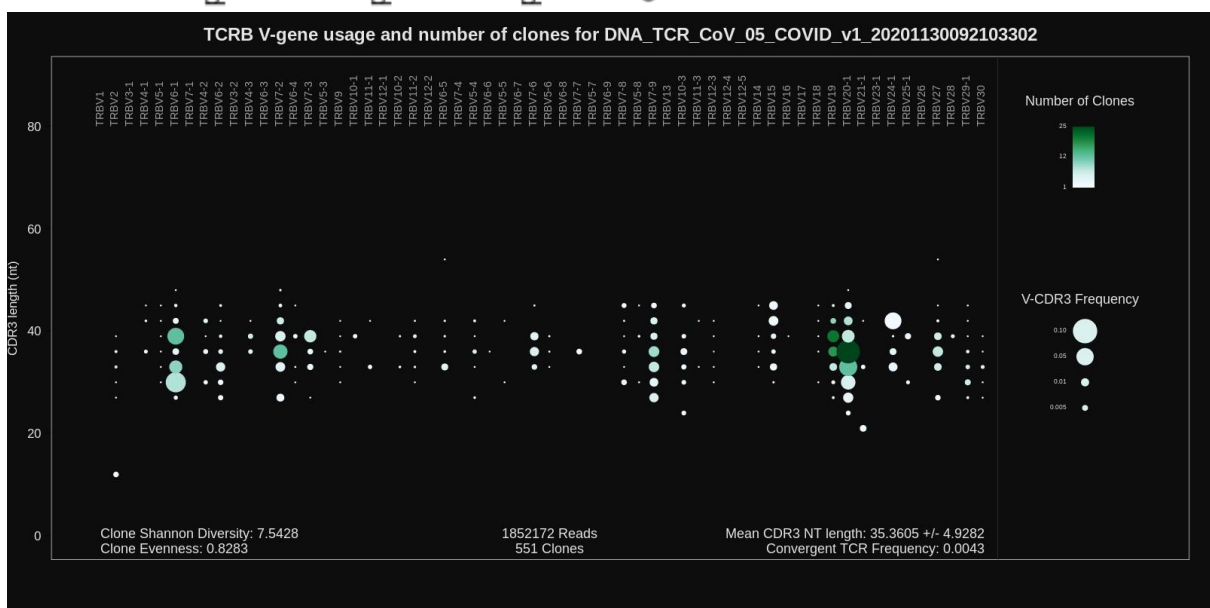
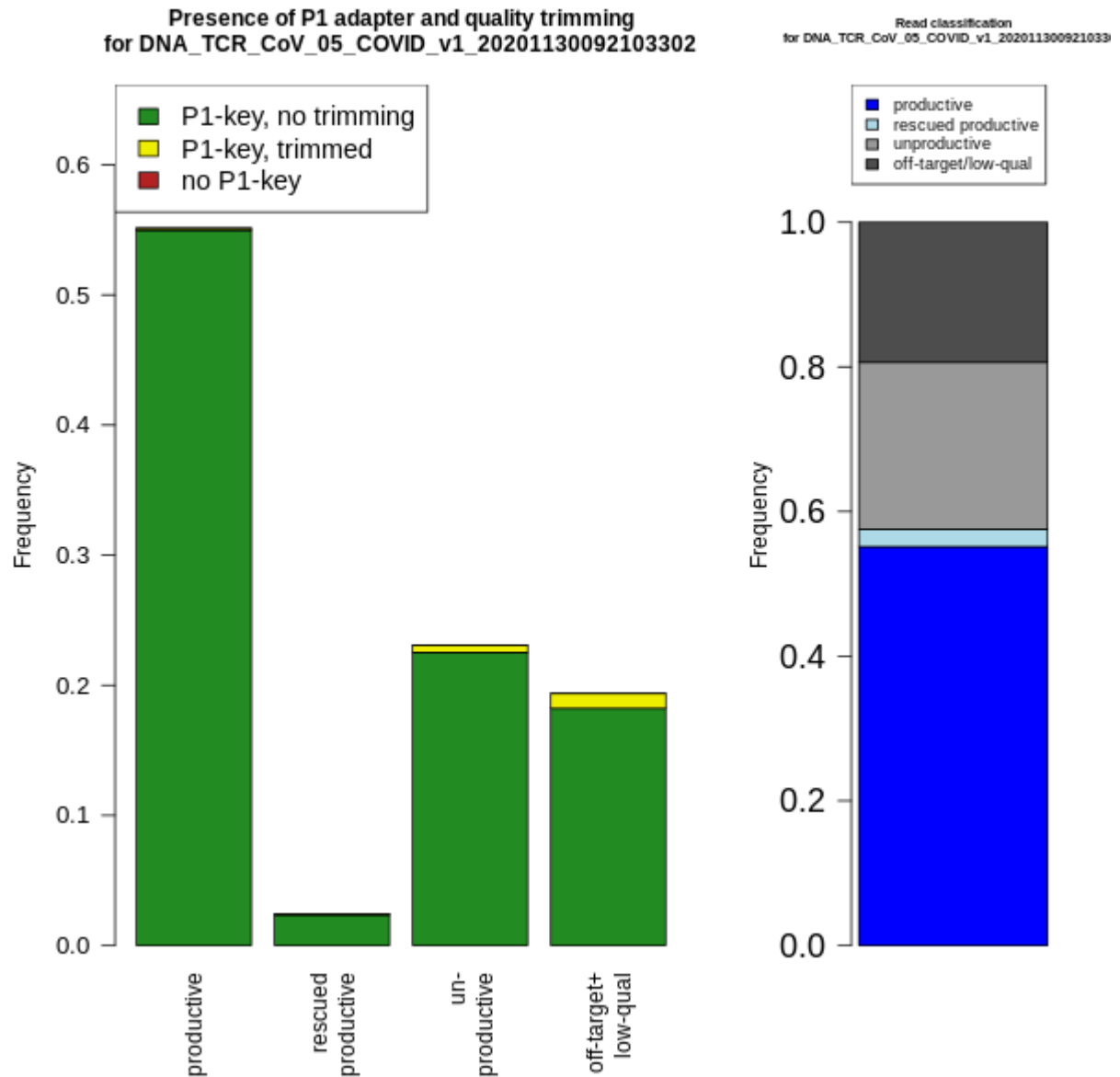


Number of clones per V-gene

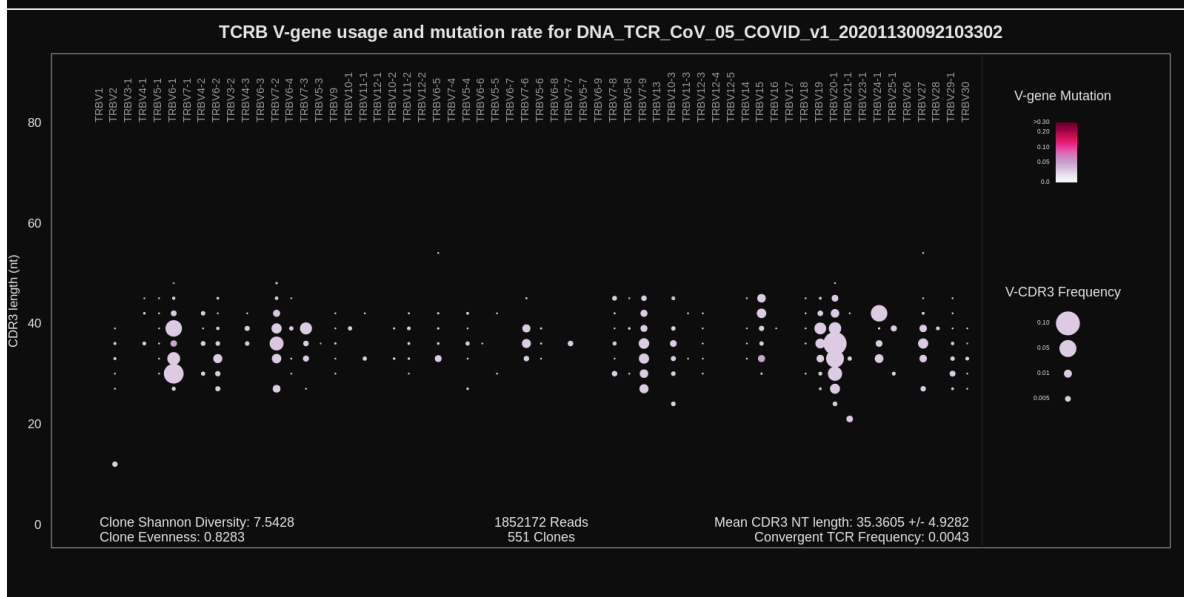
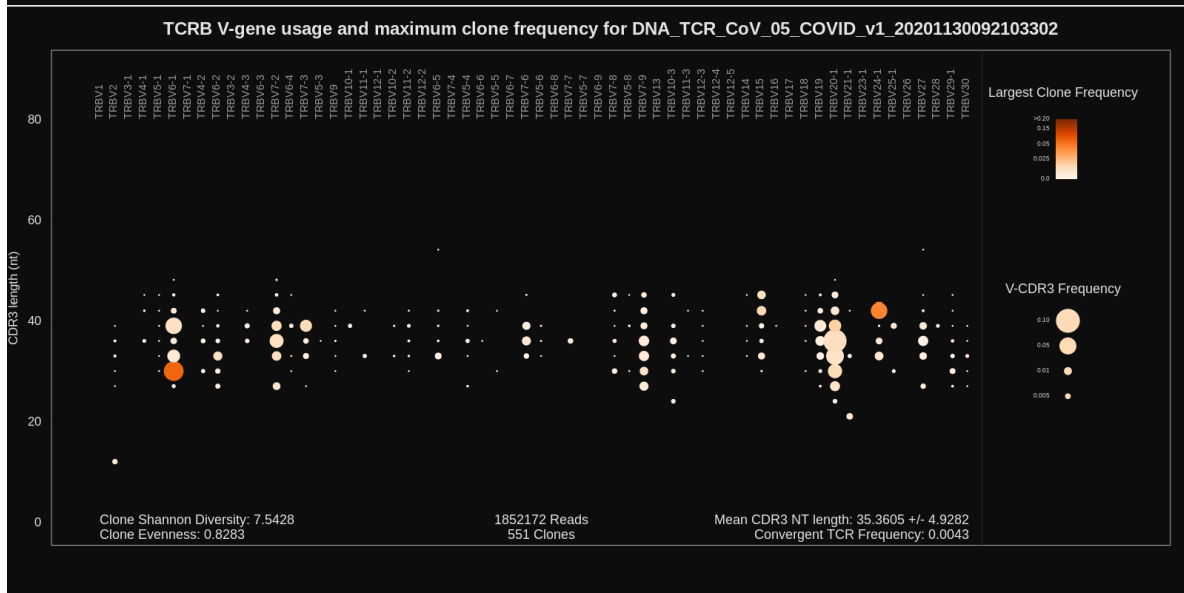
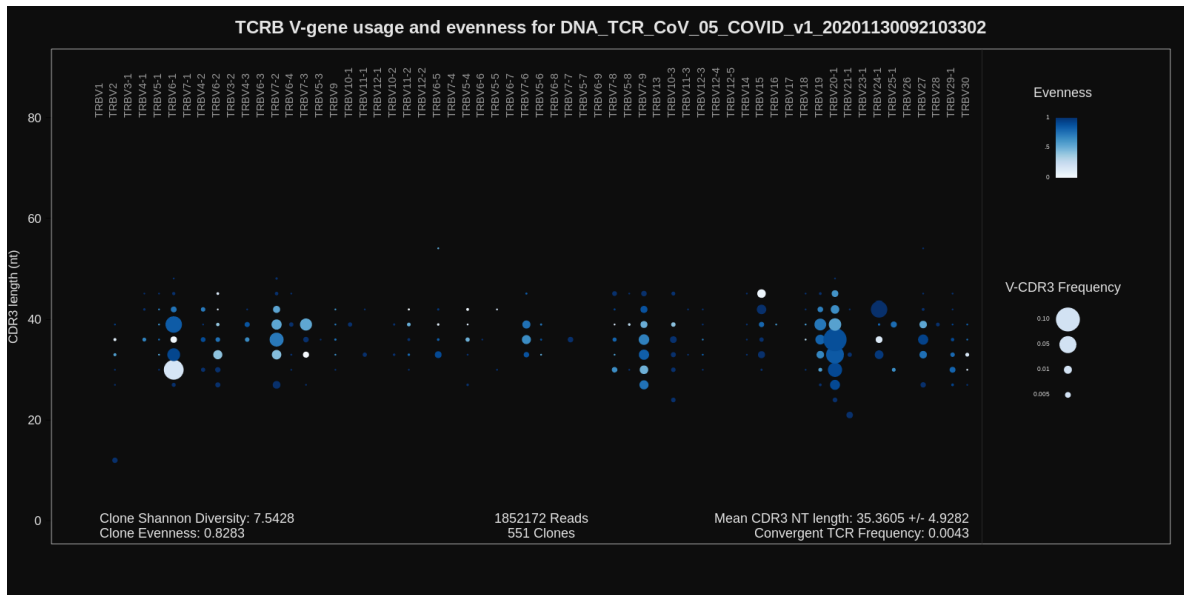
Repaired base composition
for DNA_TCR_CoV_05_COVID_v1_202011300921033



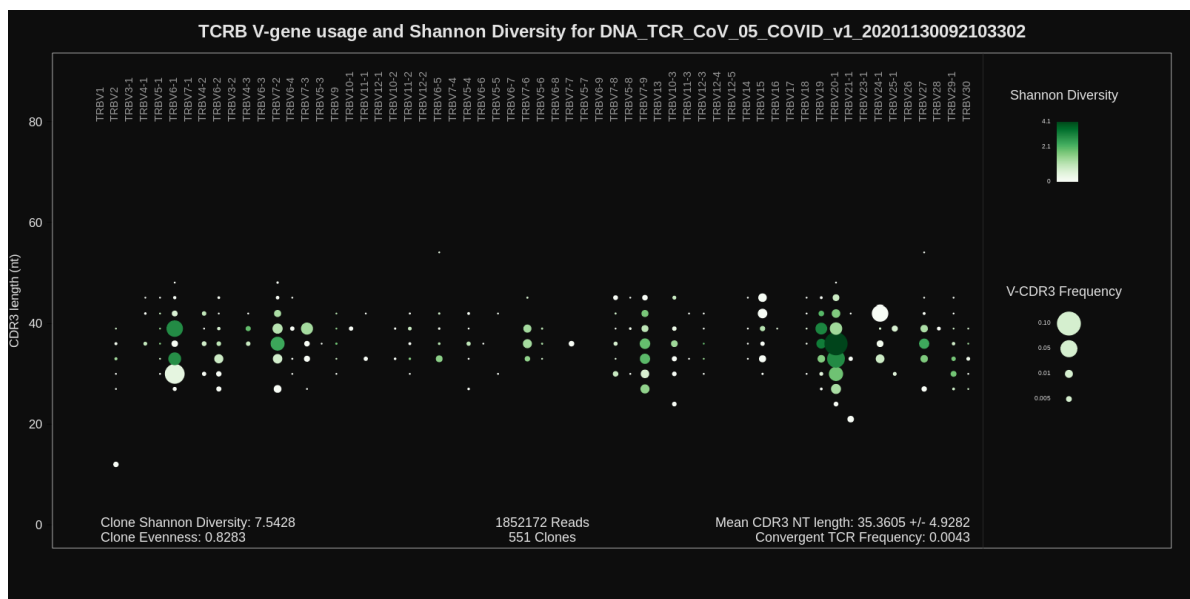




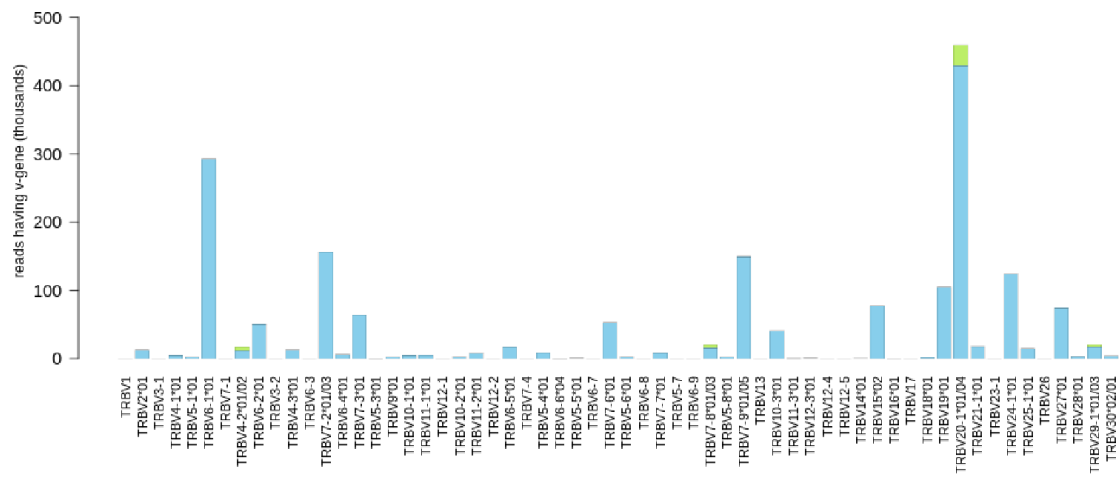
TCRB V-gene usage



TCRB V-gene usage

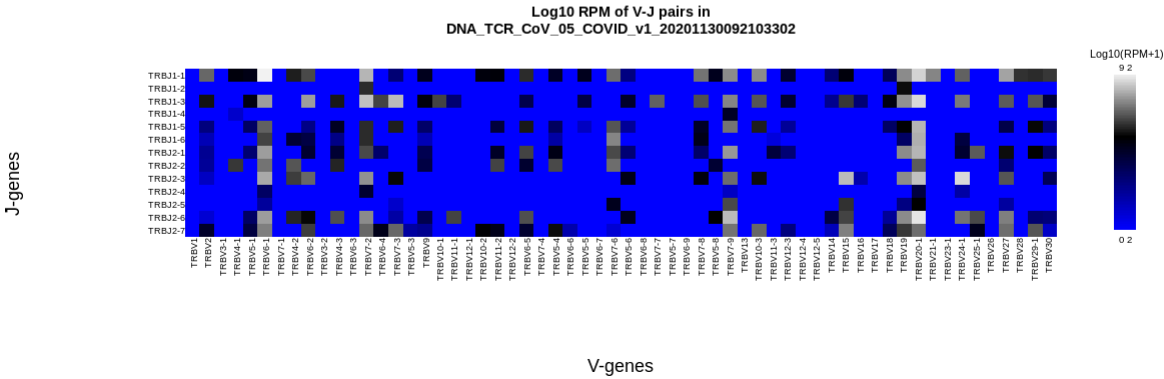
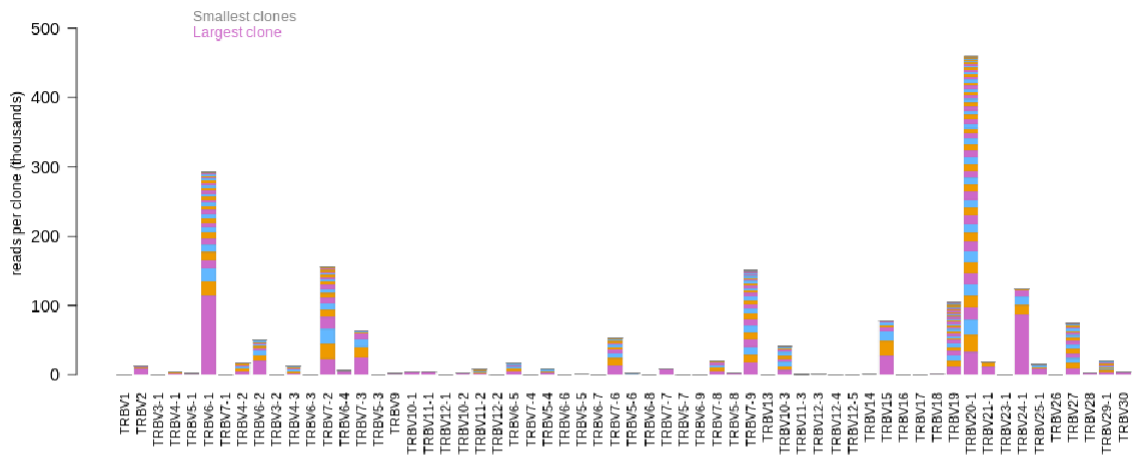


V-gene usage, colored by allele for DNA_TCR_CoV_05_COVID_v1_20201130092103302

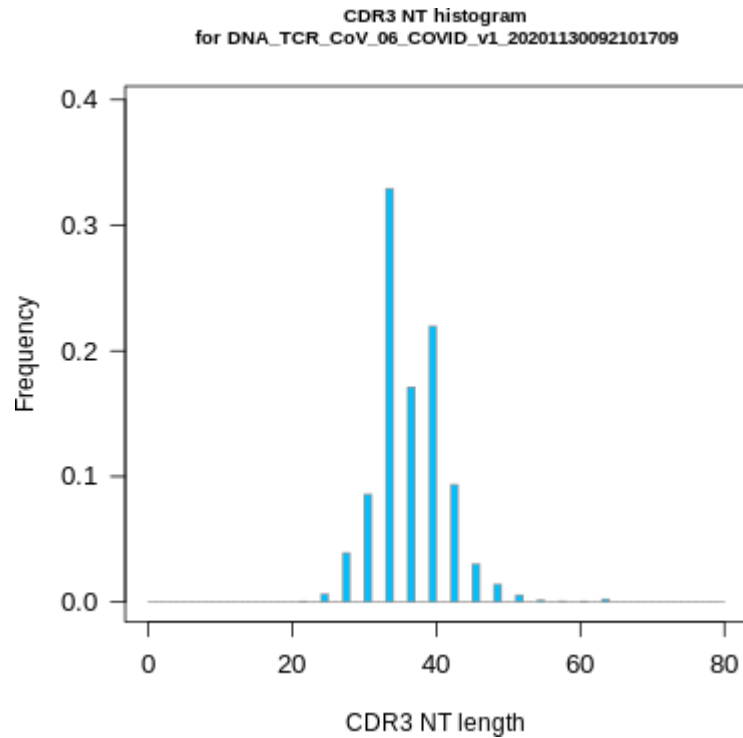


TCRB V-gene usage

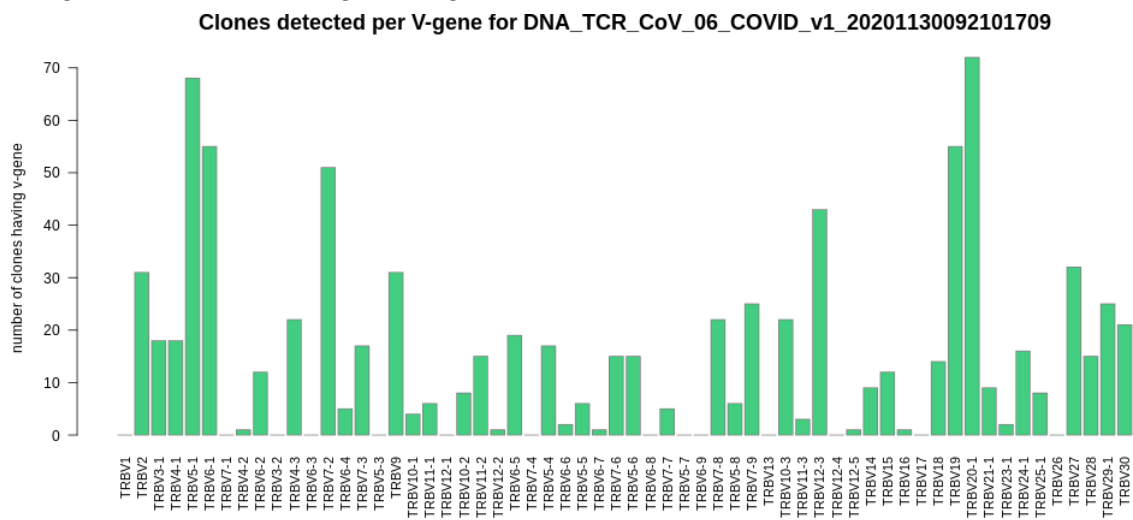
V-gene usage, colored by clone size for DNA_TCR_CoV_05_COVID_v1_20201130092103302



COVID-19 lung late stage case 2

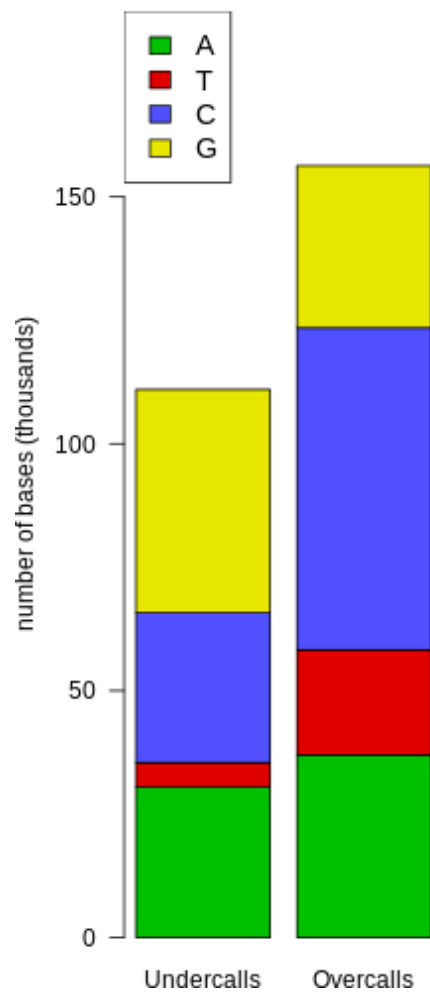


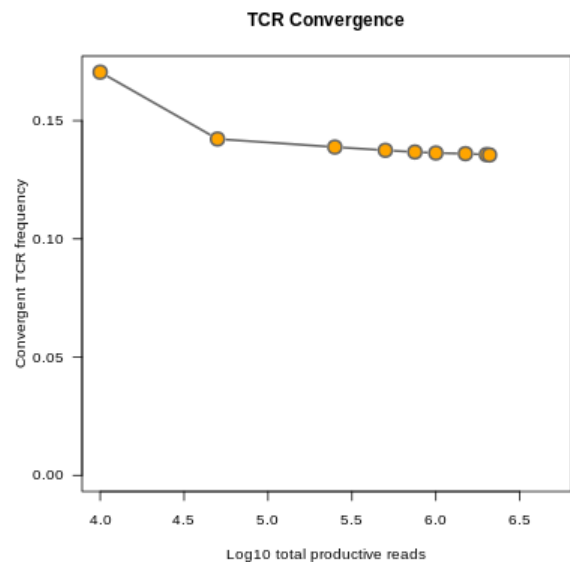
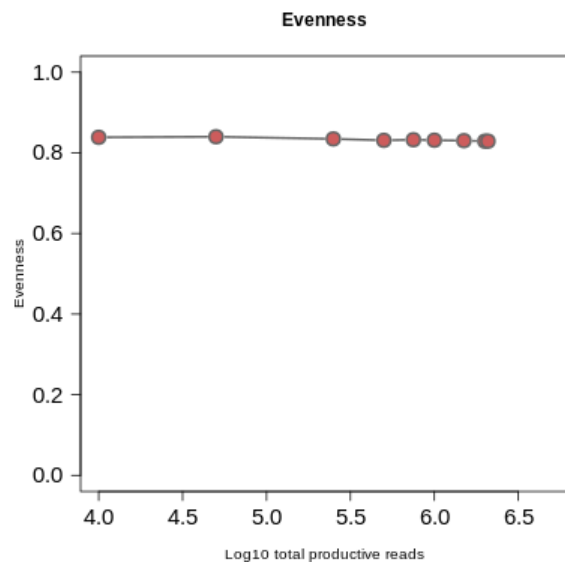
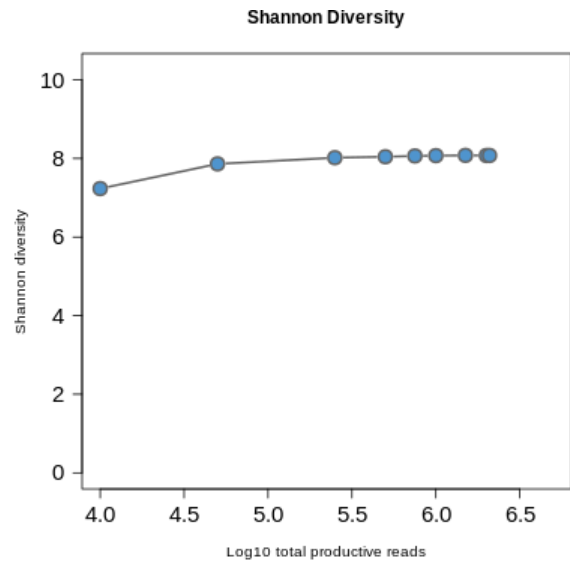
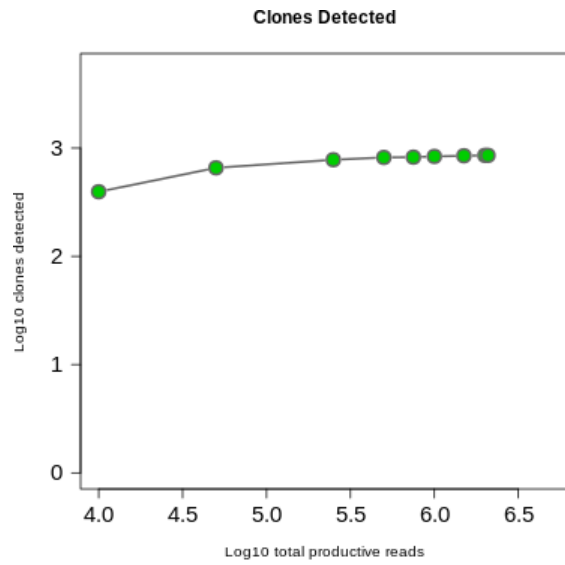
Histogram of CDR3 nucleotide length showing a normal distribution

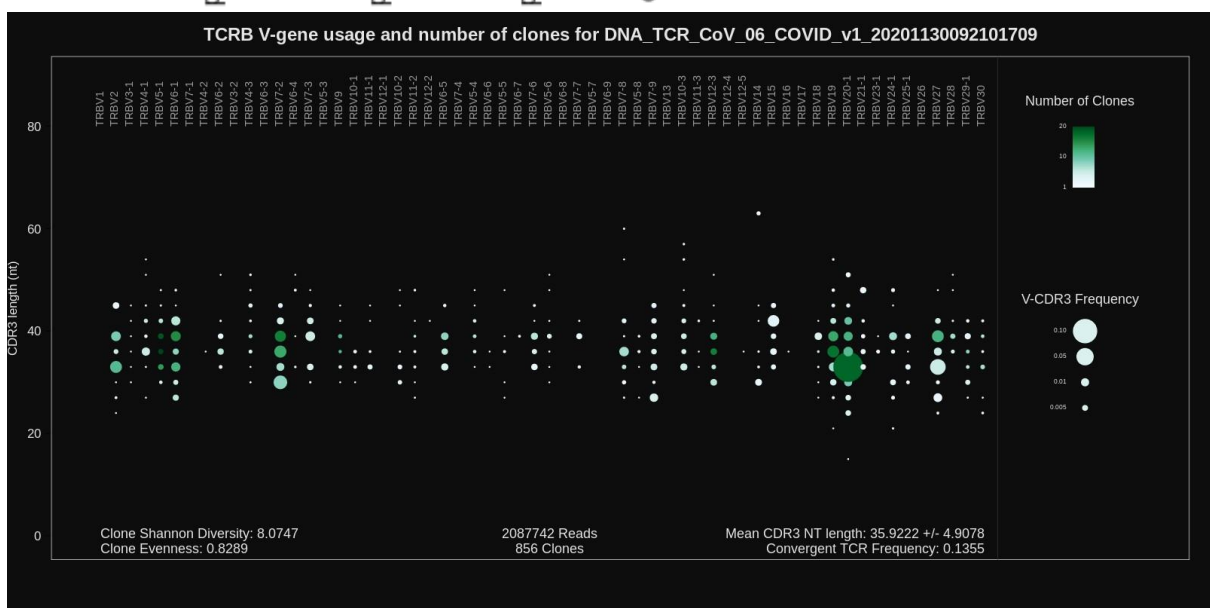
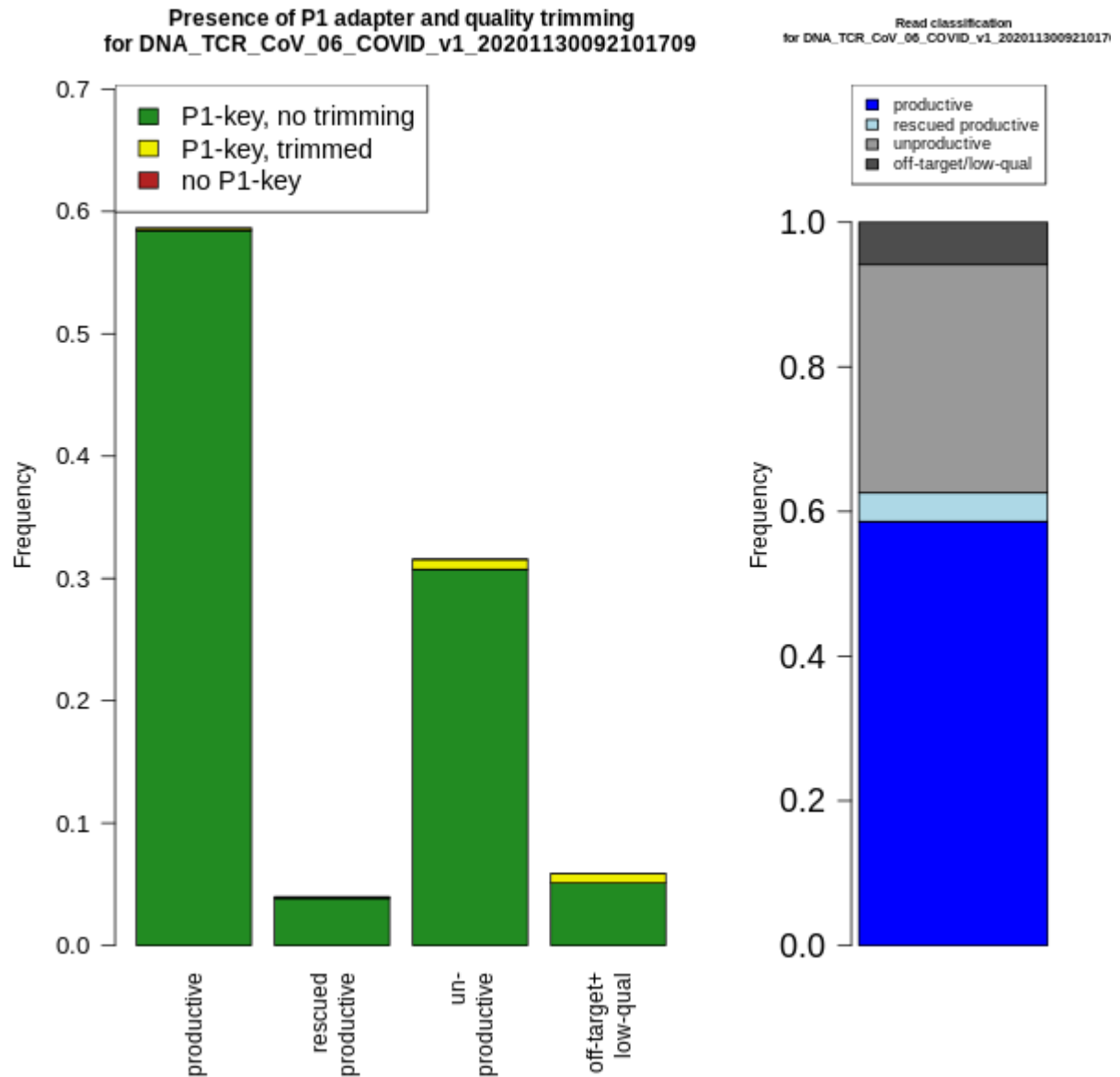


Number of clones per V-gene

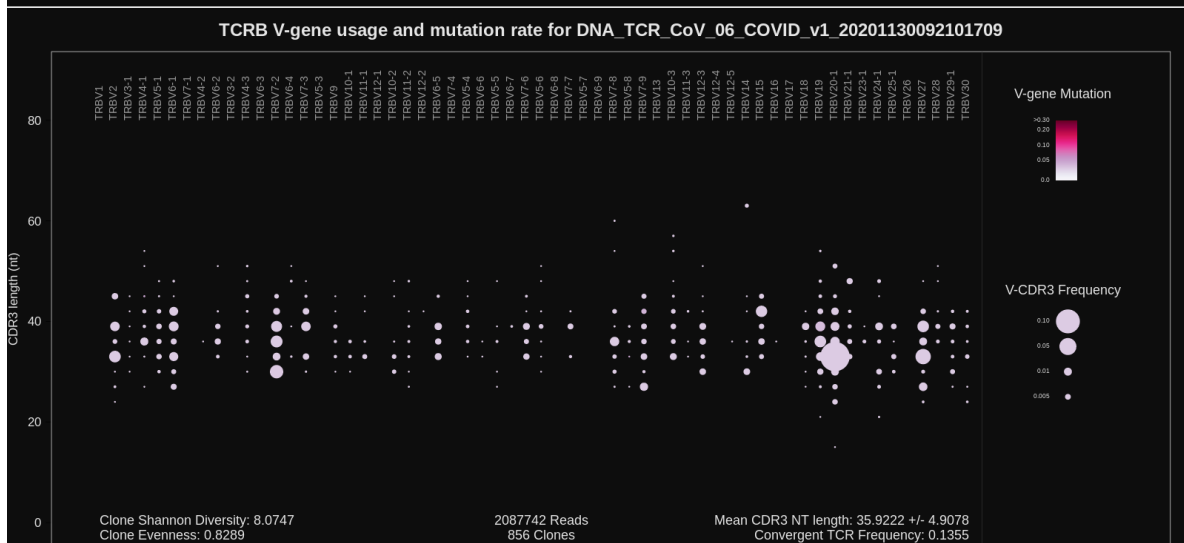
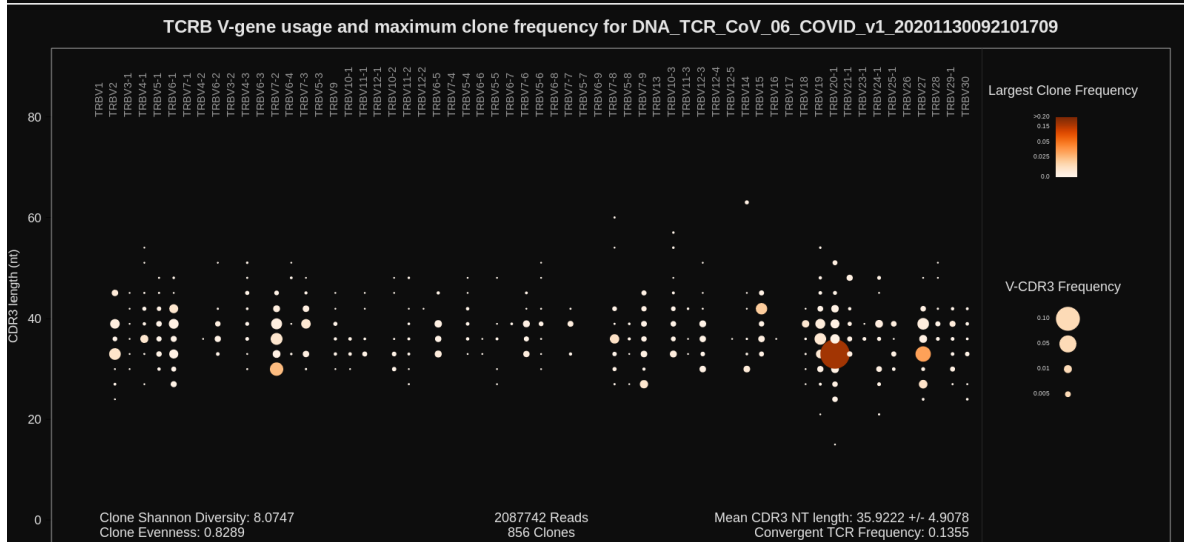
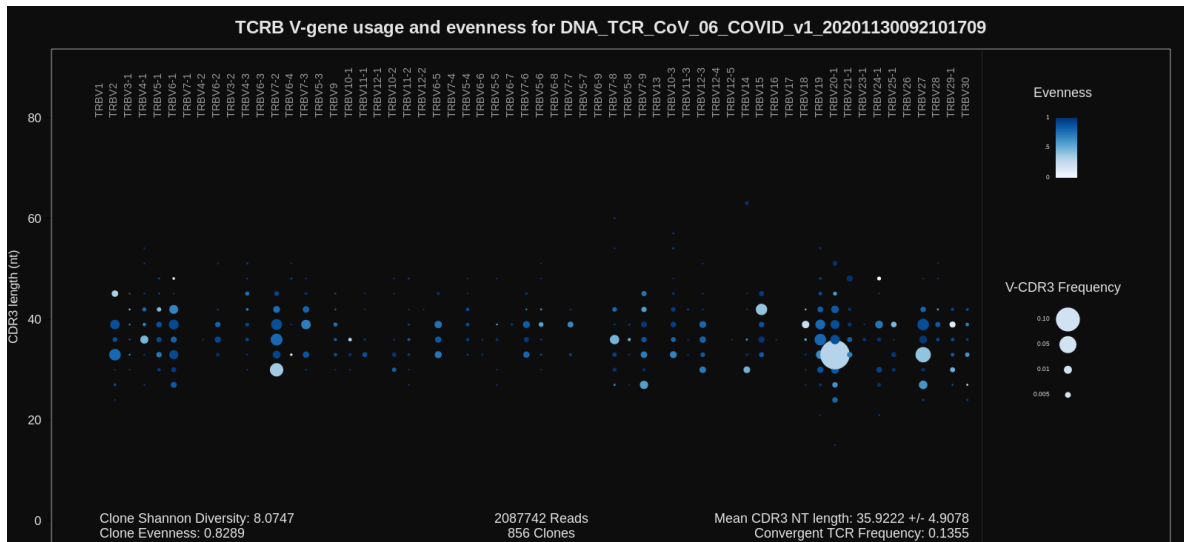
Repaired base composition
for DNA_TCR_CoV_06_COVID_v1_202011300921017



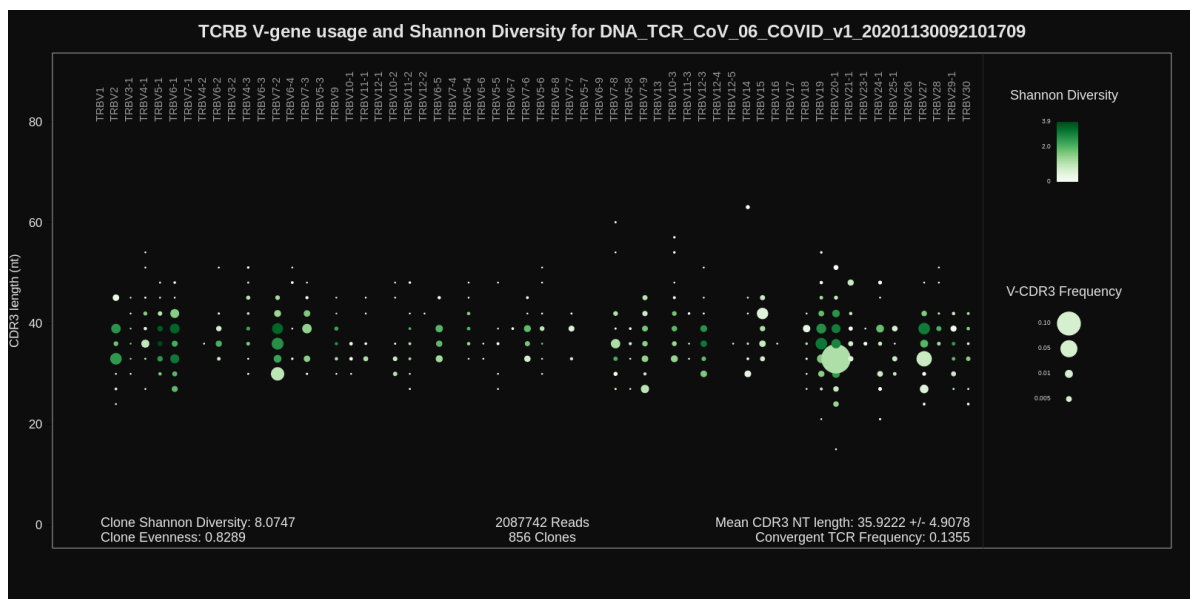




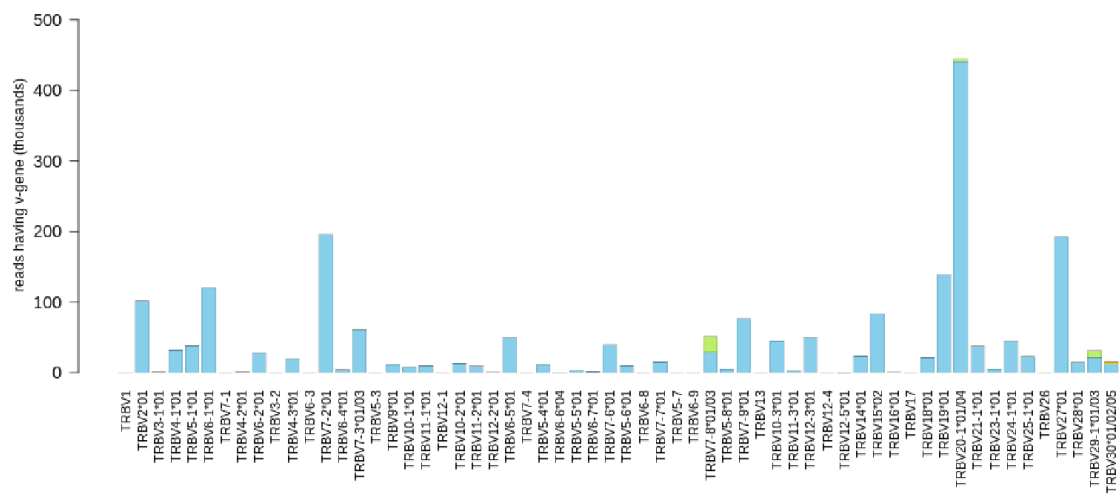
TCRB V-gene usage



TCRB V-gene usage

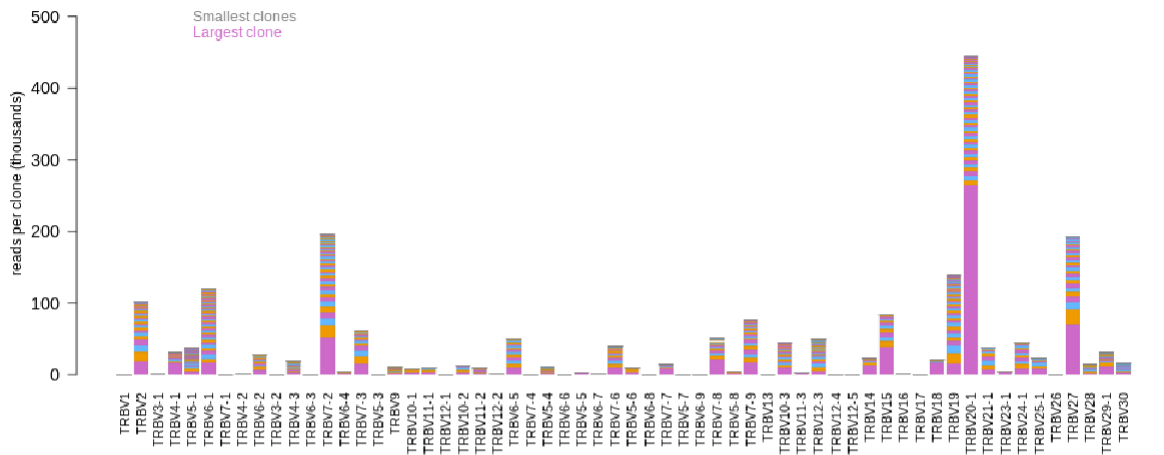


V-gene usage, colored by allele for DNA_TCR_CoV_06_COVID_v1_20201130092101709

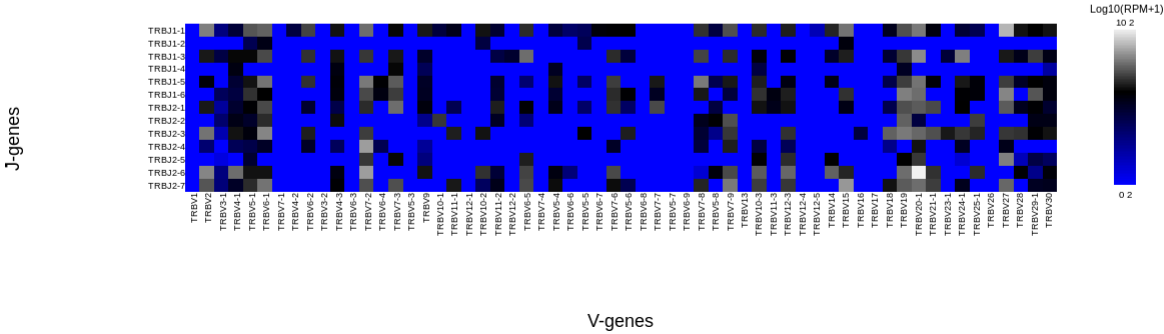


TCRB V-gene usage

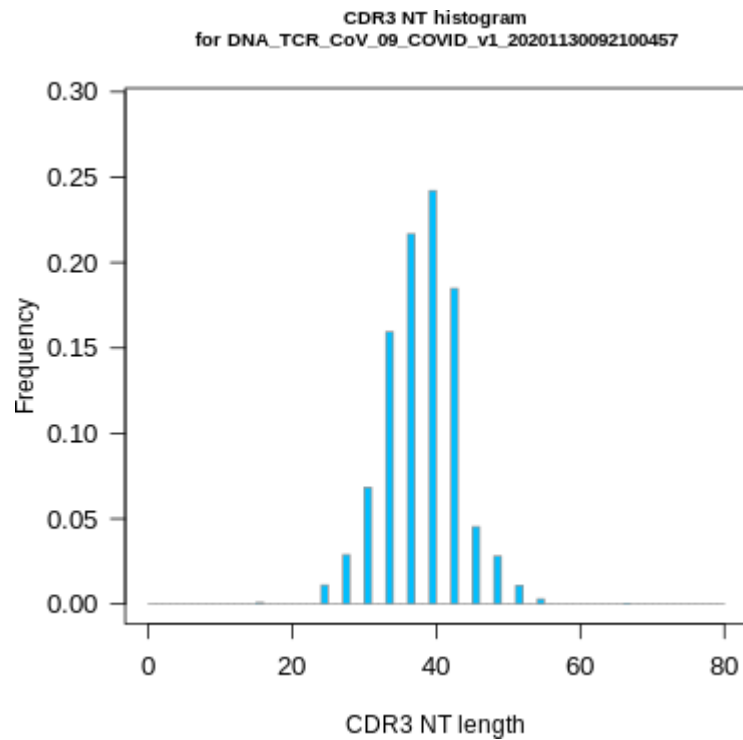
V-gene usage, colored by clone size for DNA_TCR_CoV_06_COVID_v1_20201130092101709



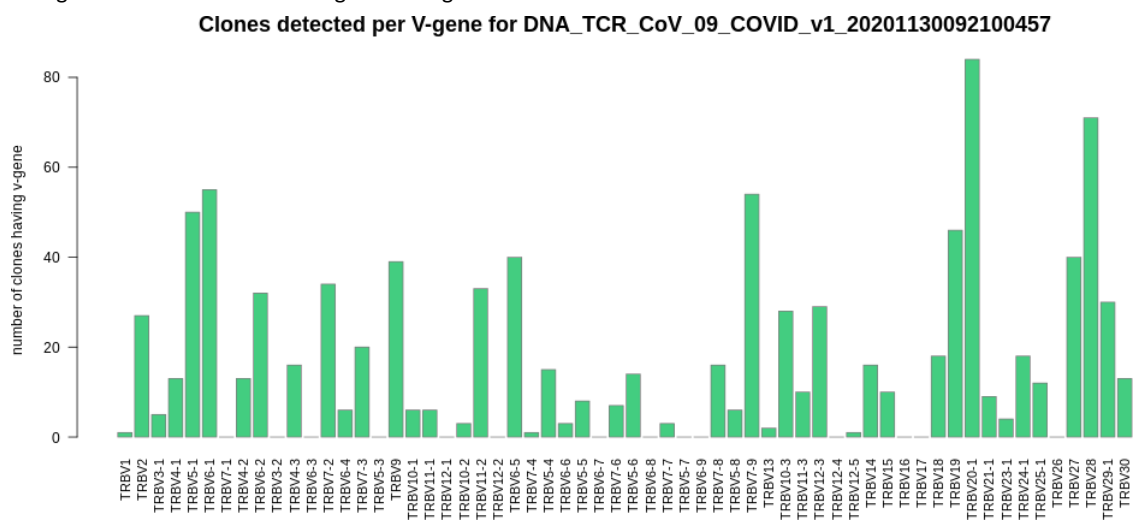
Log10 RPM of V-J pairs in
DNA_TCR_CoV_06_COVID_v1_20201130092101709



COVID-19 lung late stage case 3

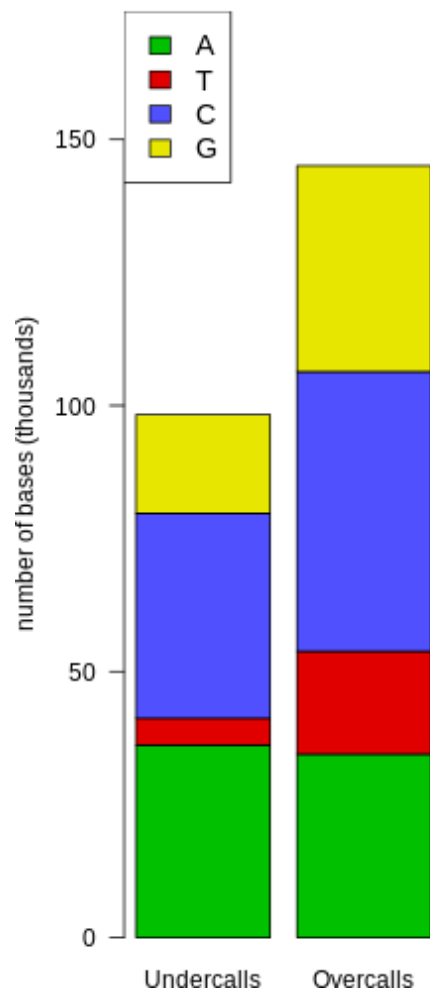


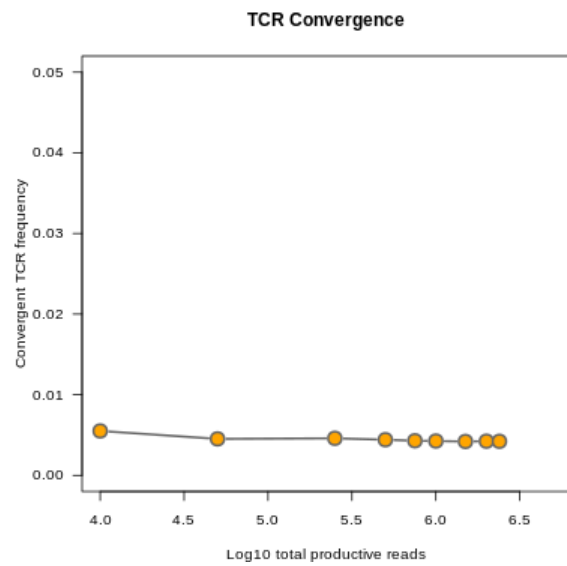
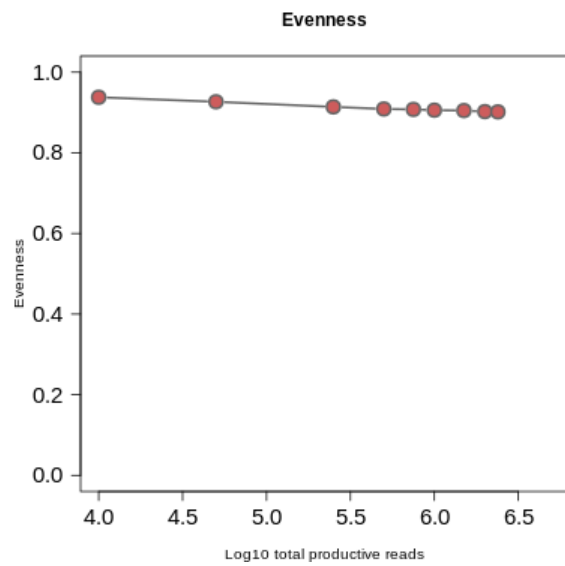
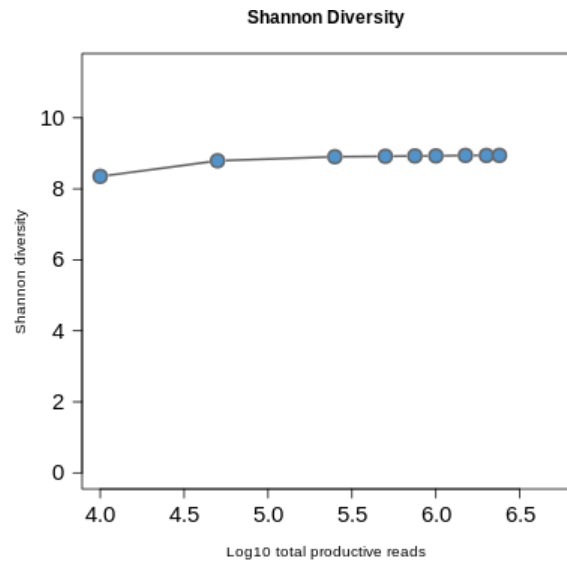
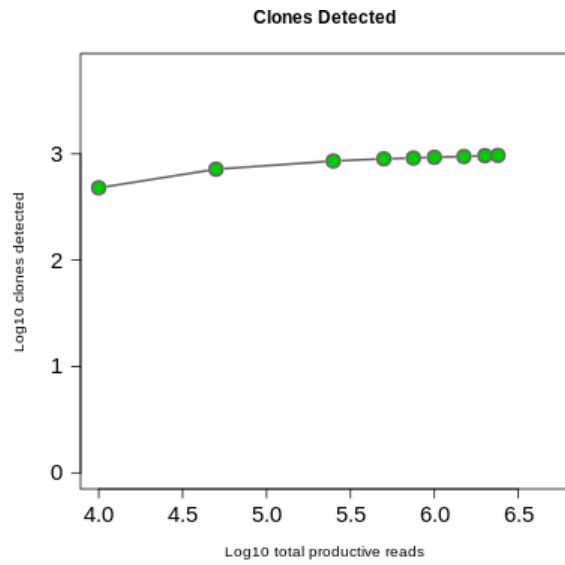
Histogram of CDR3 nucleotide length showing a normal distribution



Number of clones per V-gene

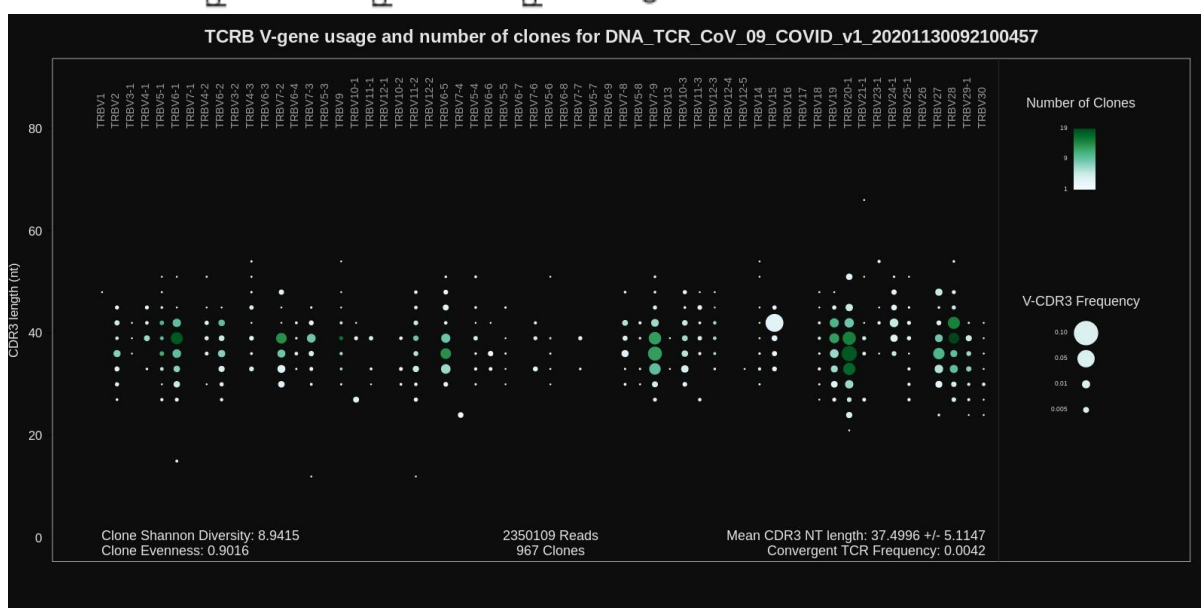
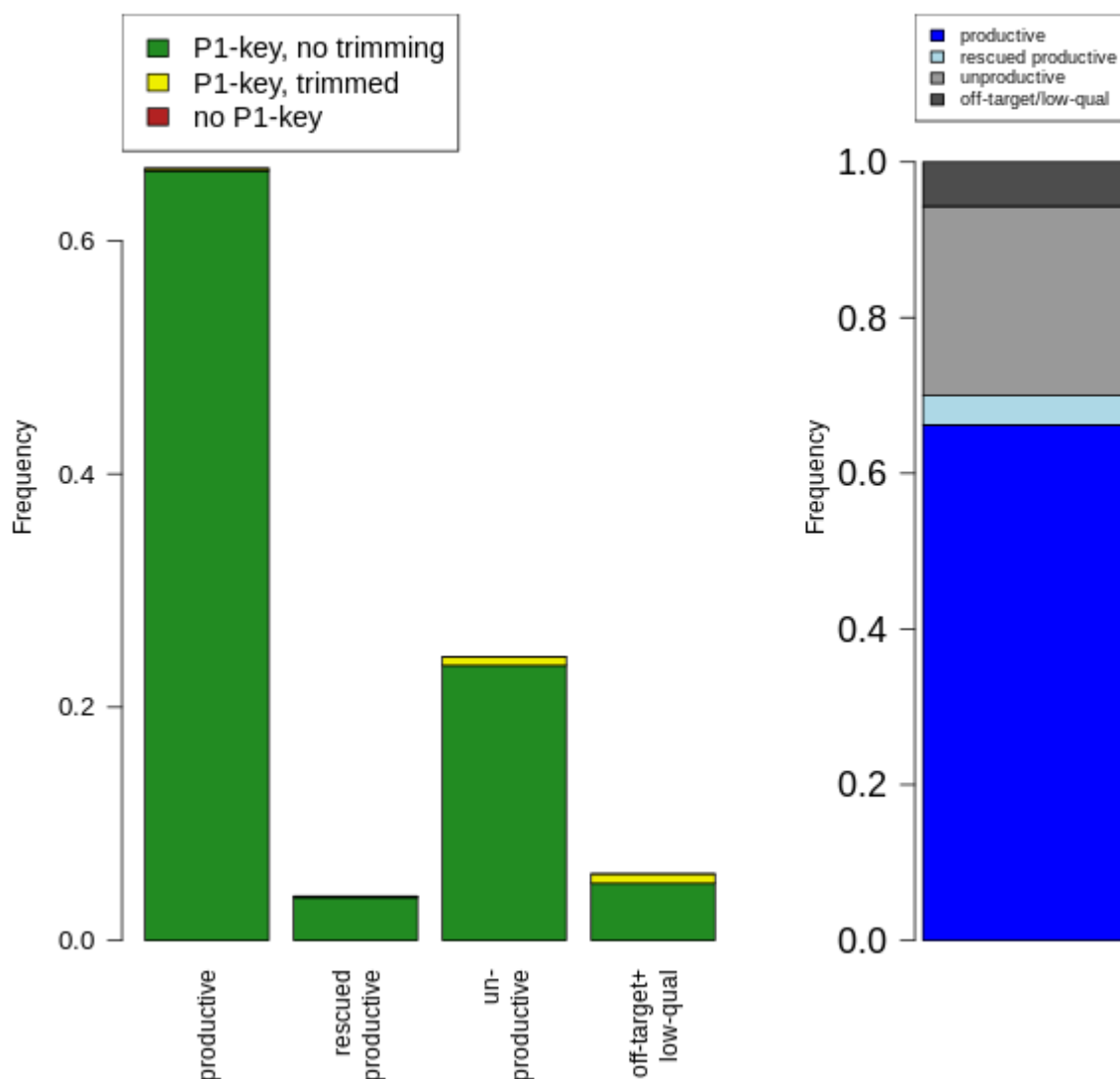
Repaired base composition
for DNA_TCR_CoV_09_COVID_v1_202011300921004



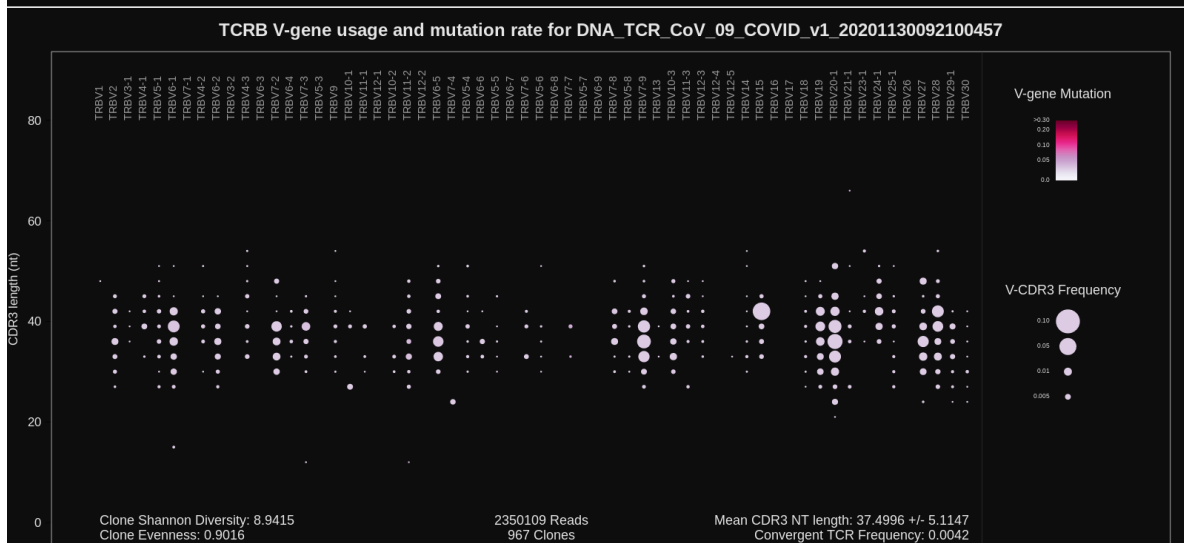
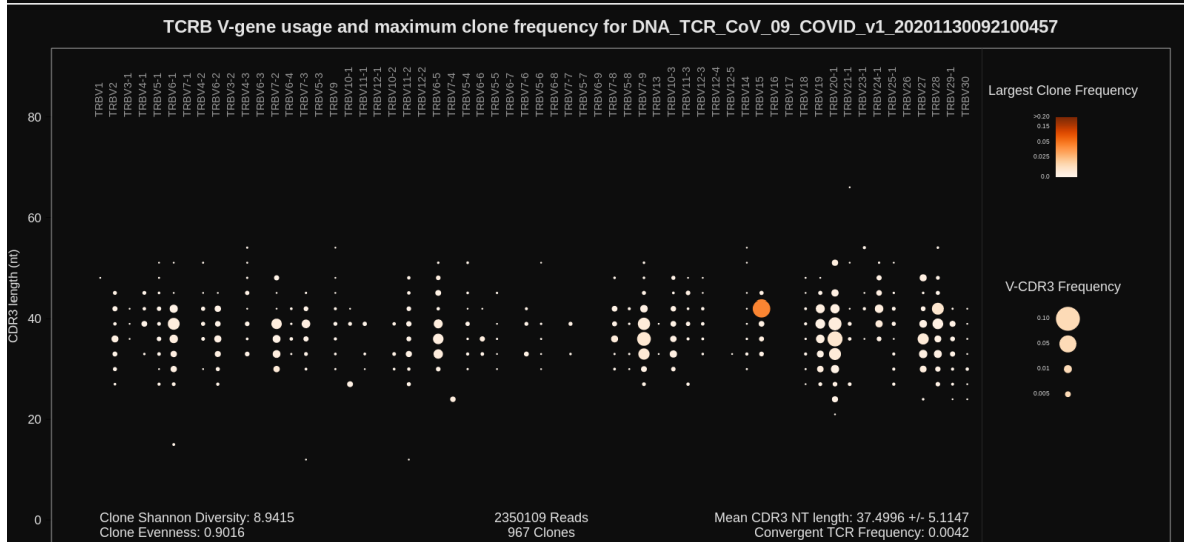
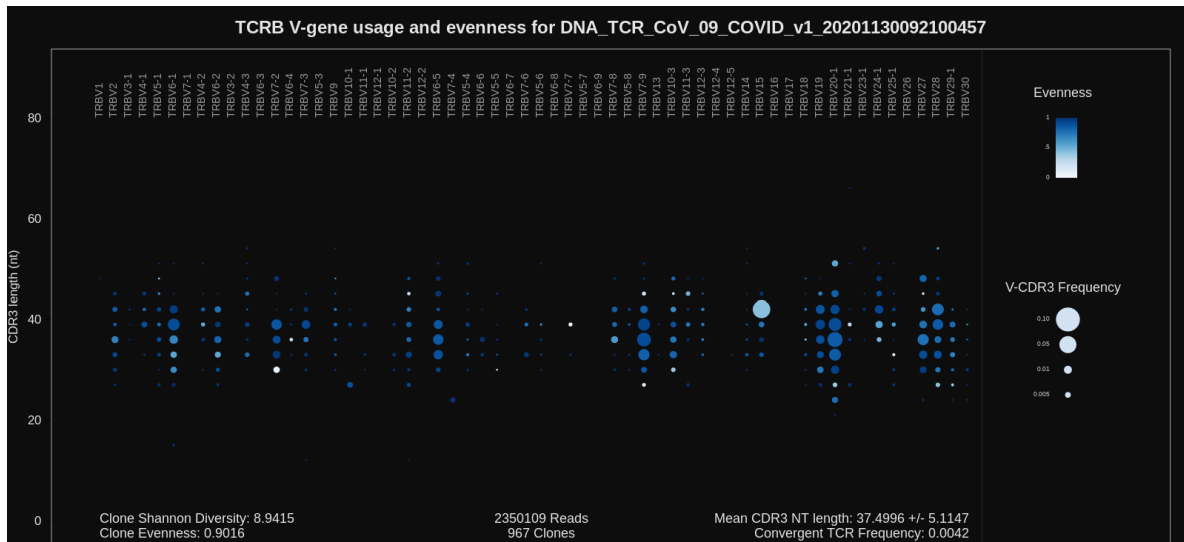


Presence of P1 adapter and quality trimming for DNA_TCR_CoV_09_COVID_v1_20201130092100457

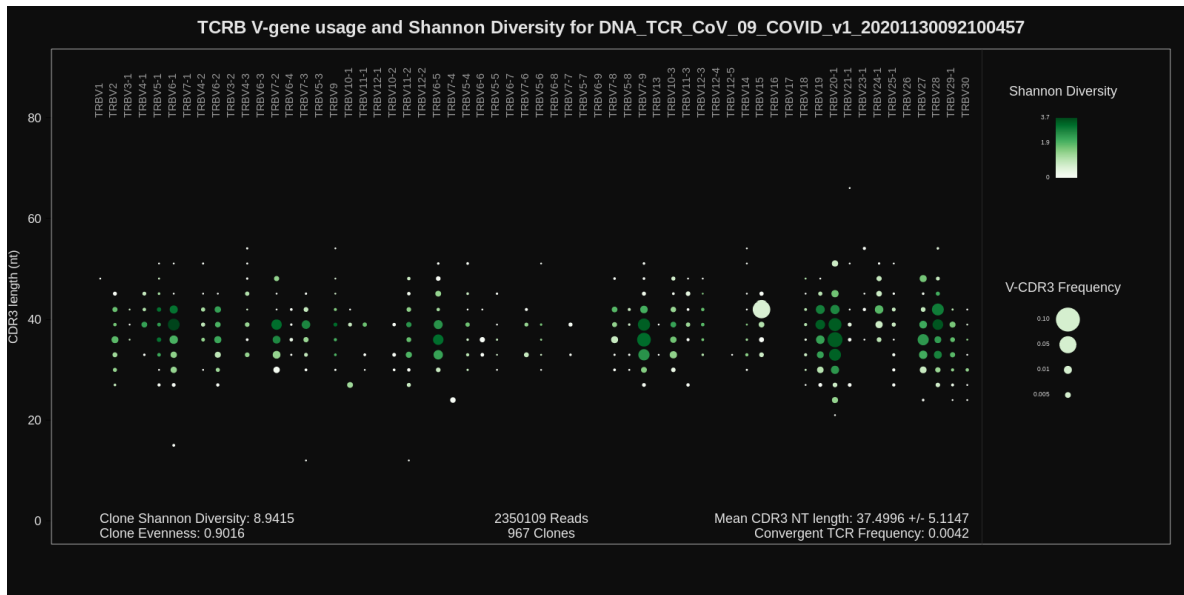
Read classification
for DNA_TCR_CoV_09_COVID_v1_202011300921004



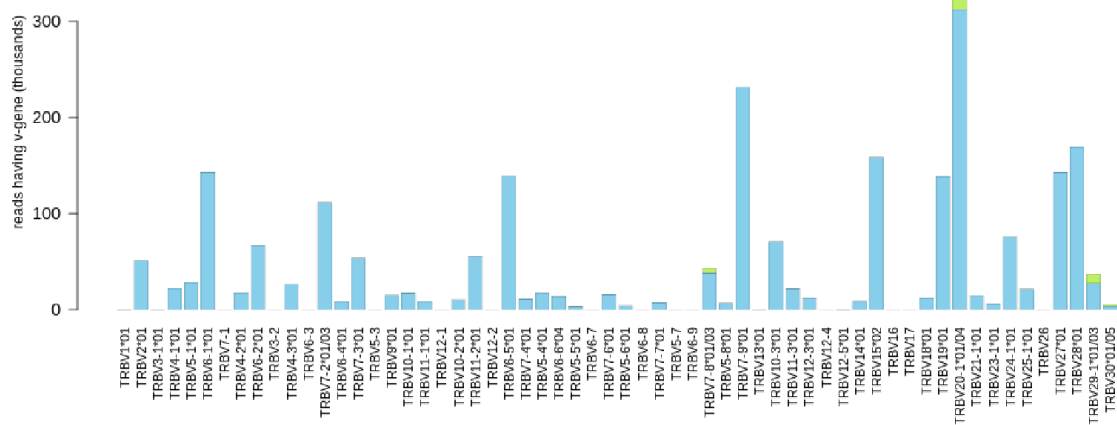
TCRB V-gene usage



TCRB V-gene usage

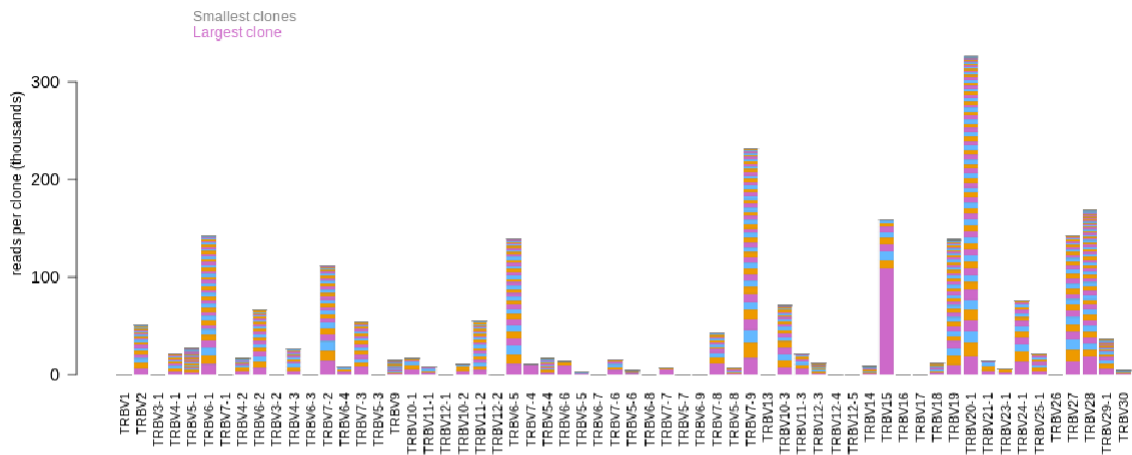


V-gene usage, colored by allele for DNA_TCR_CoV_09_COVID_v1_20201130092100457

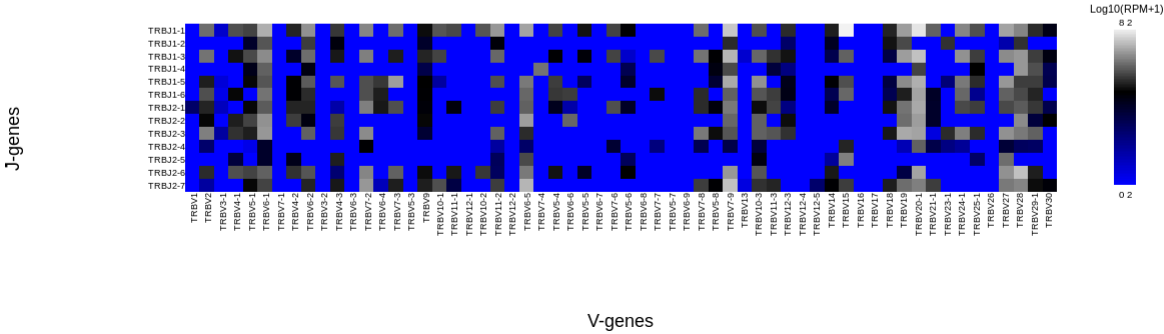


TCRB V-gene usage

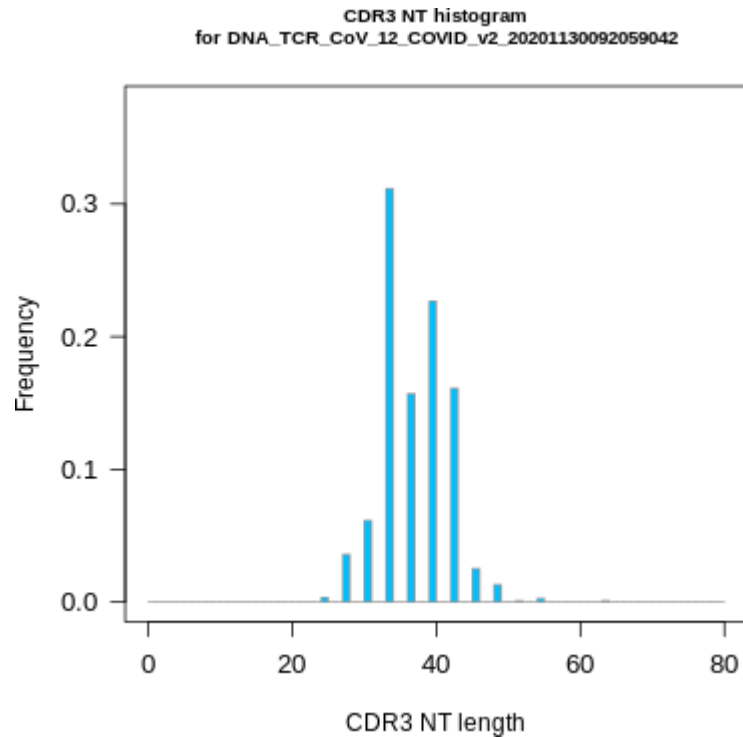
V-gene usage, colored by clone size for DNA_TCR_CoV_09_COVID_v1_20201130092100457



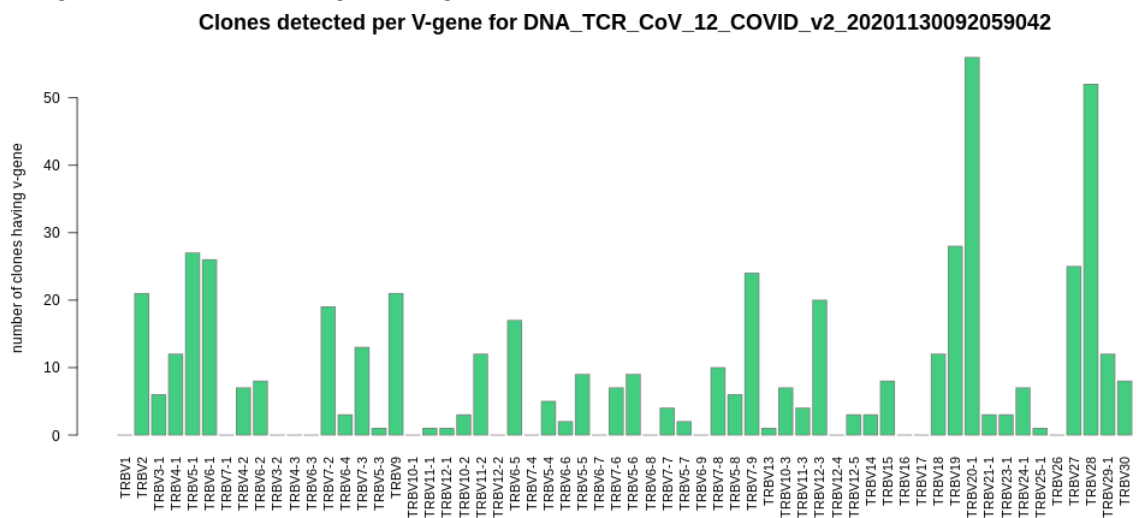
Log10 RPM of V-J pairs in
DNA_TCR_CoV_09_COVID_v1_20201130092100457



COVID-19 lung late stage case 4

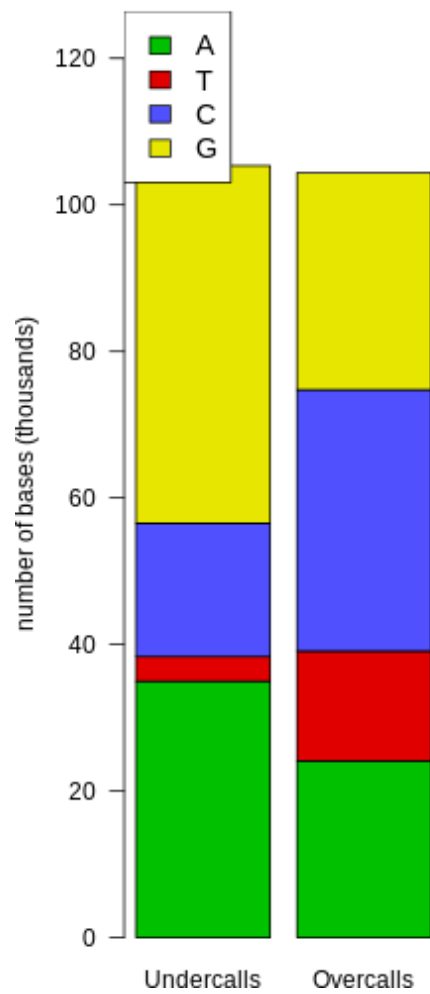


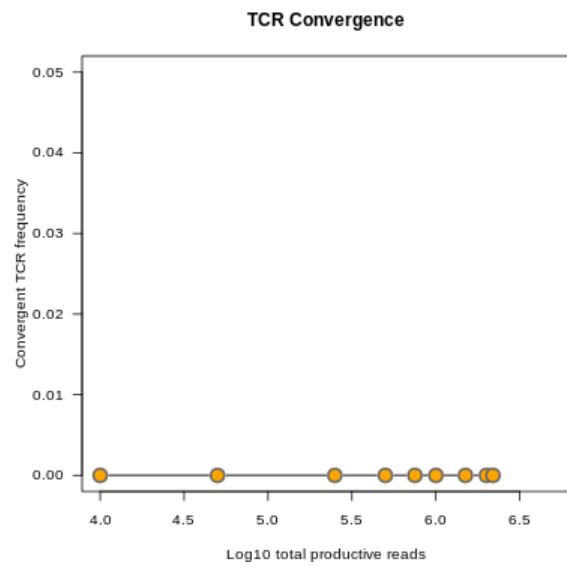
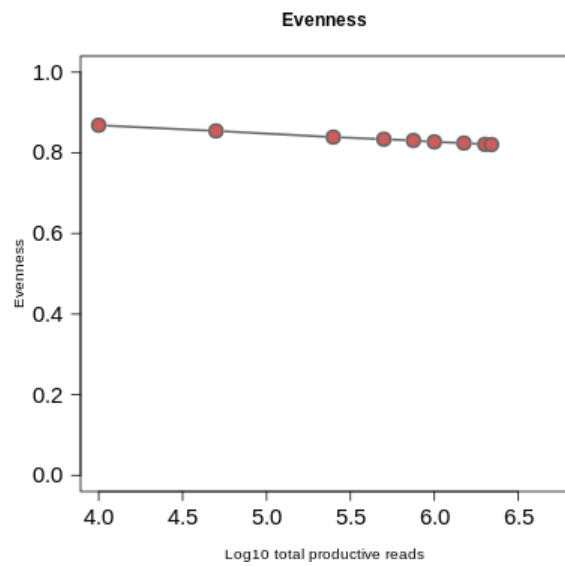
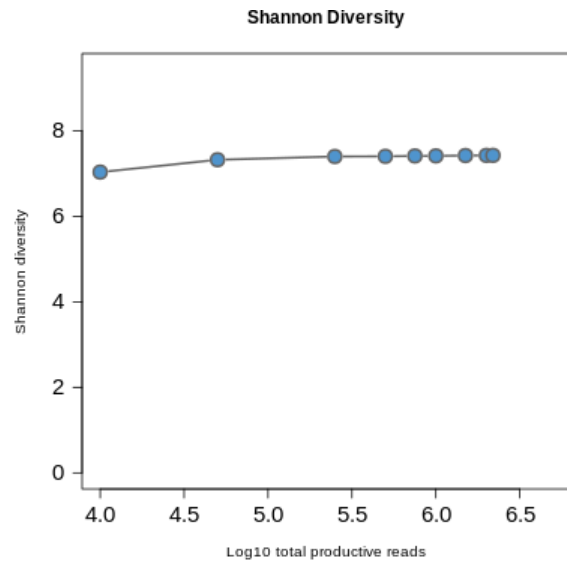
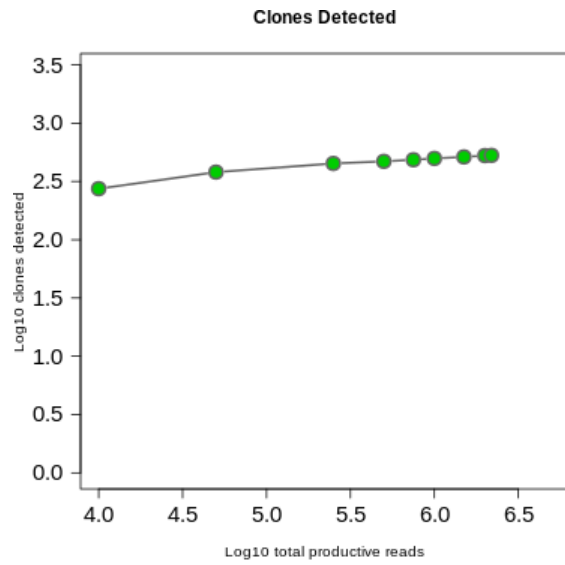
Histogram of CDR3 nucleotide length showing a normal distribution



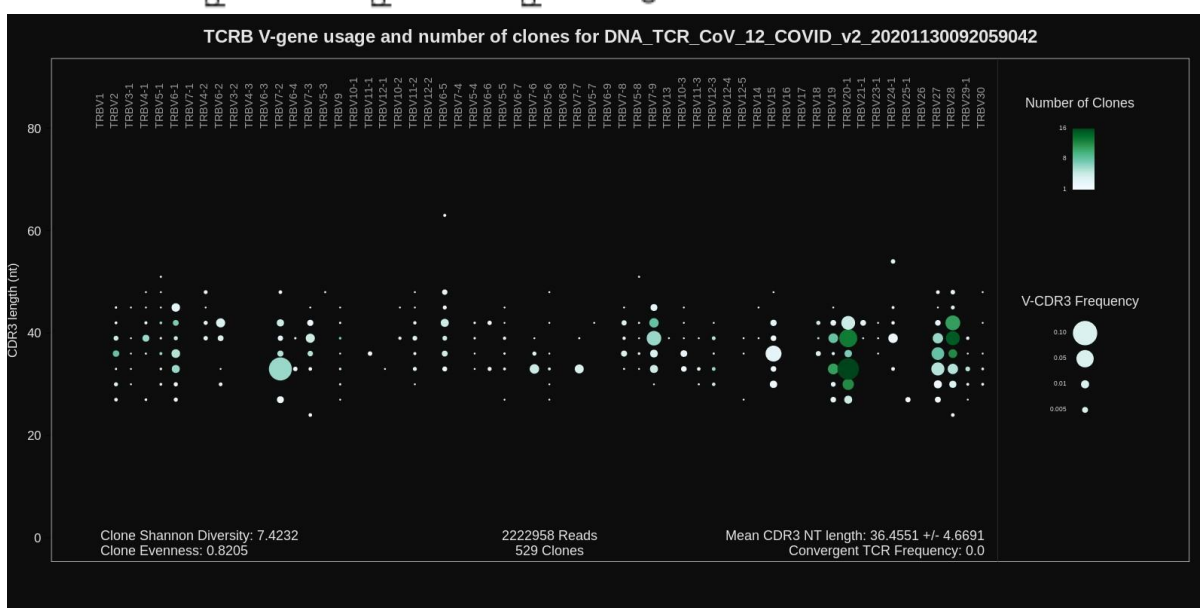
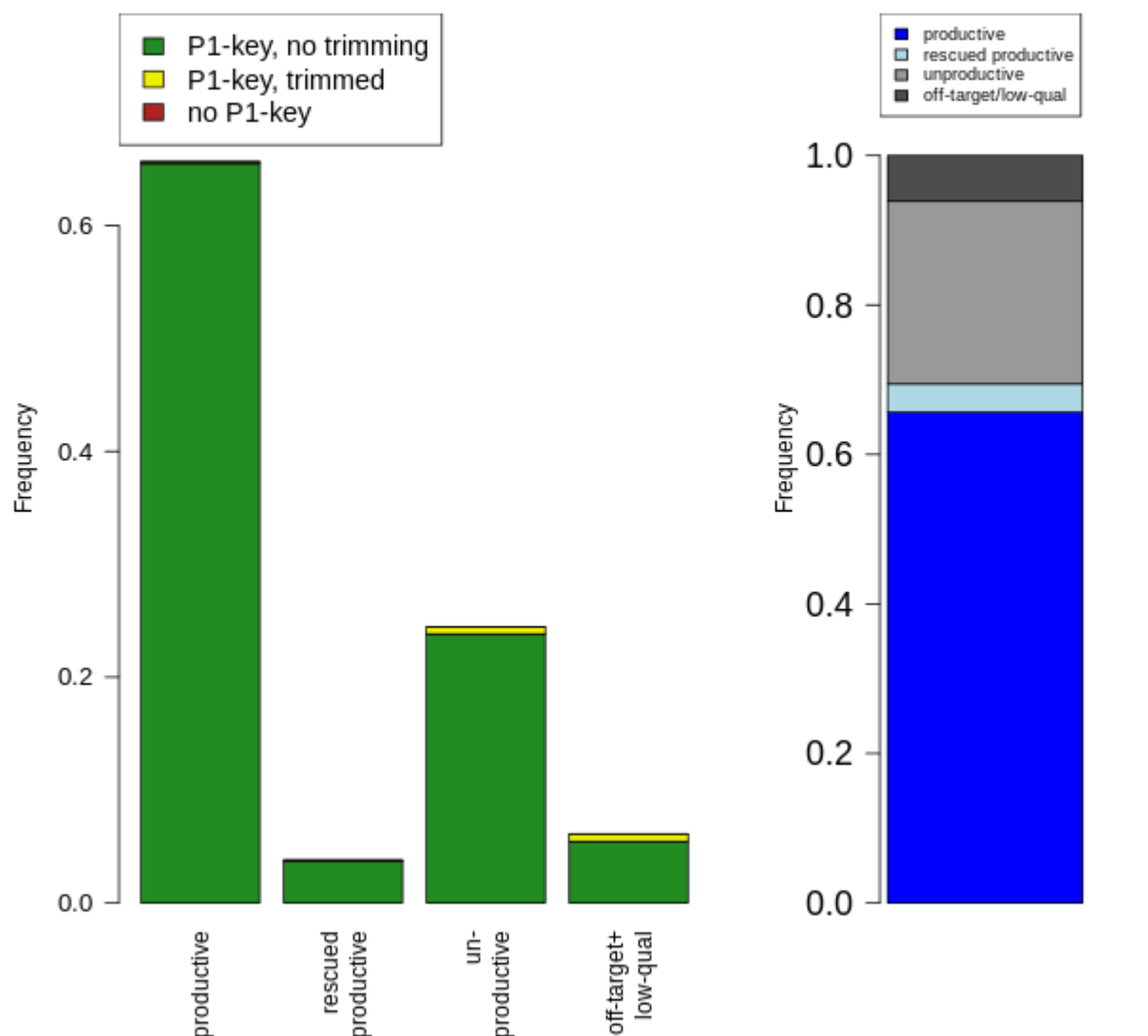
Number of clones per V-gene

Repaired base composition
for DNA_TCR_CoV_12_COVID_v2_202011300920590

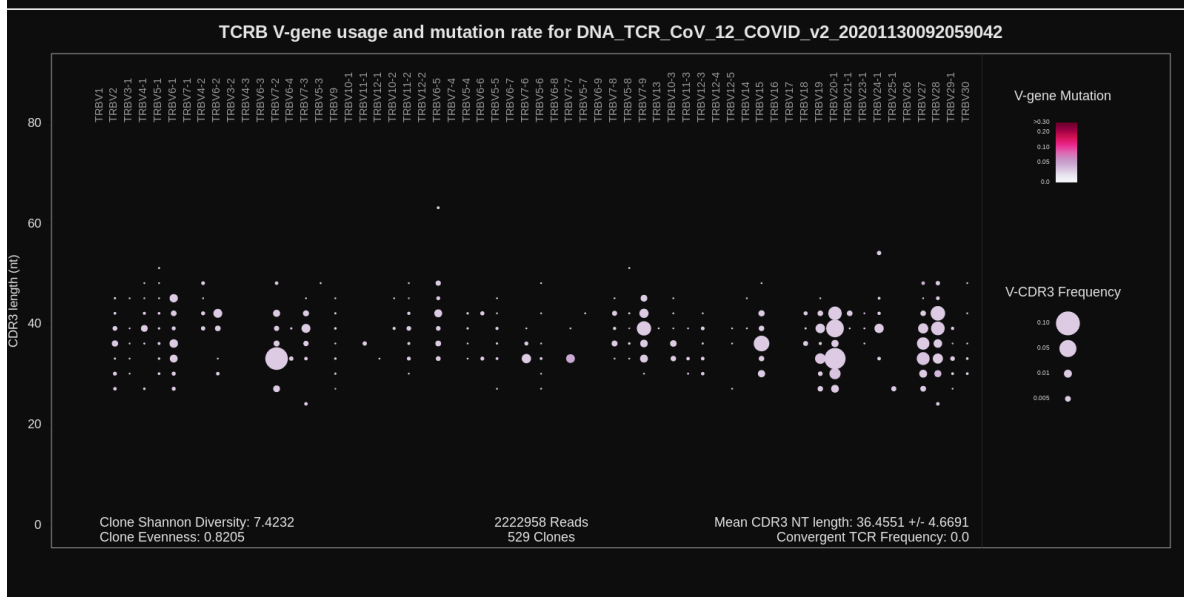
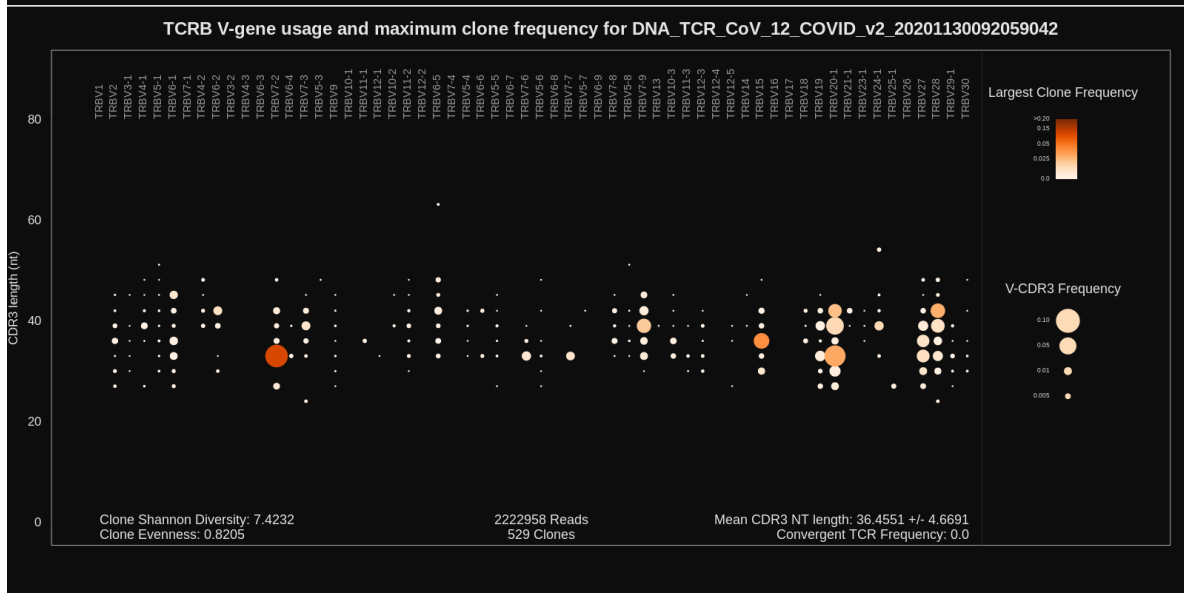
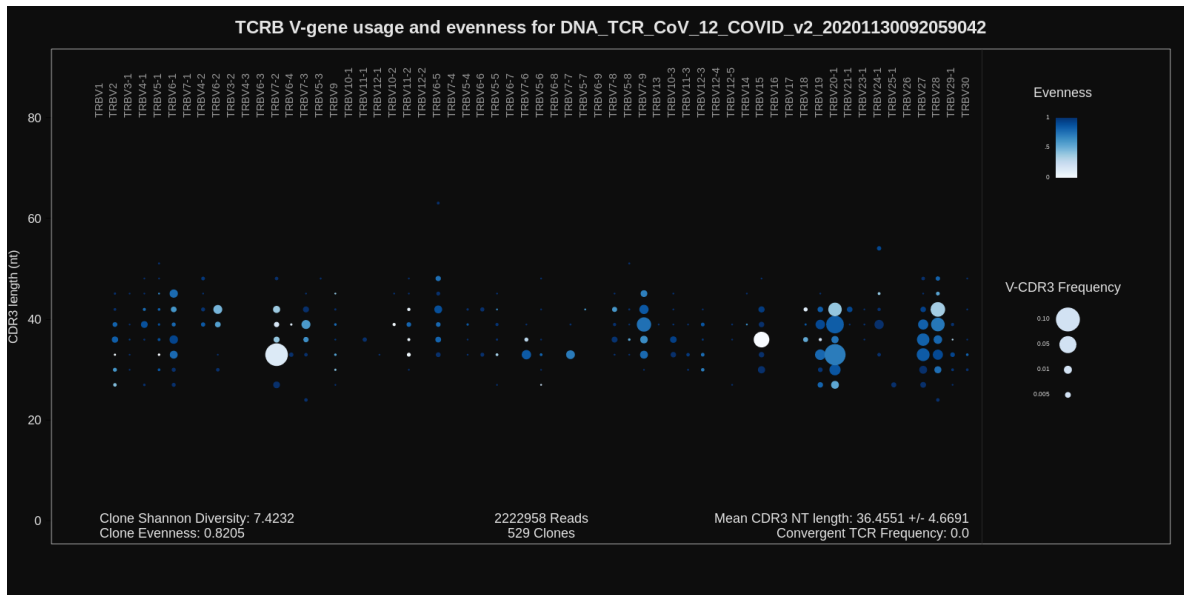




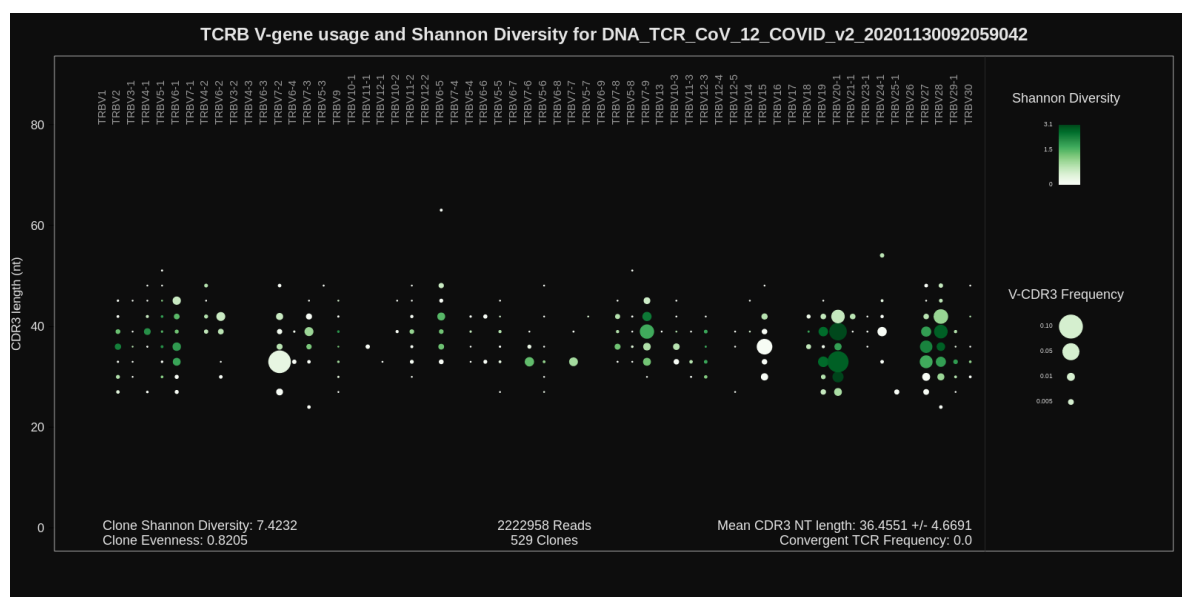
Presence of P1 adapter and quality trimming for DNA_TCR_CoV_12_COVID_v2_20201130092059042



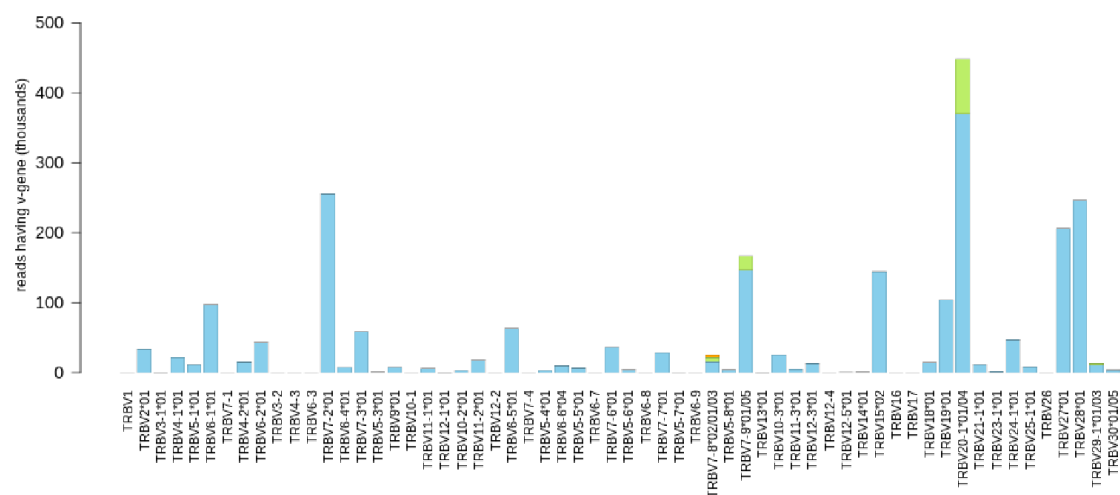
TCRB V-gene usage



TCRB V-gene usage

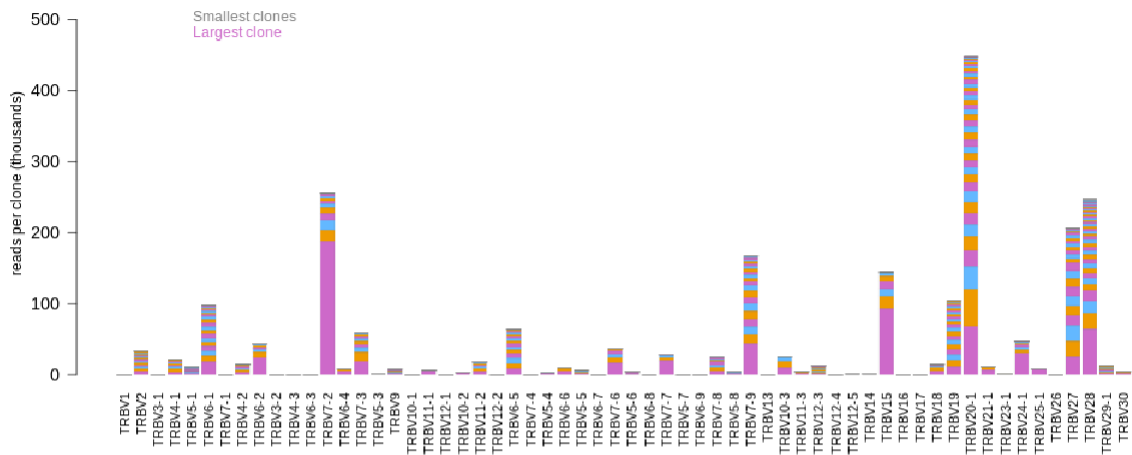


V-gene usage, colored by allele for DNA_TCR_CoV_12_COVID_v2_20201130092059042

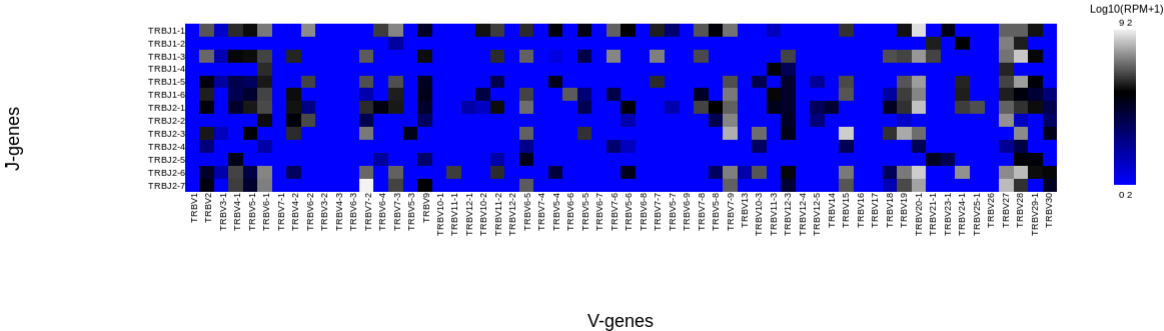


TCRB V-gene usage

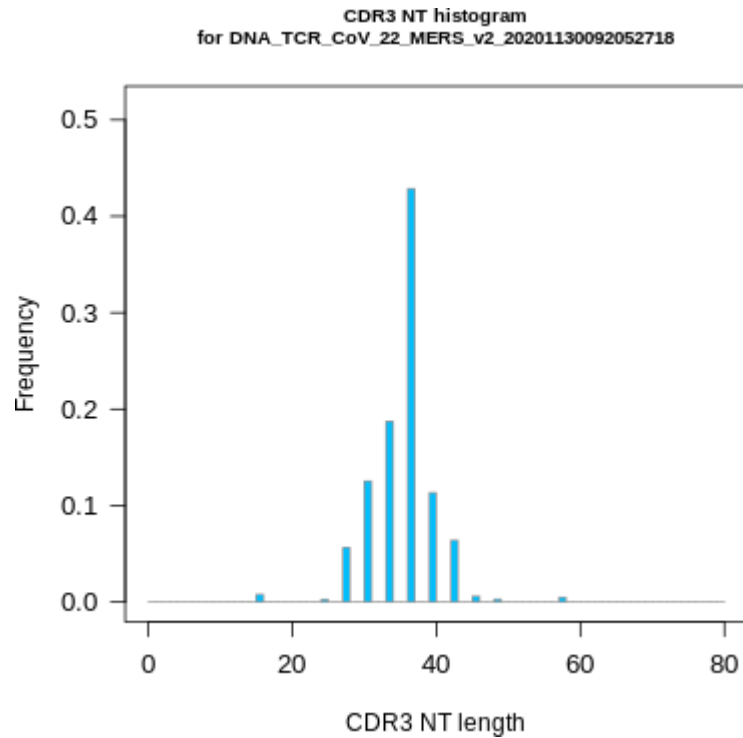
V-gene usage, colored by clone size for DNA_TCR_CoV_12_COVID_v2_20201130092059042



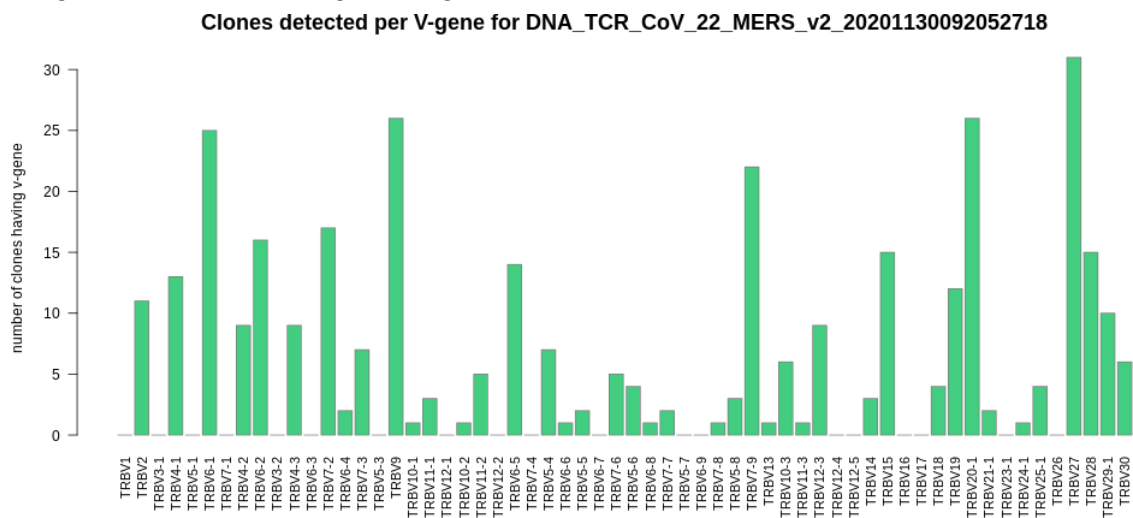
Log10 RPM of V-J pairs in
DNA_TCR_CoV_12_COVID_v2_20201130092059042



MERS lung

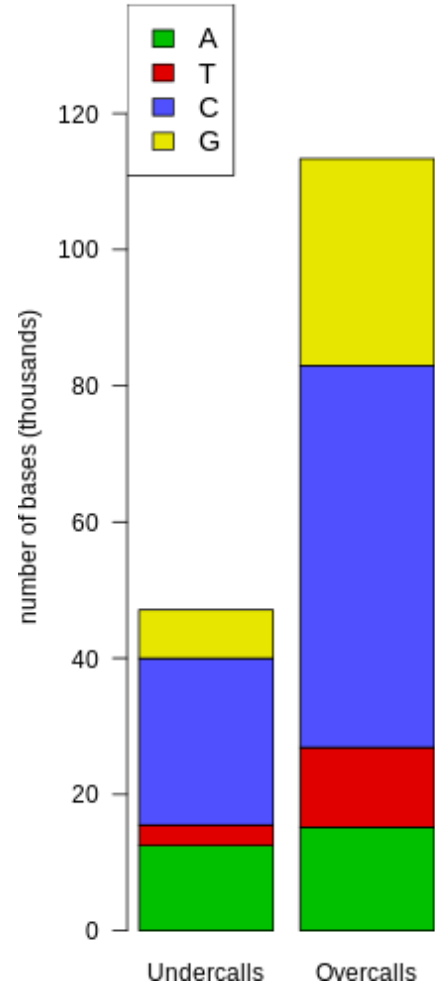


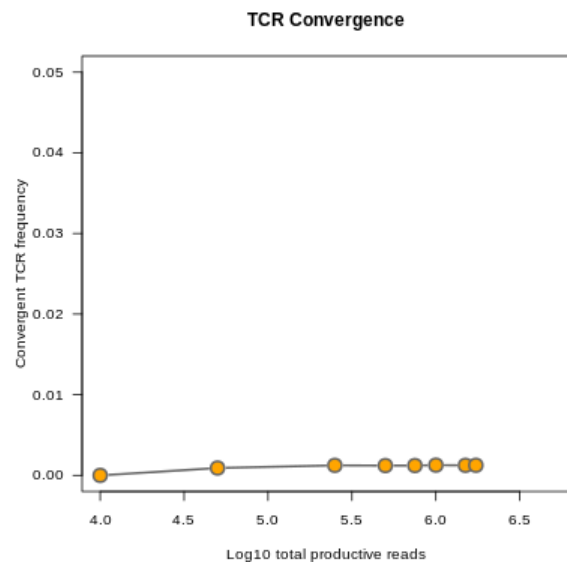
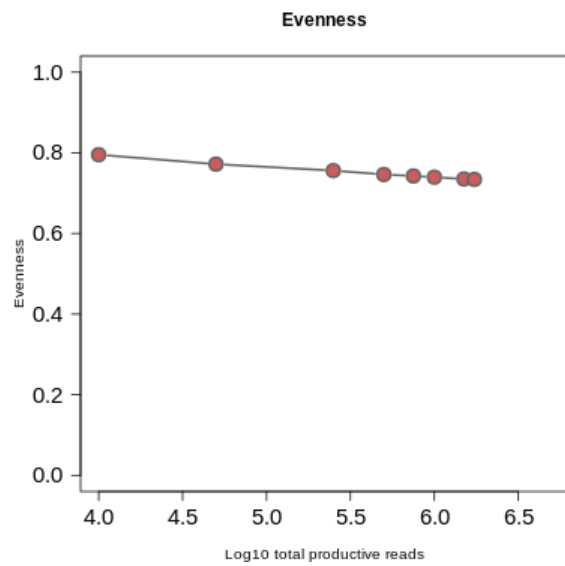
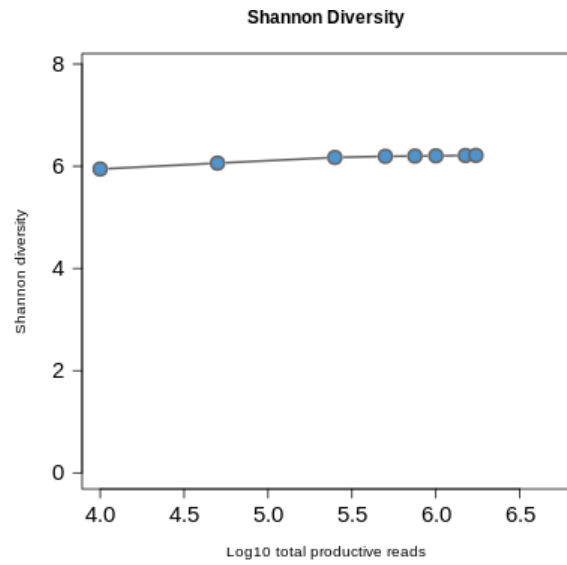
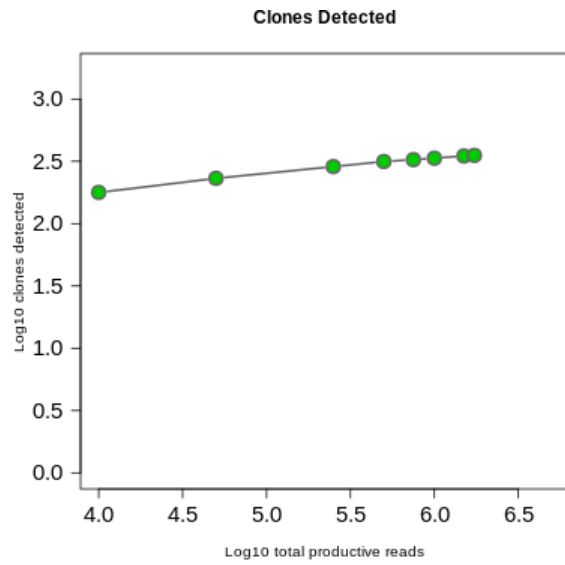
Histogram of CDR3 nucleotide length showing a normal distribution

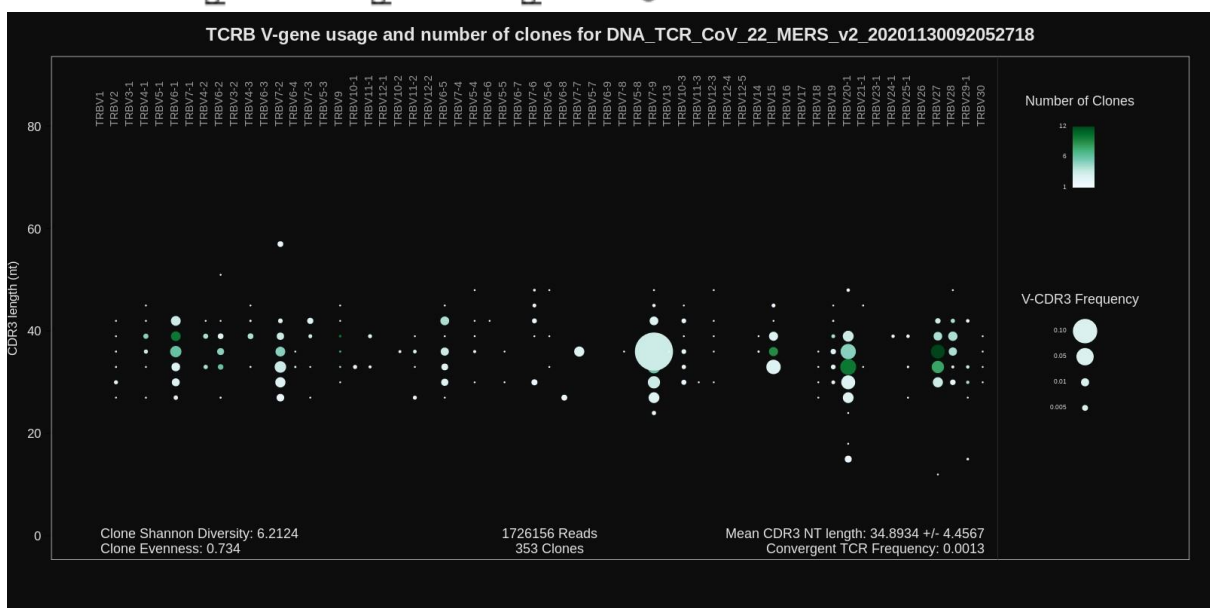
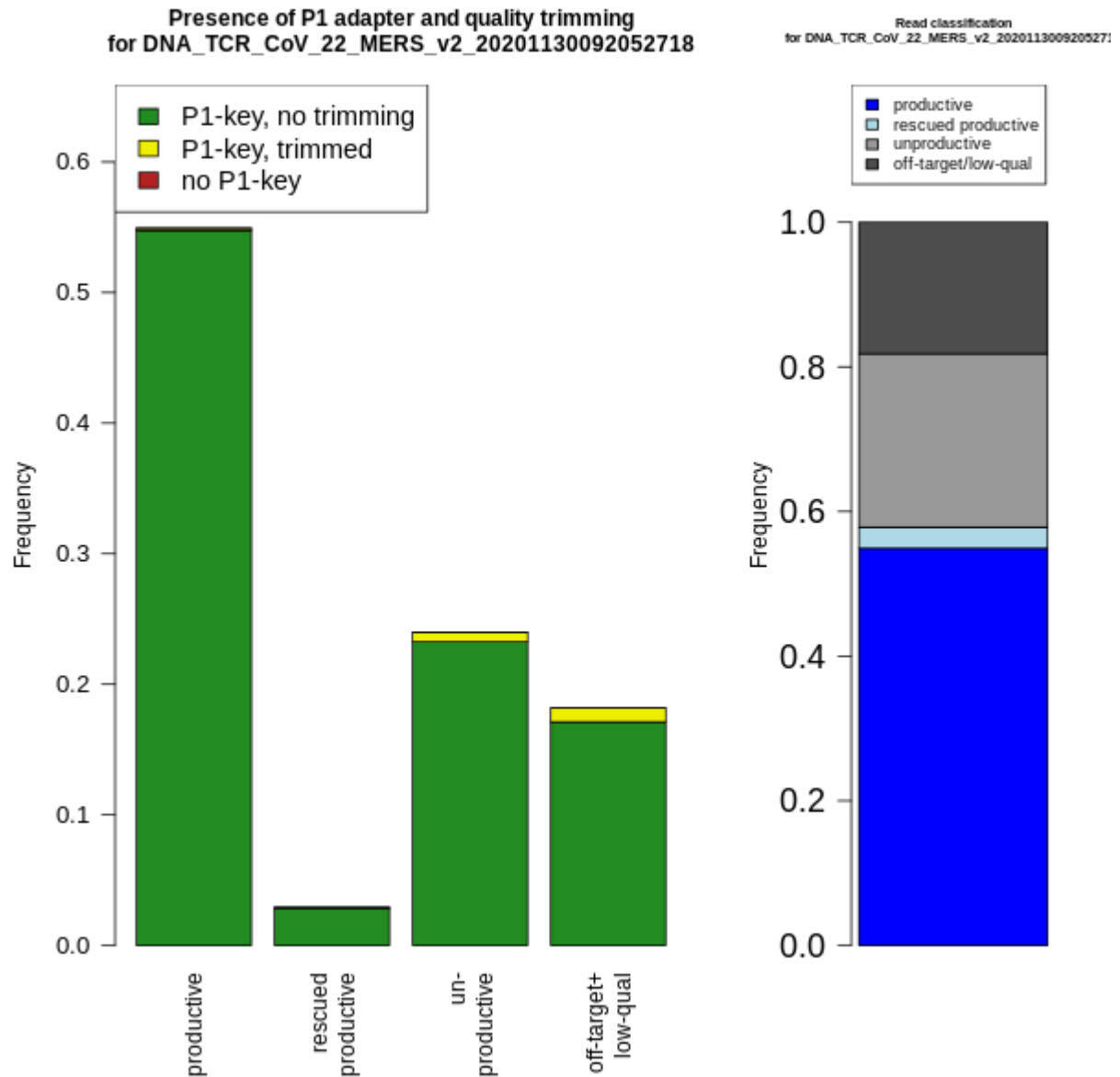


Number of clones per V-gene

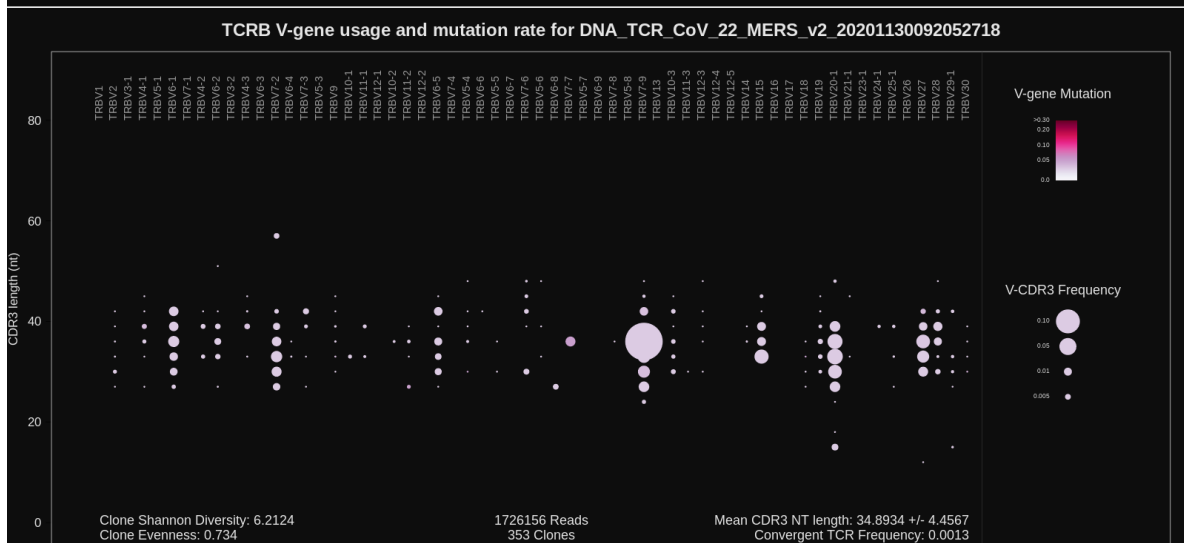
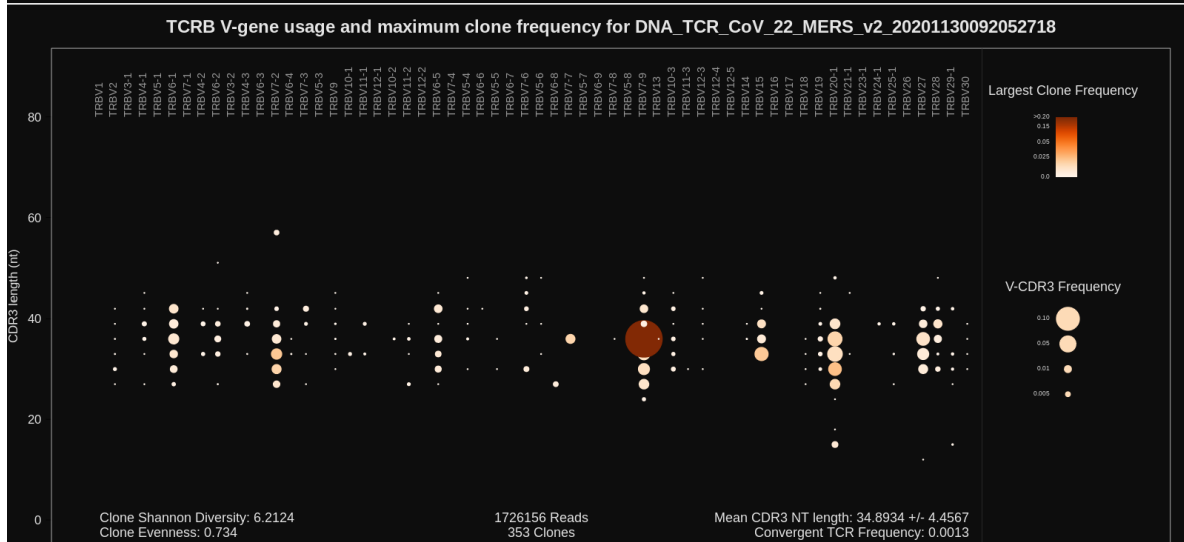
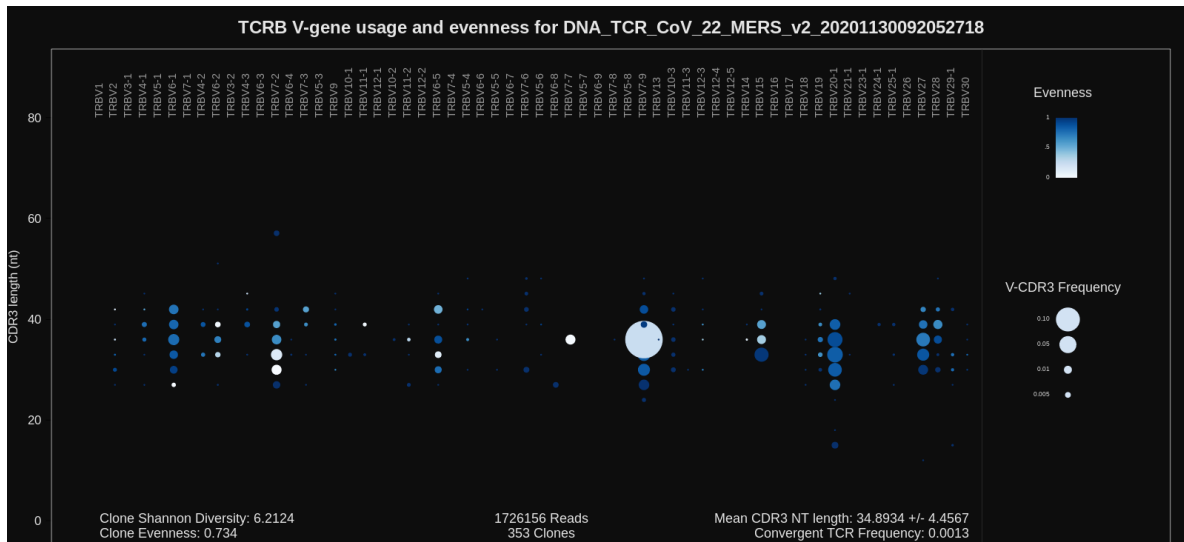
Repaired base composition
for DNA_TCR_CoV_22_MERS_v2_202011300920527:



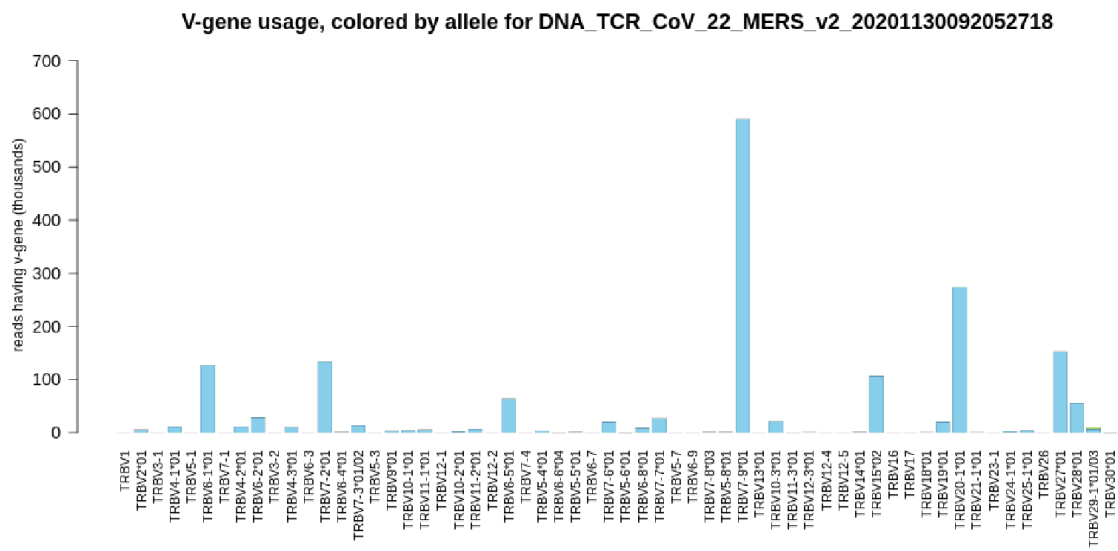
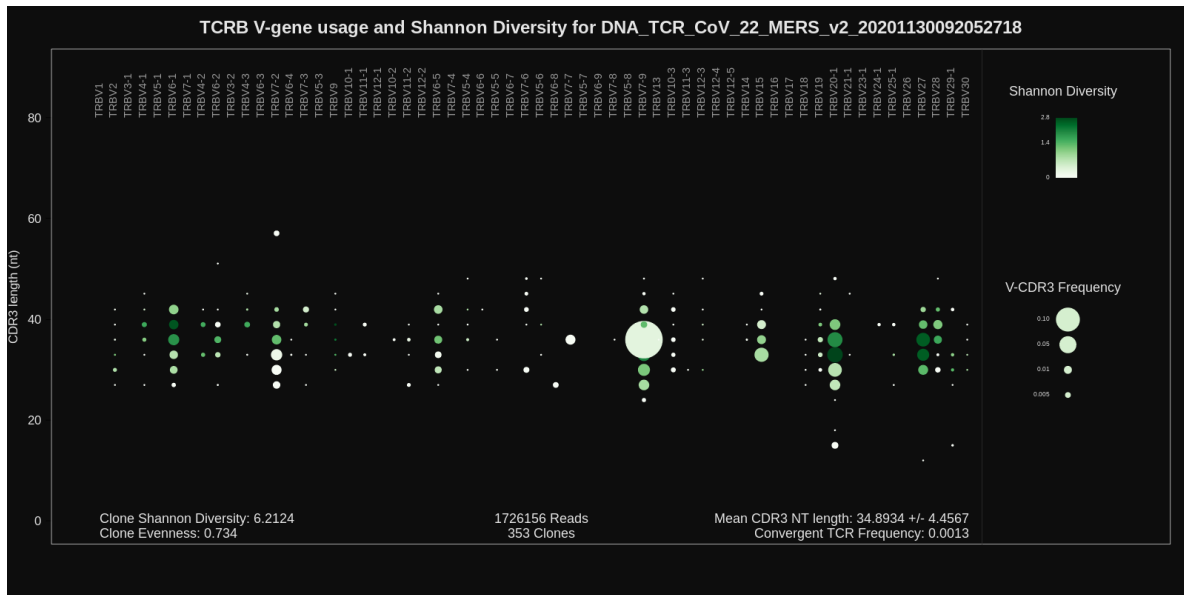




TCRB V-gene usage

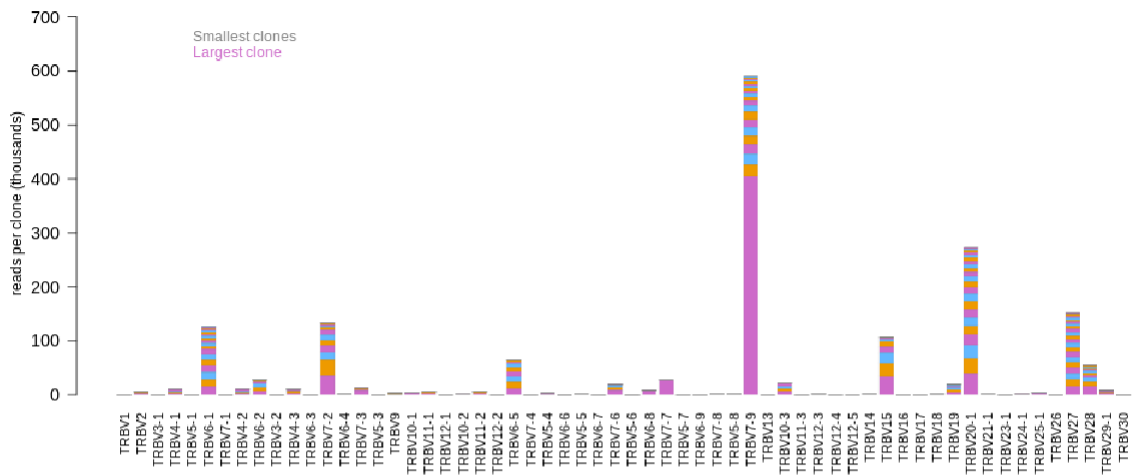


TCRB V-gene usage

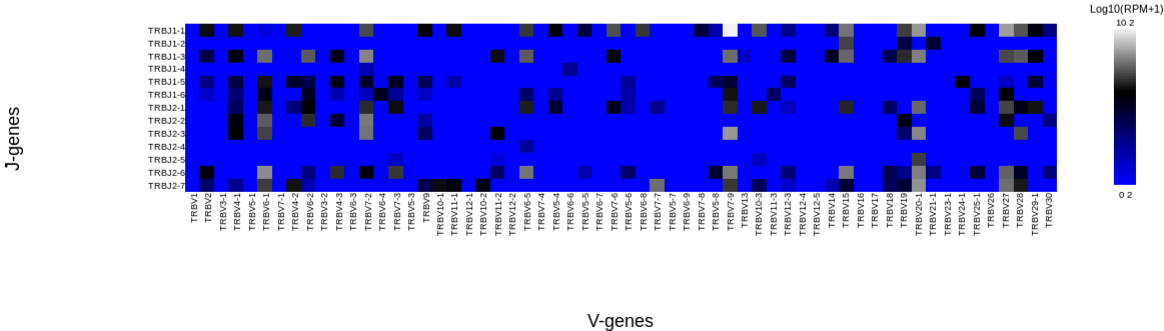


TCRB V-gene usage

V-gene usage, colored by clone size for DNA_TCR_CoV_22_MERS_v2_20201130092052718

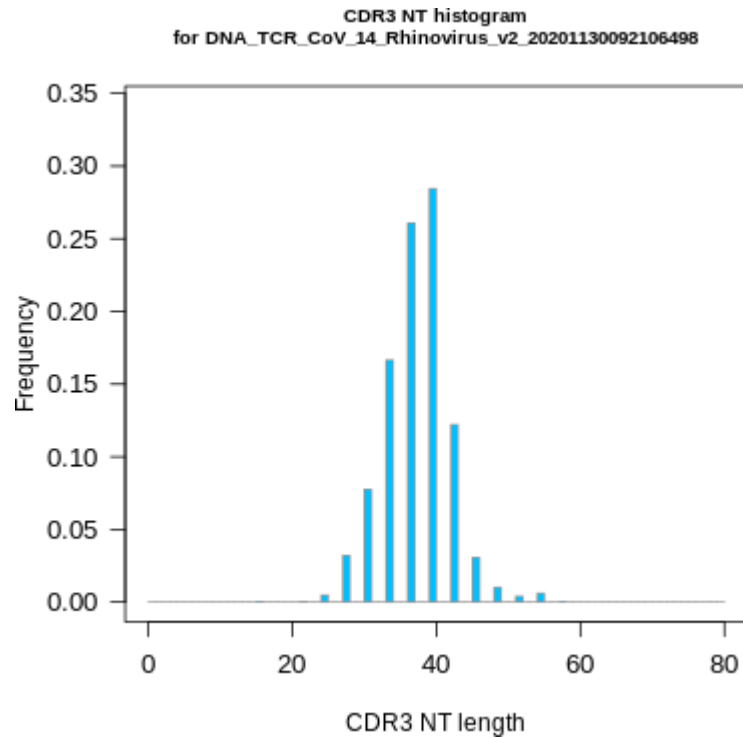


Log10 RPM of V-J pairs in
DNA_TCR_CoV_22_MERS_v2_20201130092052718

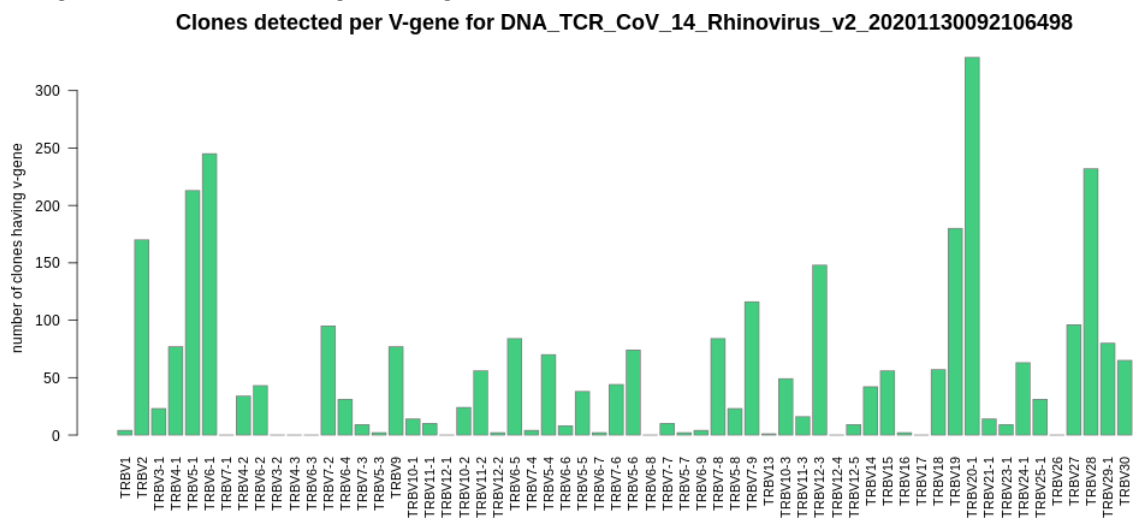


TCRB V-gene usage

Rhinovirus lung

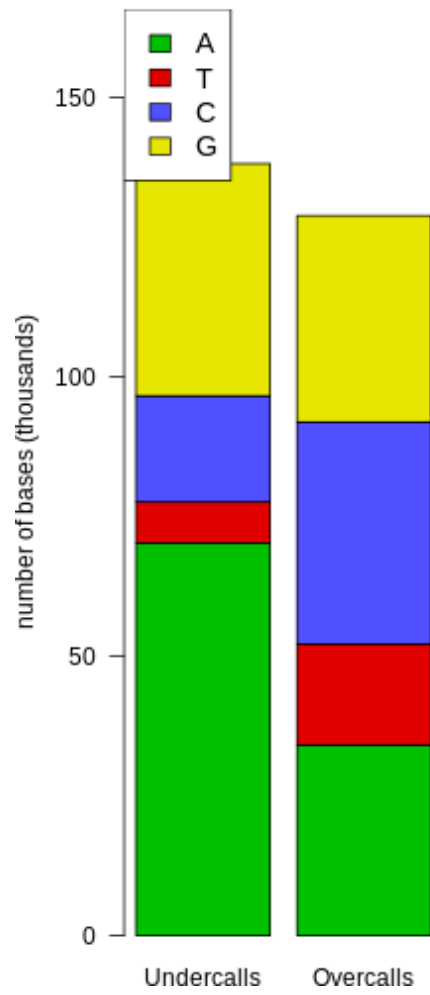


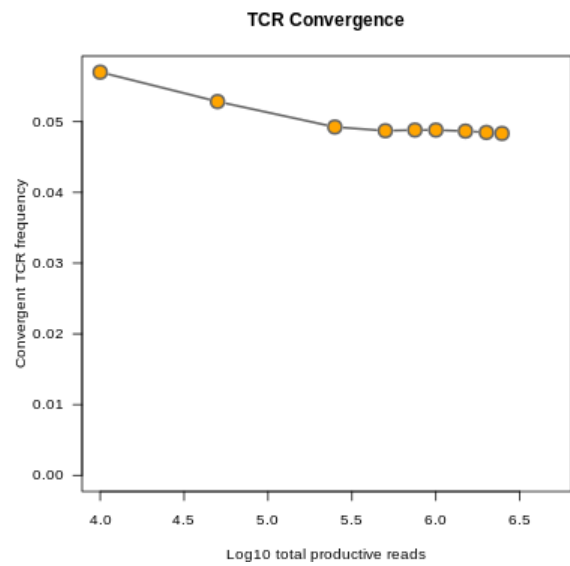
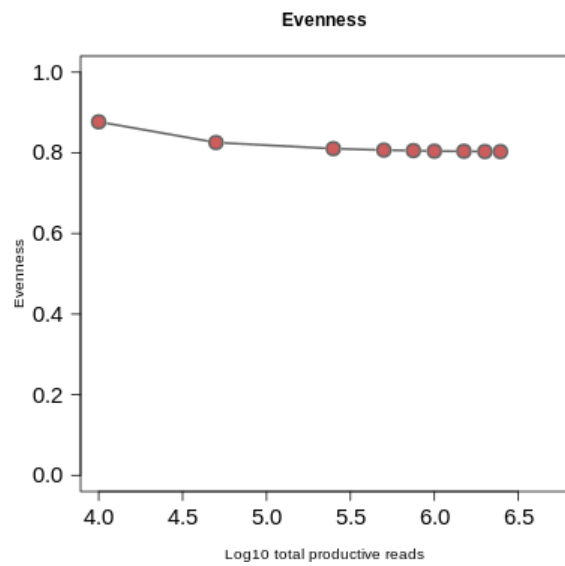
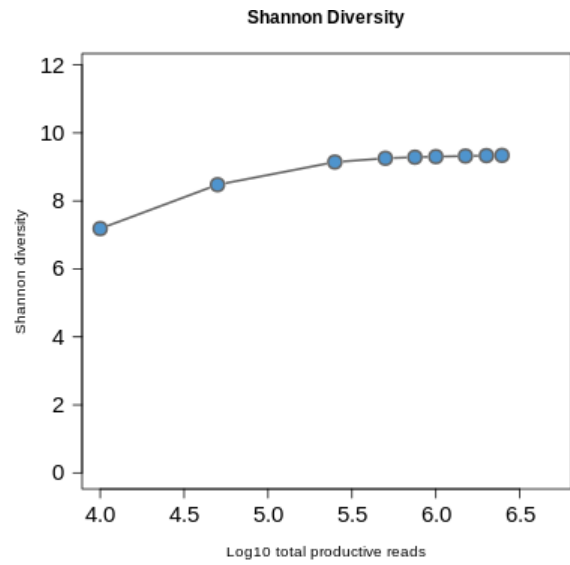
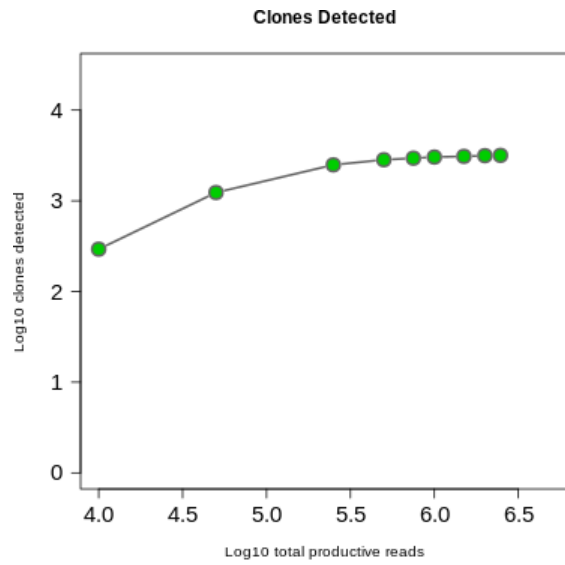
Histogram of CDR3 nucleotide length showing a normal distribution

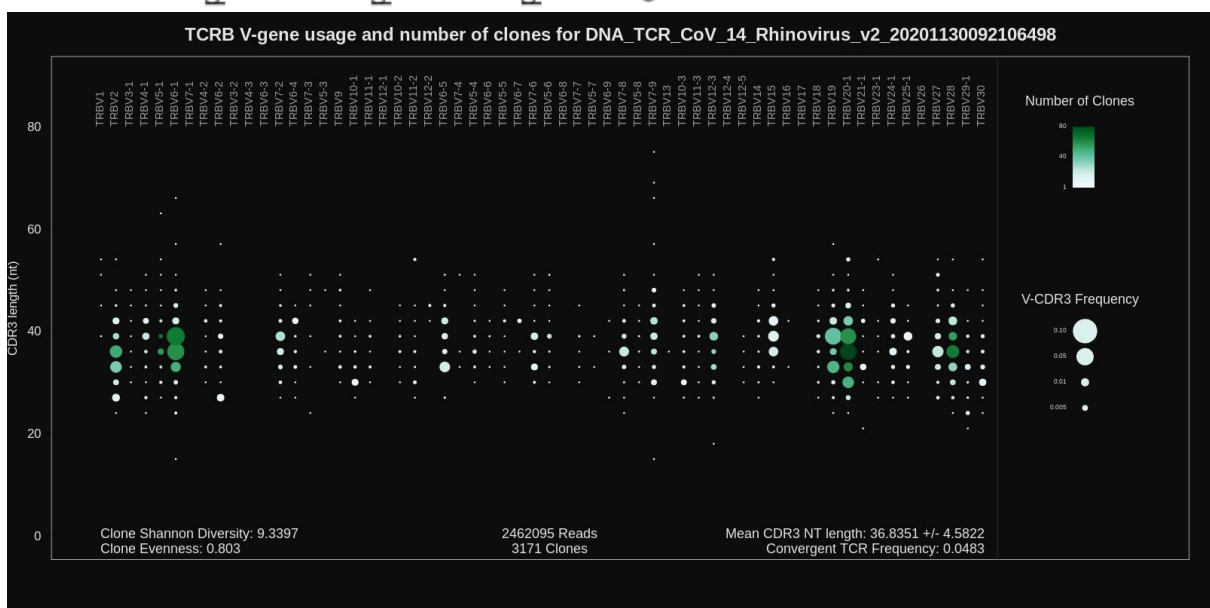
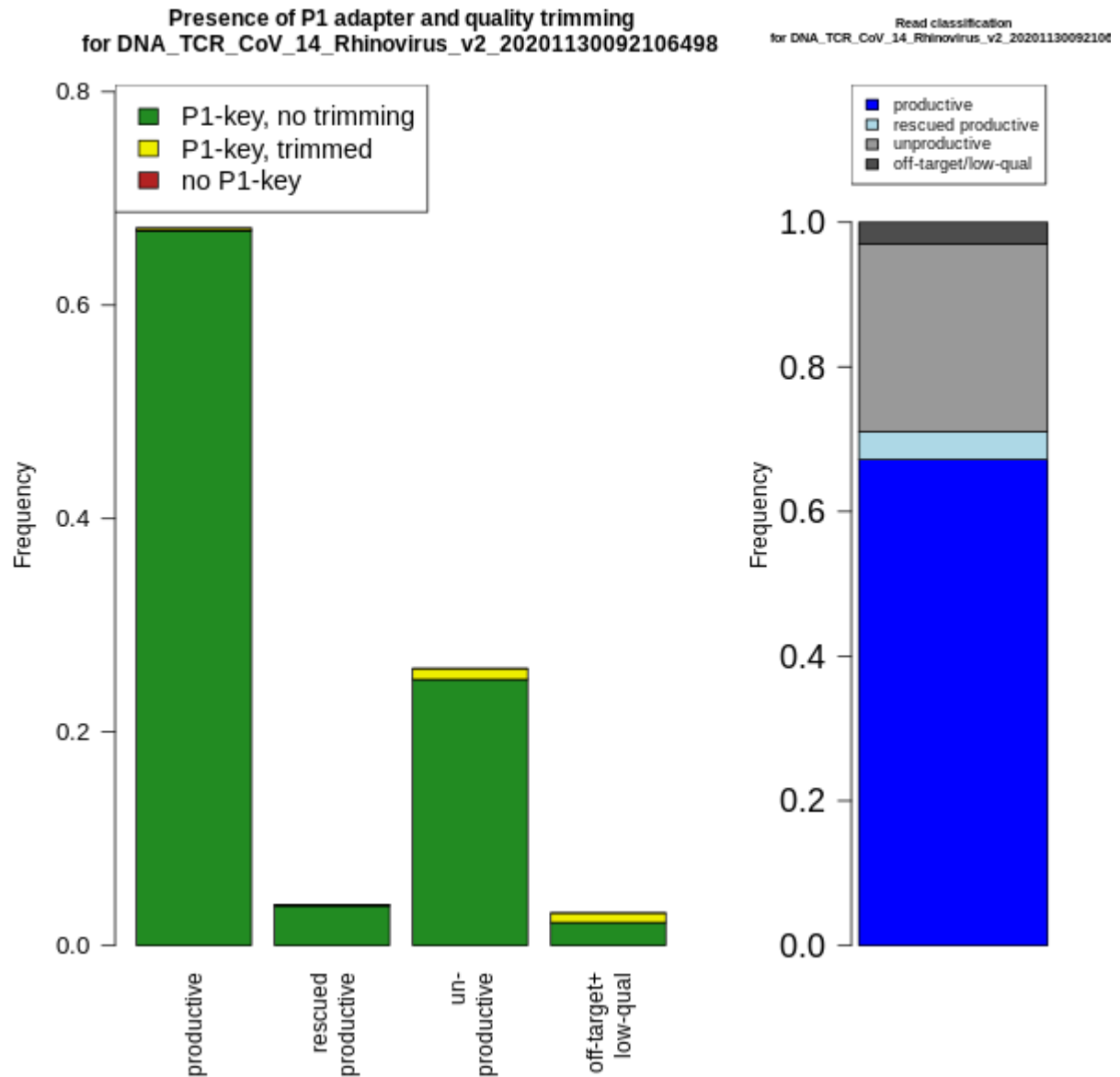


Number of clones per V-gene

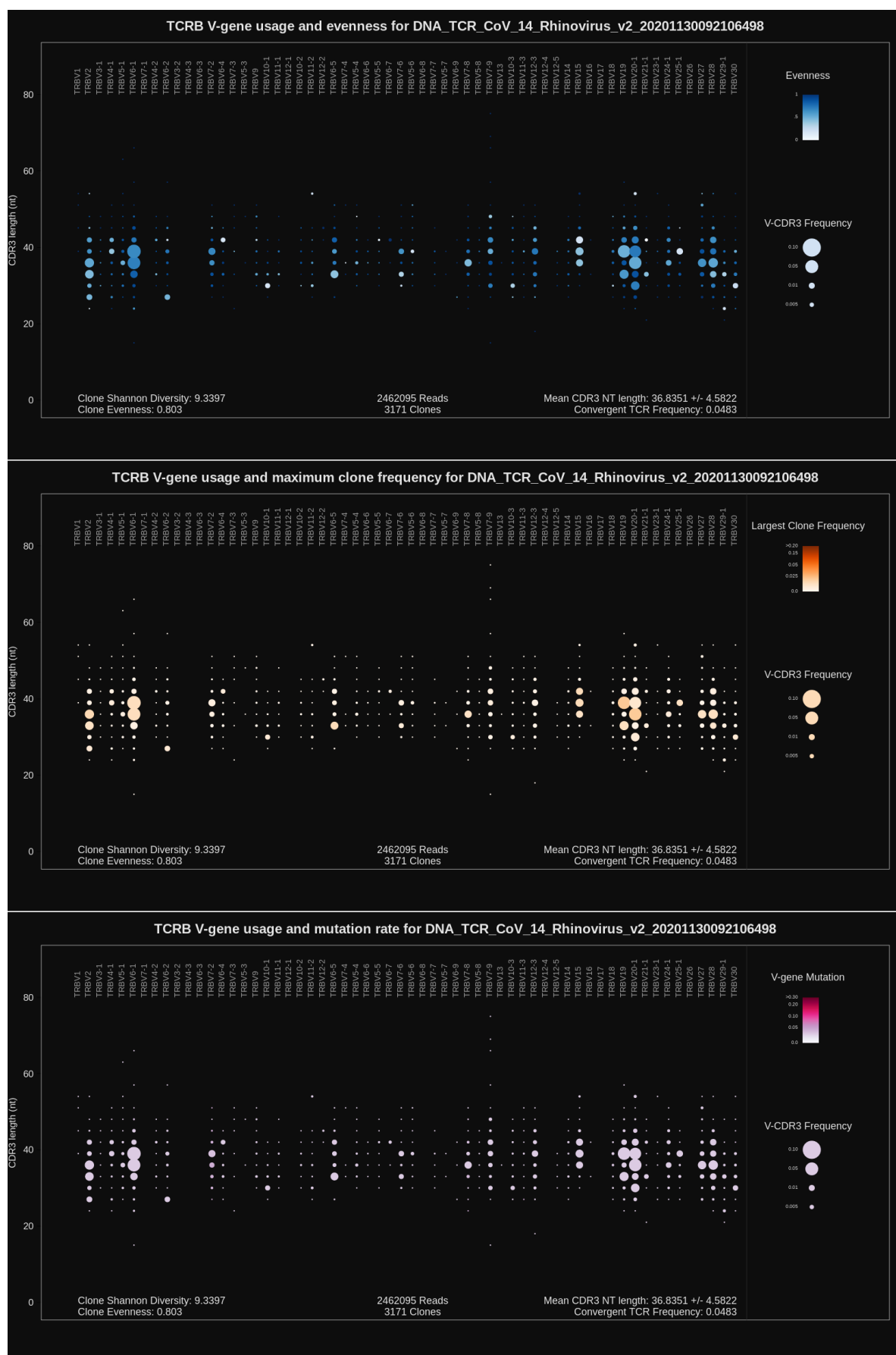
Repaired base composition
for DNA_TCR_CoV_14_Rhinovirus_v2_2020113009210





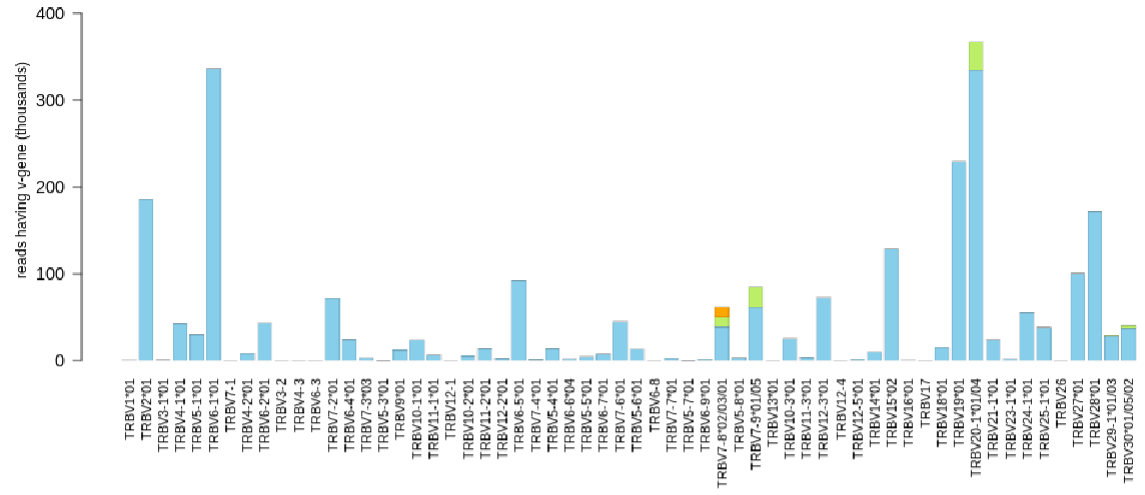


TCRB V-gene usage

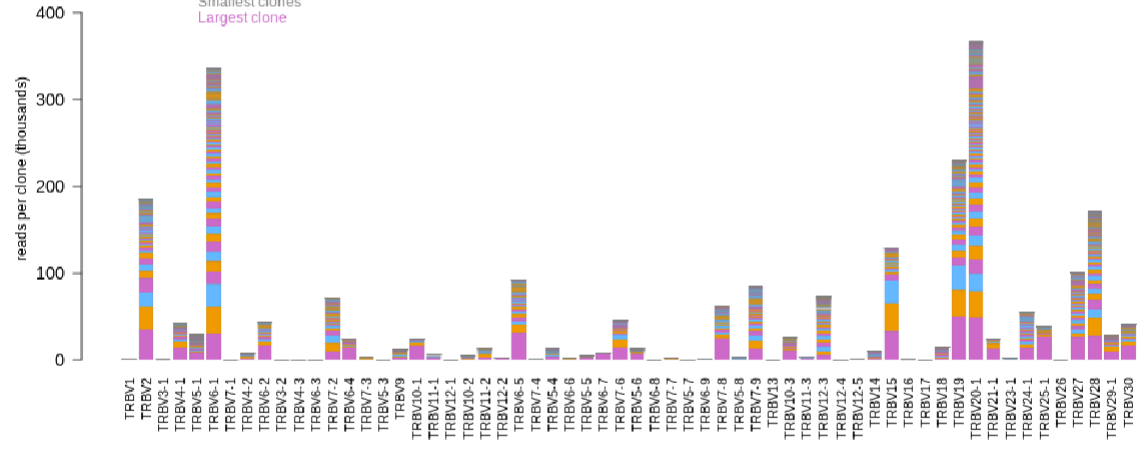


TCRB V-gene usage

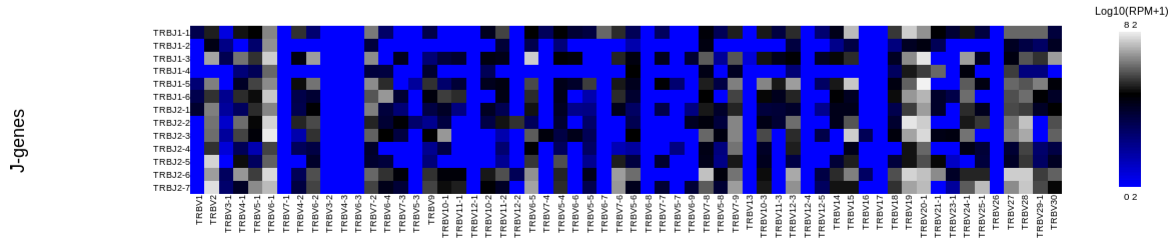
V-gene usage, colored by allele for DNA_TCR_CoV_14_Rhinovirus_v2_20201130092106498



V-gene usage, colored by clone size for DNA_TCR_CoV_14_Rhinovirus_v2_20201130092106498

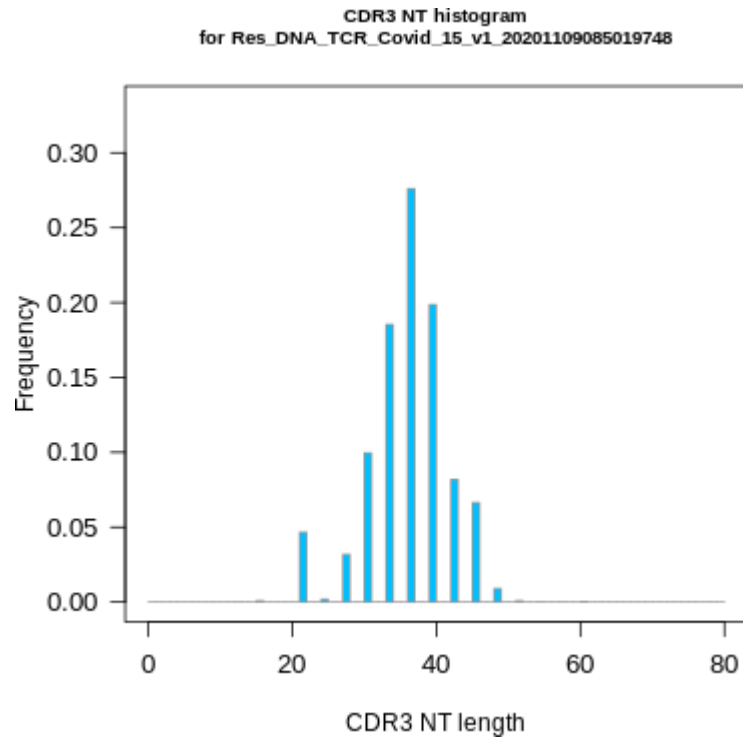


Log10 RPM of V-J pairs in
DNA_TCR_CoV_14_Rhinovirus_v2_20201130092106498

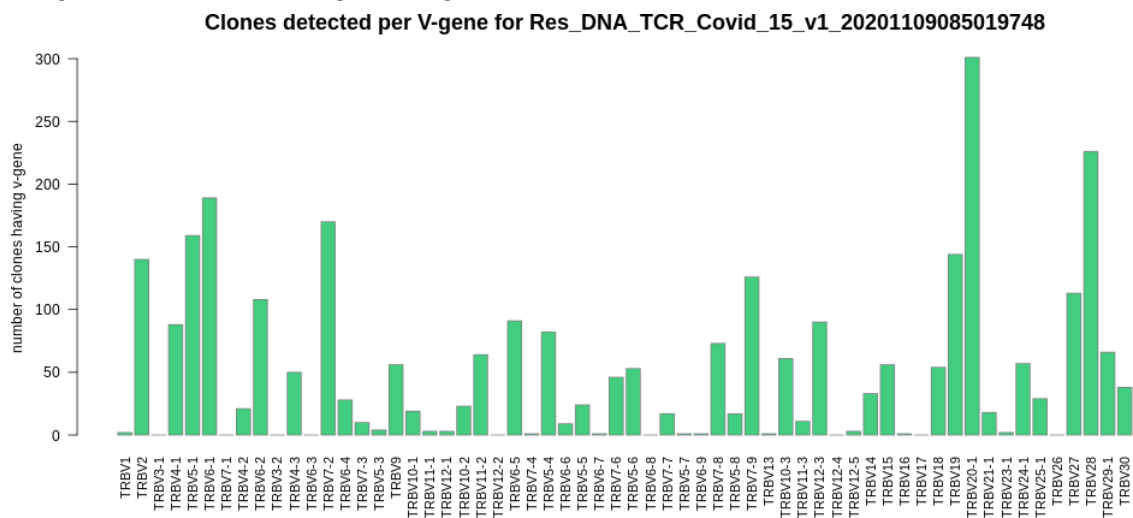


TCRB V-gene usage

Non-virus lung case 1

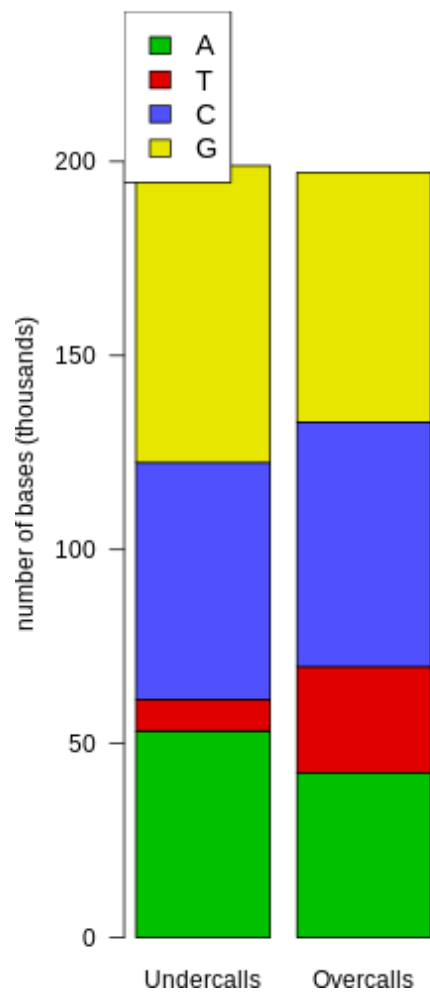


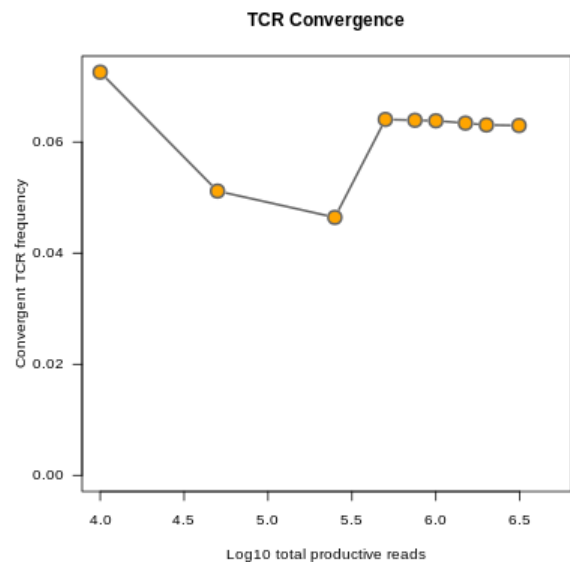
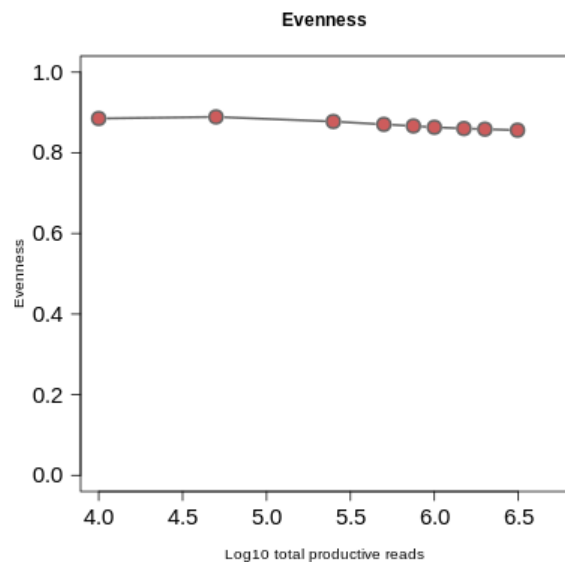
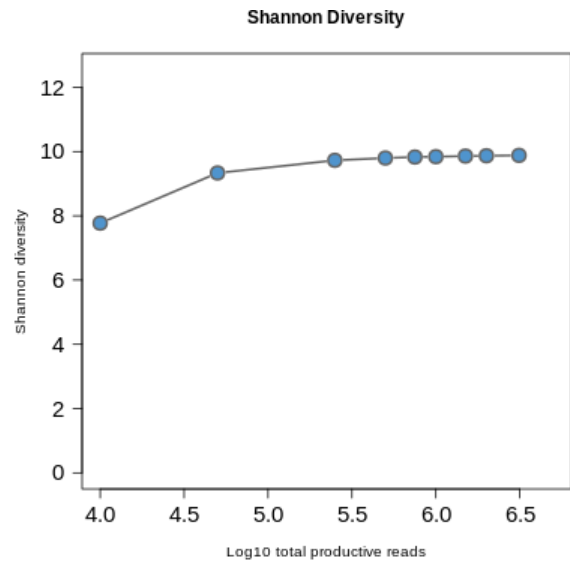
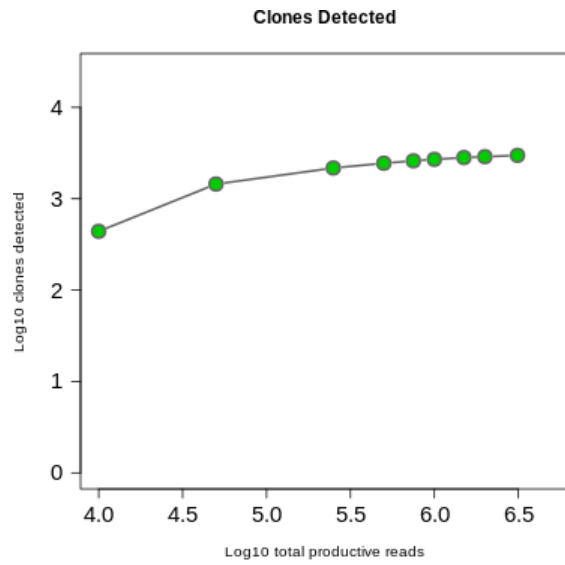
Histogram of CDR3 nucleotide length showing a normal distribution

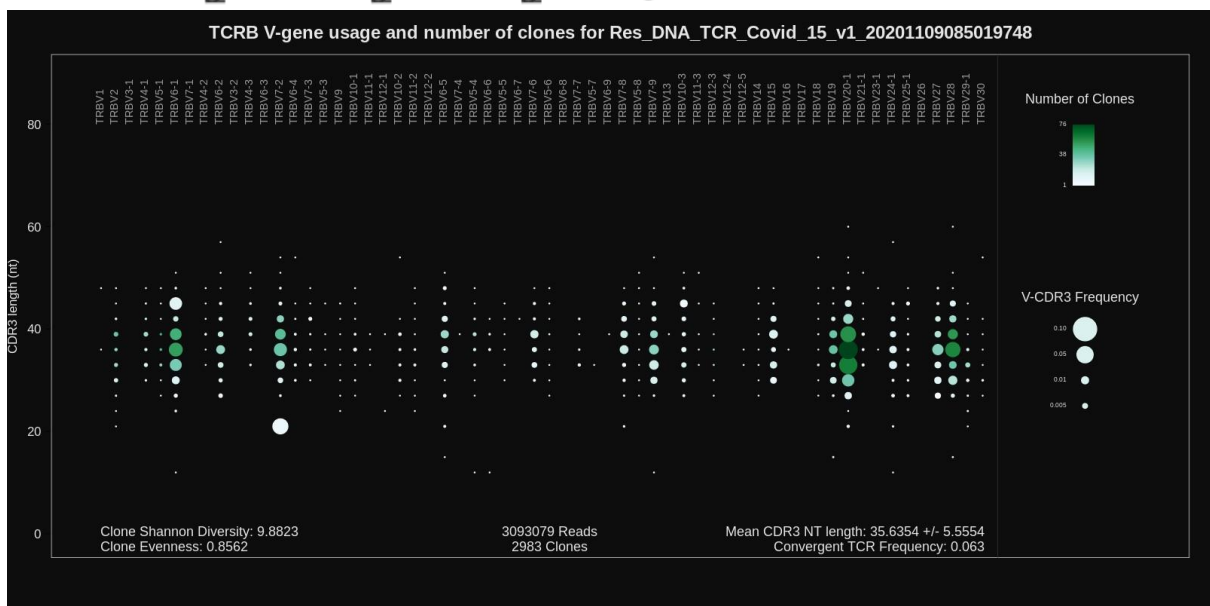
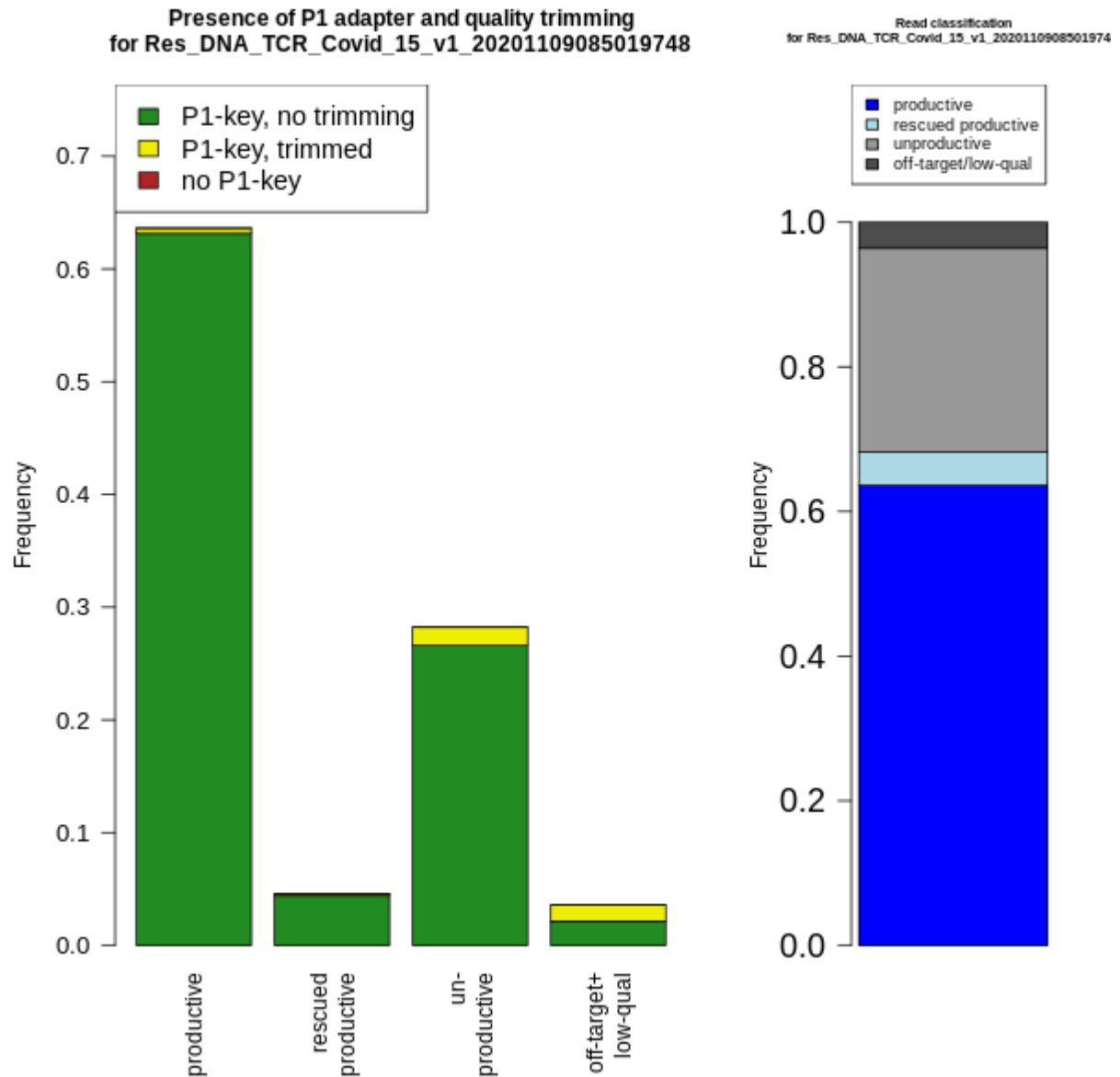


Number of clones per V-gene

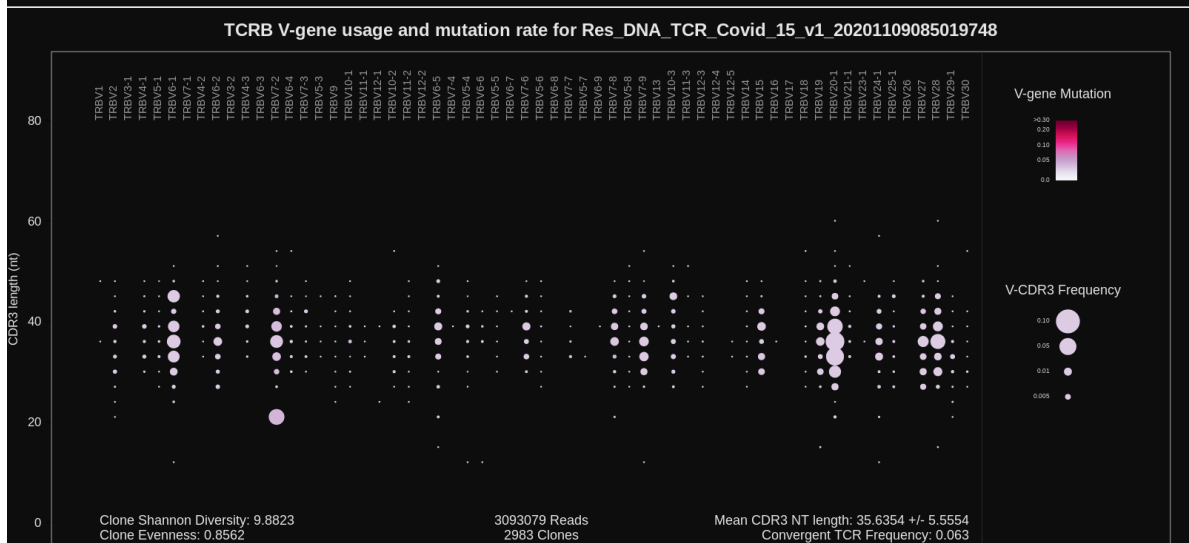
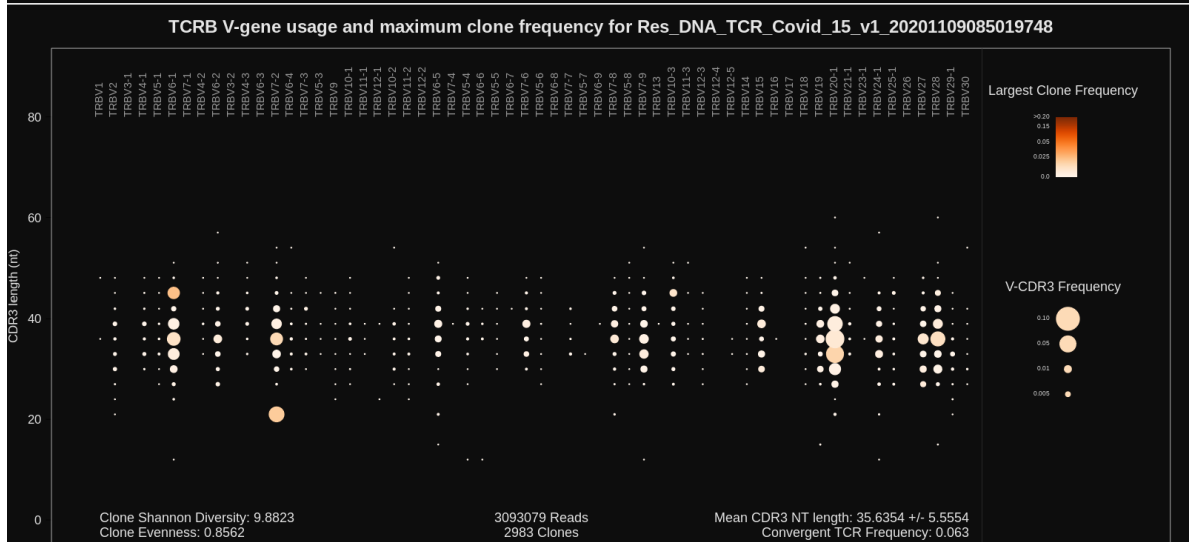
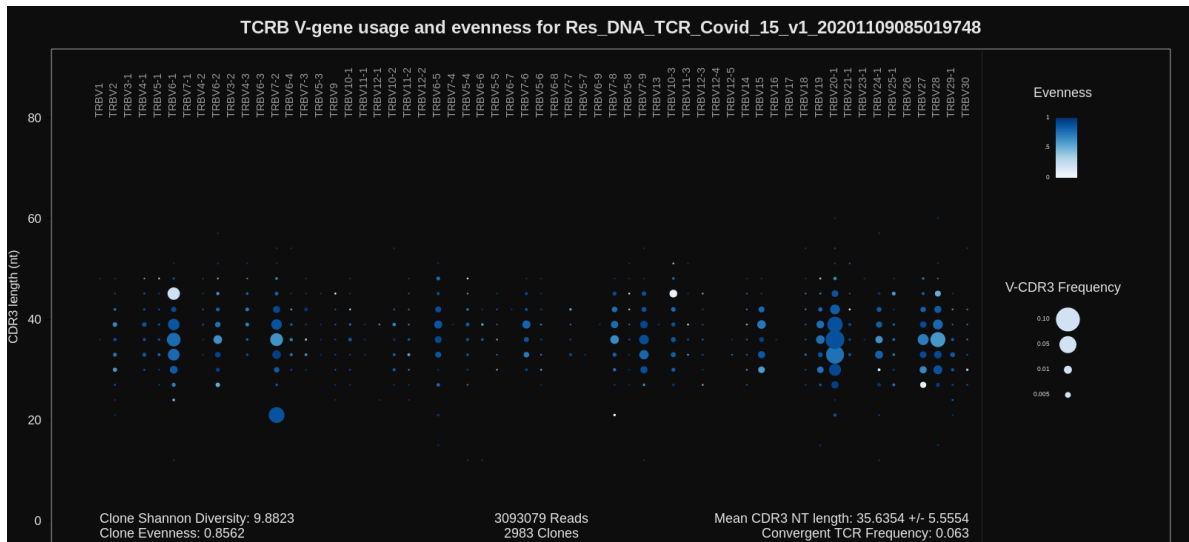
Repaired base composition
for Res_DNA_TCR_Covid_15_v1_2020110908501974



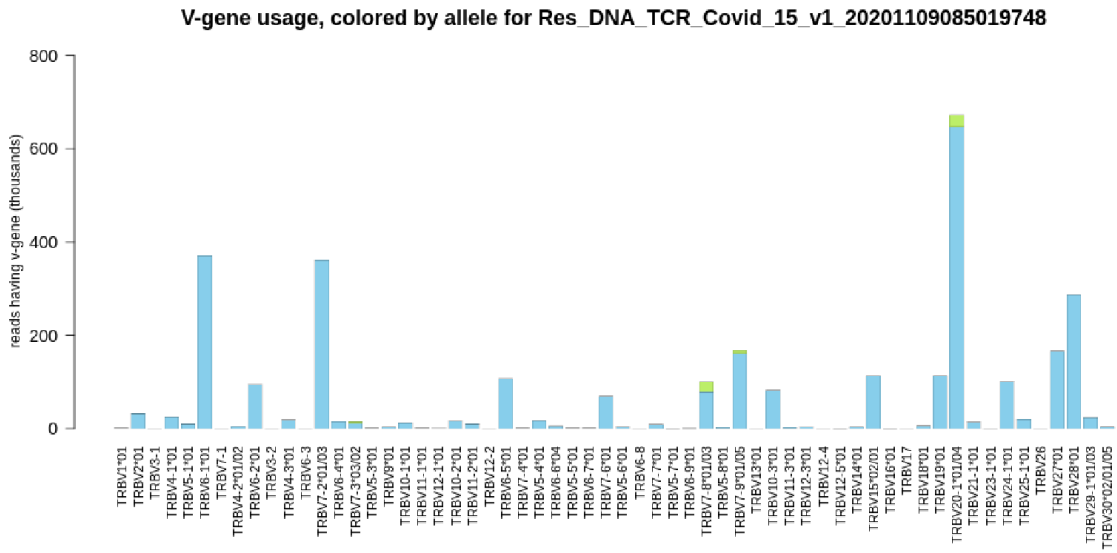
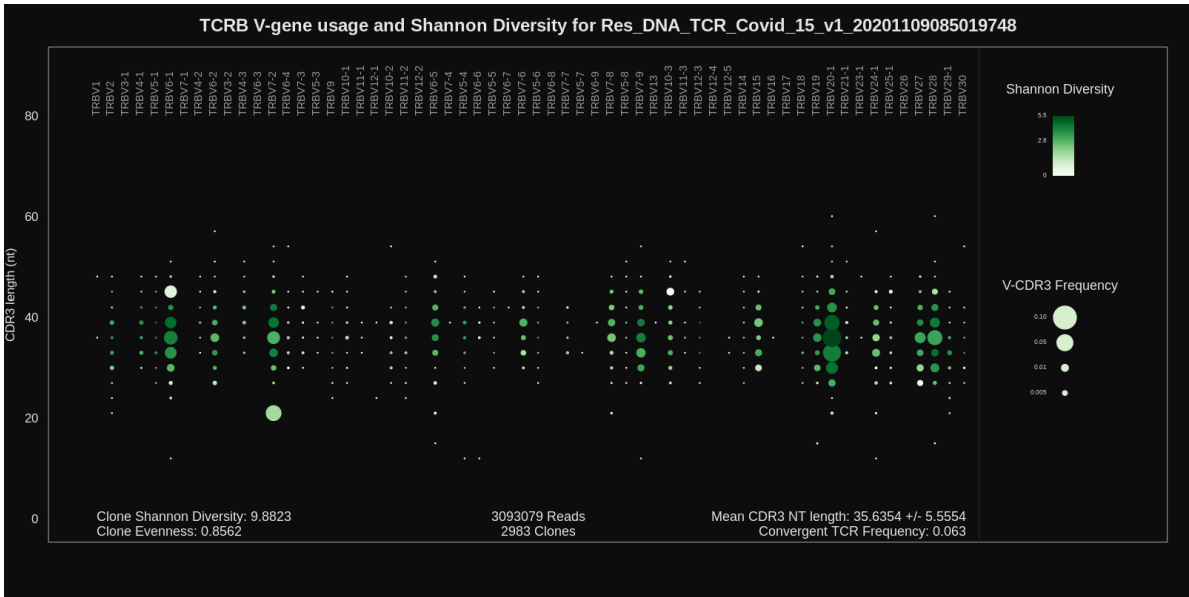




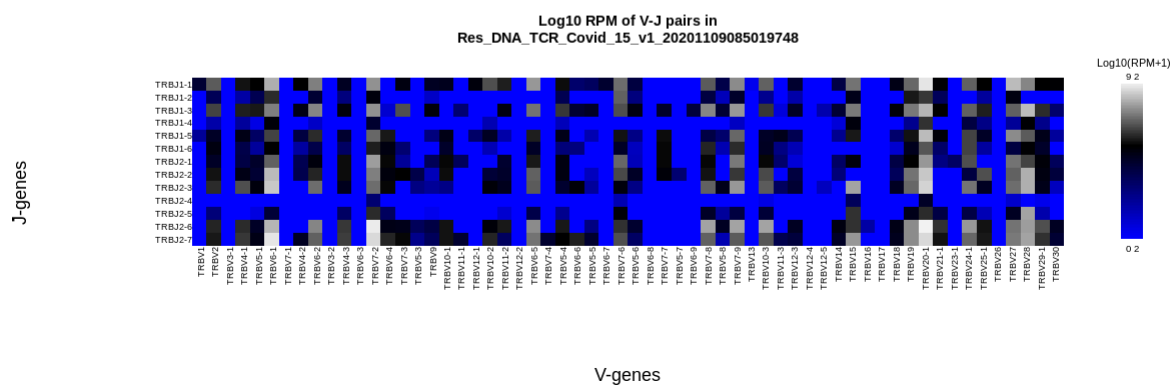
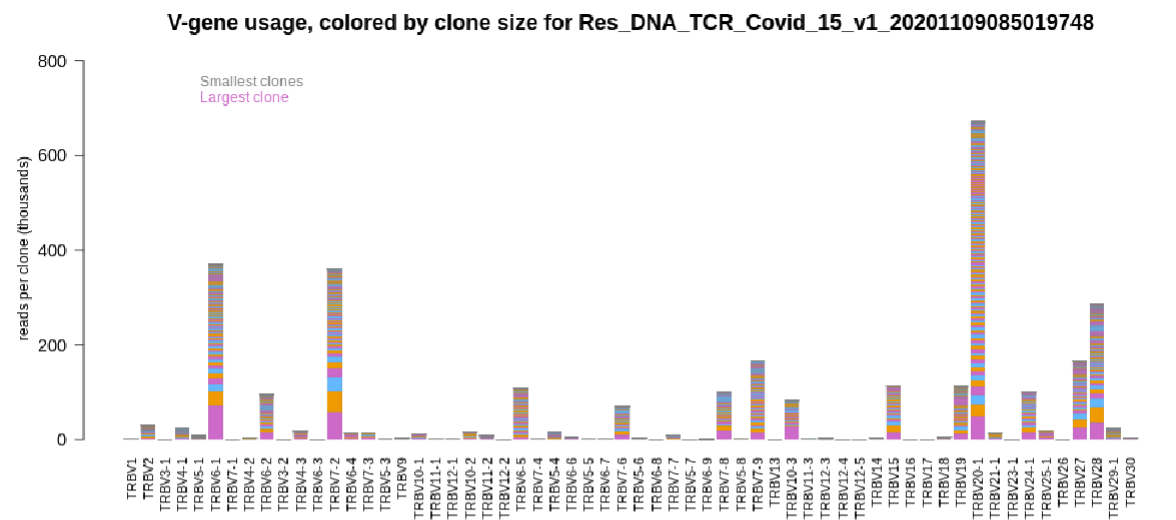
TCRB V-gene usage



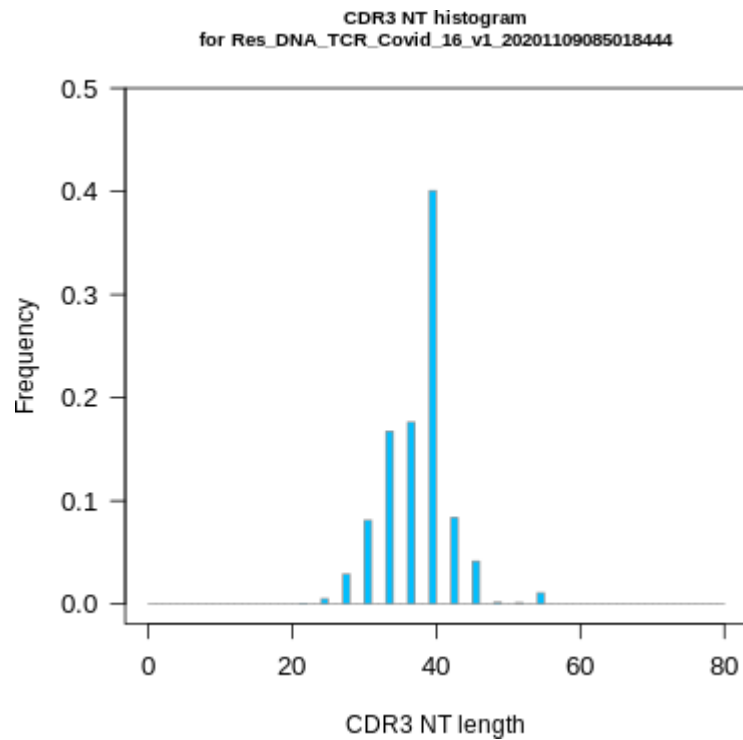
TCRB V-gene usage



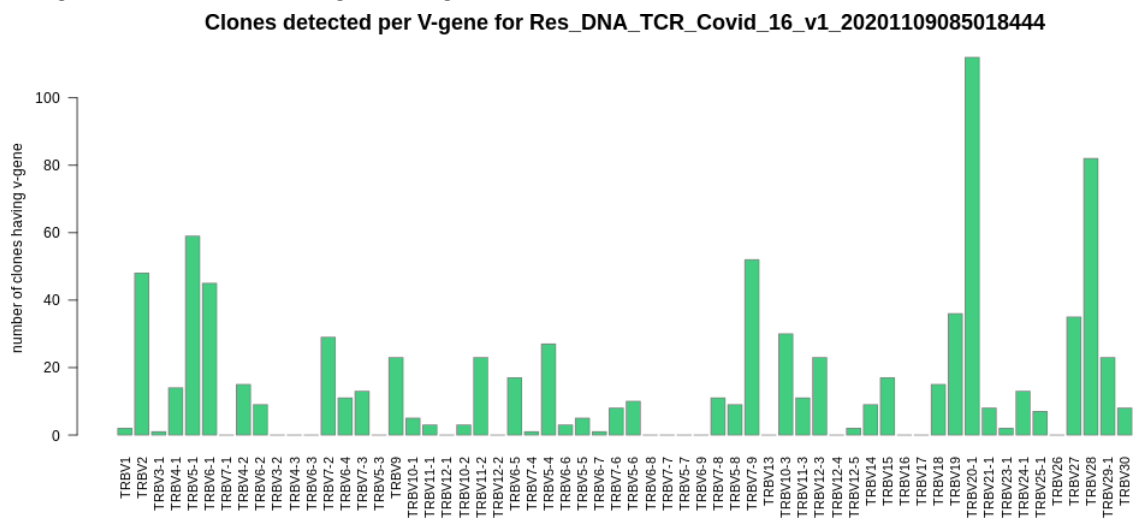
TCRB V-gene usage



Non-virus lung case 2

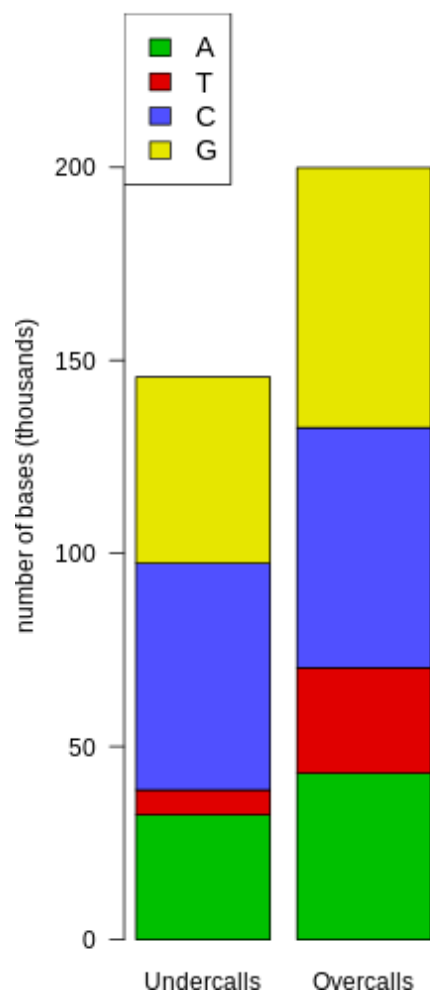


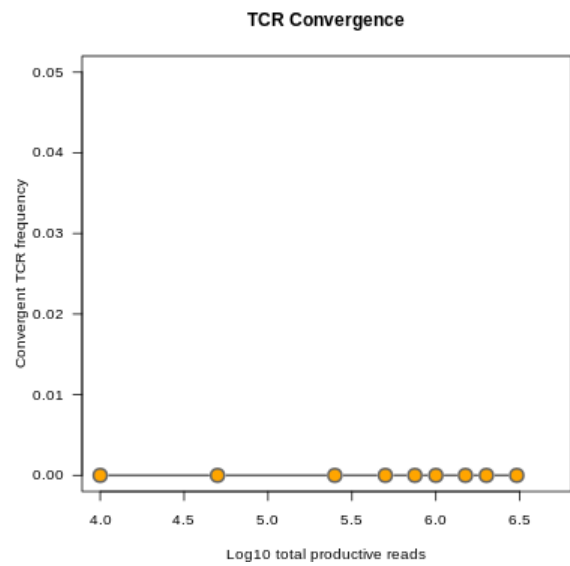
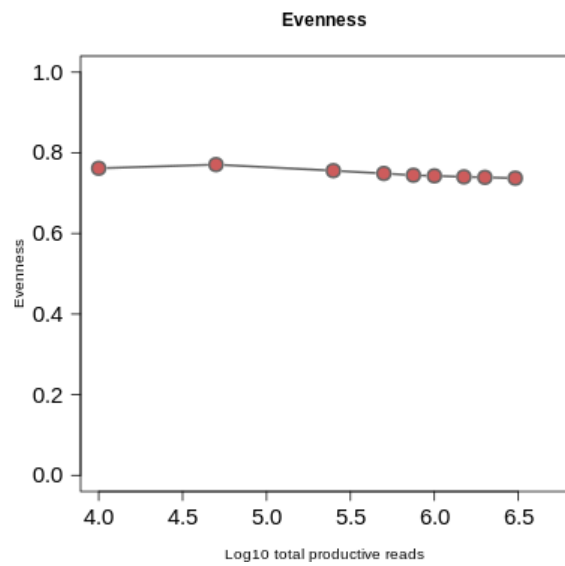
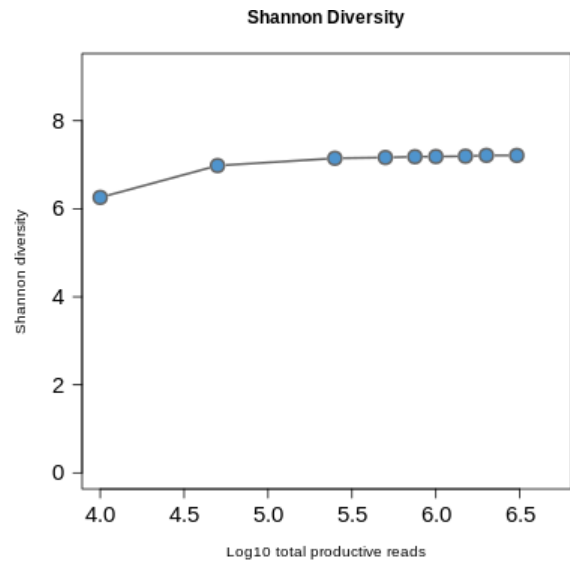
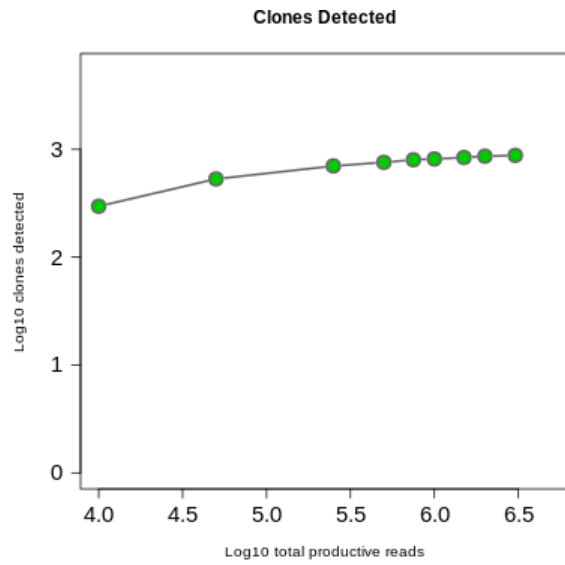
Histogram of CDR3 nucleotide length showing a normal distribution



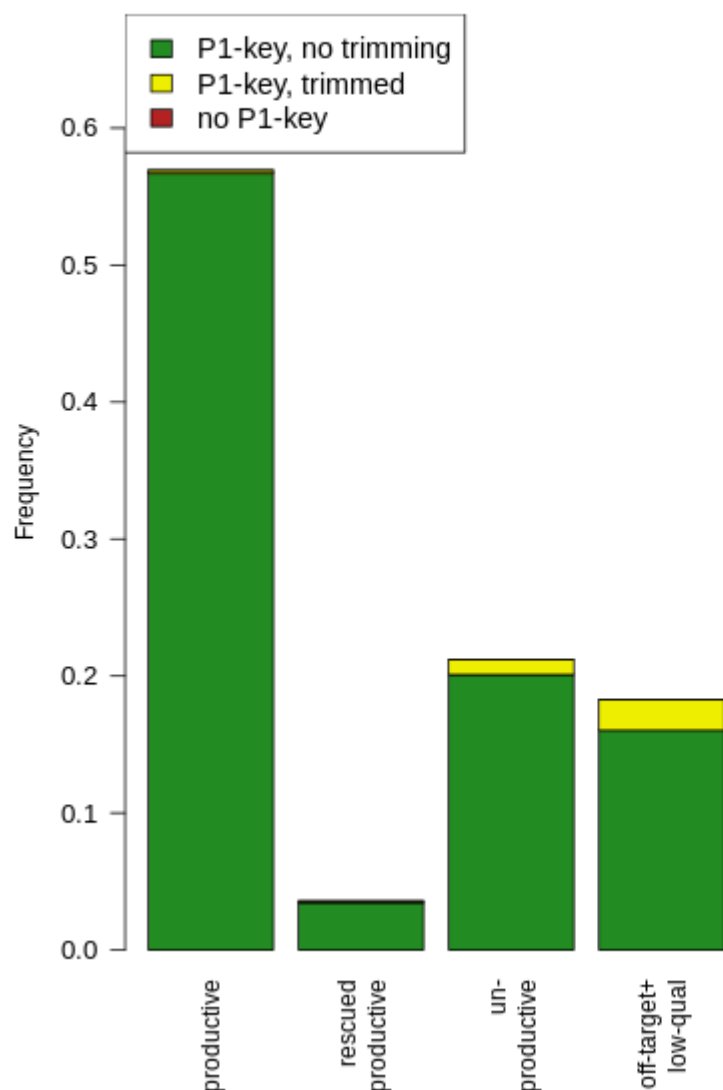
Number of clones per V-gene

Repaired base composition
for Res_DNA_TCR_Covid_16_v1_202011090850184

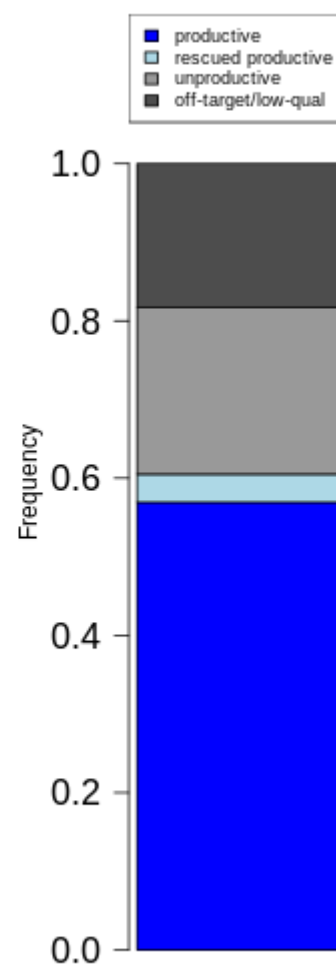




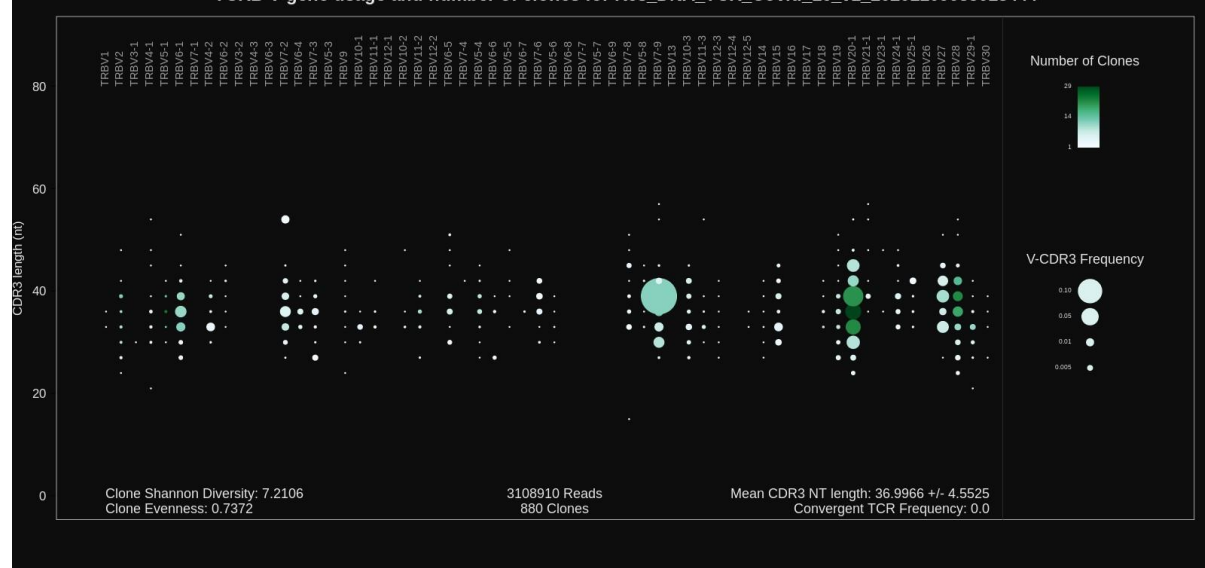
Presence of P1 adapter and quality trimming for Res_DNA_TCR_Covid_16_v1_20201109085018444

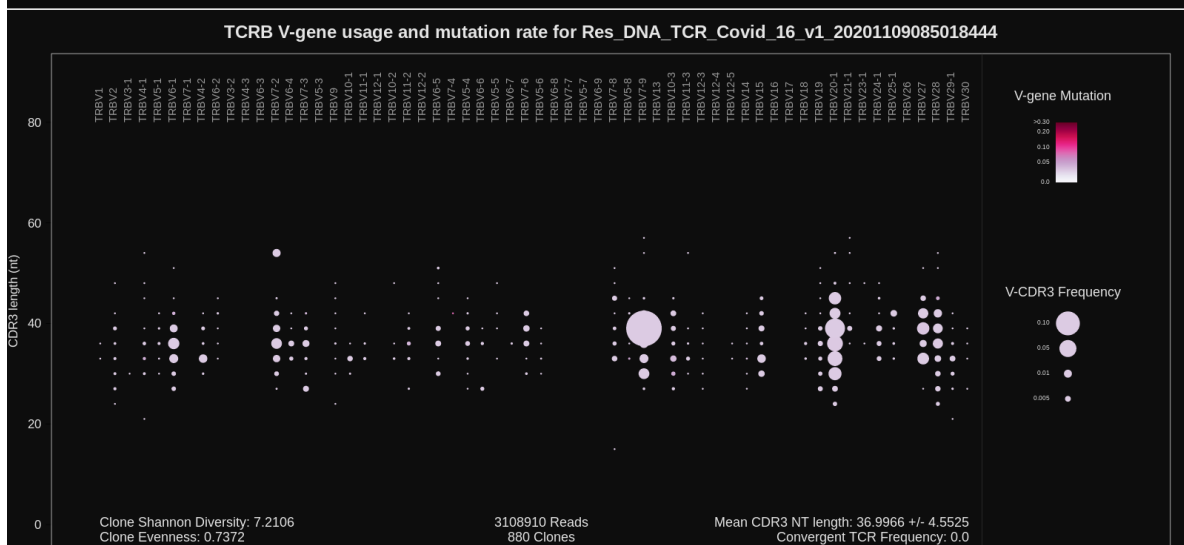
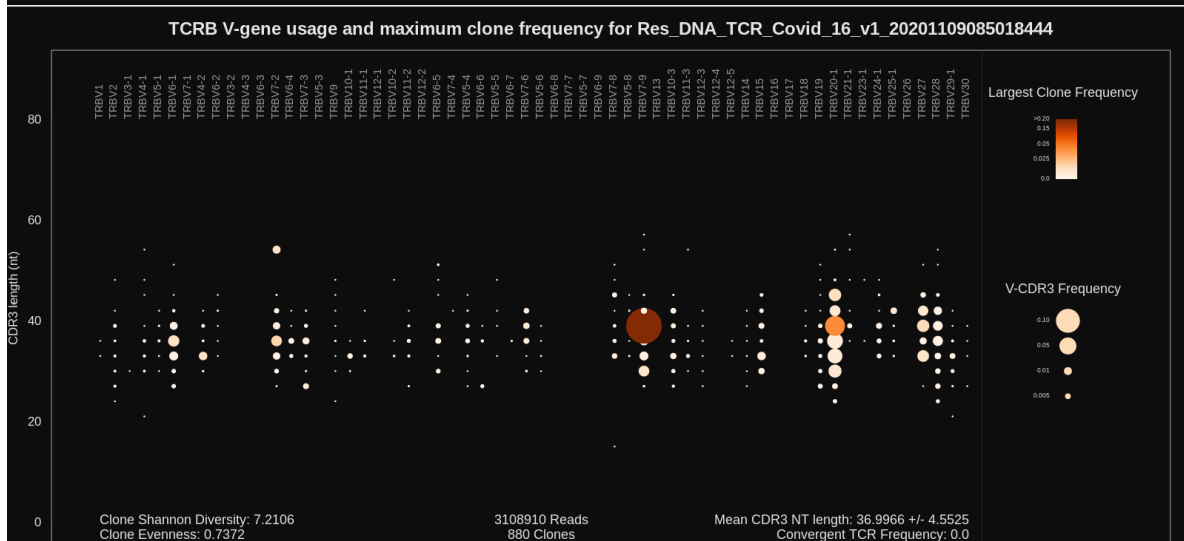
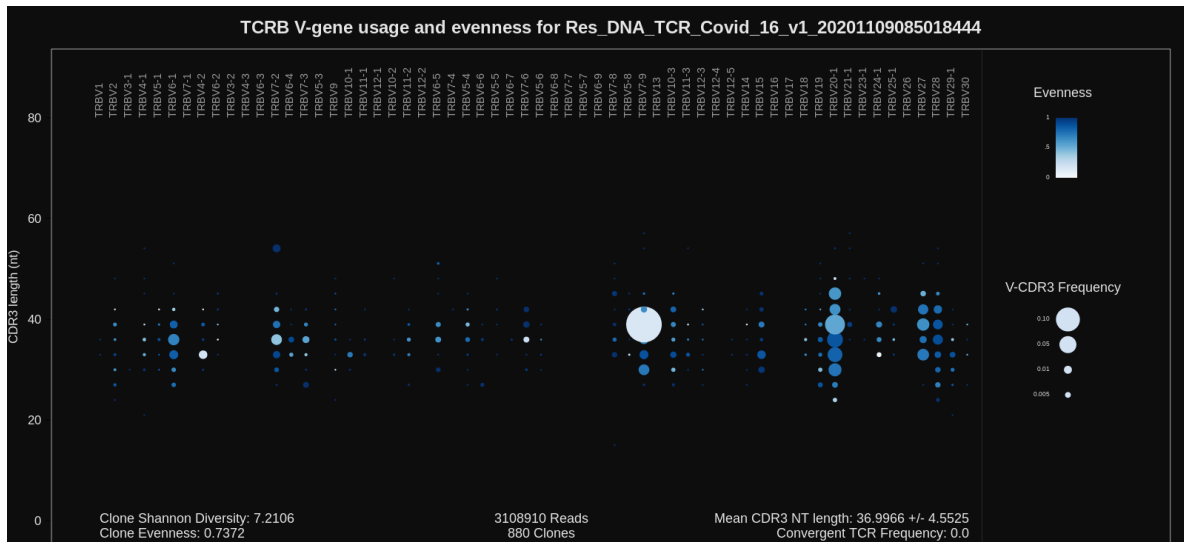


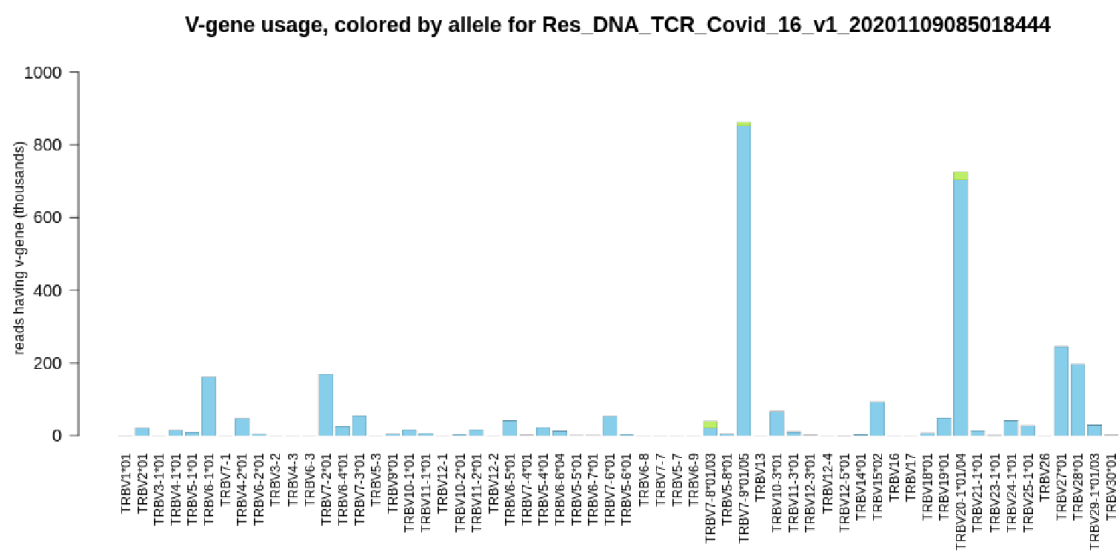
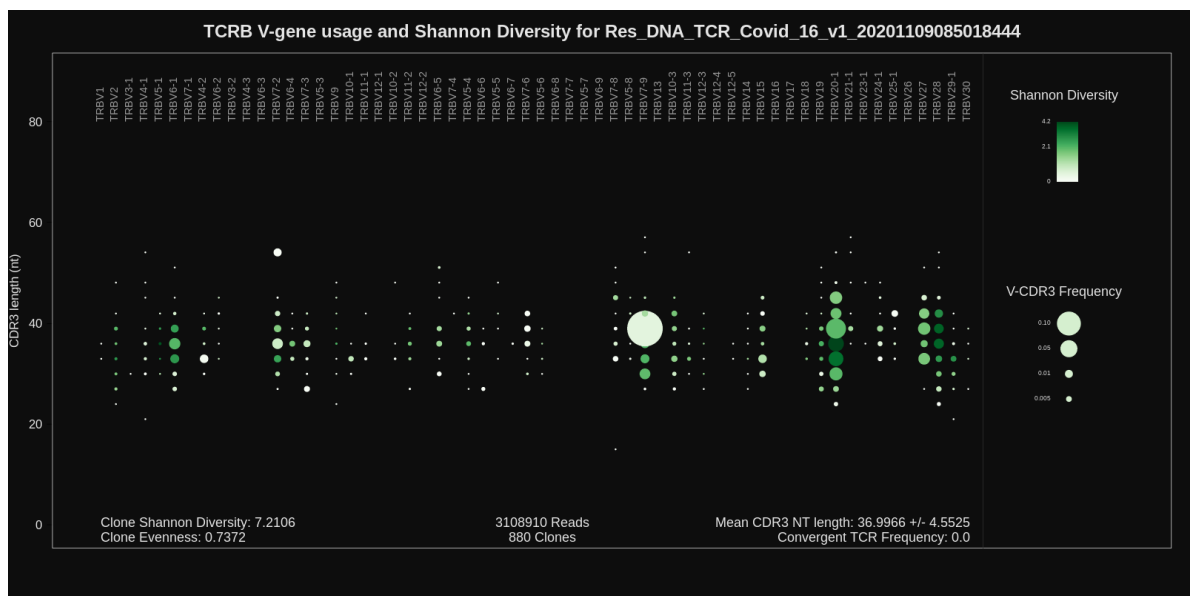
Read classification for Res_DNA_TCR_Covid_16_v1_2020110908501844



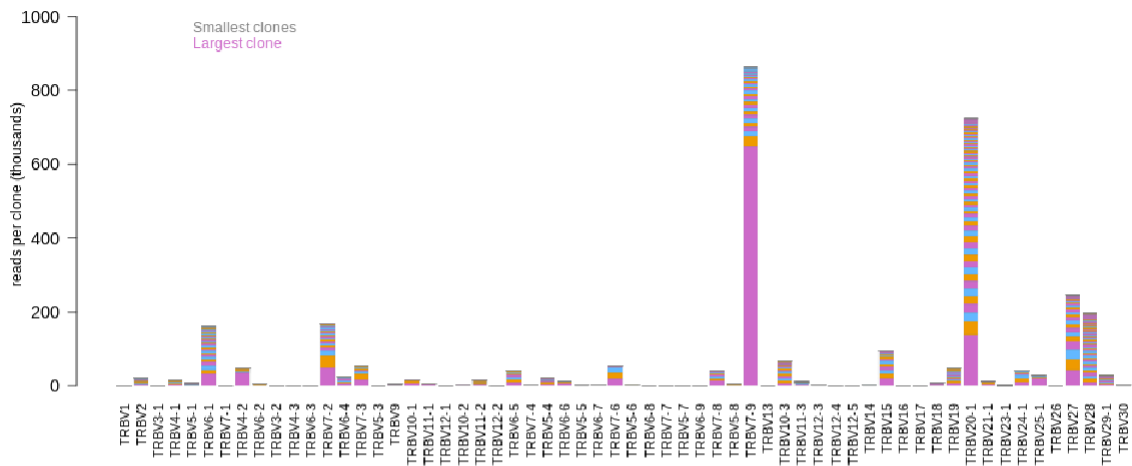
TCRB V-gene usage and number of clones for Res_DNA_TCR_Covid_16_v1_20201109085018444



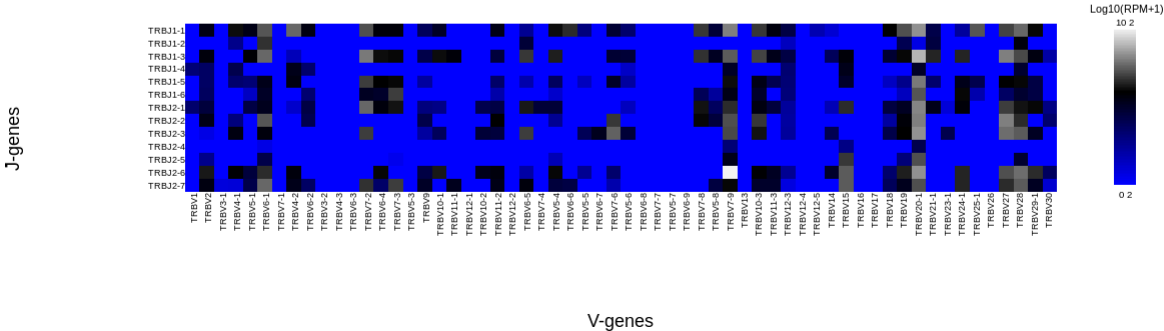




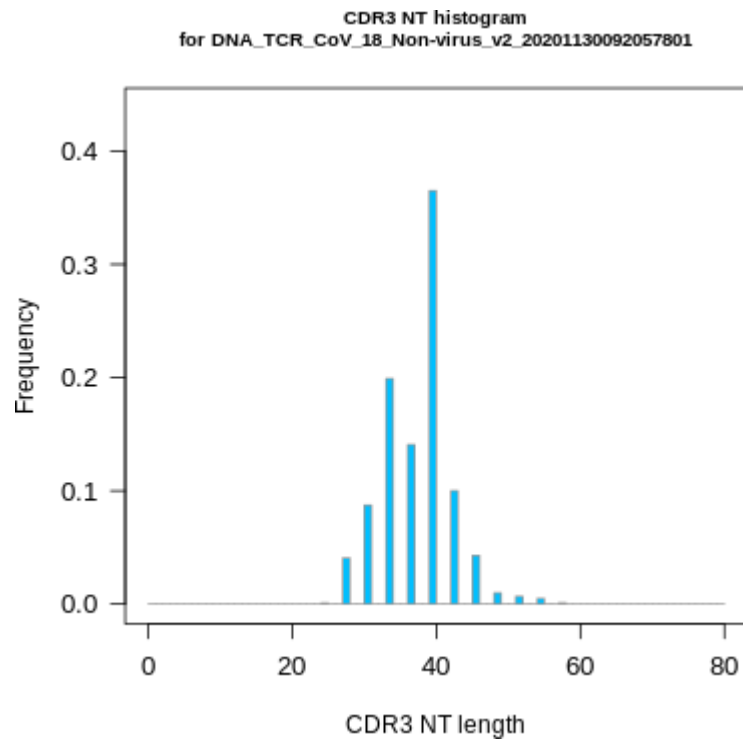
V-gene usage, colored by clone size for Res_DNA_TCR_Covid_16_v1_20201109085018444



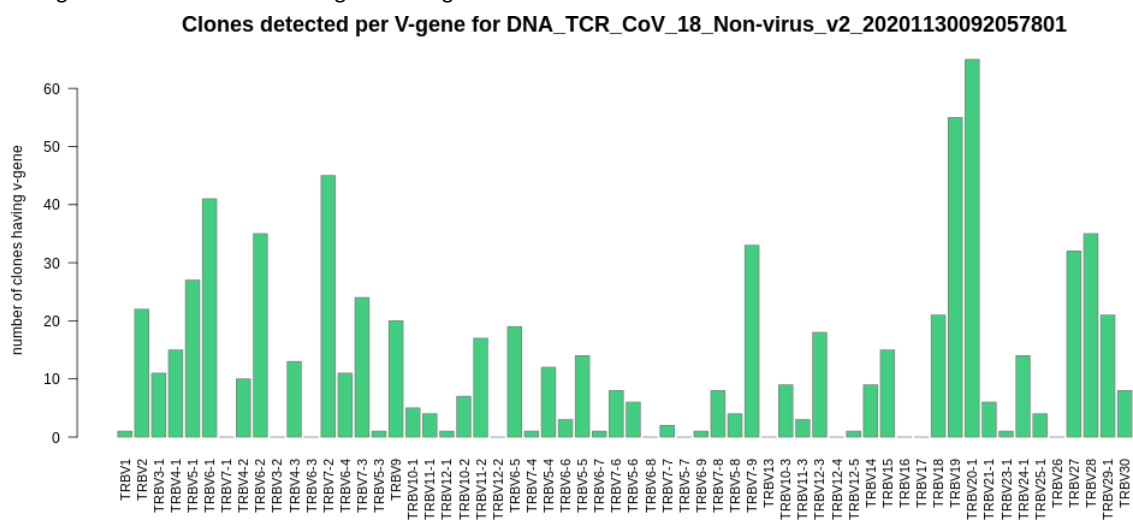
Log10 RPM of V-J pairs in
Res_DNA_TCR_Covid_16_v1_20201109085018444



Non-virus lung case 3

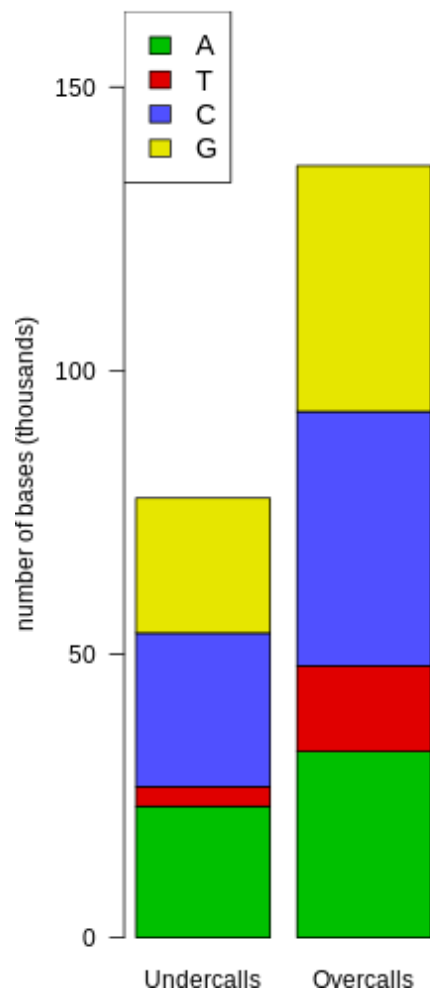


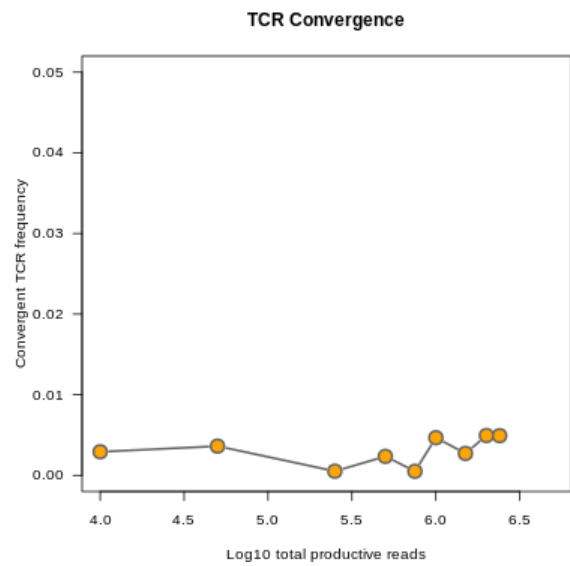
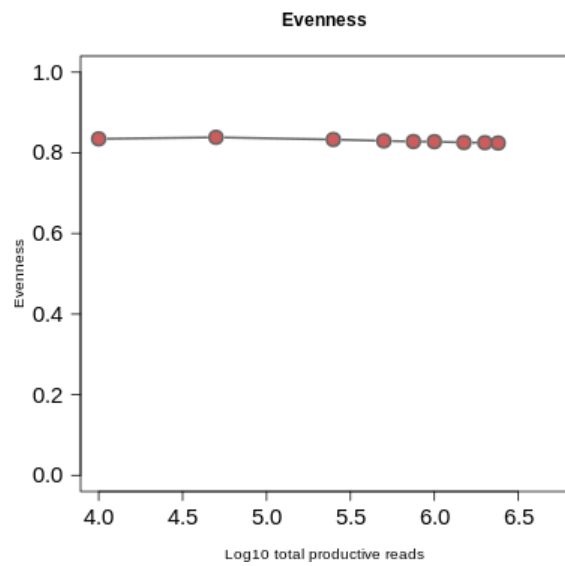
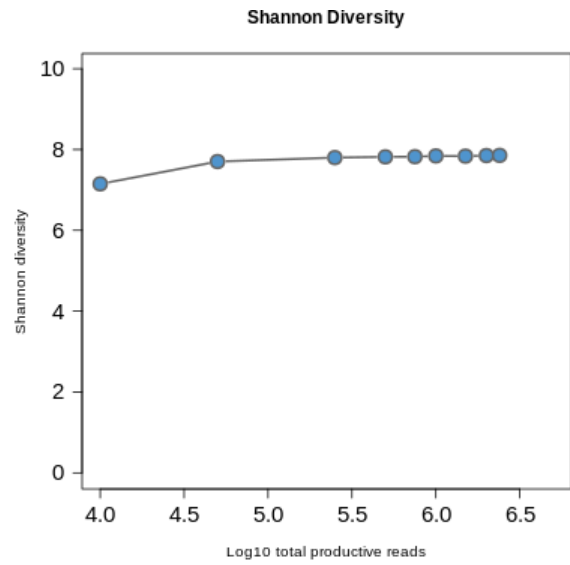
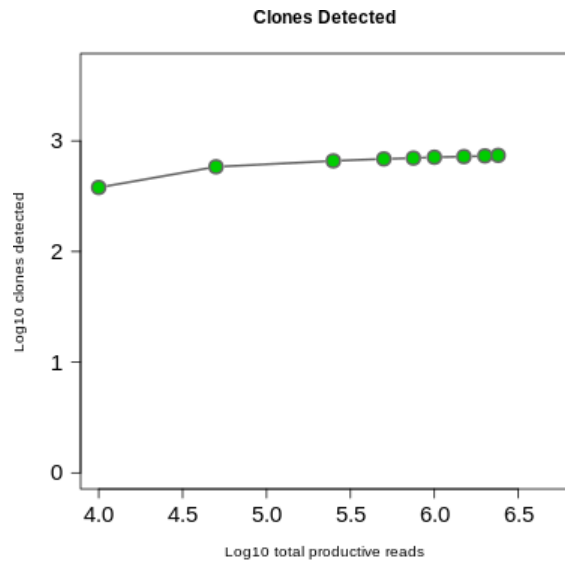
Histogram of CDR3 nucleotide length showing a normal distribution



Number of clones per V-gene

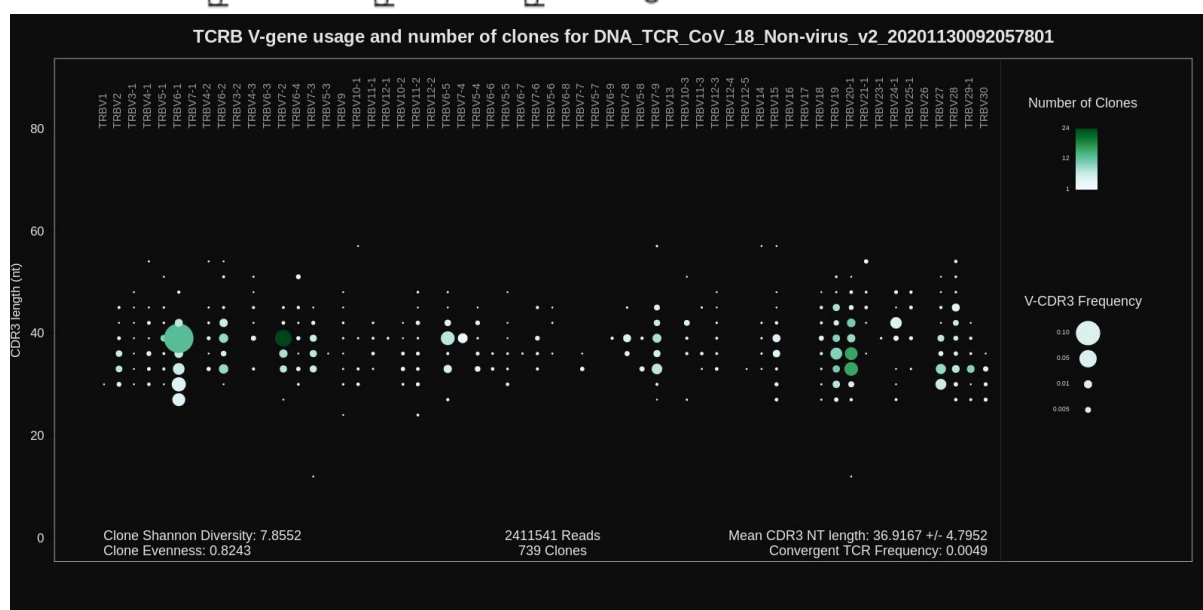
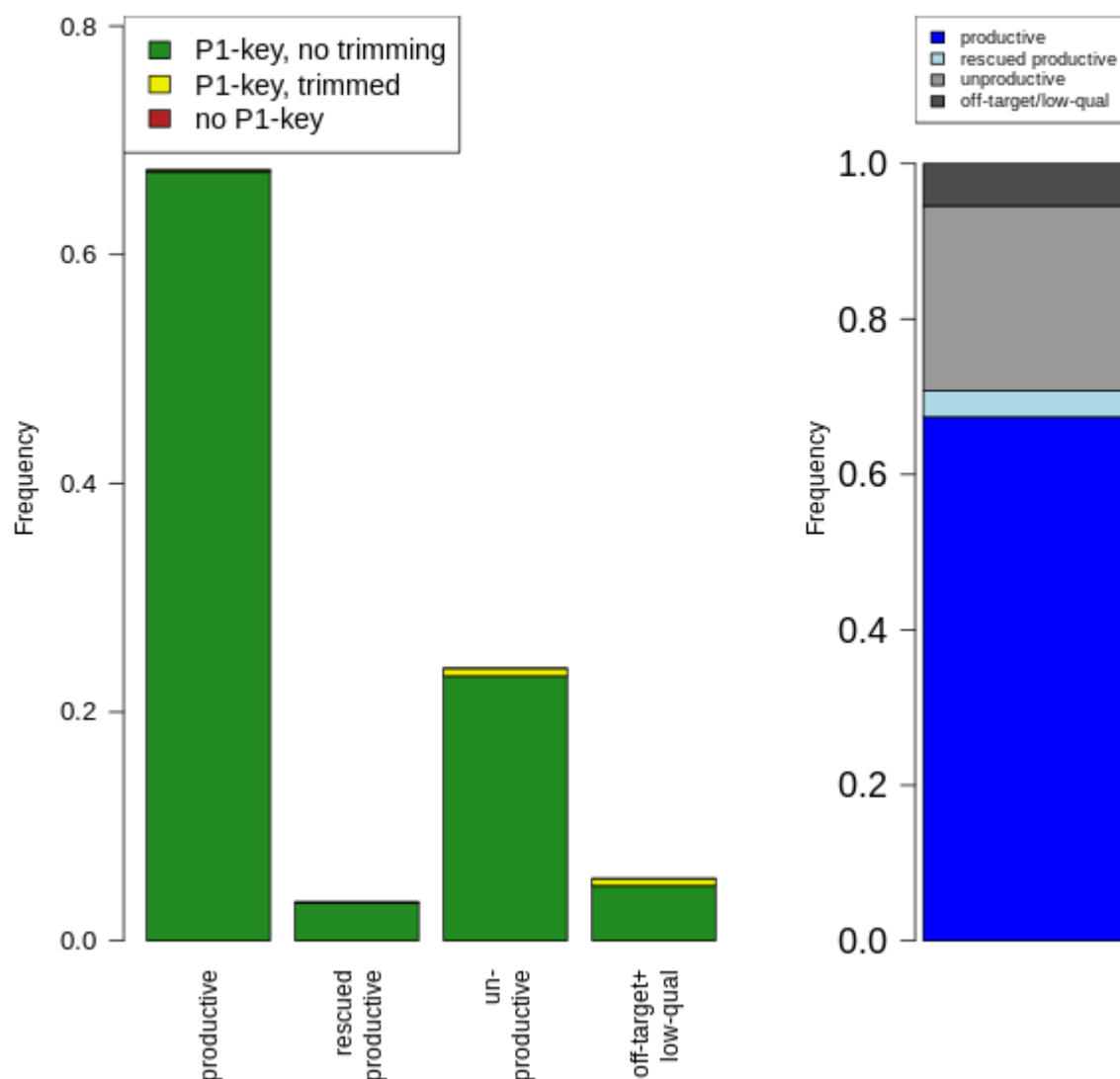
Repaired base composition
for DNA_TCR_CoV_18_Non-virus_v2_20201130092051

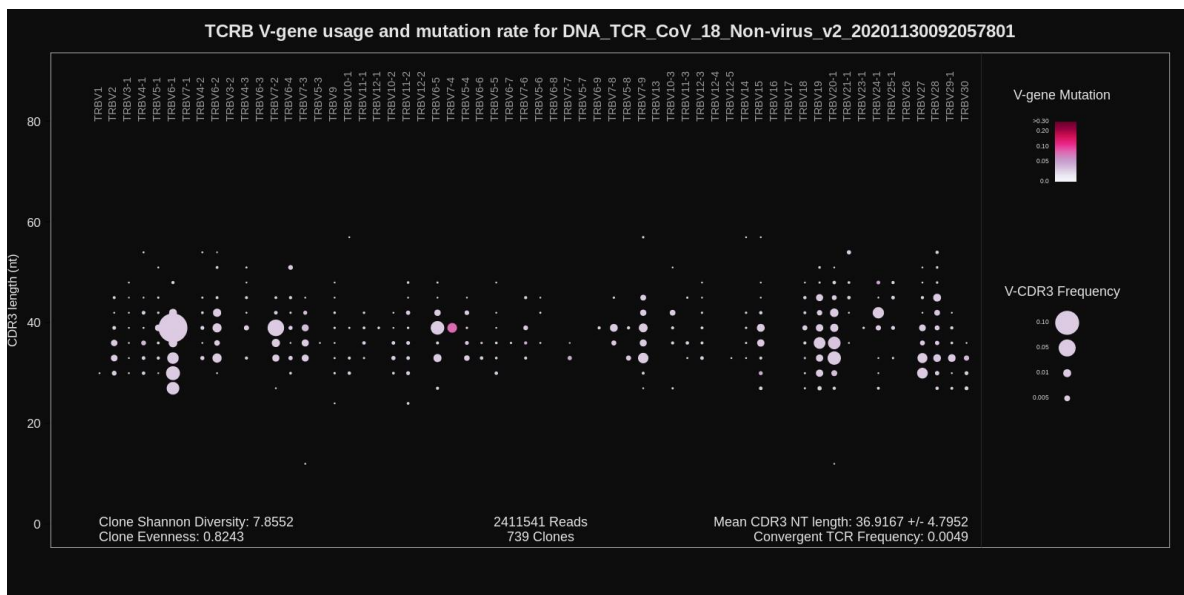
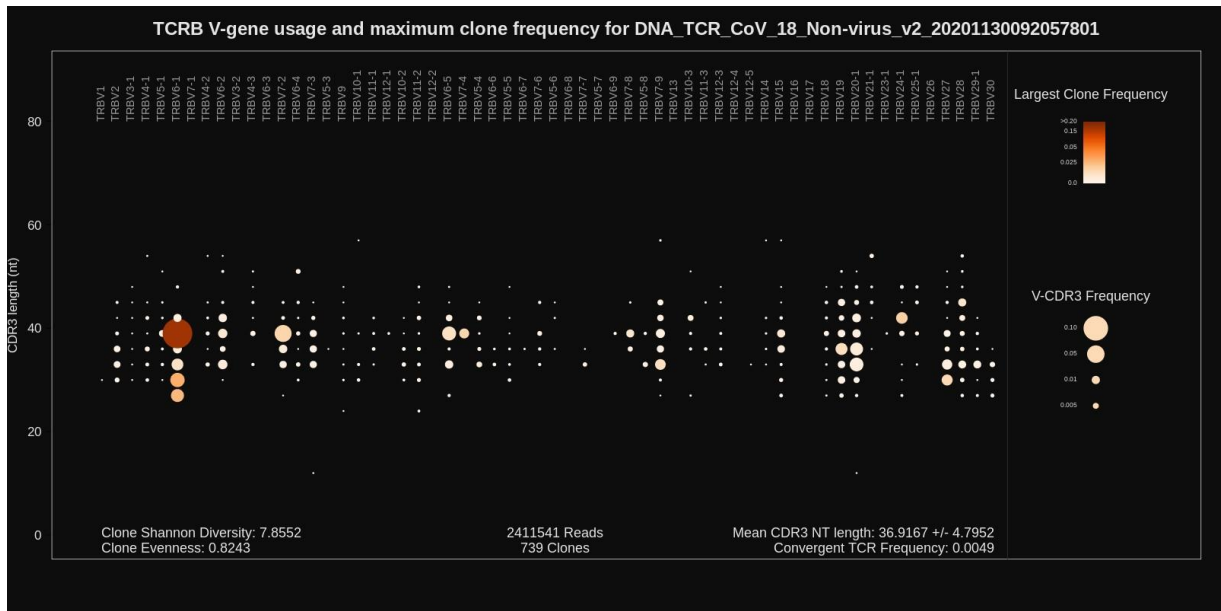
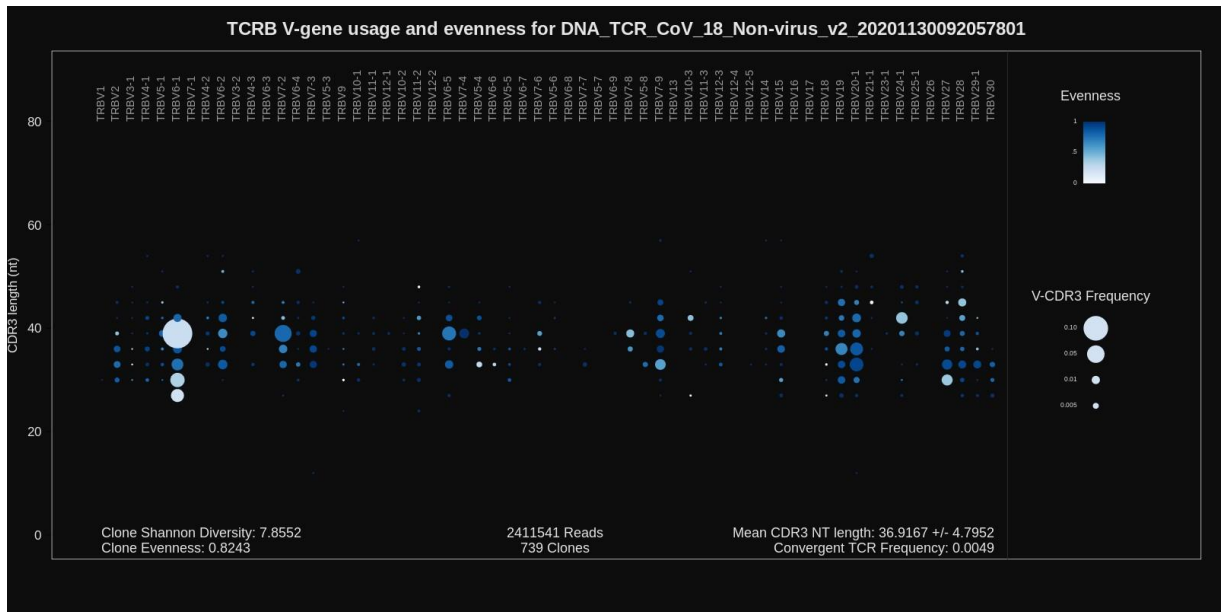




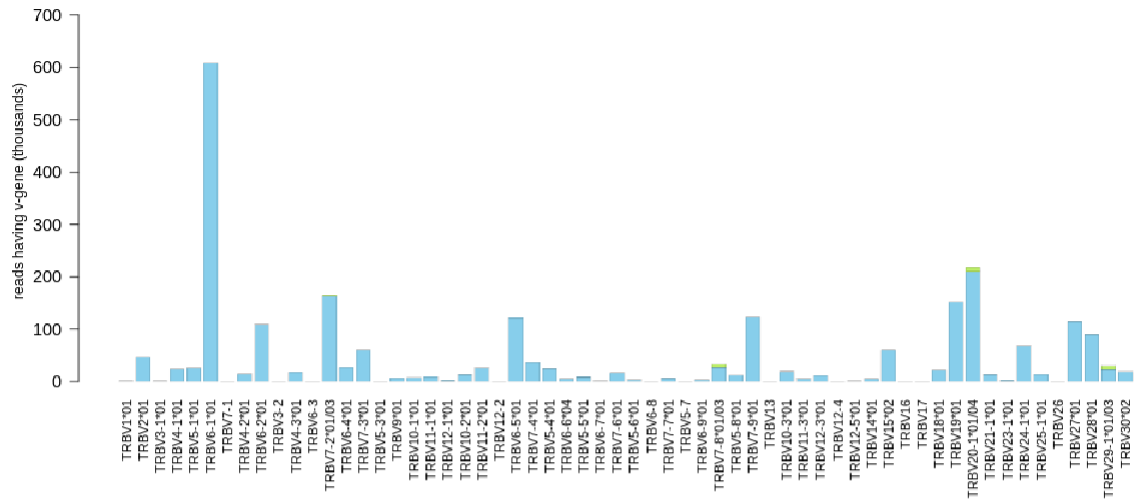
Presence of P1 adapter and quality trimming for DNA_TCR_CoV_18_Non-virus_v2_20201130092057801

Read classification
for DNA_TCR_CoV_18_Non-virus_v2_20201130092057801

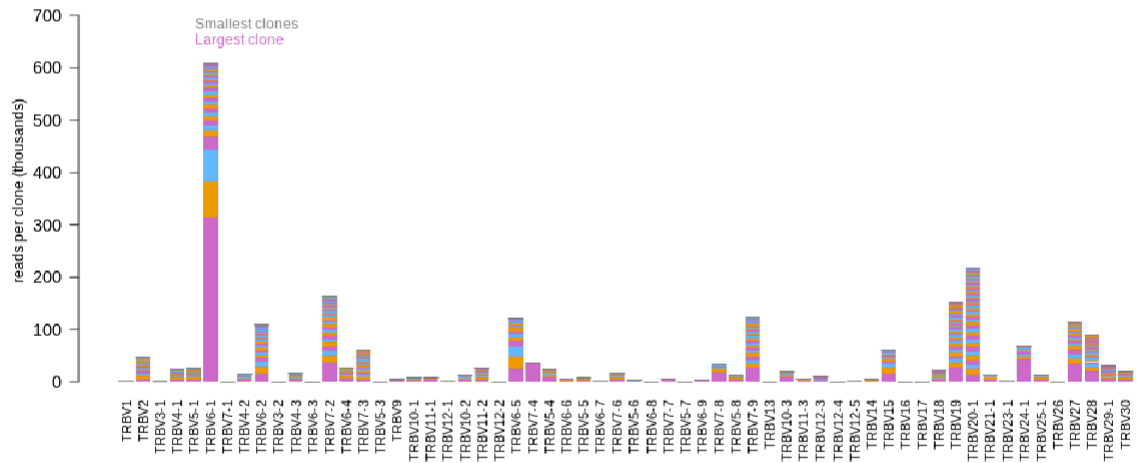




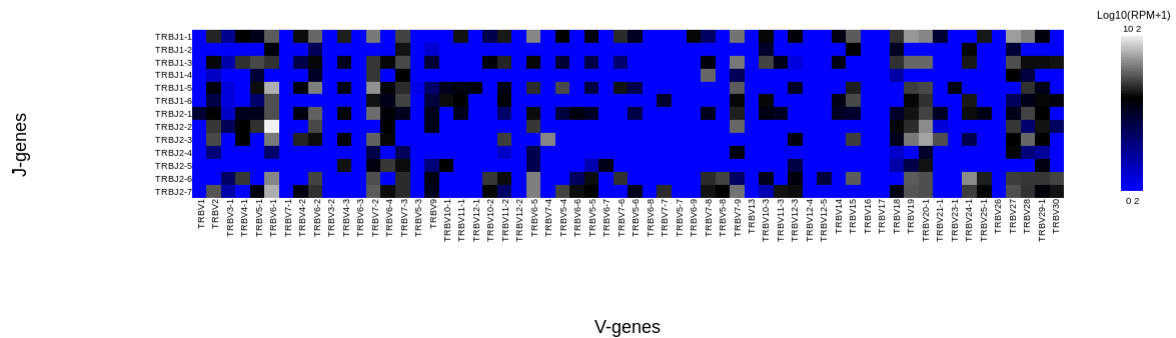
V-gene usage, colored by allele for DNA_TCR_CoV_18_Non-virus_v2_20201130092057801



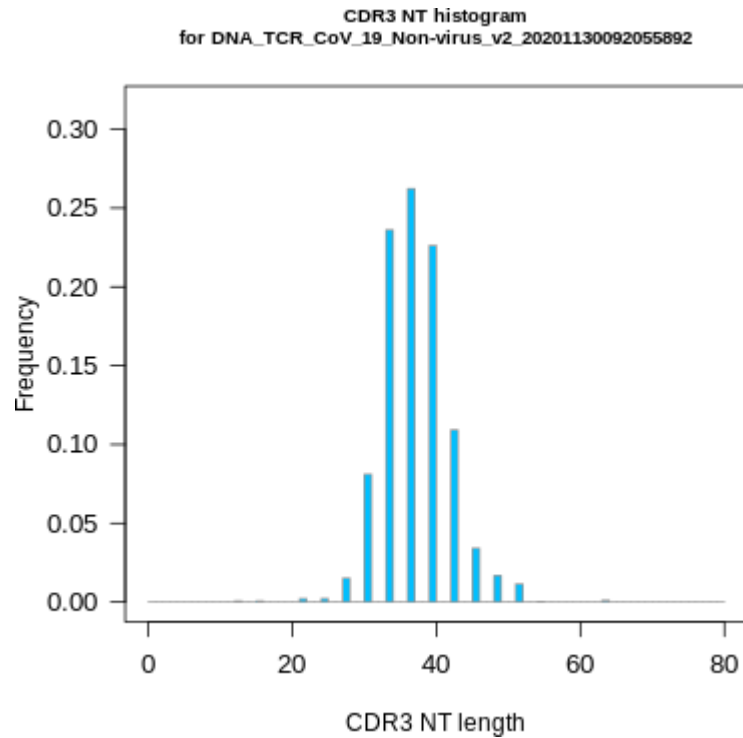
V-gene usage, colored by clone size for DNA_TCR_CoV_18_Non-virus_v2_20201130092057801



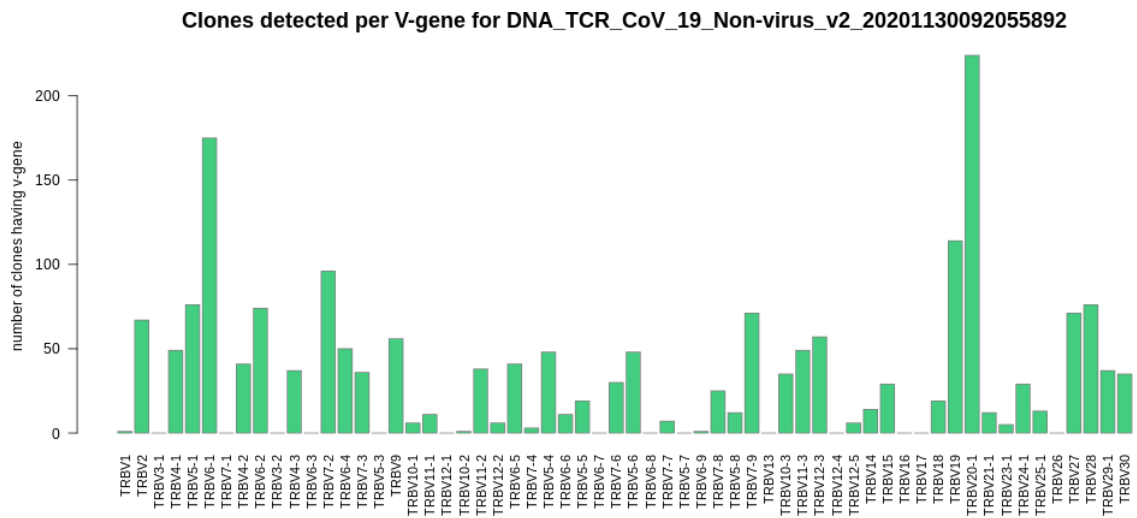
Log10 RPM of V-J pairs in
DNA_TCR_CoV_18_Non-virus_v2_20201130092057801



Non-virus lung case 4

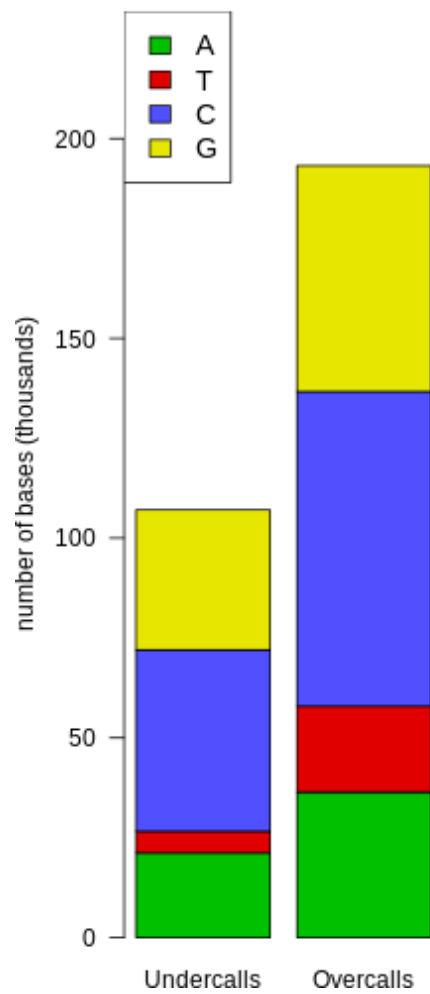


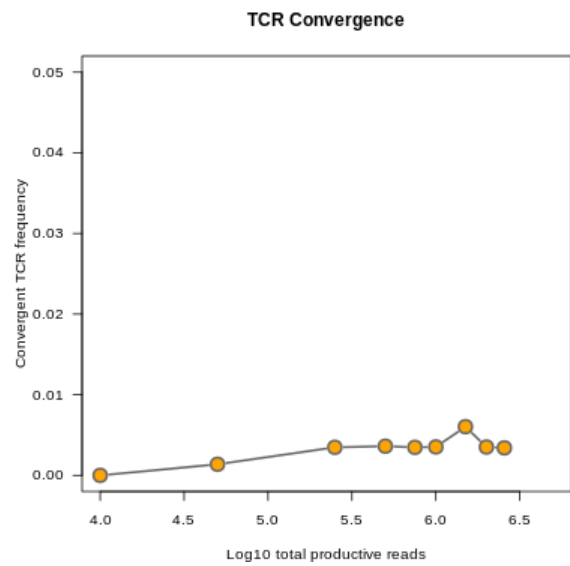
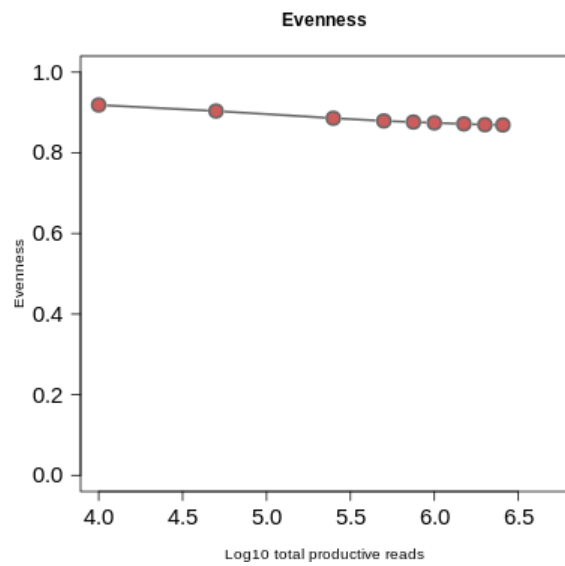
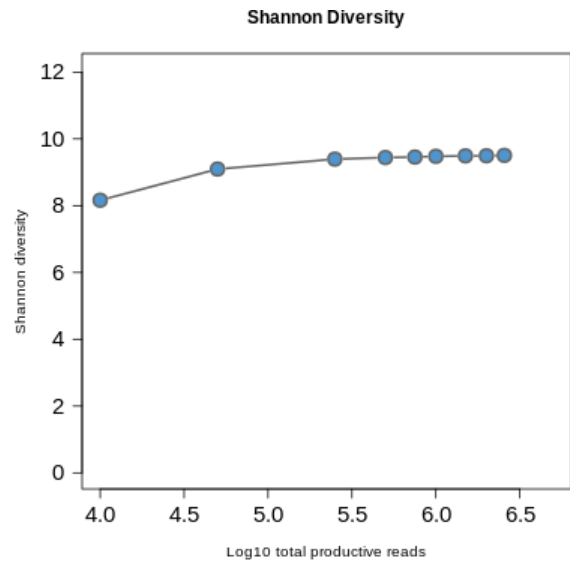
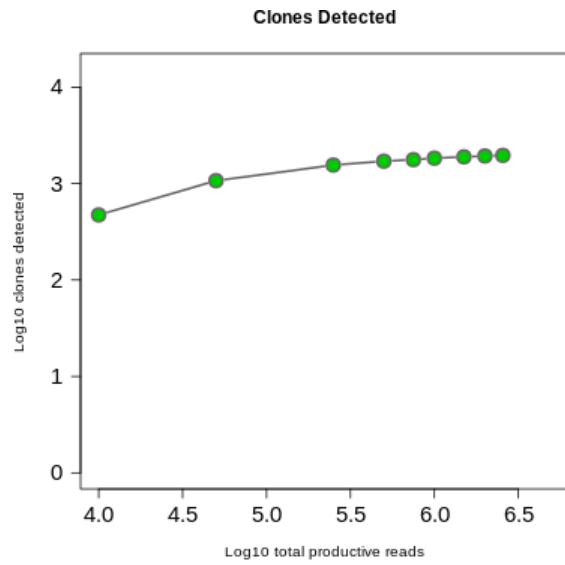
Histogram of CDR3 nucleotide length showing a normal distribution



Number of clones per V-gene

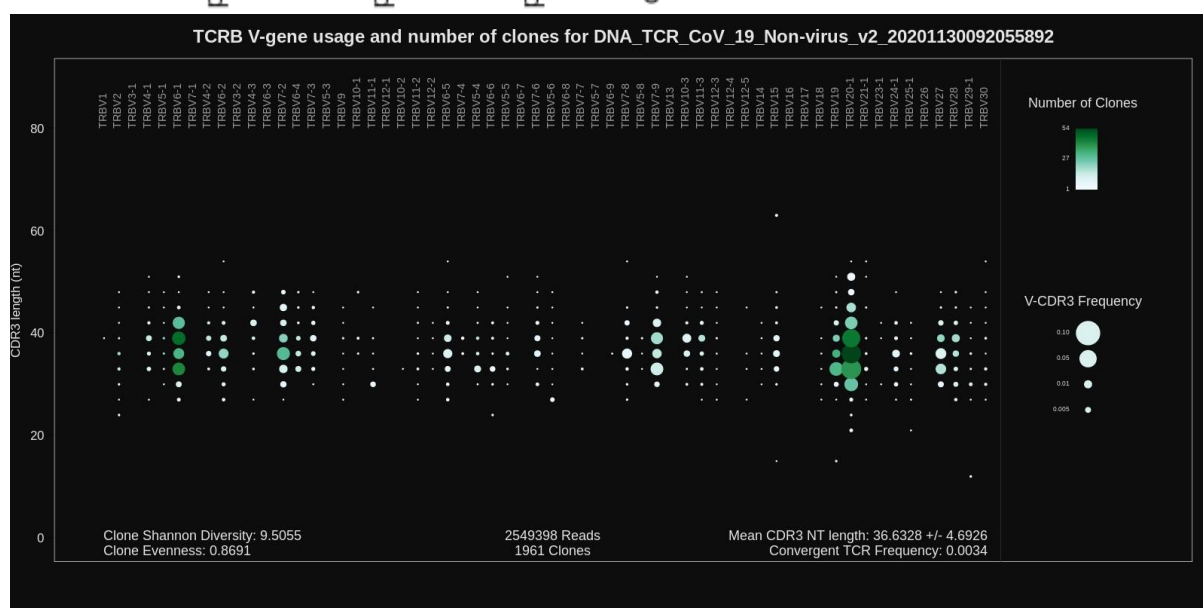
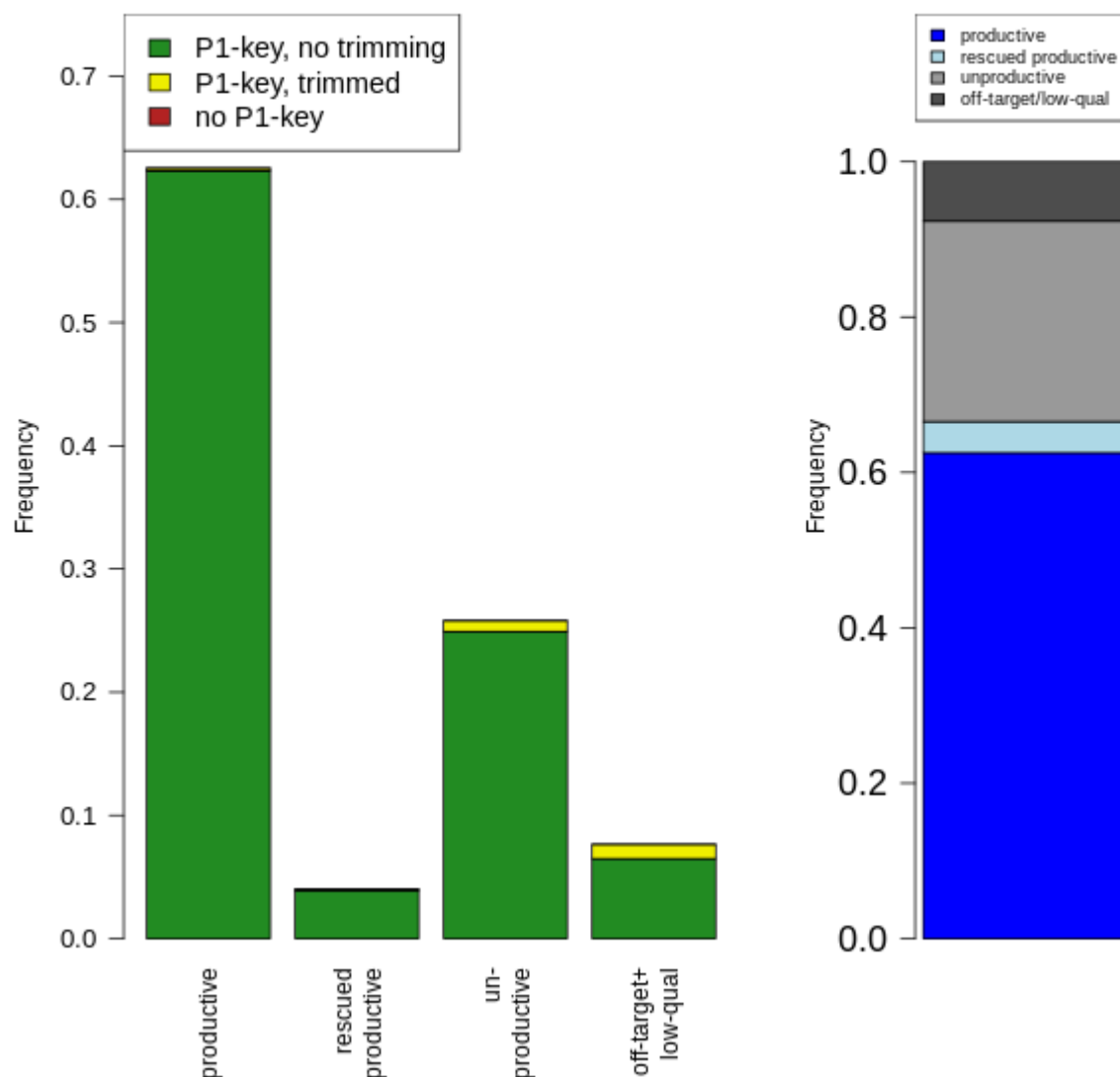
Repaired base composition
for DNA_TCR_CoV_19_Non-virus_v2_2020113009205t



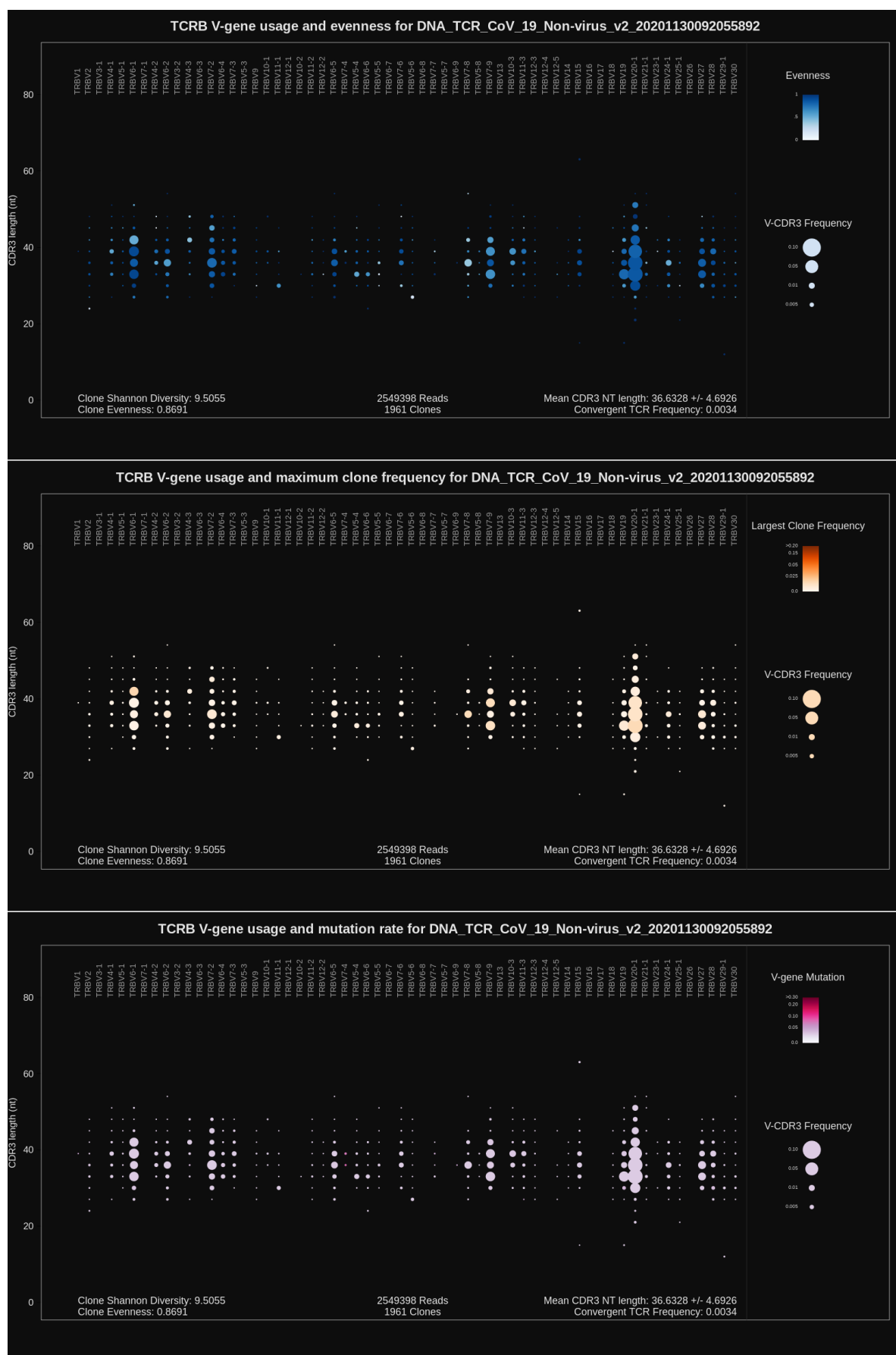


Presence of P1 adapter and quality trimming for DNA_TCR_CoV_19_Non-virus_v2_20201130092055892

Read classification
for DNA_TCR_CoV_19_Non-virus_v2_20201130092055892

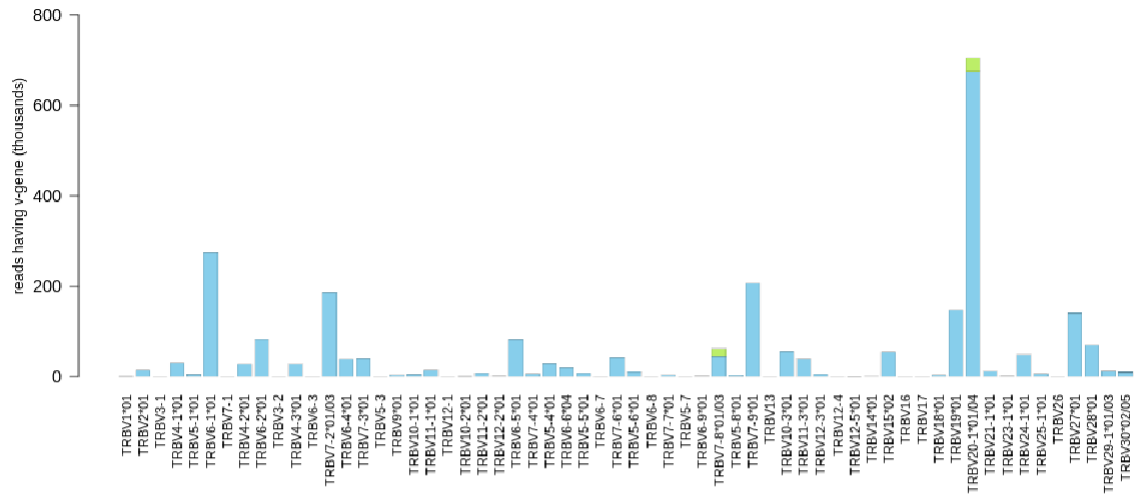


TCRB V-gene usage

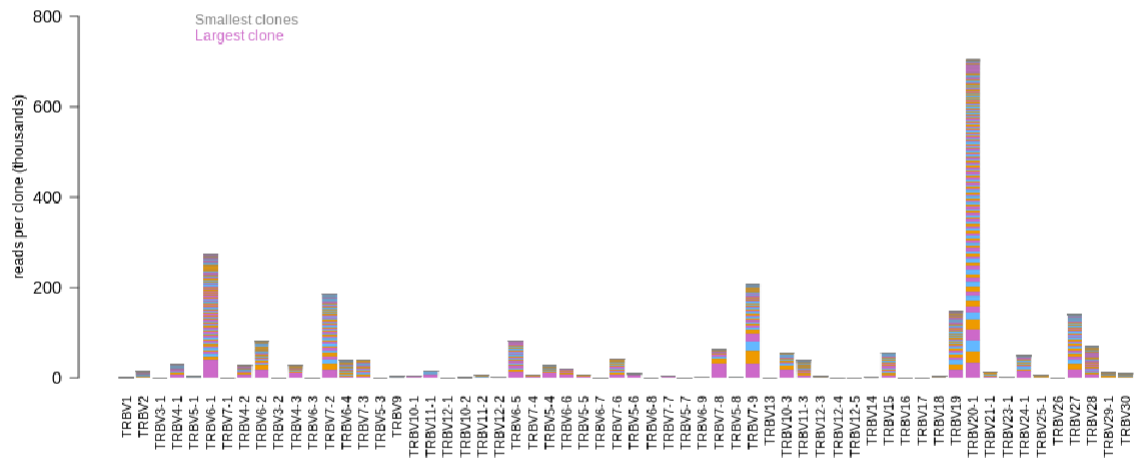


TCRB V-gene usage

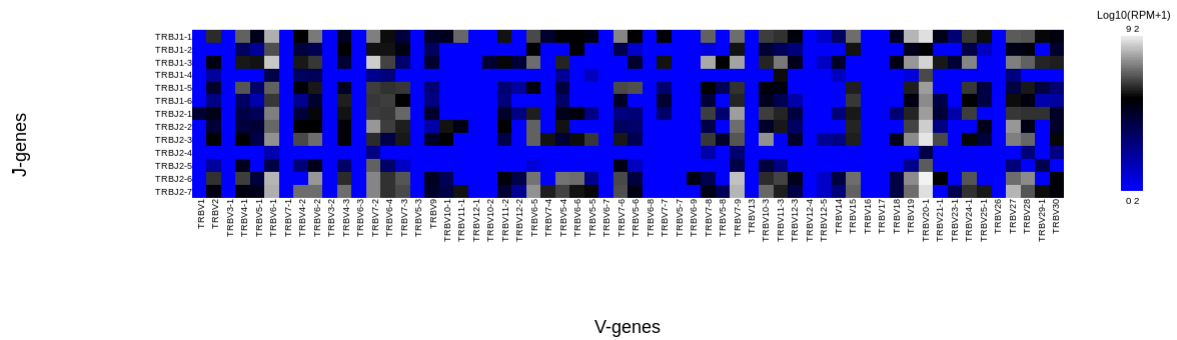
V-gene usage, colored by allele for DNA_TCR_CoV_19_Non-virus_v2_20201130092055892



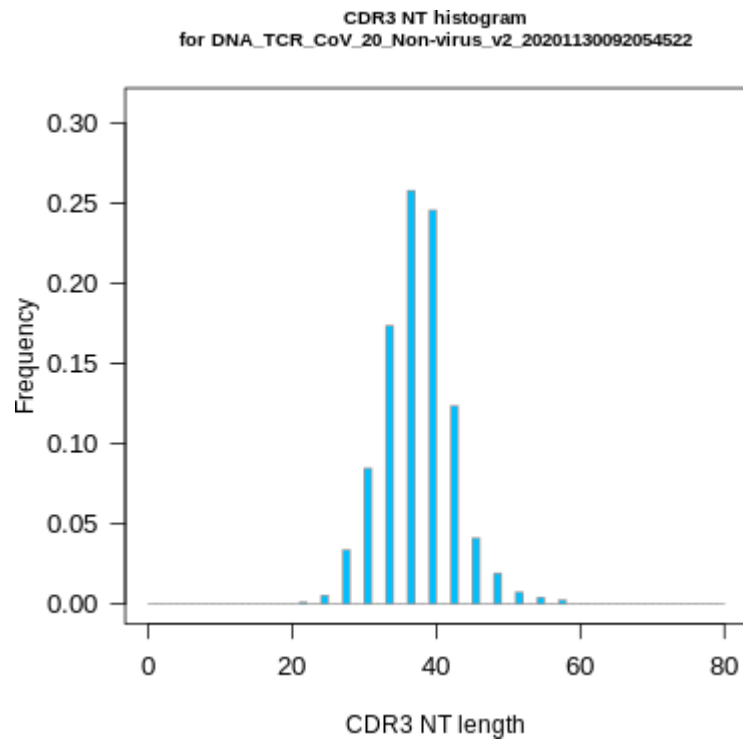
V-gene usage, colored by clone size for DNA_TCR_CoV_19_Non-virus_v2_20201130092055892



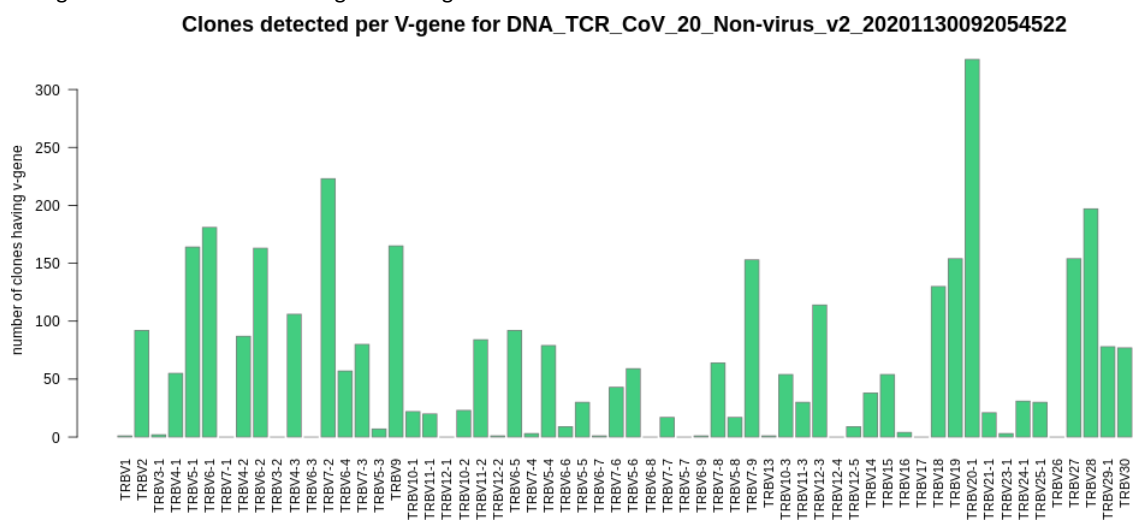
Log10 RPM of V-J pairs in
DNA_TCR_CoV_19_Non-virus_v2_20201130092055892



Non-virus lung case 5

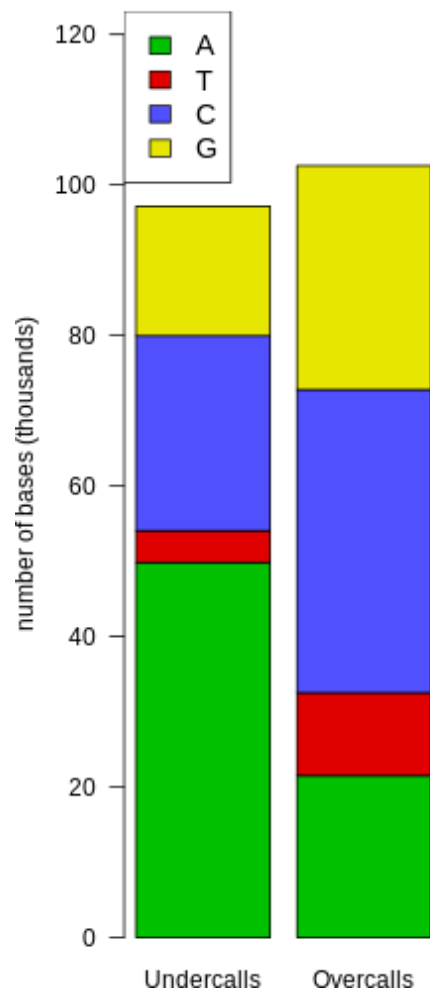


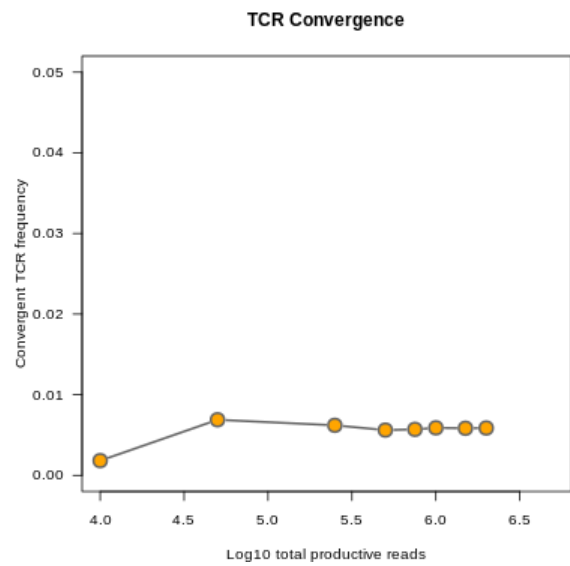
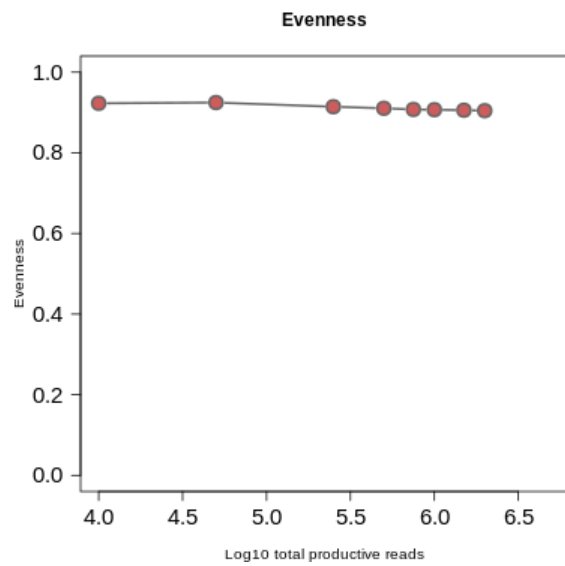
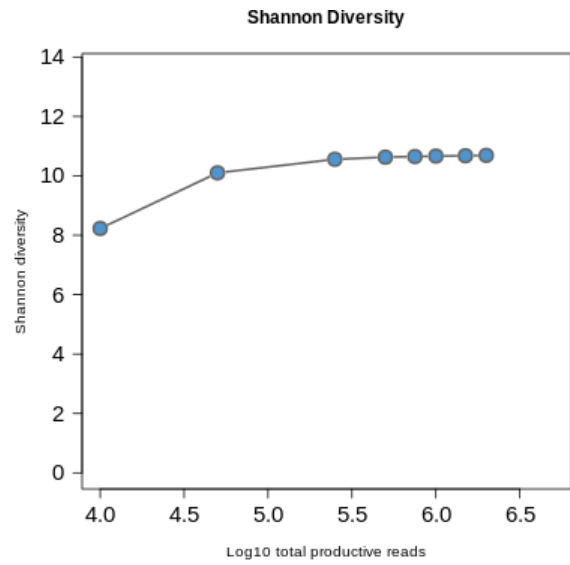
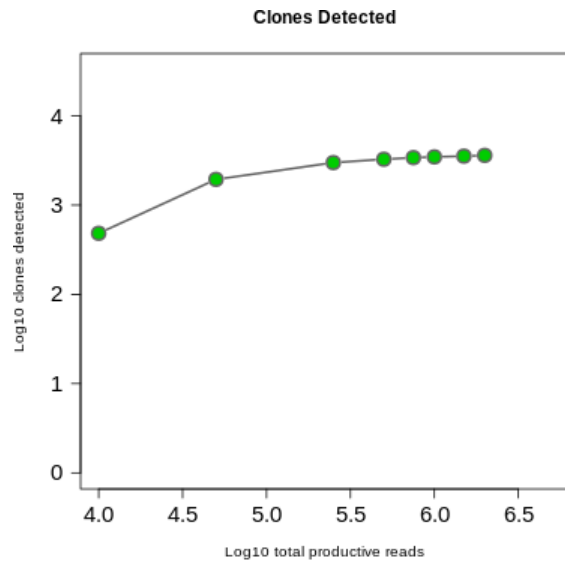
Histogram of CDR3 nucleotide length showing a normal distribution



Number of clones per V-gene

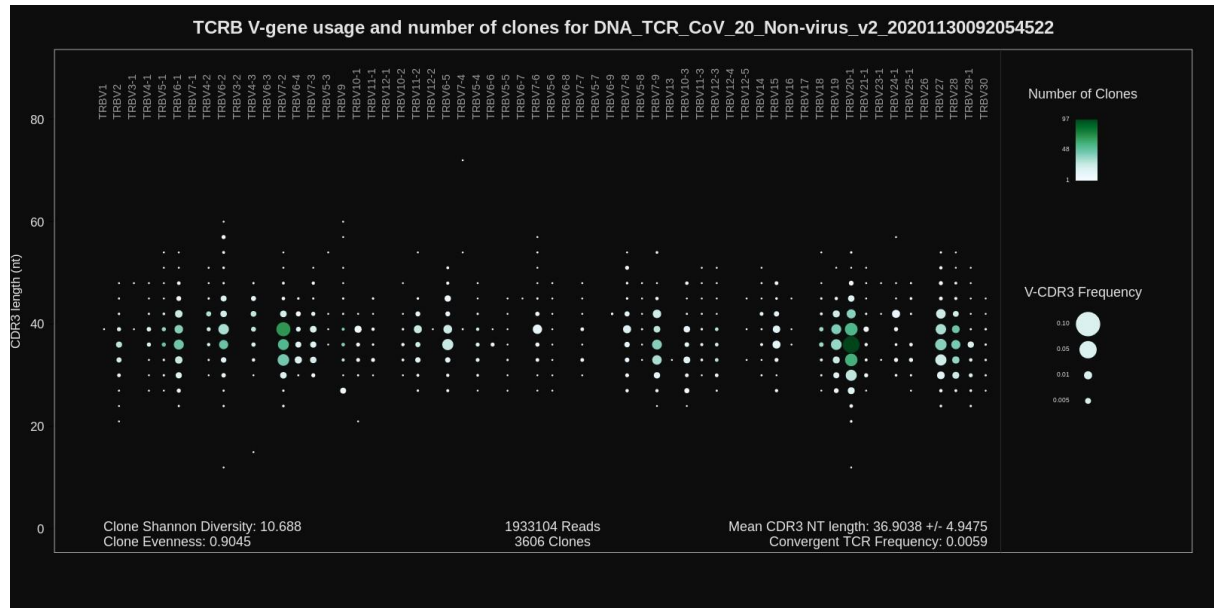
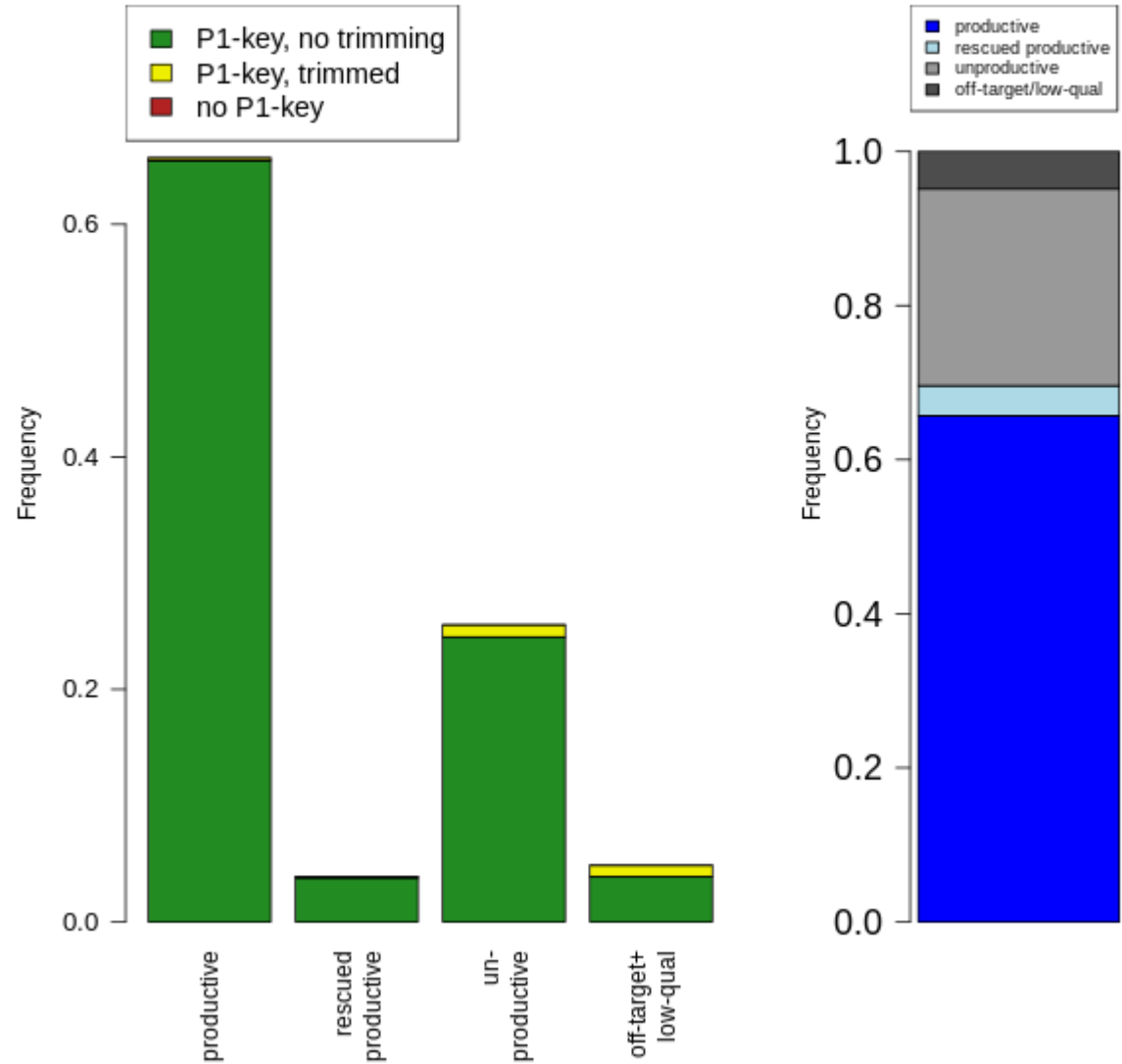
Repaired base composition
for DNA_TCR_CoV_20_Non-virus_v2_20201130092054



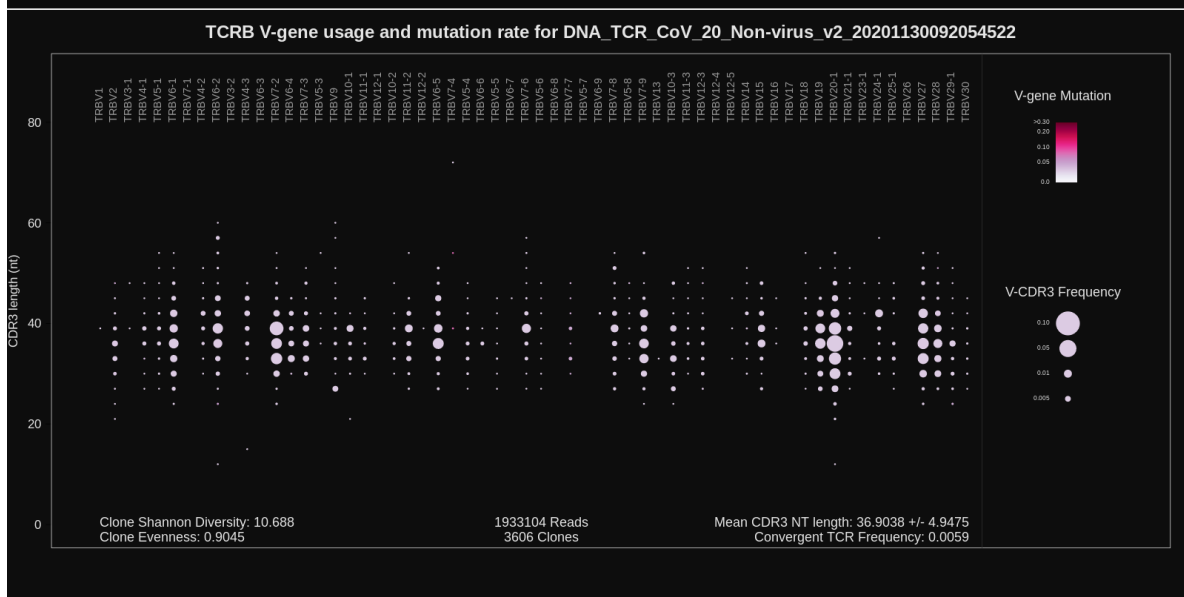
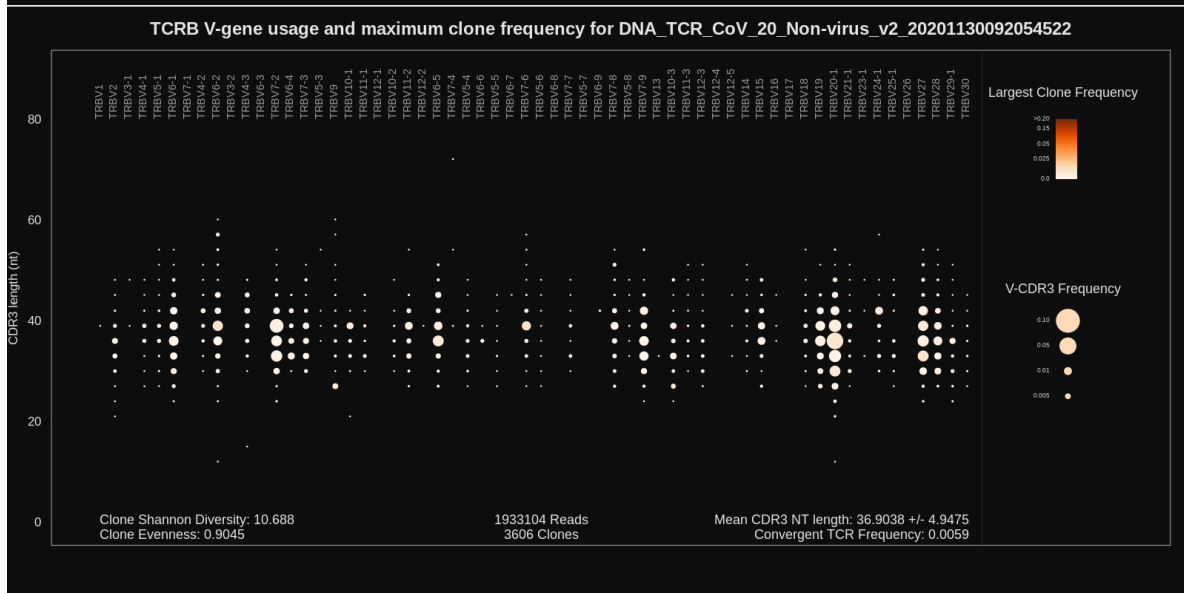
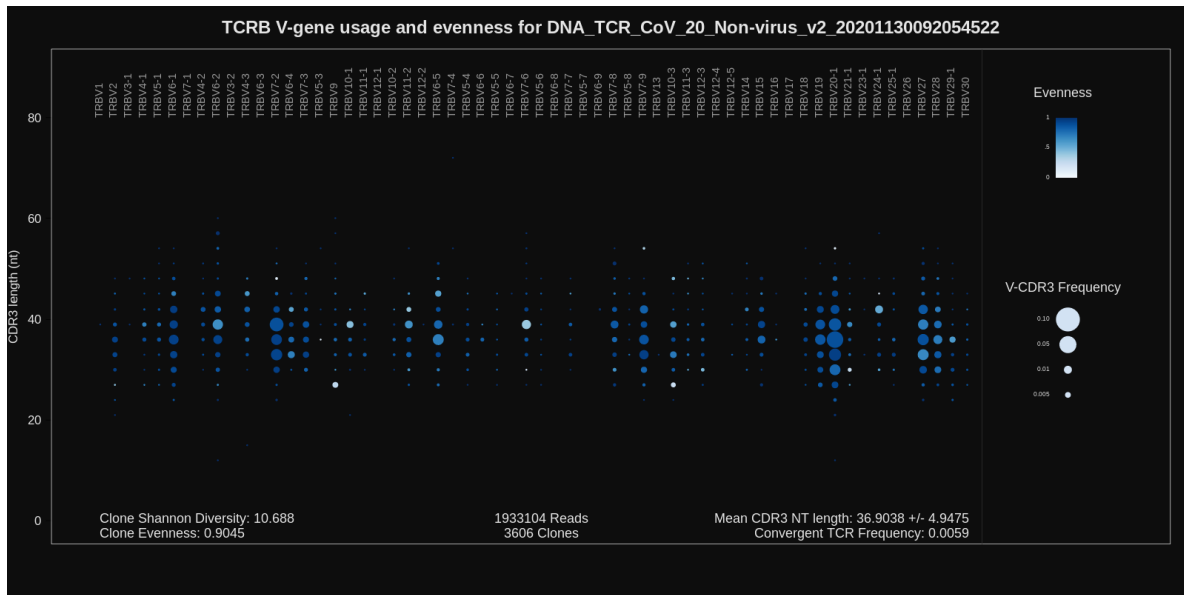


Presence of P1 adapter and quality trimming
for DNA_TCR_CoV_20_Non-virus_v2_20201130092054522

Read classification
for DNA_TCR_CoV_20_Non-virus_v2_20201130092054

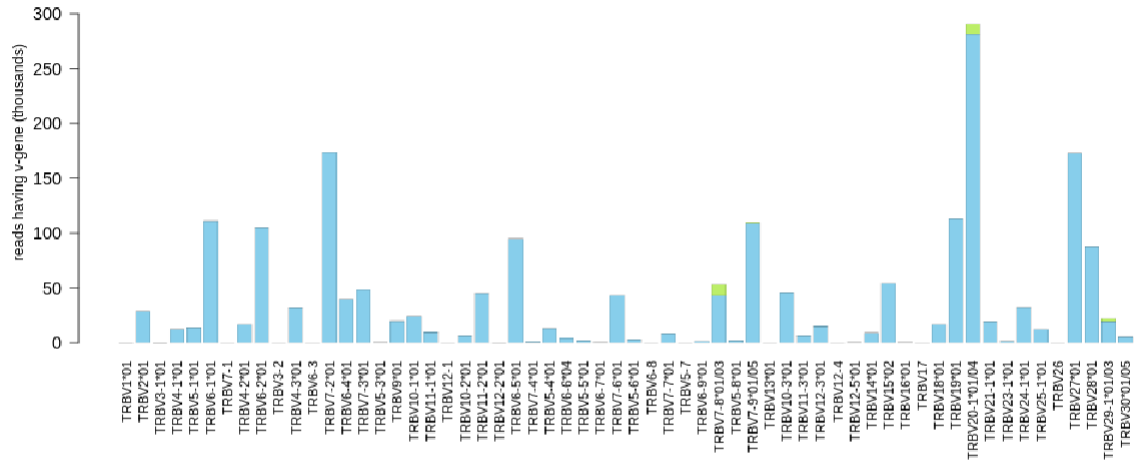


TCRB V-gene usage

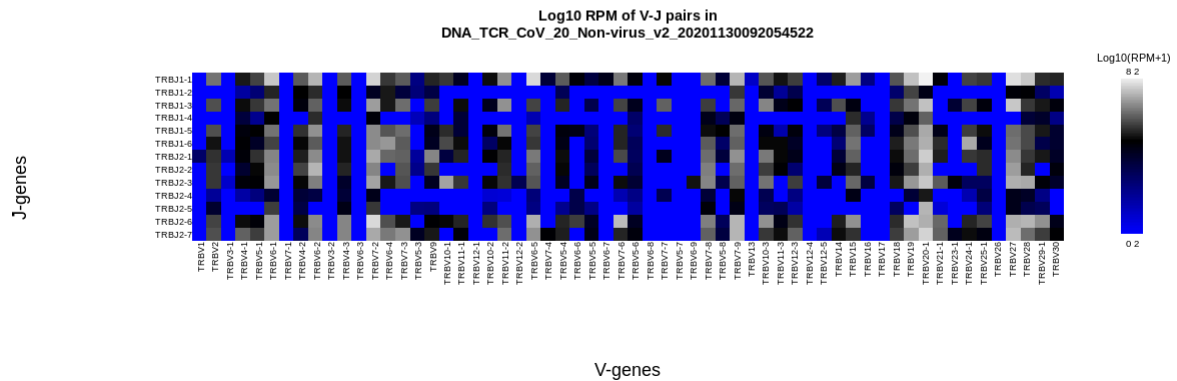
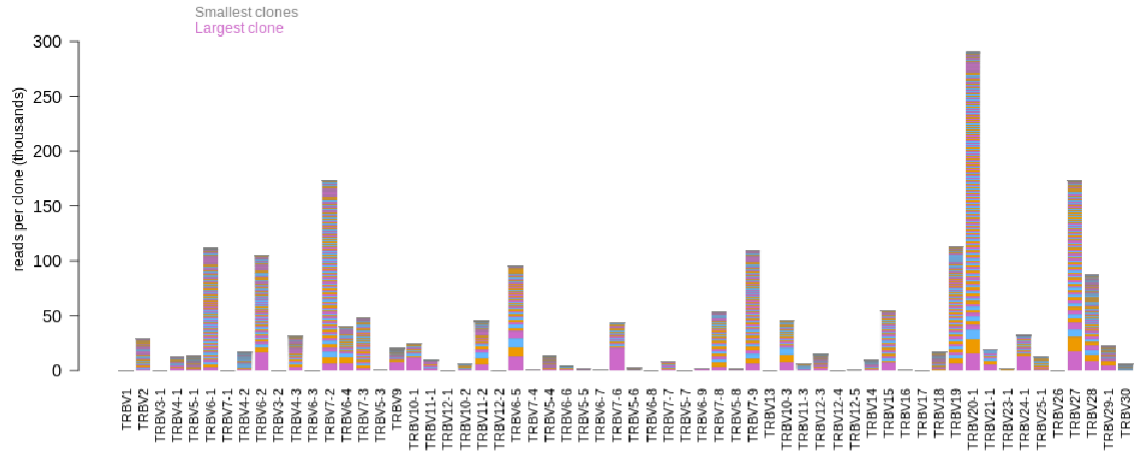


TCRB V-gene usage

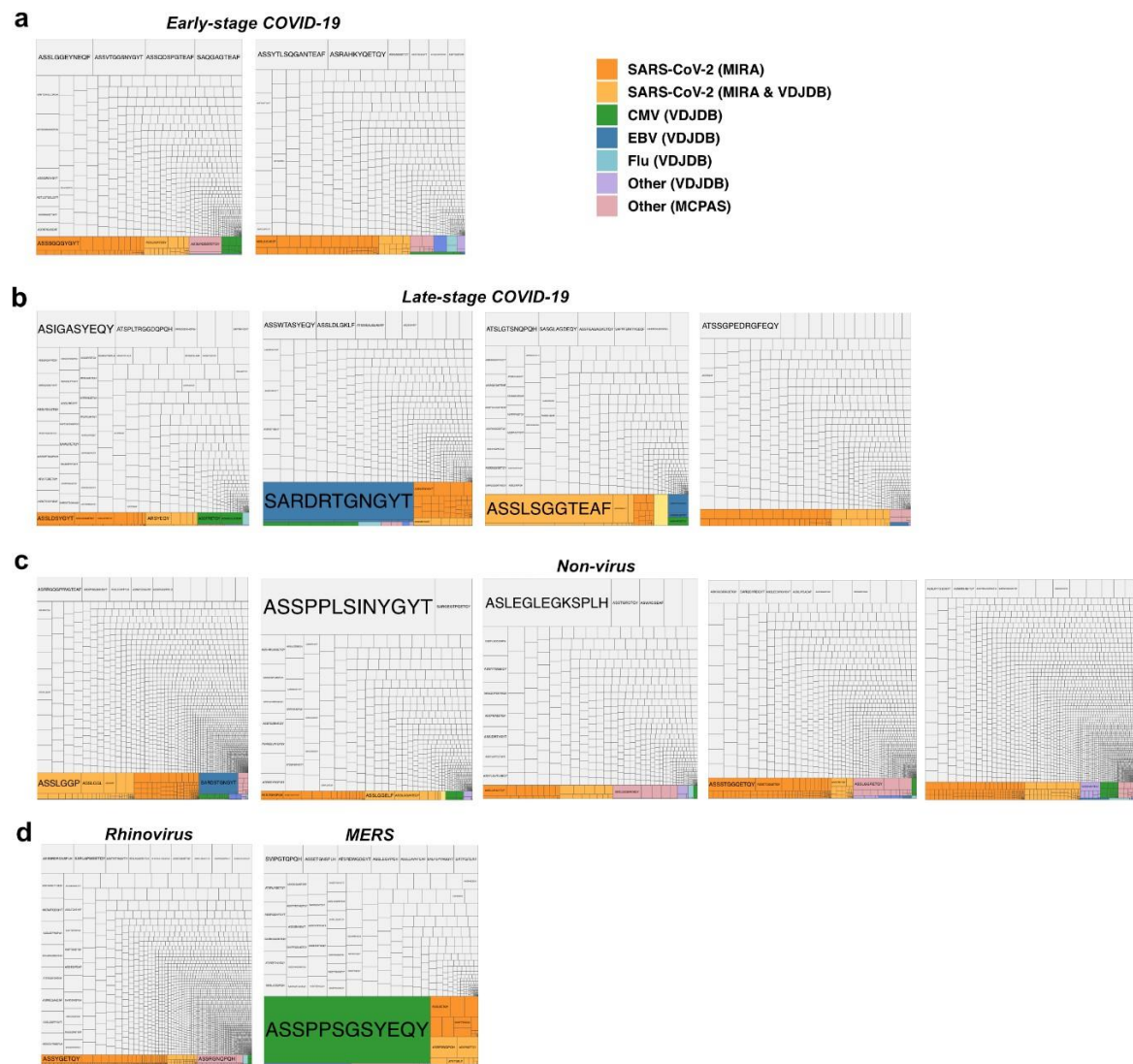
V-gene usage, colored by allele for DNA_TCR_CoV_20_Non-virus_v2_20201130092054522



V-gene usage, colored by clone size for DNA_TCR_CoV_20_Non-virus_v2_20201130092054522

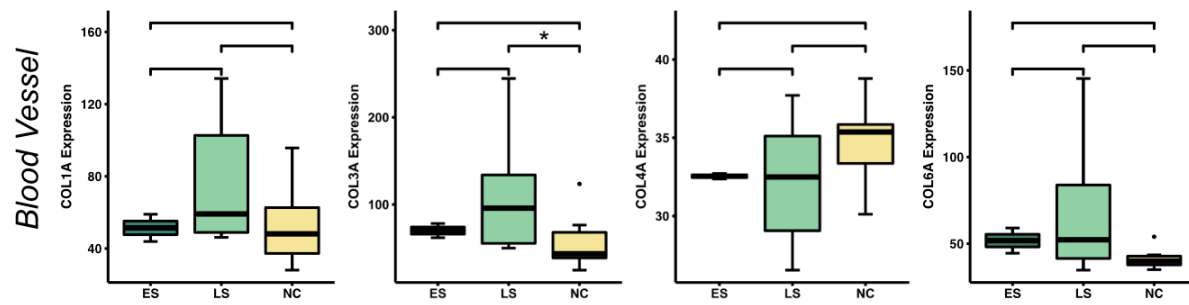


Appendix 5: Tree plots of TCR sequences



Appendix 5: Tree of TCR sequences specific for viruses in SARS-CoV-2 lungs and controls.

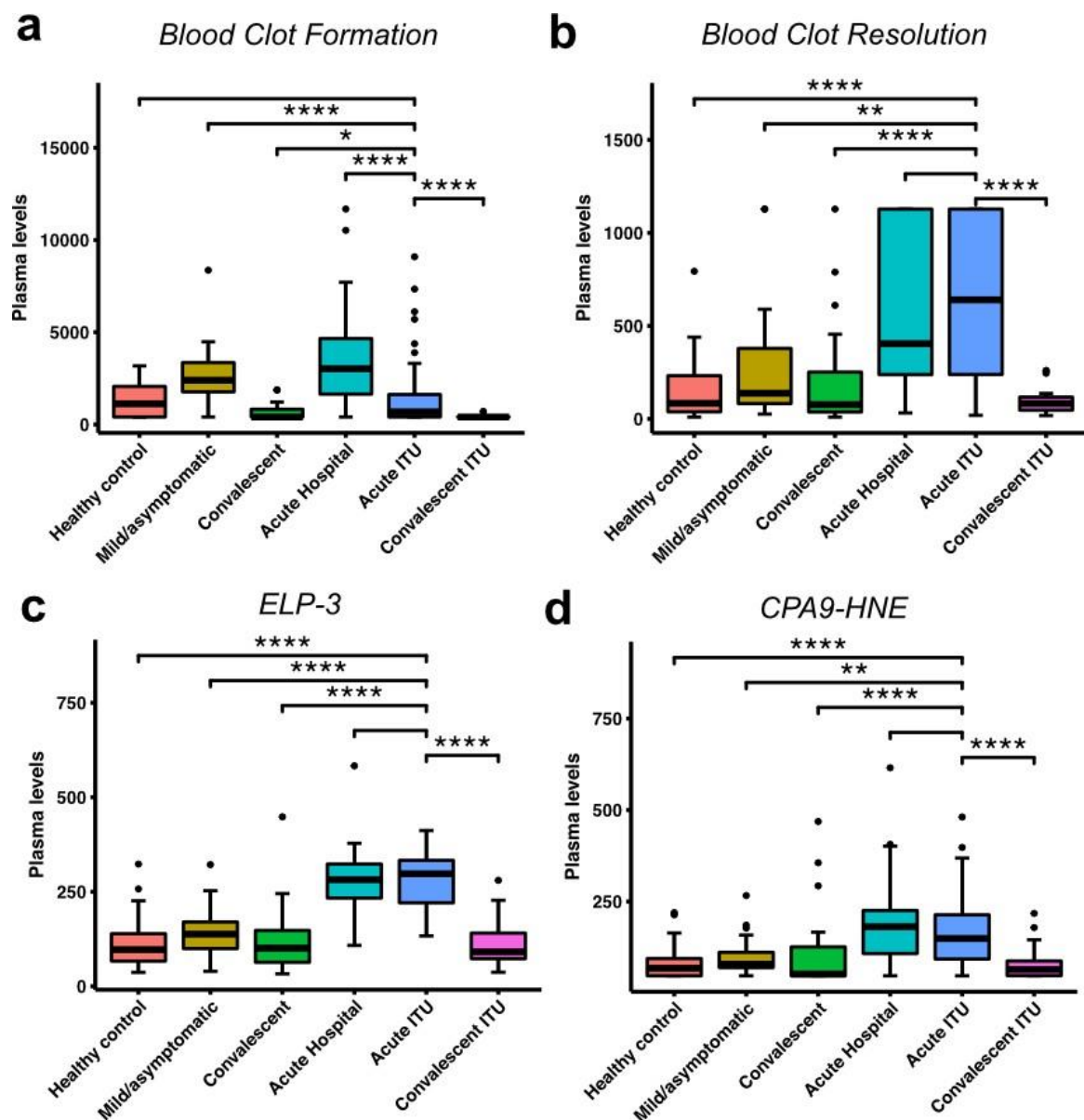
Appendix 6. Collagen gene expression in the blood vessel compartment



Appendix 6: GeoMX gene expression of collagens in the blood vessel compartment of COVID-19 lungs (ES, early stage; LS, late stage) and controls ; *= Statistically significant difference with a P-value of <0.05;

=p<0.01,*p<0.001; ****p<0.0001. (N.B. Wilcoxon statistical test performed)

Appendix 7: Serum ELISA blood clot and neutrophil markers



Appendix 7: Serum ELISA levels for of markers for blood clot formation, blood clot resolution, ELP3 and CPA9-HNE measured across SARS-CoV-2+ patients and controls. ; *= Statistically significant difference with a P-value of <0.05; **=p<0.01; ***p<0.001; ****p<0.0001. (N.B. Wilcoxon statistical test performed)

